

ABSTRACT OF DISSERTATION

Chiranjib Dutta

The Graduate School
University of Kentucky

2010

MEASUREMENT OF SINGLE-TARGET SPIN ASYMMETRIES IN THE
ELECTROPRODUCTION OF NEGATIVE PIONS IN THE SEMI-INCLUSIVE DEEP
INELASTIC REACTION $n^{\uparrow}(e, e'\pi^-)X$ ON A TRANSVERSELY POLARIZED ${}^3\text{He}$
TARGET

ABSTRACT OF DISSERTATION

A dissertation submitted in partial fulfillment of the
requirements for the degree of Doctor of Philosophy
at the University of Kentucky

By

Chiranjib Dutta

Lexington, Kentucky

Director: Dr. Wolfgang Korsch, Professor of Physics and Astronomy

Lexington, Kentucky

2010

Copyright © Chiranjib Dutta 2010

ABSTRACT OF DISSERTATION

MEASUREMENT OF SINGLE-TARGET SPIN ASYMMETRIES IN THE ELECTROPRODUCTION OF NEGATIVE PIONS IN THE SEMI-INCLUSIVE DEEP INELASTIC REACTION $n^\uparrow(e, e'\pi^-)X$ ON A TRANSVERSELY POLARIZED ${}^3\text{He}$ TARGET

The experiment E06010 measured the target single spin asymmetry (SSA) in the semi-inclusive deep inelastic (SIDIS) $n^\uparrow(e, e'\pi^-)X$ reaction with a transversely polarized ${}^3\text{He}$ target as an effective neutron target. This is the very first independent measurement of the neutron SSA, following the measurements at HERMES and COMPASS on the proton and the deuteron. The experiment acquired data in Hall A at Jefferson Laboratory with a continuous electron beam of energy 5.9 GeV, probing the valence quark region, with $x = 0.13 \rightarrow 0.41$, at $Q^2 = 1.31 \rightarrow 3.1 \text{ GeV}^2$. The two contributing mechanisms to the measured asymmetry, *viz*, the Collins effect and the Sivers effect can be realized through the variation of the asymmetry as a function of the Collins and Sivers angles. The neutron Collins and Sivers moments, associated with the azimuthal angular modulations, are extracted from the measured asymmetry for the very first time and are presented in this thesis. The kinematics of this experiment is comparable to the HERMES proton measurement. However, the COMPASS measurements on deuteron and proton are in the low- x region. The results of this experiment are crucial as the first step toward the extraction of quark transversity and Sivers distribution functions in SIDIS. With the existing results on proton and deuteron, these new results on neutron will provide powerful constraints on the transversity and Sivers distributions of both the u and d -quarks in the valence region.

Chiranjib Dutta

June 14, 2010

MEASUREMENT OF SINGLE-TARGET SPIN ASYMMETRIES IN THE
ELECTROPRODUCTION OF NEGATIVE PIONS IN THE SEMI-INCLUSIVE DEEP
INELASTIC REACTION $n^\uparrow(e, e'\pi^-)X$ ON A TRANSVERSELY POLARIZED ${}^3\text{He}$
TARGET

By

Chiranjib Dutta

Dr. Wolfgang Korsch
(Director of Dissertation)

Dr. Joseph W. Brill
(Director of Graduate Studies)

June 14, 2010
(Date)

DISSERTATION

Chiranjib Dutta

The Graduate School
University of Kentucky

2010

MEASUREMENT OF SINGLE-TARGET SPIN ASYMMETRIES IN THE
ELECTROPRODUCTION OF NEGATIVE PIONS IN THE SEMI-INCLUSIVE DEEP
INELASTIC REACTION $n^{\uparrow}(e, e'\pi^{-})X$ ON A TRANSVERSELY POLARIZED ${}^3\text{He}$
TARGET

DISSERTATION

A dissertation submitted in partial fulfillment of the
requirements for the degree of Doctor of Philosophy
at The University of Kentucky

By

Chiranjib Dutta

Lexington, Kentucky

Director: Dr. Wolfgang Korsch, Professor of Physics and Astronomy

Lexington, Kentucky

2010

Copyright © Chiranjib Dutta 2010

To my parents

Joga and Indira Dutta

ACKNOWLEDGEMENTS

This work would have not been possible without the support and encouragement of many people, both from physics and non-physics domains. Hence, I would like to take this opportunity to express my sincere gratitude to all of them who have always been with me and for me, throughout this wonderful journey.

First and foremost, I would like to thank my advisor Wolfgang Korsch for all his support since I started in the Department of Physics and Astronomy at the University of Kentucky. His excellent knowledge of physics unambiguously helped me in developing interest in this field. Wolfgang has always given me exemplary guidance to develop the necessary skills and the way to cultivate the ability to think independently as a graduate student. Besides his extensive experience with different electronics and various programming skills which motivated me learning the details of different electronic instruments thoroughly as well as improving my poor programming knowledge, his extremely jovial nature kept me inspired all the time. I consider myself very lucky to have Wolfgang as my advisor who was not only extremely caring but he also made me feel very comfortable and secured, especially when someone is thousands of miles away from home. Wolfgang has always given me freedom to work on my own. He has been there for me with his evergreen smile whether it is a research related problem due to my stupid endeavor or it is something on the personal front. I will always treasure my every single moment with Wolfgang.

I would like to thank Jian Ping Chen for all his support and critical advices as my supervisor at Jefferson Lab. His unbelievable patience in tackling any experimental problem and explaining the related physics not only helped me understanding the subject matter more vividly but also developing an efficient way of analyzing the experimental data.

I would like to thank Xiaodong Jiang, Jen Cheih Peng, Haiyan Gao and Evaristo Cisbani for their valuable advices during the experiment as well as during the analysis process. I would also like to thank Alessandro Bacchetta for all his theoretical discussions with me, especially for answering my very naïve questions.

I am indebted to a very precious group of people for their constant support throughout my stay at Jefferson Lab. I would like to express my heartiest acknowledgment to the following:

Vincent Sulkosky for introducing me to the Hall A analyzer and teaching me the very basics of data analysis. I learnt a lot of analysis skills from him during and after the

experiment.

Yi Qiang for his tremendous support in developing the target system and his judicious analysis help. I will always cherish the moments with him, be it in the experimental hall during the target installation and laser alignment or at lunch in the RED CITY buffet.

Xiaofeng Zhu for his initial support to get me started in the polarized ^3He laboratory.

Ameya Kolarkar for his patience in answering all my stupid questions even in the middle of the night. I will always appreciate his invaluable help throughout all the time.

Jaideep Singh for sharing all his expertise in ^3He target polarimetry and his excellent ability to explain the very minute details of everything. I consider the hours we sat together for different discussions most priceless in my graduate career.

Al Gavalya, Joyce Miller and Susan Esp for their dedicated endeavor dealing with the complicated target design and my naïve questions regarding different aspects of the engineering designs; Ed Folts and Jack Segal for their constant support in everything inside the experimental hall; The Jlab alignment group, especially Chris Curtis, Jim Dahlberg and company for their time and effort in helping me in the magnetic field direction measurements in the hall; Mark Taylor for providing all his electronics and laser safety support.

Bryan Moffit, Brad Sawatzky and Alexandre Camosonne for their valuable tips on C++ and other hardware issues. I will always remember the good moments at Brickhouse with them.

My fellow workers Xin Qian, Kalyan Allada, Jin Huang, Joe Katich, Yi Zhang, Youcai Wang, Yaowei and Xiaohui Zhan for all their constant support and helpful discussions during the experiment and after. The moments we spent together during those sleepless nights in the hall doing the laser alignments and going for a 3 AM meal at IHOP will be with me forever. I appreciate and greatly value the analysis help from Xin, Jin and Kalyan. I wish all of them very best for their future endeavors.

I would like to thank my closest friends over the years, Pinkoo, Aseem, Rupak, Mridupawan, Manjit and Bhaskar for making my stay in US enjoyable and being with me in all ups and downs.

Back in the Department of Physics and Astronomy at the University of Kentucky, I am extremely thankful to Susan Gardner and Renee Fatemi for their valuable insights and suggestions as my Ph.D. committee members. I would like to thank Joe Brill and Tom Troland for being very helpful as the Directors of Graduate Studies; all the office staff

for their efficient handling of all the paperwork. I acknowledge all the help provided to me by the people in the physics department. My sincere thanks to the next generation experimenters : Gretchen Phelps, Mukut Ranjan Kalita, and all others for their valuable company.

Finally, I would like to thank my parents back in India who have always been with me and who have spent difficult times not seeing me for years. I dedicate this work to them for the very simple reason that I probably would not be writing at this moment if they were not there.

TABLE OF CONTENTS

Acknowledgements	iii
List of Tables	x
List of Figures	xii
CHAPTER 1: INTRODUCTION	1
1.1 The Structure of Matter : A Never-ending Quest	1
1.2 The Early Electron Scattering Experiments	2
1.3 Quantum Chromodynamics : The Gauge Theory of Strong Interactions . .	4
1.4 Spin of the Nucleon	6
1.5 Transverse Spin: Transversity, Sivers Distribution and Collins Fragmentation Function	7
1.6 Outline of the Thesis	10
CHAPTER 2: DEEP INELASTIC SCATTERING AND TRANSVERSITY	11
2.1 Inclusive Deep-Inelastic Scattering (DIS)	11
2.1.1 General Formalism for Deep Inelastic Cross Section	13
2.1.2 The Unpolarized Spin-independent DIS Cross Section	16
2.1.3 The Polarized Spin-dependent DIS Cross Section	17
2.1.4 Experimental Measurements of Structure Functions	18
2.2 Quark Parton Model (QPM) and Quantum Chromodynamics (QCD)	23
2.2.1 Gluonic Interaction in QPM	27
2.3 Quark-quark Correlation Matrix in the QCD Improved QPM	29
2.3.1 Probabilistic Interpretation of the Distribution Function	32
2.3.2 Vector, Axial and Tensor Charge	33
2.4 Distribution Functions with Quark-nucleon Helicity Amplitudes	33
2.5 Transverse Motion of Quarks : Transverse Momentum Dependent Distribu- tion Function	37
2.6 The Semi-Inclusive Deep Inelastic Scattering (SIDIS) and Fragmentation Functions (FF)	39
2.7 The SIDIS Cross Section	42
2.8 The Collins and Sivers Moments	47
2.9 Summary of HERMES and COMPASS Results	50
CHAPTER 3: THE EXPERIMENT	54
3.1 Overview of CEBAF	54
3.1.1 Polarized Electron Source	56
3.2 Beamline	58
3.2.1 Beam Energy	58

3.2.2	Beam Current	60
3.2.3	Beam Position	63
3.3	Beam Polarization	64
3.3.1	Compton Polarimeter	65
3.3.2	Møller Polarimeter	67
3.4	Hall A Left High Resolution Spectrometer (LHRS)	70
3.4.1	LHRS Design and Characteristics	70
3.4.2	Detector Package	71
3.4.3	Vertical Drift Chambers (VDCs)	73
3.4.4	Lead-Glass Counters	76
3.4.5	Gas Čerenkov Counter	77
3.4.6	Aerogel Čerenkov Counter A1	78
3.4.7	RICH Detector	79
3.4.8	S1 and S2m Scintillator Planes	81
3.5	The BigBite Spectrometer	82
3.5.1	Multi-Wire Drift Chambers	83
3.5.2	Scintillators	84
3.5.3	Shower and Preshower Detectors	85
3.6	Hall A Data Acquisition System (DAQ)	86
3.7	Trigger Formation and Electronics	86
3.8	Scaler and Dead Time Measurement	89
CHAPTER 4: THE POLARIZED ^3He TARGET		95
4.1	Polarized ^3He Nuclei As An Effective Neutron Target	95
4.2	Basic Principle	96
4.2.1	Optical Pumping	96
4.2.2	The Spin Exchange	98
4.2.3	More On Hybrid Spin-Exchange and Polarization of ^3He	99
4.3	The Target System	101
4.3.1	The ^3He Cell	102
4.3.2	Target Ladder	104
4.3.3	Oven, Heater, and Airflow System	105
4.3.4	Holding Field Set Up	106
4.4	Laser and Polarizing Optics	108
4.4.1	Laser and Optical Fibers	108
4.4.2	Optics	109
4.5	Polarimetry	111
4.5.1	Nuclear Magnetic Resonance (NMR)	111
4.5.2	Electron Paramagnetic Resonance (EPR)	115
4.6	Polarimetry Analysis and Results	126
4.6.1	EPR Analysis	126
4.6.2	Water NMR Calibration	131
4.7	Magnetic Field Direction Measurement	135
4.8	Target Spin Flip System	143

CHAPTER 5: DATA ANALYSIS	146
5.1 Left High Resolution Spectrometer (LHRS) Calibrations	146
5.1.1 Vertical Drift Chambers (VDC)	146
5.1.2 Gas Čerenkov (GC)	148
5.1.3 Aerogel Čerenkov (A1)	150
5.1.4 Lead-Glass Counter (Pion Rejector)	150
5.1.5 Scintillator (S2m)	150
5.2 BigBite Spectrometer	153
5.2.1 BigBite Multi Wire Drift Chamber (MWDC)	154
5.2.2 Preshower/Shower Detector	156
5.2.3 Scintillator Plane	157
5.3 Detector Efficiency Study	158
5.3.1 Gas Čerenkov (GC) Efficiency in the LHRS	158
5.3.2 Lead Glass Counter Efficiency	160
5.3.3 Aerogel (A1) Efficiency	162
5.4 LHRS Contamination Study	165
5.4.1 Electron Contamination to Pions	165
5.4.2 Pion Contamination to Electrons	167
5.5 BigBite Optics	167
5.6 LHRS Optics Calibration	170
5.7 Coincidence Time-of-Flight	172
5.7.1 LHRS Timing Calibration	175
5.7.2 BigBite Timing Calibration	181
5.7.3 Two Arm Coincidence Time Calibration	183
5.8 Calibration and Analysis of Elastic Events	184
5.8.1 Physics Formalism of Elastic $\bar{e}^{-3}\text{He}$ Scattering	185
5.8.2 Elastic Asymmetry Results and Target Spin Sign Convention	187
5.9 Delta ($\Delta(1232)$) Asymmetry Results	192
5.10 N_2 Dilution in ^3He	194
5.11 BigBite Spectrometer Contamination Study	196
5.11.1 π^{-} Contamination Study	201
5.11.2 Photon Induced Electron Contamination	203
CHAPTER 6: ASYMMETRY ANALYSIS AND RESULTS	206
6.1 The Analysis Flow	206
6.2 Asymmetry Formalism	209
6.3 Asymmetry : Local Pair Method/Super Local Pair Method	209
6.4 Detector PID Cuts, Acceptance and Kinematic (SIDIS) Cuts	210
6.5 Phase Space and Angular Coverage	213
6.6 Inclusive Asymmetries in the LHRS	214
6.7 Inclusive Asymmetries in the BigBite Spectrometer	219
6.8 Coincidence Single Spin Asymmetry	220
6.8.1 Extraction of Collins and Sivers Moments for π^{-} Mesons	221
6.9 Systematic Uncertainties	225
6.10 Nuclear Correction	228
6.10.1 Effective Nucleon Polarization in ^3He	228

6.11 The Collins and Sivers Moments for π^- Mesons On the Neutron	230
CHAPTER 7: SUMMARY AND OUTLOOK	233
APPENDIX A: LIGHT-CONE COORDINATES	236
APPENDIX B: OPTICAL THEOREM	238
APPENDIX C: RADIATION LENGTH	240
APPENDIX D: ACCEPTANCE CUTS (R-CUT)	242
APPENDIX E: TARGET WINDOW ASYMMETRY IN THE LHRS	244
APPENDIX F: EXTRACTION OF THE NEUTRON SINGLE SPIN ASYMMETRY FOR SIDIS OFF TRANSVERSELY POLARIZED ^3He	247
APPENDIX G: SYSTEMATIC UNCERTAINTY BUDGET	250
Bibliography	251
Vita	258

LIST OF TABLES

2.1	Important kinematic variables in DIS. Here the mass of the incoming electron is neglected and a fixed target is assumed. Also, $\hbar = c = 1$ is adopted.	13
2.2	The three independent variables ϕ_h , z , and P_h , in addition to x and Q^2 , in terms of which the cross section in SIDIS can be expressed.	14
3.1	The Arc measurement result during E06-010. The corresponding result from the Tiefenbach method is also shown.	60
3.2	The Møller polarization measurement results during E06-010.	70
3.3	LHRS characteristics	71
3.4	The different triggers formed during the experiment. T1, T3 and T5 are the relevant ones.	89
4.1	A few useful parameters associated with a typical hybrid cell and the spin exchange process. Most of these quantities are explained in [1]. T represents the temperature in Kelvin. The densities of ^3He , N_2 , and alkali atoms are typical values at our working temperature of 230°C	101
4.2	The respective numbers are from the University of Virginia and the College of William and Mary database. V_p is the volume of the pumping chamber, V_t is the volume of the target chamber, and V_{tt} is the volume of the transfer tube.	103
4.3	Dimensions of the Helmholtz coils used in the experiment to produce the magnetic field holding the spins of the ^3He spins.	106
4.4	Current settings for the three pairs of Helmholtz coils. \vec{B} stands for the holding magnetic field direction, I_S for the current in the small coils, I_L for the current in the large coils, and I_V for the current in the vertical coils. The small and the large coils are the two pairs used to produce the field in horizontal directions. The typical magnitude of the magnetic field generated in any of these two directions is 25 Gauss.	107
4.5	The laser parameters used throughout the experiment. It is important to mention here that the diode temperatures were adjusted a few times during the experiment. They were more or less consistent with the numbers listed.	108
4.6	Data were taken with three sets of current settings in the vertical coil. $\theta_{BB=0}$ represents the measured angle when the BigBite magnetic field was off while $\theta_{BB=1}$ represents the angle when the BigBite magnetic field was on.	140
4.7	The fitting parameters from the Eq.(4.69) for the center position.	142
4.8	The final values of the currents in all the three Helmholtz coils for a vertical magnetic field in E06010.	142
5.1	Gas Čerenkov detector efficiencies with the standard cut on the ADC sum (<250).	160
5.2	Lead glass detector efficiencies with the standard cut on $\frac{E}{p} < 0.6$	162
5.3	The filling densities of ^3He and N_2 for all the three cells used in the experiment.	195
5.4	N_2 dilution factors for each x bin for π^- production.	196
5.5	The T5 events pion to electron contamination study in BigBite.	203
5.6	The γ -induced electron contamination of the DIS electrons in the BigBite spectrometer for the coincidence events (T5 trigger).	205

6.1	Inclusive single spin asymmetries in the LHRS for the vertical target polarization. The asymmetries are corrected for polarization. No correction has been applied for the N ₂ dilution.	218
6.2	Inclusive single spin asymmetries in the LHRS for the transverse target polarization. The asymmetries are corrected for ³ He polarization. No correction has been applied for the N ₂ dilution.	219
6.3	The systematic uncertainties in E06010 for the SIDIS process ³ He↑(e, e'π ⁻)X. Type A represents the systematic uncertainty with respect to the central value of the asymmetry. The type B represents the systematic uncertainty as percentage of the statistical uncertainty in the asymmetry.	227
6.4	The values of the neutron dilution factors used in the extraction of the neutron asymmetries from the measured ³ He asymmetries.	230
6.5	The results of the Collins (<i>A_C</i>) and Sivers moments (<i>A_S</i>) on the neutron for four <i>x</i> bins. The statistical and the total systematic uncertainties are represented by σ_{stat} and σ_{sys} , respectively.	232
C.1	The radiation lengths of different materials. These were used in the MC studies and other optics calibrations for the detectors.	241
G.1	Systematic uncertainties contributing to the extracted asymmetries which are not included in the fitting procedure. The uncertainties presented in the table are in percent of the statistical error bars in the asymmetries. The contributions to the Collins and Sivers moments represent the uncertainty values in the four <i>x</i> bins used in E06010. In the calculation of the uncertainties for ³ He, the small dilution due to proton (-2.8%) was not taken into account. .	250

LIST OF FIGURES

1.1	σ/σ_{Mott} as a function of Q^2 for $W = 2, 3,$ and 3.5 GeV at $\theta = 10^\circ$.(Reproduced from [2]).	3
1.2	Summary of measurements of α_s as a function of Q where the curves represent the QCD predictions for the combined world average value of α_s . M_Z is the rest mass of the Z° boson. The full symbols are results based on N3LO QCD, open circles are based on NNLO, open triangles and squares on NLO QCD. The cross filled square is based on lattice QCD. The figure is reproduced from [3]. The details of the calculations and measurements can also be found in [3].	5
2.1	Schematic of Deep Inelastic Scattering (DIS) process. The leptonic tensor $L_{\mu\nu}$ and the hadronic tensor $W_{\mu\nu}$ are described in the text in subsection (2.1.1).	12
2.2	The world data on the spin independent proton structure function F_2 [4]. The error bars shown in the plot are the combined statistical and systematic errors in quadrature. In the plot F_2 is multiplied by 2^{i_x} where i_x is the number of x bins ranging from $i_x = 1$ to $i_x = 28$ (corresponds to $0.85 < x < 0.00006$).	21
2.3	The world data on the spin independent deuteron structure function F_2 [4]. The error bars shown in the plot are the combined statistical and systematic errors in quadrature. In the plot F_2 is multiplied by 2^{i_x} where i_x is the number of x bins ranging from $i_x = 1$ to $i_x = 29$ (corresponds to $0.85 < x < 0.0009$).	22
2.4	The world data on the spin dependent structure function g_1 [4].	23
2.5	Partons in the nucleon carrying a momentum fraction x of the nucleon viewed collectively as a beam.	25
2.6	Deep inelastic scattering interpretation in QMP.	25
2.7	The $\mathcal{O}(\alpha\alpha_s)$ correction due to the gluon radiated by a quark.	28
2.8	The handbag diagram for the DIS process involving the quark-quark correlation function Φ . Here, P and S are the momentum and the spin of the nucleon respectively in the initial state. q is the four momentum transfer and p represents the initial four momentum of the quark.	29
2.9	The handbag diagrams for the unpolarized distribution $q(x)$ (left), helicity distribution $\Delta q(x)$ (middle) and the transversity distribution $\delta q(x)$ (right). There are helicity flips of both quark and nucleon in case of $\delta q(x)$ and hence helicity is not conserved. In each of the diagrams, the top pair of signs (+ or -) represents the helicities of the quark and the bottom pair represents the helicities of the nucleon.	34
2.10	The Q^2 evolution of the transversity distribution function $\delta q(x)$ and the helicity distribution $\Delta q(x)$ for <i>up</i> and <i>down</i> quarks. This Chiral Quark Soliton Model calculation shows that for both <i>up</i> and <i>down</i> quarks, the Q^2 evolutions of the respective distributions differ in the low x region. These figures have been taken from [5].	36
2.11	The Q^2 evolution of the transversity distribution function $\delta q(x)$ and the helicity distribution $\Delta q(x)$ for <i>anti-up</i> and <i>anti-down</i> quarks. This Chiral Quark Soliton Model calculation shows that for both <i>anti-up</i> and <i>anti-down</i> quarks, the Q^2 evolutions of the respective distributions differ in the low x region [5].	37
2.12	The Soffer bound for the twist-2 distribution functions [5].	38

2.13	The transverse momentum dependent (TMD) parton distribution functions. Only leading twist functions are shown. The large circle represents the nucleon and the small circle depicts the quark inside it. The arrow associated with the respective nucleon and the quark signifies the spin orientation of them.	39
2.14	The transverse momentum dependent (TMD) fragmentation functions (twist-2). The unpolarized fragmentation function is shown in the left while the Collins fragmentation function is depicted on right. The large circle represents the unpolarized hadron produced by the fragmenting quarks which are represented by the small circle inside the large one.	41
2.15	Schematic of the kinematic planes and azimuthal angles related to the transverse component of the target spin $\vec{S}_{\perp}^{\vec{z}}$ and the transverse component of the momentum of the produced hadron $\vec{P}_{h\perp}$	43
2.16	The Collins (left) and the Sivers (right) moments for the charged hadrons as a function of x , z and $P_{h\perp}$. The systematic uncertainties are represented by the shaded band [6].	50
2.17	The Collins moments for the charged hadrons and K° as a function of x , z and P_T^h [7].	51
2.18	The Sivers moments for the charged hadrons and K° as a function of x , z and P_T^h [7].	52
2.19	The Collins moments for the unidentified charged hadrons as a function of x , z and P_T^h [8].	52
2.20	The Sivers moments for the unidentified charged hadrons as a function of x , z and P_T^h [8].	53
3.1	The CEBAF aerial view in Newport News. The three experimental Halls are also shown [9].	54
3.2	Schematic of the accelerator and its components. Reproduced from [10]. . .	55
3.3	A typical RF cavity.	56
3.4	Different layers of GaAs and the degenerate states available for optical pumping.	57
3.5	Schematic of the complete angle measurement in the arc energy method. The wire scanners and the mirrors in the middle of the arc are shown with their respective angles.	59
3.6	The BCM system reproduced from [11].	61
3.7	The electronics in the BCM system.	62
3.8	The beam position monitors.	63
3.9	Schematic of the Compton polarimetry set up.	66
3.10	Schematic of the Møller polarimeter reproduced from [10].	68
3.11	The Møller measurement results during E06010.	71
3.12	The schematic of the LHRS showing the geometrical configuration of the QQDQ layout. The first VDC plane is also shown [12].	72
3.13	The layout of the detector packages in the LHRS [13].	73
3.14	Schematic diagram of the LHRS VDC planes. Reproduced from [12].	74
3.15	The 5-cell configuration in LHRS VDCs [13].	76
3.16	Pion Rejector: Layer1 and Layer2. Reproduced from [12].	77
3.17	Schematic of the A1 counter.	79
3.18	The RICH detector working principle [13].	80

3.19	A schematic of the S1 scintillators for reference. S2m has the same structure except it has 16 paddles and the paddles do not overlap. This figure is reproduced from [13].	82
3.20	The schematic of the BigBite spectrometer package [14].	83
3.21	The orientation of the U, V and X planes in MWDC.	84
3.22	Schematic of preshower and shower blocks. The scintillators are also shown.	85
3.23	The general flow chart of the CODA configuration [15].	87
3.24	Schematic of the trigger electronics in LHRS [16].	91
3.25	The preshower and shower energy sum formation for the trigger in BigBite [15].	92
3.26	A schematic of the trigger electronics in BigBite [15]	93
3.27	Schematic of the coincidence trigger logic [15].	94
3.28	The relative timing scheme of the triggers used in E06010. The timing of the T5 is given by the leading edge of T1 [15].	94
4.1	Different ground state wave functions of ${}^3\text{He}$. The pink circle represents a proton and the red circle represents a neutron.	96
4.2	The process of optical pumping (left) and the polarization transfer from Rb to K and K to ${}^3\text{He}$ via spin exchange (right) [10].	98
4.3	A typical spin up curve for one of the hybrid cells used in E06010. The fitting function is $A(1 - Be^{-t/C})$ where the fitting parameter A represents the expected maximum value of the NMR amplitude and C represents the spin up time. B is irrelevant to our measurement. In the plot, $A = 46.53 \pm 0.08$ mV and $C = 4.42 \pm 0.04$ hours.	102
4.4	Orientation of the hybrid cell in the Hall A coordinate system. The pumping chamber and a part of the transfer tube are inside the oven which is not shown here.	103
4.5	Schematic diagram of the target ladder system.	105
4.6	Schematic diagram of the Helmholtz coil system used in E06010 in Hall A. The RF coils and the pick up coils are also shown [9].	107
4.7	Schematic diagram of the optics setup. This setup was for the vertical pumping. For the transverse pumping, another mirror was attached to the oven not shown in the figure. The reflected light from the big mirror MB2, in this case, was incident on that mirror mounted on the oven. The rest of the setup was the same.	110
4.8	The electronic set up for the NMR measurements. The figure is reproduced from [10].	114
4.9	NMR frequency sweep signal fitted to the square root of a Lorentzian function.	115
4.10	The splitting of the $S_{1/2}$ and $P_{1/2}$ states of Rb into sub-states in the presence of an external magnetic field. The absorption and the emission of the 795 nm laser light are also shown for a few selected transitions.	117
4.11	Schematic diagram of the EPR setup in the experiment. The blue connections correspond to the GPIB controls and the arrows represent the connections with the BNC cables.	120
4.12	A typical EPR frequency lineshape spectrum recorded in the lock-in amplifier. The blue lines show the region where the frequency needs to be locked with the feedback mechanism discussed in the text. The region between point A and point B is fitted with a first order polynomial in order to determine the slope. The range of the fit is ~ 50 kHz.	122

4.13	A typical EPR AFP spectrum. $\vec{B} + \Delta\vec{B}$ ($\vec{B} - \Delta\vec{B}$) corresponds to the state when the magnetic field generated by ^3He is parallel (anti-parallel) to the holding field.	123
4.14	EPR PI feedback circuit used in the experiment.	124
4.15	The polarization results from the all the EPR measurements for all the cells in the transverse (top) and the vertical (bottom) target polarization configuration. The polarization numbers are determined using the direct extraction method.	130
4.16	The EPR AFP spectrum and the corresponding NMR signals for each ^3He spin flip during AFP.	131
4.17	The calibration constants from the EPR measurements for the transverse and vertical target polarizations. The red points correspond to the constants determined from the <i>sweep up</i> signals and the blue points correspond to the constants from the <i>sweep down</i> signals.	132
4.18	A typical water NMR signal (2000 sweeps).	133
4.19	The 40 cm longitudinal compass. During the measurements, point A and B were surveyed by the survey group.	136
4.20	The side view of the vertical compass assembly. This figure is obtained from Ref. [17].	136
4.21	Definition of the vertical angle θ with respect to the incoming beam.	139
4.22	The direction of the vertical field as a function of vertical coil current with the BigBite magnetic field turned on and off.	141
4.23	The deviation of the measured vertical angle and the angle determined from the fit.	142
4.24	Schematic diagram of the spin flip distribution scheme.	144
4.25	Schematic diagram of the spin flip system structure.	145
5.1	A drift-time spectrum of a VDC plane.	147
5.2	The corrected timing spectra of the four VDC planes after calibration.	148
5.3	The Gas Čerenkov ADC sum spectrum after calibration.	150
5.4	All 10 ADC spectra for the Gas Čerenkov after calibration.	151
5.5	The A1 Čerenkov detector ADC sum spectrum after calibration.	152
5.6	The Lead-glass counter E/p spectrum after calibration.	152
5.7	The incoming particle hitting the two adj-ascent paddles in the S2m.	153
5.8	A typical distribution of the wire hits in the U1 plane in the first chamber in E06010. The separation of different read-out amplifier cards are represented by the red lines [18].	155
5.9	The drift time spectrum in the X -plane of the second chamber. The left plot shows the spectrum for all the events and the right plot shows the drift time for the particles for which a valid track was reconstructed. t_0 is also shown [18].	155
5.10	$\frac{E}{p}$ for the electrons in the preshower and shower detectors for two different incident beam energies. E is the total energy deposited by the electron having momentum p	158
5.11	The lead glass layer 1 and layer 2 energies. The graphical cuts used in the analysis are also shown.	159

5.12	The Gas Čerenkov detector response to the lead glass counter cuts. The left figure shows the comparison of a typical GC spectrum and a GC spectrum triggered by the electrons chosen in the lead glass counters. The right figure shows a comparison of a typical GC spectrum and a GC spectrum triggered by the pions chosen in the lead glass counters.	160
5.13	The Gas Čerenkov detector efficiencies with the standard Aerogel ADC sum cut > 150	161
5.14	The Gas Čerenkov detector efficiencies without any Aerogel detector ADC sum cut.	161
5.15	The lead glass counter efficiencies with a standard Aerogel detector ADC sum cut >150	163
5.16	$\frac{E}{p}$ spectra of the lead-glass counter with different GC detector cuts.	163
5.17	The energy of lead glass layer 1 vs. the energy of layer 2 with different GC detector cuts.	164
5.18	The (e', π) coincidence time spectrum. The pink lines show the cut region to select coincidence pions. This plot corresponds to the coincidence spectrum for the hadrons when the LHRS polarity was positive and hence, there is a proton peak on the left, ~ 7 ns away from the pion peak.	164
5.19	The A1 detector pion detection efficiencies as a function of ADC sum cuts.	165
5.20	The BigBite vertex reconstruction at a momentum of 1.2 GeV/c.	169
5.21	The reconstructed sieve plate with different correction terms [18].	170
5.22	The BigBite spectrometer momentum reconstructions at beam energies of 1.200 GeV/c and 2.396 GeV/c.	171
5.23	The z-component of the LHRS reaction vertex: each of the carbon foil peaks was fitted and compared to the actual position from the survey report.	172
5.24	The reconstructed LHRS sieve slit plate.	173
5.25	The x and θ dependences of RF without (left) and with (right) pathlength corrections.	177
5.26	The y and ϕ dependences of RF without (left) and with (right) pathlength corrections.	178
5.27	The x projection of the tracks in the S2m paddles and the time offsets before (left) and after (right) correction.	179
5.28	Timewalk effect for the electrons in S2m (paddle 8).	180
5.29	Timewalk effect for the pions in S2m (paddle 8).	180
5.30	The RF structure in the LHRS for pions and electrons after all the corrections have been applied. The resolution of the pions is ~ 141 ps while that of the electrons is ~ 132 ps.	181
5.31	The RF structure in the BigBite scintillator for electrons after all the corrections were applied. The resolution in this case is ~ 270 ps [19].	183
5.32	The final CTOF spectrum for the reaction $(e, e'\pi)$. Here, the CT spectrum is shown for the LHRS with positive polarity. When the LHRS was in negative polarity, the spectrum looks the same except that there would not be any proton peak on the left [19].	184

5.33	The polarization of the target during the elastic data taking. A few measurements of polarization were performed in between the runs. The points corresponding to each run were determined after an interpolation of the measured polarization value between the runs. The huge drop between the third and the fourth points was due to some technical issues in the Hall where we had to stop the beam and waited for some time without polarizing the target.	188
5.34	The ^3He raw elastic asymmetries.	189
5.35	The ^3He physics elastic asymmetries.	190
5.36	Raw Δ resonance asymmetries. The asymmetry changes sign as the polarization direction is reversed from transverse + to transverse -. All these measurements were done with the beam half wave plate inserted.	193
5.37	The N_2 dilution factors for all the four x bins. The three points for each bin correspond to the three cells used in the experiment. The points are for <i>Astral</i> , <i>Maureen</i> , and <i>Brady</i> respectively from the left for each x .	195
5.38	The optics validity cut in the BigBite spectrometer. The black points show all the reconstructed events in the spectrometer while the red points show the events that pass the optics validity cut. As can be seen, the events corresponding to the edges of the magnet have been removed.	197
5.39	The energy deposition in the preshower vs. the $\frac{E}{p}$ of the total shower.	199
5.40	The reconstructed vertex. Electron like events were chosen to generate the plot. The cuts for the coincidence as well as singles events are shown which are slightly different.	200
5.41	The pion contamination to electrons in BigBite for various momentum bins for T1 events.	202
5.42	The yields of electron-like events in the negative polarity mode compared to the positron-like events in the positive polarity mode in the BigBite spectrometer. The red data points represent the positrons and the black data points represent the electrons. Both negative and positive polarities in the LHRS were considered. The large error bars indicate the low statistics of the positron-like events [18].	204
6.1	The analysis flow of the data in experiment E06010.	207
6.2	The charge asymmetry comparison between the <i>local pair method</i> (left) and the <i>super local pair method</i> (right) [18].	211
6.3	Q^2 distribution for each x-bin. The violet line shows the cut $Q^2 > 1 \text{ GeV}^2$.	212
6.4	The invariant mass spectrum for each x-bin. The violet line shows the cut $W > 2 \text{ GeV}$.	212
6.5	The invariant mass spectrum of the pions for each x-bin. The violet line shows the cut $W' > 1.5 \text{ GeV}$.	213
6.6	To ensure the current fragmentation region, a cut $0.3 < z < 0.7$ is chosen. z is shown for four different x-bins.	213
6.7	The phase space for the reaction $n^\dagger(e, e'\pi^-)X$ in E06010. The plots are generated after applying all the relevant cuts used in the analysis [18].	214
6.8	The angular coverage of the target spin angle (ϕ_S) and the outgoing hadron plane angle (ϕ_h) with respect to the scattering plane. The coverages for all the x-bins are shown [18].	215

6.9	The single spin asymmetries measured in the LHRS for all the particles detected in the vertical ^3He polarization configuration. The particles include electrons, pions, and protons.	216
6.10	The single spin asymmetry measured in the LHRS for all the particles detected in the transverse ^3He polarization configuration. The particles include electrons, pions, and protons.	217
6.11	The formation of a scalar in case of inclusive reactions for both transverse (left) and vertical (right) target polarization configurations. \vec{k}_1 , \vec{k}_2 , and \vec{S}_T are defined in the text.	217
6.12	A_N for π^+ , π^- , and π^0 mesons as a function of x_F . The figure is reproduced from [20].	218
6.13	Single target spin asymmetries for the negatively charged hadrons in the BigBite spectrometer in the four momentum bins. The asymmetries are corrected for target polarization. However, no N_2 dilution factor has been taken into account. The red points correspond to the events with the T6 trigger and the black points correspond to the events with the T1 trigger.	219
6.14	Single target spin asymmetries for the positively charged hadrons in the BigBite spectrometer in the four momentum bins. The asymmetries are corrected for target polarization. However, no N_2 dilution factor has been taken into account. The red points correspond to the events with the T6 trigger and the black points correspond to the events with the T1 trigger.	220
6.15	Single target spin asymmetries for π^- -mesons in the SIDIS $^3\text{He}^\uparrow(e, e'\pi^-)X$ reaction for different momentum bins in the BigBite spectrometer. The asymmetries are corrected for ^3He polarization, but not for N_2 dilution.	221
6.16	The single target spin asymmetries for the SIDIS $^3\text{He}^\uparrow(e, \pi^-\pi^-)X$ reaction for different momentum bins in the BigBite spectrometer. The asymmetries are corrected for ^3He polarization, but not for N_2 dilution.	222
6.17	The single target spin asymmetries for the SIDIS $^3\text{He}^\uparrow(e, \gamma\pi^-)X$ reaction for different momentum bins in the BigBite spectrometer. Only the correction for ^3He polarization has been applied. N_2 dilution factor has not been taken into account.	222
6.18	The Collins and Sivers moments extracted from different fitting methods of the angular dependences of ^3He raw asymmetries.	223
6.19	The Collins and Sivers moments for π^- mesons extracted from the ^3He asymmetries for different x bins. The error bars show the statistical uncertainties. The blue band represents the systematic uncertainties. The theoretical prediction from Anselmino <i>et al.</i> is shown by the purple line [21]. The dashed line is drawn to show zero. The results are prior to any radiative corrections (Preliminary).	225
6.20	The neutron dilution factors from model calculations for all the four x bins in π^- meson production.	230
6.21	The Collins and Sivers moments for π^- -mesons produced off neutrons and protons as predicted by Anselmino <i>et al.</i> [21].	231

6.22	The neutron Collins and Sivers moments for π^- meson production as a function of x . The statistical uncertainties are shown as the error bars associated with the points. The blue band represents the experimental systematic uncertainties. Different theoretical predictions are shown for comparison. The purple curve shows the prediction by Anselmino <i>et al.</i> [21], the green curve shows the prediction by Pasquini, [22], and the black curve is from Ma <i>et al.</i> [23], [24]. The dashed line shows indicates zero. The results are prior to any radiative corrections (Preliminary).	232
A.1	The light-cone coordinates.	236
B.1	The optical theorem relates the cross section in DIS to the imaginary part of the forward virtual Compton scattering [25].	238
C.1	The incoming and outgoing electron after scattering. The scattering angle $\theta = 16^\circ$	241
D.1	The acceptance cuts for the LHRS used in the analysis. The solid boundary represents the cuts. All the events inside the boundary were chosen for the asymmetry analysis [19].	243
E.1	The reaction vertex along the ^3He target with the target windows included (top) and the target windows only (bottom).	244
E.2	The measured asymmetries from the target windows for the identified particles in the case of the vertical magnetic field configuration.	245
E.3	The measured asymmetries from the target windows for the identified particles in the case of the transverse magnetic field configuration.	246
F.1	The Collins asymmetry (left) and the Sivers asymmetry (right) of the neutron for the electroproduction of π^- mesons. The full curve shows the complete calculation of the asymmetries while the dotted curve represents the corresponding asymmetries with only neutron polarization. The dashed curve is the relevant one for our purpose where the effective polarizations of both neutrons and protons along with their dilution factors are taken into account. The plots are corresponding to $z = 0.3, 0.45,$ and 0.6 from the top to bottom panels. For all of them, a Q^2 value of $2.2 \text{ GeV}^2/c^2$ is considered. The figure is taken from Ref. [26].	249

CHAPTER 1: INTRODUCTION

1.1 The Structure of Matter : A Never-ending Quest

The internal structure of matter has been the most interesting and the most exciting quest since the onset of human civilization. Both in the realms of science and philosophy, human minds have been trying to seek answers to the most fundamental thoughts such as: what is the origin of nature, what is nature made of, what are the fundamental particles and how do they create matter? In the process of understanding nature, people have come a long way and learned a lot about the constituents of matter and their various properties. However, there are still very important and challenging aspects that needed to be addressed regarding the internal structure of matter.

Before 1897, people had the strong belief of fact that atoms were not only the building blocks of matter but they were also indivisible. In 1897, the British physicist J.J. Thomson in the Cavendish Laboratory at Cambridge University discovered the “corpuscles” which were later termed as electrons. His venture into the interior of atoms and the resulting discovery of electrons was one of the biggest milestones in the history of science. This discovery of negatively charged electrons in the atom tremendously boosted the curiosity of the scientists to know more and more about the inner structure of atoms. Then almost 14 years later, the discovery of nucleus followed. In 1911, Ernest Rutherford discovered the nucleus, having observed the backward scattering of the alpha particles off a thin gold foil. The quest continued to look for the interior of the nucleus and, eventually, protons and neutrons were discovered. J. Chadwick won the Nobel prize for discovering the neutron. The protons and neutrons constitute the nucleus and are termed *nucleons*. Once the nucleons were discovered, the study of the properties of the nucleons lead to the further understanding of their structures and as a result, the concept of *quarks* emerged for the first time in 1964 when physicist Murray Gell-Mann [27] and George Zweig [28] independently proposed *quarks* as the building blocks of the nucleons. The nucleons belong to the general class called *hadrons*. Prior to the *elementary quark model* describing the formation of the *hadrons* from the *quarks*, Gell-Mann [29] and Yuval Ne’eman [30] introduced a classification scheme based on SU(3) symmetry, which placed the hadrons into families on the basis of

spin and parity. The quark model was a way to generate this classification scheme [2].

The study of the structure of hadrons in terms of the quarks themselves is a different and specific area of particle physics these days and it is referred to as *hadronic physics*. Hadrons are further classified into *baryons* and *mesons*. *Baryons* are hadrons with three constituent quarks and *mesons* are hadrons composed of a quark and an anti-quark. The *baryons* are hadrons of $1/2$ integer spin while the *mesons* are hadrons having integer spins. The very first quark model postulated three types of quarks, each being a spin- $1/2$ particle: up (u), down (d), and strange (s), with electric charges $2/3$, $-1/3$ and $-1/3$ respectively. Also in this model, a new degree of freedom was assigned to each quark called *flavor*. Even though the elementary quark model, which is often referred to as the constituent quark model, described the hadrons in terms of their properties such as spin, mass, charge etc., it was still considered just a mathematical representation. People were skeptical about the real existence of quarks until a few inelastic electron-nucleon scattering experiments were conducted. These experiments confirmed the physical identity of quarks. Nucleons are composite structures consisting of point-like spin- $1/2$ particles having fractional charges consistent with those of quarks. A comprehensive discussion on the key issues in hadronic physics can be found in Refs. [31], [32].

1.2 The Early Electron Scattering Experiments

The very first electron scattering experiment that revealed the existence of quarks in a hadron was performed at the Stanford Linear Accelerator Center (SLAC). The details of the experiments can be found in Refs. [33], [34]. The usual electron scattering experiment involves the incidence of a focused electron beam on a target and the detection of the scattered electrons, yielding information about the structure of the target. The experiments at SLAC used electrons scattered off a hydrogen target and the *virtual photon*¹ acted as a mediator of the electromagnetic interaction. The square of the four-momentum of the *virtual photon*, denoted commonly by Q^2 , is a measure of the resolution of the experiment.

¹The electron, being a charged particle, and the nucleon interact by electromagnetic force. This force is carried by a mediator or an exchange particle called the *virtual photon*. In the electron scattering process, it is not the incoming electron which probes the nucleon but the virtual photon which carries a fraction of the momentum of the electron and transfers it to the nucleon.

The high energy $e-p$ inelastic scattering at SLAC was dedicated to investigate the electromagnetic structure and interactions of the proton. With incident energies from 7 to 17 GeV at scattering angles of 6° to 10° , cross sections of the scattered electrons were measured up to a Q^2 value of $7.4 \text{ GeV}^2/c^2$. The results of the experiment are shown in Fig. 1.1 where the ratio of the differential cross section to the Mott cross section (scattering cross section from a point particle) is plotted as a function of the momentum transfer squared (Q^2) for a scattering angle $\theta = 10^\circ$. Data are shown for three different values of the invariant mass²(W) as well as for the $e-p$ elastic scattering.

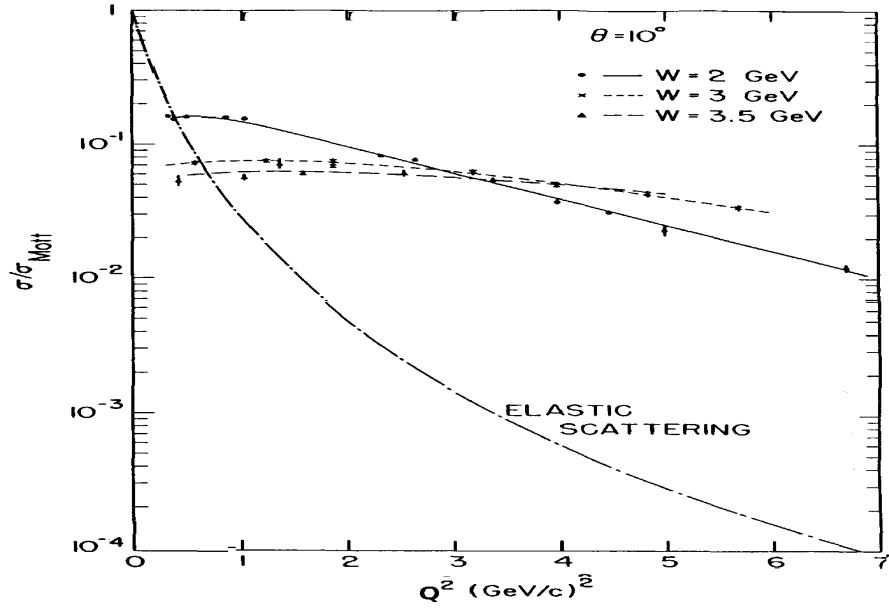


Figure 1.1: σ/σ_{Mott} as a function of Q^2 for $W = 2, 3,$ and 3.5 GeV at $\theta = 10^\circ$. (Reproduced from [2]).

As can be seen clearly, with an increase of the invariant mass W from 2 GeV to 3.5 GeV , the dependence of the ratio on Q^2 gets weaker with respect to the elastic case.

Following these results, J. Bjorken postulated that the scattering cross sections, instead, depend on a single variable (x) later named as *Bjorken-x*. The variable x is a dimensionless quantity which is defined as $x = \frac{Q^2}{2.M.\nu}$ where M is the mass of the target nucleon, ν is the energy loss between the incoming and the scattered electrons and Q^2 is the four momentum

²The invariant mass of a particle or a system of particles is a mathematical combination of the total energy and momentum of the particle or the system of particles which is independent of the inertial frame of reference. If the system is at rest, the invariant mass is the total energy of the system divided by c^2 where c is the velocity of light.

transfer carried by the *virtual photon* as mentioned earlier. This independence of the cross section on Q^2 and the dependence on x is termed *scaling* [35] and will be discussed later. This *scaling behavior* was then interpreted by Feynman, leading to the introduction of the parton model which describes the proton to be composed of point-like particles called *partons* at that time and later known as quarks. It turned out that the *Quark Parton Model* enjoyed a great triumph and was a profound complement to the prevailing postulates by Gell Mann *et al.* regarding the behavior of the quarks in explaining different properties of the proton. However, as time passed by, new unexpected experimental results gradually started demanding more explanations which required the refinement of the existing Quark-Parton model or the definition of an improved theory which will be summarized in the next section.

1.3 Quantum Chromodynamics : The Gauge Theory of Strong Interactions

The Quark-Parton model was successful in describing various aspects of the structure of hadrons in terms of quarks, yet it could not explain all the observed experimental results. For instance, the model was not sufficient to interpret the missing momentum of the nucleons. It was discovered experimentally that only half of the nucleon's momentum came from the constituent quarks. Another important aspect that drew attention to many physicists was the nature of the binding of the quarks inside a nucleon. The quarks are bound and confined very strongly in order to form the nucleon in such a way that realization of a free isolated quark is unrealistic in practice. This situation is technically termed as *quark confinement*. On the other hand, in the scattering process of electrons off a nucleon at very high four momentum transfers (Q^2), the quark inside the nucleon can behave like an isolated particle which is probed by the *virtual photon*. This situation can be realized in the deep inelastic scattering characterized by $Q^2 > 1 \text{ GeV}^2/c^2$ and $W > 2 \text{ GeV}$ and referred to as *asymptotic freedom*. In order to describe and support these observations, a general theory was needed. The notion of *quark confinement* was addressed by assigning a new quantum number *color* to the quarks which requires that they can not be isolated and observed directly. The situation of *asymptotic freedom* was explained by D. Gross, F. Wilczek, and D. Politzer using non-abelian quantum field theory and finally this was followed by the introduction of Quantum Chromodynamics (QCD). QCD is the theory of strong interaction that was proposed to describe the binding of quarks and gluons together to form the hadrons.

In a more technical language, it is a field theory of color interactions discussed extensively in Refs. [36], [37], [38].

Following the formalism of Quantum Electrodynamics (QED), where an electromagnetic coupling constant α determines the strength of the electromagnetic interaction, a strong coupling constant α_s can be introduced in QCD to determine the strength of the strong or color interaction. Fig. 1.2 shows the running of α_s as a function of Q . *Asymptotic freedom* can be described by QCD because the coupling between the quarks is very weak at large Q or at short distances. In this region, perturbation theory can be applied because α_s is small; α_s can be used as a perturbative expansion parameter. On the other hand, at low Q , as can be seen from the plot, α_s is large and hence, perturbative QCD can not be used to describe the *confinement* of quarks. Non-perturbative QCD should be able to address *confinement* as a fundamental property. The lattice QCD [39] displays *confinement* in the non-perturbative region; the confining potential between the quarks increases linearly with the separation if the quark mass is made infinitely heavy.

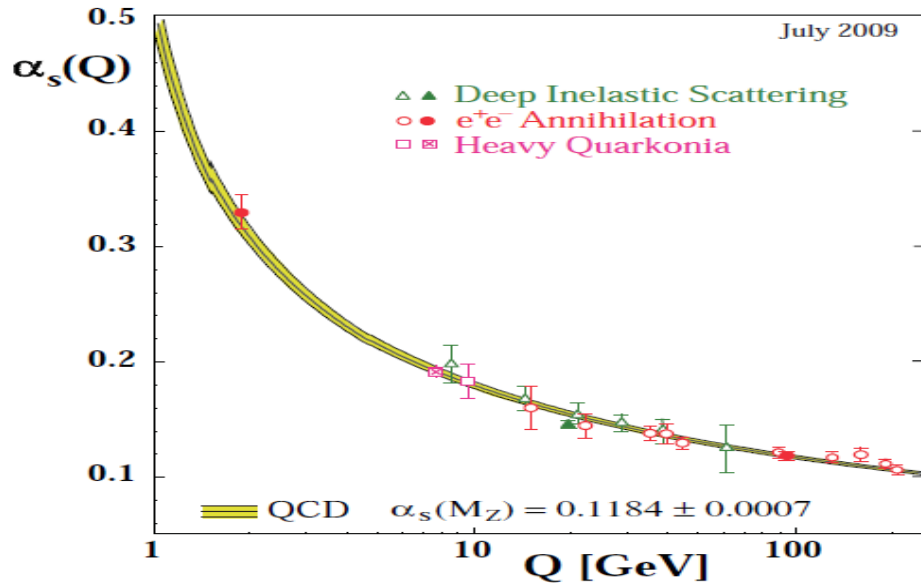


Figure 1.2: Summary of measurements of α_s as a function of Q where the curves represent the QCD predictions for the combined world average value of α_s . M_Z is the rest mass of the Z^0 boson. The full symbols are results based on N3LO QCD, open circles are based on NNLO, open triangles and squares on NLO QCD. The cross filled square is based on lattice QCD. The figure is reproduced from [3]. The details of the calculations and measurements can also be found in [3].

1.4 Spin of the Nucleon

The spin of the nucleon is one of the most exciting intrinsic properties the origin of which has been the least known of all the other interesting properties. Numerous efforts have been made in terms of theoretical model predictions as well as in the experimental frontiers in order to understand the origin of the spin of the nucleon and the different contributing factors to it. However, yet after more than two decades, the contributions to the spin of the nucleon are only partially known. The spin structure of the nucleons can not be accessed by any means with an unpolarized beam and an unpolarized target. Instead, in order to probe the internal spin dynamics in a nucleon, polarized beams and polarized targets are used.

The first ever polarized electron-polarized proton scattering measurements were conducted at SLAC. The E80 and E130 collaborations measured the spin dependent asymmetries in the inclusive³ deep inelastic scattering of longitudinally polarized electrons off a longitudinally polarized proton target, aiming to measure the spin-dependent structure functions of proton [40], [41]. Data were taken in a high Q^2 range and a x region between 0.18 to 0.70. On the theoretical front, Ellis and Jaffe [42] predicted the contribution of the quarks' spin to the nucleon spin, separated from the gluon spins and orbital angular momentum contributions, to be $\sim 58\%$ where they assumed that the sea quarks⁴ do not contribute to the spin of the nucleon. In 1988, the EMC collaboration measured the spin asymmetry in deep inelastic scattering of longitudinally polarized muons off longitudinally polarized protons over a large x range, $0.01 < x < 0.7$, and determined the spin-dependent structure function g_1 for the proton. The spin dependent structure function g_1 is related to the difference between the probability of finding the quarks whose spins are aligned parallel to the spin of the nucleon and the probability of those whose spins are aligned anti-parallel to that of the nucleon. In this case, the nucleon is longitudinally polarized, i.e., the spin of the nucleon is parallel to the incoming electron beam. The result of the experiment was in complete disagreement with what Ellis and Jaffe predicted in their calculations. The results are explained in Refs. [43] and [44]. It was found that the contribution from the quarks to

³In case of inclusive scattering, only the scattered electrons are detected and nothing else. Other particles produced in the reaction remain undetected.

⁴Sea quarks are virtual quark-antiquark pair which do not contribute to the quantum numbers of the parent hadron.

the nucleon spin was rather small. It turned out that the majority of the nucleon spin is not carried by the quarks which was the very first unexpected finding in the history of spin physics and was often referred to as *Spin Crisis*. The EMC results were further confirmed by a set of experiments at SLAC (SMC) and CERN (E142) for both the proton and the neutron.

The surprising results of these experiments subsequently created great excitement and interest among the theorists and they started thinking about different possible contributions to the nucleon spin. The most probable candidates were the spin of the gluons (ΔG), the orbital angular momentum of the quarks (L_q) and the orbital angular momentum of the gluons (L_g). Since the total angular momentum of the nucleon is always conserved, the spin 1/2 of the nucleon can be written as :

$$\frac{1}{2} = \frac{1}{2}\Delta\Sigma + \Delta G + L_q + L_g, \quad (1.1)$$

where $\Delta\Sigma$ is the contribution only from the helicity⁵ of the valence and sea quarks. HERMES and COMPASS measured this contribution to a high precision and concluded that the quark spin contribution to the nucleon spin is of the order of 30%. Different experiments have been dedicated to measure the two contributions $\Delta\Sigma$ and ΔG during the last couple of decades (Note Ref. [45] and the references in it). However, the possible contribution from the angular momentum of quarks and gluons was still to be measured. Hence, the basic question still remains : How is the nucleon spin distributed among all the contributions?

1.5 Transverse Spin: Transversity, Sivers Distribution and Collins Fragmentation Function

So far we talked about the contribution of the quark spin to the nucleon spin given by the distribution function g_1 and usually denoted by Δq which is already measured to a very high precision. This is often called the *helicity distribution*. In order to interpret the structure of the nucleon in terms of spin and momentum, three distribution functions or naïvely three different probabilities have to be defined. These are the momentum distri-

⁵The helicity of a particle is defined as the projection of its spin onto its direction of momentum. The helicity of a particle is said to be *right handed* if the direction of its spin is the same as the direction of its momentum. On the other hand, if the particle has a spin which is aligned opposite to the direction of its momentum, the helicity of the particle is said to be *left handed*.

bution function $q(x, Q^2)$, the helicity distribution function $\Delta q(x, Q^2)$ and the transversity distribution function $\delta q(x, Q^2)$. They can be interpreted as follows:

- $q(x, Q^2)$: The probability of finding the quarks carrying a fraction x of the nucleon momentum within the nucleon. This is the unpolarized and spin independent distribution function.
- $\Delta q(x, Q^2)$: The difference between the probabilities of finding the quarks in a longitudinally polarized nucleon having their spins parallel and anti-parallel to the nucleon spin.
- $\delta q(x, Q^2)$: The difference between the probabilities of finding the quarks in a transversely⁶ polarized nucleon having their spins parallel and anti-parallel to the nucleon spin.

The unpolarized distribution $q(x, Q^2)$ and the helicity distribution $\Delta q(x, Q^2)$ have been measured very well, but the measurement of the transversity distribution $\delta q(x, Q^2)$ is in its very early stage. HERMES and COMPASS completed their proposed measurements of various single spin asymmetries with the motivation of extracting the transversity distribution function using proton and deuterium targets. The existing results of these measurements are discussed in chapter 2. However, at this moment only one global analysis has been performed with the available data and the transversity distribution function is extracted [46]. The difference between the transversity distribution and the other two distributions is that the transversity distribution function is a *chiral odd*⁷ object which can not be accessed in inclusive deep inelastic scattering (DIS). Unlike the other two distributions, $\delta q(x, Q^2)$ does not carry a probabilistic interpretation in the helicity basis. Due to its *chiral odd* nature, it has not been measured so far in the DIS experiments as the strong and electromagnetic interactions conserve chirality⁸. In order to access to $\delta q(x, Q^2)$, another *chiral odd* object

⁶The term *transverse* here refers to the direction where the spin of the nucleon is aligned perpendicular to the scattering plane in the reaction. Two configurations can be realized experimentally: the target spins lying in the scattering plane and perpendicular to the incoming lepton beam and the target spins oriented perpendicular to the scattering plane containing the incoming lepton beam.

⁷See the definition of chirality

⁸Chirality of a particle is a more abstract concept in relation to its helicity. The helicity of a particle is the projection of its spin in the direction of its momentum. Hence, if the particle has its spin aligned (anti-aligned) along the direction of its momentum, its helicity is positive (negative). The chirality of a particle is same as the helicity in the massless limit i.e. chirality and the helicity are the same for a massless particle. For a particle having non-zero mass, the chirality basis is a linear combination of the helicity states. Specifically when a distribution (fragmentation) function is *chiral odd*, it involves the flipping of the helicities of both the quark and the nucleon during the scattering process. In other words, the initial and the final states do not preserve chirality.

(the *Collins Fragmentation Function* defined below) has to be measured together with the transversity distribution so that the chirality is conserved during the process. This can be achieved by detecting one of the hadrons produced in the final state of the scattering process which is termed as semi-inclusive deep inelastic scattering (SIDIS). The process can be expressed as :

$$e + N \longrightarrow e' + h + X, \quad (1.2)$$

where the incoming electron e is scattered off the nucleon N and the final scattered electron e' together with the hadron h are detected. X denotes the undetected final state. The electron in this case is specific to our experiment. In SIDIS, in principle it can be any leptons such as electrons, muons, etc. Another important distribution function named the Sivers distribution function can be accessed in SIDIS. The Sivers distribution function is believed to be associated with the angular momentum of the quarks. However, the exact relation between the angular momentum of quarks and the Sivers function is still under investigation [47]. Hence, in the near future the study of these distribution functions will be expected to shed some light on the missing part of the spin contribution to the nucleon as well as on many other interesting properties.

The SIDIS experiment E06010 in Hall A at Jefferson Lab which aimed at measuring the SSA on a polarized ^3He target finished acquiring data almost a year ago. It is the first experiment to use the polarized ^3He as a neutron target to measure the SSA in the x range $0.13 < x < 0.41$ with $Q^2 = 1.31 \rightarrow 3.1 \text{ GeV}^2/c^2$. In this experiment, the SSA is measured in the electroproduction of π^- on the transversely polarized ^3He target. The expected SSA is attributed to two independently contributing effects: the *Collins effect* and the *Sivers effect*. The contribution of the Collins effect to the measured SSA is associated with the *chiral odd* Collins fragmentation function⁹ convoluted with the transversity distribution function. Similarly, the contribution of the Sivers effect is associated with the Sivers distribution function convoluted with the spin-independent fragmentation function. The naïve probabilistic interpretations of the Collins and Sivers functions are given below:

- Sivers distribution function : The Sivers distribution function gives the probability of finding an unpolarized quark in a transversely polarized nucleon. It relates the

⁹The fragmentation function is related to the probability of formation of the final state hadron from the quarks in the nucleon during the scattering process.

transverse momentum of the quarks to the spins of the nucleon and hence it is called the Transverse Momentum Dependent (TMD) distribution function [48].

- Collins fragmentation function : The Collins fragmentation function gives the probability of polarized quarks fragmenting into unpolarized hadrons. It describes the correlation between the spin of the struck quark and the transverse momentum of the produced hadron [49].

While HERMES and COMPASS presented their results on Single Spin Asymmetry (SSA) on transversely polarized proton and deuteron target, E06010 in Hall A at Jefferson Lab completed its data taking from November 2008 to February 2009 on a transversely polarized ^3He target. As mentioned earlier, this is the first experiment on polarized ^3He to study the SSA on neutron. The single spin asymmetry of the neutron and the extraction of the Collins and Sivers moments¹⁰ in the electroproduction of π^- from the data is presented in this thesis. The inclusive single spin asymmetry results for different particles are also presented.

1.6 Outline of the Thesis

The theory and formalism of inclusive and semi-inclusive deep inelastic scattering in terms of the leptonic and hadronic tensors is discussed in chapter 2. In addition, a detailed formalism of the transverse degrees of freedom of the nucleon with emphasis on the transversity distribution function and the Sivers distribution function as well as the Collins fragmentation function is presented. Chapter 3 is dedicated to describe the experimental set up for E06010. The different detector packages and the beam line components in the experimental hall are addressed in this chapter. Chapter 4 deals with the detailed description of the polarized ^3He target and the polarimetry analysis. The detector calibrations and other related analysis are extensively discussed in chapter 5. The asymmetry analysis, the extraction of Collins and Sivers moments and the systematic studies are presented in chapter 6. The conclusions and the outlook are presented in chapter 7.

Copyright © Chiranjib Dutta 2010

¹⁰The SSA measured is contributed by the Collins and Sivers effects. Each of these contributions is realized with the convolution of a distribution function with a fragmentation function. These convolutions remain as they are and no separation can be done experimentally. The so called moments are measured. Hence, for instance, the Sivers moment refers to the convolution of both the Sivers distribution function and the unpolarized fragmentation function integrated over the transverse momentum of the hadrons.

CHAPTER 2: DEEP INELASTIC SCATTERING AND TRANSVERSITY

The unpolarized and polarized inclusive inelastic lepton scattering off a hadron result in a number of interesting and surprising aspects of the behavior of the partons inside a nucleon. However, the transverse polarization distributions of the nucleon can not be probed with the inclusive deep inelastic processes. Semi-inclusive deep inelastic scattering (SIDIS) has been adopted as one of the powerful tools to access the transverse degrees of freedom in the nucleon where, as mentioned earlier, one of the final-state hadrons is detected together with the scattered electron. The basic formalism of the deep inelastic scattering (DIS) process and the semi-inclusive deep inelastic scattering (SIDIS) process as an extension of it will be discussed in this chapter. The transversity and Sivers distribution functions and the Collins fragmentation function and their properties in terms of contributions to the observed single spin asymmetry in the $n^\uparrow(e, e'\pi^-)X$ reaction are also addressed.

2.1 Inclusive Deep-Inelastic Scattering (DIS)

A typical inclusive DIS process involves an incoming beam of leptons scattered off a hadronic target and the scattered leptons get detected. Here, I will focus only on the process with a fixed hadronic target and a continuous beam of electrons as the incoming leptons. Consider an electron with an initial energy E and momentum \vec{k} scattering off a fixed target which will be treated as a nucleon of rest mass M . In other words, the four-momenta of the incoming and the outgoing electrons are $k = (E, \vec{k})$ and $k' = (E', \vec{k}')$, respectively, while that of the initial target nucleon is $P = (M, \vec{0})$. The electron interacts with the nucleon via a virtual photon having a moderate four-momentum squared (Q^2) exchanged to the nucleon. Thus having absorbed the photon momentum, the target nucleon breaks apart and produces a final state X of hadrons. In inclusive measurements, the final state X of the hadrons is left undetected while only the scattered electron is detected. The schematic of the inclusive DIS process with one photon exchange is shown in the Fig. 2.1. The kinematic variables of a DIS process are summarized in Table 2.1.

The two parameters which characterize the scattering process are Q^2 and x . As mentioned earlier, Q^2 is the four-momentum transfer to the target carried by the virtual photon and defines the spatial resolution of the process. The larger the Q^2 the better the resolution to probe the inner structure of the nucleon and in the range of deep inelastic scattering

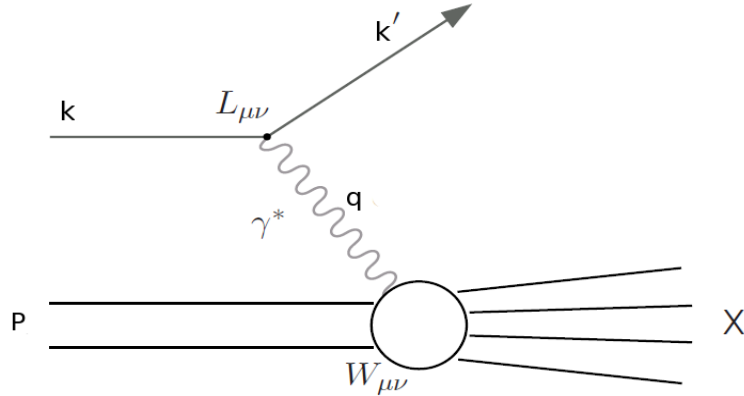


Figure 2.1: Schematic of Deep Inelastic Scattering (DIS) process. The leptonic tensor $L_{\mu\nu}$ and the hadronic tensor $W_{\mu\nu}$ are described in the text in subsection (2.1.1).

where $Q^2 > 1 \text{ GeV}^2$ ¹, the resolution is small enough to get deeper insight into the nucleon. The Bjorken x is a measure of the fraction of the nucleon's momentum carried by the struck quark at the photon virtuality Q^2 . Bjorken introduced with this variable a property known as *scaling* (introduced in chapter 1) which demands that the structure functions are independent of Q^2 and are functions of x only. The invariant mass of the final hadronic system can be written as :

$$W^2 = M^2 + 2M\nu - Q^2 = M^2 + 2P \cdot q - Q^2 \quad (2.1)$$

The invariant mass of the final state X should be either larger (in case of deep inelastic scattering) than or equal (in case of elastic scattering) to the mass of the nucleon. Hence, in general,

$$W^2 \geq M^2 \quad (2.2)$$

$$\Rightarrow M^2 + 2P \cdot q - Q^2 \geq M^2 \quad (2.3)$$

$$\Rightarrow \frac{Q^2}{2P \cdot q} \leq 1 \quad (2.4)$$

$$\Rightarrow x \leq 1 \quad (2.5)$$

On the other hand, if we look into the definition of x , it represents a momentum fraction of the nucleon and it depends on the energy loss of the electron or the energy transferred

¹ $c = 1$ convention is adopted in the formalism

Table 2.1: Important kinematic variables in DIS. Here the mass of the incoming electron is neglected and a fixed target is assumed. Also, $\hbar = c = 1$ is adopted.

E	energy of the incoming electron
$P=(M,0,0,0)$	four-momentum of the target
(θ,ϕ)	(polar,azimuthal) scattering angle in the lab frame
E'	energy of the outgoing electron
$k=(E,0,0,E)$	four-momentum of the incoming electron
$k'=(E',E'\sin\theta\cos\phi,E'\sin\theta\sin\phi,E'\cos\phi)$	four-momentum of the outgoing electron
$q=k-k'$	four momentum transfer
$\nu=E-E'=\frac{P\cdot q}{M}$	energy transfer
$y = \frac{\nu}{E} = \frac{P\cdot q}{P\cdot k}$	fractional energy transfer
$Q^2 = -q^2 = 4EE'\sin^2\frac{\theta}{2}$	squared invariant mass of the virtual photon
$x = \frac{Q^2}{2M\nu} = \frac{Q^2}{2P\cdot q}$	Bjorken scaling variable
$W^2 = (P+q)^2 = M^2+2M\nu-Q^2$	squared invariant mass of the final hadronic system

to the nucleon. Also, since Q^2 is always positive, the value of x can at least be 0 , but not negative. Hence, the physically allowed range of x is:

$$0 \leq x \leq 1 \quad (2.6)$$

In the special case when $x=1$, $W^2=M^2$ and it corresponds to the case of elastic scattering. Thus, x is a measure of the inelasticity of the scattering process. The deep inelastic scattering regime is defined by $Q^2 > 1 \text{ GeV}^2$ and $W^2 > 4 \text{ GeV}^2$ to avoid the resonance region.

In case of semi-inclusive deep inelastic scattering (SIDIS), one of the hadrons in the final state is detected in coincidence with the scattered electron. In E06010 in Hall A at Jefferson Lab, pions and kaons were detected which were coincident with the scattered electrons off a polarized ^3He target. In this case, three additional independent variables can completely define the kinematics. These are summarized in Table 2.2.

2.1.1 General Formalism for Deep Inelastic Cross Section

The general expression for the differential cross section of the deep inelastic scattering explained above can be written in terms of the leptonic and hadronic tensors as follows :

$$\frac{d^2\sigma}{d\Omega dE'} = \frac{\alpha^2}{2Mq^4} \frac{E'}{E} L_{\mu\nu} W^{\mu\nu}, \quad (2.7)$$

Table 2.2: The three independent variables ϕ_h , z , and P_h , in addition to x and Q^2 , in terms of which the cross section in SIDIS can be expressed.

$P_h = (E_h, \vec{p}_h)$	four momentum of the detected outgoing hadron
ϕ_h	azimuthal angle of the hadron plane w.r.t. scattering plane
$z = \frac{P \cdot P_h}{P \cdot q} = \frac{E_h}{\nu}$	momentum fraction carried by the outgoing hadron
$P_{h\perp} = \frac{\vec{P}_h \times \vec{q}}{q}$	the transverse momentum of the hadron w.r.t. the virtual photon

where $d\Omega = d\cos\theta d\phi$ is the solid angle which covers the detection of the scattered electrons in the energy range $(E', E' + dE')$ in the laboratory frame. $L_{\mu\nu}$ is the leptonic tensor describing the interaction at the leptonic (in this case electron) vertex whereas the hadronic tensor $W^{\mu\nu}$ depicts the interaction at the hadronic vertex. α is the electromagnetic coupling constant, and q is the four-momentum of the virtual photon as defined earlier.

The leptonic tensor $L_{\mu\nu}$

$L_{\mu\nu}$ can be defined in terms of the γ matrices and spinors following the conventions of [50] as follows :

$$L_{\mu\nu}(k, s; k', s') = [\bar{u}(k', s')\gamma_\mu u(k, s)]^* [\bar{u}(k', s')\gamma_\nu u(k, s)] \quad (2.8)$$

Here, k and k' represent the four momenta of the incoming lepton and the scattering lepton respectively. However, the spinors here are normalized to $2E$ unlike described in Ref. [50]. Now the leptonic tensor can be decomposed into two parts: the symmetric part S in (μ, ν) and the anti-symmetric part A in (μ, ν) [51]. Hence,

$$\begin{aligned} L_{\mu\nu}(k, s; k', s') &= L_{\mu\nu}^S(k; k') + iL_{\mu\nu}^A(k, s; k') \\ &+ L'_{\mu\nu}{}^S(k, s; k', s') + iL'_{\mu\nu}{}^A(k, ; k', s') \end{aligned} \quad (2.9)$$

Since we do not measure the polarization of the scattered electron in the process, we can sum over s' and for the unpolarized case, in addition to the summation over the final spins s' , the initial spins of the electrons can be averaged out and it results in only the symmetric part of the leptonic tensor ($= 2L_{\mu\nu}^S$). On the other hand, in case of the polarized cross section, the above equation still has the spin-dependent, anti-symmetric part and, hence,

one can write the leptonic tensor without averaging the spins of the incoming electrons as :

$$L_{\mu\nu}(k, s; k') = L_{\mu\nu}^S(k; k') + iL_{\mu\nu}^A(k, s; k') \quad (2.10)$$

Calculation of the trace of Eq.(2.8) yields :

$$L_{\mu\nu}^S(k; k') = k_\mu k'_\nu + k'_\mu k_\nu - g_{\mu\nu}(k \cdot k' - m_e^2) \quad (2.11)$$

$$L_{\mu\nu}^A(k, s; k') = m_e \epsilon_{\mu\nu\gamma\delta} s^\gamma (k - k')^\delta, \quad (2.12)$$

where m_e is the mass of the electron, $g_{\mu\nu}$ is the usual metric tensor, and $\epsilon_{\mu\nu\gamma\delta}$ is the Levi-Civita tensor defined in Appendix A.

The hadronic tensor $W_{\mu\nu}$

The hadronic tensor $W_{\mu\nu}$ is the interesting part in the cross section since it reveals the hadronic structure comprehensively. However, it is non-trivial to calculate the hadronic tensor as the non-perturbative effects in the strong interaction can not be explained by QCD. It can be expressed in terms of the structure functions while preserving the parity and time reversal invariance of the interaction. Similar to the leptonic tensor, the hadronic tensor can also be decomposed into a symmetric (S) and an anti-symmetric (A) part :

$$W_{\mu\nu}(q; P, S) = W_{\mu\nu}^S(q; P) + iW_{\mu\nu}^A(q; P, S), \quad (2.13)$$

where S is the spin of the target nucleon. The spin-independent and spin dependent parts are given by Eqs.(2.14) and (2.15) :

$$\begin{aligned} \frac{1}{2M} W_{\mu\nu}^S(q; P) &= \left(-g_{\mu\nu} + \frac{q_\mu q_\nu}{q^2} \right) W_1(P \cdot q, q^2) \\ &+ \left[\left(P_\mu - \frac{P \cdot q}{q^2} q_\mu \right) \left(P_\nu - \frac{P \cdot q}{q^2} q_\nu \right) \right] \frac{W_2(P \cdot q, q^2)}{M} \end{aligned} \quad (2.14)$$

$$\begin{aligned} \frac{1}{2M} W_{\mu\nu}^A(q; P, S) &= \epsilon_{\mu\nu\gamma\delta} q^\gamma \left[M S^\delta G_1(P \cdot q, q^2) \right. \\ &\left. + \left((P \cdot q) S^\delta - (S \cdot q) P^\delta \right) \frac{G_2(P \cdot q, q^2)}{M} \right] \end{aligned} \quad (2.15)$$

In the deep inelastic region, when $Q^2 \rightarrow \infty$ and $x = \frac{Q^2}{2M\nu}$ is fixed, the inelastic form factors

can be parametrized by the dimensionless structure functions that depend on x and Q^2 .

$$MW_1(P \cdot q, q^2) \equiv F_1(x, Q^2) \quad (2.16)$$

$$\nu W_2(P \cdot q, q^2) \equiv F_2(x, Q^2) \quad (2.17)$$

$$\frac{(P \cdot q)^2}{\nu} G_1(P \cdot q, q^2) \equiv g_1(x, Q^2) \quad (2.18)$$

$$\nu(P \cdot q)G_2(P \cdot q, q^2) \equiv g_2(x, Q^2) \quad (2.19)$$

The structure function $F_1(x, Q^2)$ and $F_2(x, Q^2)$ are called the *unpolarized structure functions* since they do not depend on the spin of the nucleon. The other two structure functions, $g_1(x, Q^2)$ and $g_2(x, Q^2)$, are spin-dependent and hence termed as *polarized structure functions*. These structure functions are Lorentz invariant and can be measured experimentally. The unpolarized structure functions can be measured using an unpolarized target and an unpolarized beam. On the other hand, both beam and target need to be polarized in order to access the polarized structure functions. The spin-independent and spin-dependent parts of the hadronic tensor can now be expressed in terms of these structure functions as follows :

$$W_{\mu\nu}^S(q; P) = 2 \left(-g_{\mu\nu} + \frac{q_\mu q_\nu}{q^2} \right) F_1(x, Q^2) + \frac{2}{P \cdot q} \left[\left(P_\mu - \frac{P \cdot q}{q^2} q_\mu \right) \left(P_\nu - \frac{P \cdot q}{q^2} q_\nu \right) \right] F_2(x, Q^2) \quad (2.20)$$

$$W_{\mu\nu}^A(q; P, S) = 2M \epsilon_{\mu\nu\gamma\delta} q^\gamma \left[S^\delta g_1(x, Q^2) + \left(S^\delta - \frac{(S \cdot q)}{P \cdot q} P^\delta \right) \frac{g_2(x, Q^2)}{P \cdot q} \right] \quad (2.21)$$

Thus with the symmetric and anti-symmetric parts in both the leptonic and hadronic tensors, we can write the general form of the cross section in the DIS process as :

$$\frac{d^2\sigma}{d\Omega dE'} = \frac{\alpha^2}{2Mq^4} \frac{E'}{E} \left[L_{\mu\nu}^S W^{\mu\nu S} - L_{\mu\nu}^A W^{\mu\nu A} \right] \quad (2.22)$$

2.1.2 The Unpolarized Spin-independent DIS Cross Section

In case of spin-independent deep inelastic cross section, Eq.(2.22) yields only the spin independent symmetric part when all the initial spin states of the scattering process are averaged. The cross section in terms of the unpolarized structure functions is :

$$\frac{d^2\sigma_U}{dxdy} = \frac{4\pi\alpha_s^2}{s(xy)^2} \left[xy^2 F_1(x, Q^2) + \left(1 - y - \frac{M^2 x^2 y^2}{Q^2} \right) F_2(x, Q^2) \right] \quad (2.23)$$

where \sqrt{s} is the center-of-mass energy of the system. The unpolarized structure functions clearly represent the deviation of the cross section from scattering off a point-like particle. The scattering off a point-like particle is the pure elastic scattering and the modification of the scattering cross section in Eq.(2.23) in terms of F_1 and F_2 in the inelastic case is due to the high energy transfer of the virtual photon into the nucleon. Thus, these unpolarized structure functions are the most relevant tools to know the electric and magnetic charge distributions of the nucleon. Different experiments were conducted in order to measure these functions to a very high precision and these are known for over half a century now.

2.1.3 The Polarized Spin-dependent DIS Cross Section

In case of the polarized beam and polarized target, both the spin dependent parts in the leptonic and hadronic tensors come into play as well. With all the terms in both the symmetric and anti-symmetric parts in the respective tensors contributing to the cross section, one can not access the spin dependent contribution directly from the cross section. Hence, a cross section difference is usually formed between two different target spin orientations. The target can be polarized in two ways : *longitudinal* and *transverse* with respect to the incoming beam. In both the cases, the cross sections can be measured with the target spins aligned parallel as well as anti-parallel to the beam. Thus, taking the difference of the cross sections between the two target spin states cancels the unpolarized terms and isolates the spin dependent terms. Depending on the direction of the target polarization, two distinct cases arise:

Cross section for a longitudinally polarized target

Consider the scattering of a longitudinally polarized lepton beam off a target which is polarized along the direction of the beam. The cross section difference is given by :

$$\frac{d^3\sigma^{\rightarrow\Rightarrow}}{dx dy d\phi_s} - \frac{d^3\sigma^{\rightarrow,\Leftarrow}}{dx dy d\phi_s} = \frac{4\alpha_s^2}{sxy} \left[\left(2 - y - \frac{4M^2x^2y^2}{2Q^2} \right) g_1(x, Q^2) - \frac{4M^2x^2y}{Q^2} g_2(x, Q^2) \right], \quad (2.24)$$

where \rightarrow represents the helicity or the spin orientation of the leptons and \Rightarrow (\Leftarrow) denotes the orientation of target spins aligned (anti-aligned) with respect to the leptons. ϕ_s is the azimuthal angle of the target spin vector with respect to the electron beam. As can be seen from the expression, the structure function g_2 is suppressed by a factor of $\frac{M^2}{Q^2}$. This difference in the cross section is used to measure the structure function g_1 .

Cross section for a transversely polarized target

Now consider a scattering of a longitudinally polarized beam of leptons off a target which is polarized perpendicular with respect to the scattering plane containing the incoming beam.

The cross section difference can be expressed as :

$$\frac{d^3\sigma^{\rightarrow\uparrow}}{dx dy d\phi_s} - \frac{d^3\sigma^{\rightarrow\downarrow}}{dx dy d\phi_s} = \frac{4\alpha_s^2}{sxy} \sqrt{1-y - \frac{4M^2x^2y^2}{2Q^2}} \left[\frac{2Mx}{Q} g_1(x, Q^2) + 2g_2(x, Q^2) \right] \cos\phi_s \quad (2.25)$$

Here, the two target spin orientations are represented by \uparrow and \downarrow while the lepton spin is indicated by \rightarrow .

2.1.4 Experimental Measurements of Structure Functions

There have been a considerable number of experiments using different targets and beams dedicated to measure the unpolarized and the polarized structure functions. Even though a very explicit dependence of the different cross sections on the structure functions are realized in theory as we have seen in the previous subsections, it is extremely non-trivial experimentally to access each of them individually. Hence, usually the experimental results are presented in terms of cross section ratios dependent on virtual photon polarization (for F_1 and F_2) and asymmetries dependent on the target spin polarization (for g_1 and g_2). It is worthwhile to mention a few words here to show how these structure functions are realized in terms of the measured quantities in the experiments.

For the unpolarized structure functions, instead of separating them individually, $F_2(x, Q^2)$ and a combination of $F_1(x, Q^2)$ and $F_2(x, Q^2)$ known as R are presented as experimental results. R is defined as the ratio of the photo-absorption cross sections of longitudinally (L) and transversely (T) polarized virtual photons:

$$R = \frac{\sigma_L(x, Q^2)}{\sigma_T(x, Q^2)} \equiv \left(1 + \frac{4M^2x^2}{Q^2}\right) \left[\frac{F_2(x, Q^2)}{2xF_1(x, Q^2)} \right] - 1, \quad (2.26)$$

where $\sigma_L(x, Q^2)$ ($\sigma_T(x, Q^2)$) represents the photo-absorption cross section for longitudinal (transverse) photons.

On the other hand, the polarized structure functions g_1 and g_2 are often accessed in the measurements of various asymmetries. The term asymmetry here refers to the ratio of the polarized cross section difference to the unpolarized cross section. For a longitudinally polarized target, the asymmetry measured can be defined as :

$$A_{||} \equiv \frac{\frac{d^3\sigma^{\rightarrow\rightarrow}}{dxdy d\phi_s} - \frac{d^3\sigma^{\rightarrow\leftarrow}}{dxdy d\phi_s}}{\frac{d^2\sigma_U}{dxdy}}, \quad (2.27)$$

where the numerator and the denominator are given by Eq.(2.24) and Eq.(2.23), respectively. Similarly, for a transversely polarized target, the asymmetry is :

$$A_{\perp} \equiv \frac{\frac{d^3\sigma^{\rightarrow\uparrow}}{dxdy d\phi_s} - \frac{d^3\sigma^{\rightarrow\downarrow}}{dxdy d\phi_s}}{\frac{d^2\sigma_U}{dxdy}}, \quad (2.28)$$

where the numerator is given by Eq.(2.25). Now $A_{||}$ and A_{\perp} can be related to the virtual photon-nucleon asymmetries A_1 and A_2 as follows :

$$A_{||} = D(A_1 + \eta A_2) \quad (2.29)$$

$$A_{\perp} = d(A_2 + \xi A_2), \quad (2.30)$$

where the photon asymmetries and the other kinematic factors are defined below :

$$A_1 = \frac{g_1 - \frac{4M^2 x^2}{Q^2} g_2}{F_1}, \quad (2.31)$$

$$A_2 = \frac{2Mx}{Q} \left[\frac{g_1 + g_2}{F_1} \right] \quad (2.32)$$

$$D = \frac{1 - (1 - y)\epsilon}{1 + \epsilon R} \quad (2.33)$$

$$\epsilon = 1 / \left[1 + 2 \left(1 + \left[\frac{4M^2 x^2}{Q^2} \right]^{-1} \right) \tan^2 \left(\frac{\theta}{2} \right) \right] \quad (2.34)$$

$$\eta = \frac{(\epsilon \sqrt{Q^2})}{E - E' \epsilon} \quad (2.35)$$

$$\xi = \frac{\eta(1 + \epsilon)}{2\epsilon} \quad (2.36)$$

$$d = D \sqrt{\frac{2\epsilon}{(1 + \epsilon)}}, \quad (2.37)$$

where θ is the polar angle of the scattered lepton and ϵ is usually called as the virtual photon's transverse polarization.

Measurements of both $A_{||}$ and A_{\perp} can be used to extract the values of g_1 and g_2 directly. However, most of the experiments were dedicated to the measurement of $A_{||}$ and only g_1 was reported neglecting the contribution from g_2 . However, g_2 has been measured and a few of the important measurements of g_2 in Jefferson Lab are summarized in [52].

Among the previously conducted experiments, the ZEUS collaboration and the H1 collaboration at HERA measured F_2 of the proton in the deep inelastic e^+P scattering. Between 1970 and 1985, a series of eight experiments at SLAC acquired data in deep inelastic $e - p$ and $e - d$ scattering and reported F_2 values of the proton as well as of the deuteron. The BCDMS collaboration used the deep inelastic scattering of muon off a hydrogen target and presented the F_2 of the proton. Other measurements on proton and deuteron include the measurements by E665 collaboration and the New Muon Collaboration. All these results for protons and the deuterons are shown in Fig. 2.2 and Fig. 2.3.

The polarized g_1 for protons and deuterons have been reported by various measurements, *viz.*, the Spin Muon Collaboration (SMC) [53], [54], HERMES [55], the E155 collaboration [56], [57], the E154 collaboration, the E142 collaboration, and the E143 collaboration ([58]) while the first result of polarized g_2 was published by E155 collaboration [59] for both proton and deuteron. The SMC at CERN was involved in a very high energy muon (190 GeV) deep inelastic scattering while the E155 collaboration at SLAC opted for electron scattering off a polarized deuteron target. Measurements of g_1 and g_2 in Jefferson Lab are presented in [52] and the references therein. Figure 2.4 on the next page shows the world data of the polarized structure function g_1 .

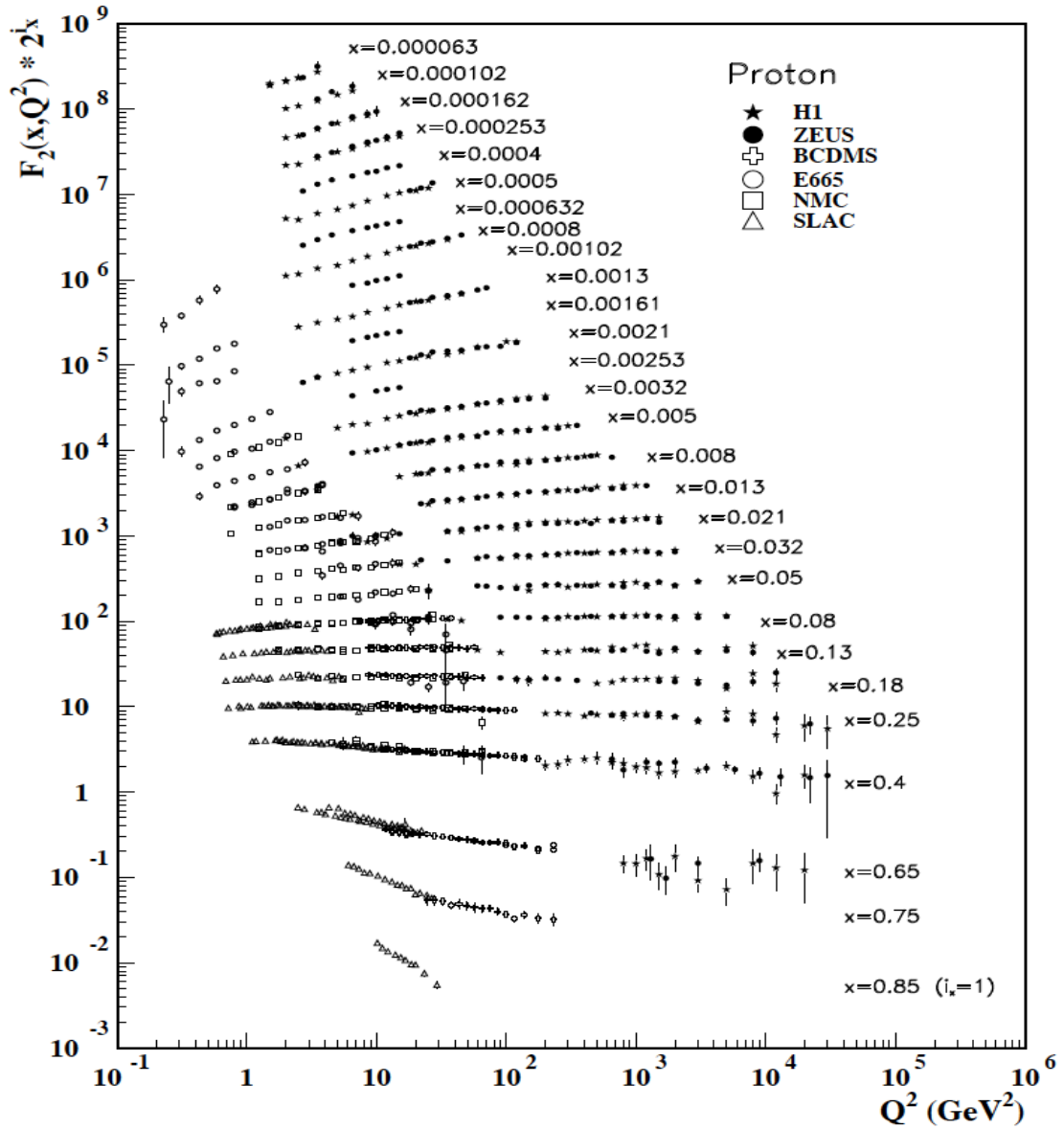


Figure 2.2: The world data on the spin independent proton structure function F_2 [4]. The error bars shown in the plot are the combined statistical and systematic errors in quadrature. In the plot F_2 is multiplied by 2^{i_x} where i_x is the number of x bins ranging from $i_x = 1$ to $i_x = 28$ (corresponds to $0.85 < x < 0.00006$).

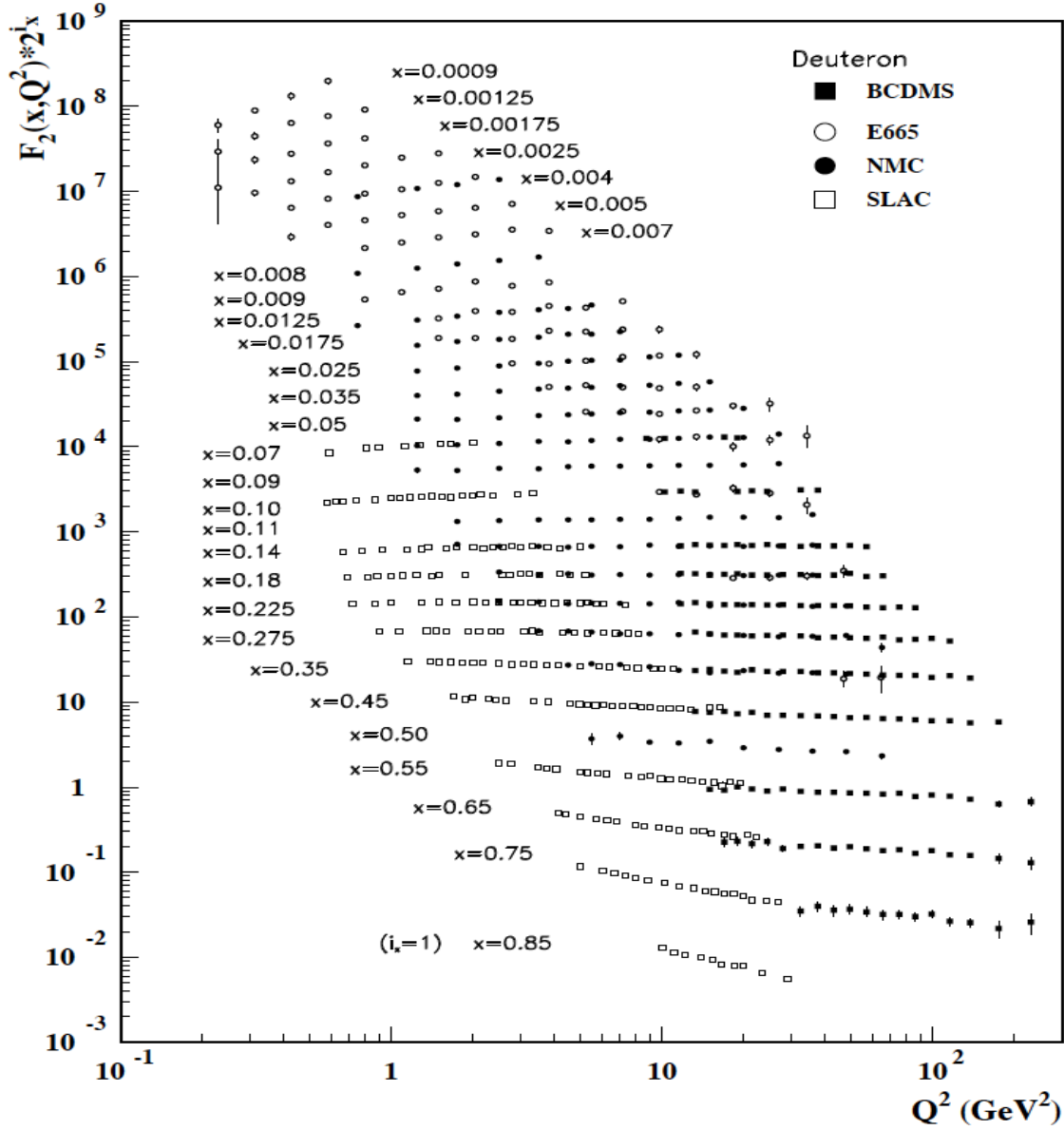


Figure 2.3: The world data on the spin independent deuteron structure function F_2 [4]. The error bars shown in the plot are the combined statistical and systematic errors in quadrature. In the plot F_2 is multiplied by 2^{i_x} where i_x is the number of x bins ranging from $i_x = 1$ to $i_x = 29$ (corresponds to $0.85 < x < 0.0009$).

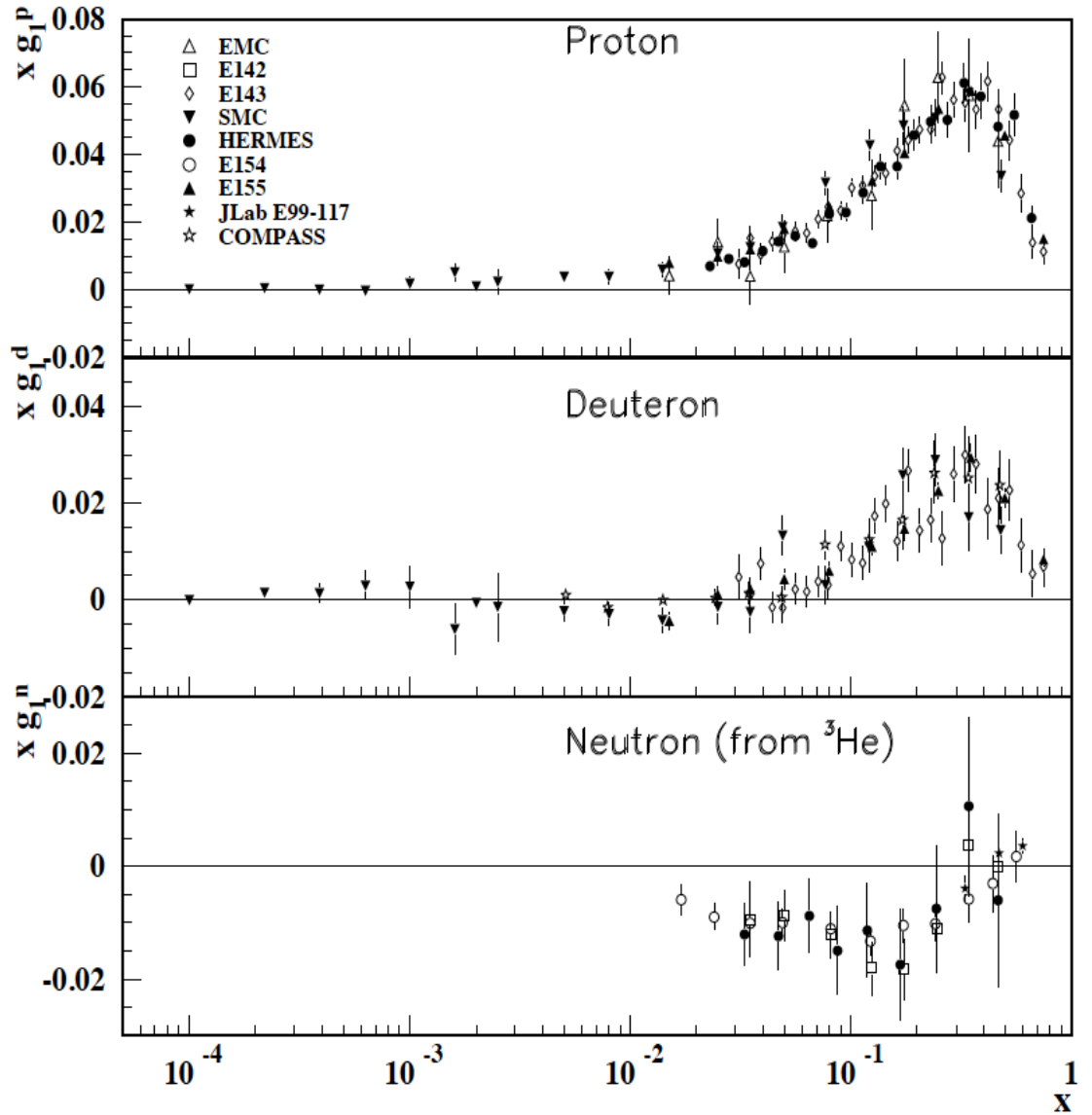


Figure 2.4: The world data on the spin dependent structure function g_1 [4].

2.2 Quark Parton Model (QPM) and Quantum Chromodynamics (QCD)

The Quark Parton Model (QPM) was introduced well before the period when the theory of Quantum Chromodynamics (QCD) started enjoying its triumph [60]. The basic hypothesis of the *naïve* QPM is when the energy and the momentum of the interacting virtual photon is very high, it interacts with the constituents of the nucleons incoherently and the constituents

are quasi-free. The fundamental assumption is that with large enough four momentum transfer squared (Q^2), the virtual photon can resolve the inner structure of the nucleon. In this case, the constituents of the nucleon can be treated as a *frozen* collection of point-like particles called partons. This follows from the fact that the time scale defining the interaction among the point-like constituents varies as $\frac{1}{\sqrt{Q^2}}$ and in the limit $Q^2 \rightarrow \infty$, the time will be much less than the typical time scales of the interactions among the partons. This is sometimes referred to as *Impulse Approximation*. This *naïve* parton model could reasonably explain the weak dependence of F_1 and F_2 on Q^2 . The electron scattering in the parton model can be viewed as interaction of the virtual photon with effectively massless partons moving with a very high momentum. The momentum of a parton can in general be expressed as $p = xp_z + p_T$ where x is the ratio of parton's z-component of momentum to that of the nucleon and p_z and p_T are the longitudinal and transverse components of the parton's momentum with respect to the nucleon respectively. However, in this momentum frame (commonly known as *infinite-momentum frame*) where the momentum of the nucleon itself and the parton are considered to be very high, $p_z \rightarrow \infty$ and one can neglect the transverse component p_T as well as the parton and target masses. Hence, the four momentum of each parton can be written as $p_i = x_i P$ where P is the nucleon momentum. In this situation, the nucleon can be thought of a group of collinear partons. Fig. 2.5 shows the nucleon in the *infinite momentum frame* imagined to be a beam of partons moving with a very high velocity. The index i represents the different partons (quarks) with their respective charges. Hence, a parton momentum distribution $f_i(x)$ can be defined as the probability of carrying a momentum fraction x of the the parent nucleon P by the struck parton i such that:

$$\sum_i \int dx x f_i(x) = 1, \quad (2.38)$$

where i is the sum over all the partons.

In this formalism, the deep inelastic scattering of the lepton can be treated as the elastic scattering off a parton inside the nucleon where the virtual photon is absorbed by the respective parton. This is shown in Fig. 2.6. The absorption of the photon and the mass-shell requirement of the final quark yields :

$$(P + q)^2 = 0 \quad (2.39)$$

Now let us go back to Eq.(2.38) where the parton momentum distribution $f_i(x)$ was introduced. In the QPM, the properties of the nucleon are defined in terms of the parton

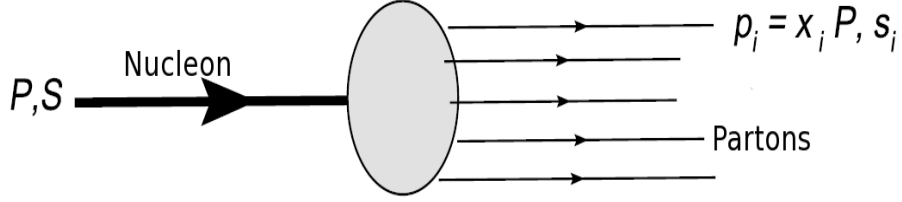


Figure 2.5: Partons in the nucleon carrying a momentum fraction x of the nucleon viewed collectively as a beam.

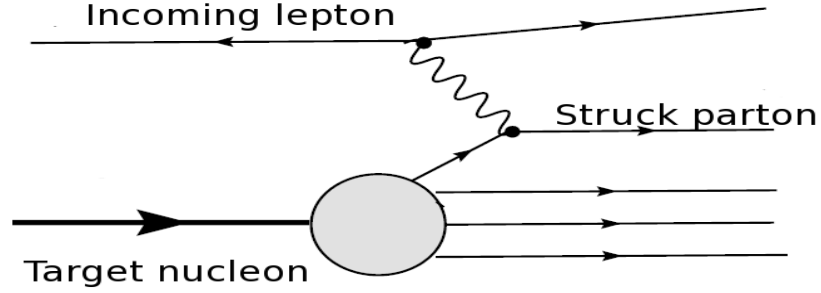


Figure 2.6: Deep inelastic scattering interpretation in QMP.

distribution function which is nothing but the probabilistic interpretation of $f_i(x)$ as mentioned earlier. Attributing the more usual nomenclature to the interpretation, let us denote $q_i(x)(\bar{q}_i(x))$ as the number density of a quark (anti-quark) of flavor i carrying a momentum fraction x of the nucleon. Then the unpolarized structure function $F_1(x)$ can be expressed as the charge-weighted sum of the quark and anti-quark flavor i :

$$F_1(x) = \frac{1}{2} \sum_i e_i^2 [q_i(x) + \bar{q}_i(x)], \quad (2.40)$$

where e_i is the charge of the quark.

If the nucleon is longitudinally polarized with respect to the incoming lepton, then the spin-dependent structure function $g_1(x)$ is given by :

$$g_1(x) = \frac{1}{2} \sum_i e_i^2 [\Delta q_i(x) + \Delta \bar{q}_i(x)] \quad (2.41)$$

and

$$\Delta q(x) = q^+(x) - q^-(x) \quad (2.42)$$

$q^+(x)$ and $q^-(x)$ are the number densities of quarks with spins aligned and anti-aligned, with respect to the longitudinal spin direction of the nucleon.

The other unpolarized structure function, F_2 , can be extracted from the relation expressed in Eq.(2.26). In case of longitudinally polarized photons, the photo-absorption cross section vanishes which results in $R \rightarrow 0$. Neglecting the small contribution from the $\frac{4M^2x^2}{Q^2}$ term in the limit $Q^2 \rightarrow \infty$, Eq.(2.26) yields :

$$F_2(x) = 2xF_1(x) \quad (2.43)$$

This is known as the Callan-Gross relation [61]. However, the spin-dependent structure function $g_2(x)$ can not be interpreted directly in the simple QPM as it involves the transverse momentum distribution of quarks. In order to understand $g_2(x)$ more comprehensively, one has to rely on the operator product expansion (OPE) method which is outside the scope of this thesis.

Using the Callan-Gross relation and the definition of $F_1(x)$, the structure function $F_2(x)$ for neutron can be written in terms of the valence and the sea quarks. The neutron consists of one u- quark and two d- quarks. Denoting these valence quark densities as $u(x) = u$ and $d(x) = d$, one can explicitly write :

$$F_2^n = x\left[\left(\frac{2}{3}\right)^2u + \left(-\frac{1}{3}\right)^2d + \left(\frac{2}{3}\right)^2(u_s + \bar{u}_s) + \left(-\frac{1}{3}\right)^2(d_s + \bar{d}_s) + \left(-\frac{1}{3}\right)^2(s_s + \bar{s}_s)\right], \quad (2.44)$$

where subscript s represents the *sea* quark and anti-quark densities for the flavors up (u), down (d), and strange (s). Now assuming uniform *sea* quark-antiquark densities, i.e. $u_s = \bar{u}_s = d_s = \bar{d}_s = s_s = \bar{s}_s = S$,

$$F_2^n = x\left[\frac{1}{9}(u + 4d) + \frac{4}{3}S\right] \quad (2.45)$$

Similarly for proton,

$$F_2^p = x\left[\frac{1}{9}(4u + d) + \frac{4}{3}S\right] \quad (2.46)$$

Here the *isospin* property of the nucleons is used where the following relations for the valence quarks hold :

$$u^p(x) = d^n(x) = u(x) \quad (2.47)$$

$$u^n(x) = d^p(x) = d(x) \quad (2.48)$$

Spin Crisis

One of the most interesting discoveries by the European Muon Collaboration (EMC) was the *Spin Crisis*. The spin dependent structure function $g_1(x)$ expressed in Eq.(2.41) can be expressed as a linear combination of quark densities which undergo transformation properties under the group of flavor transformation $SU(3)$ [62] :

$$g_1(x) = \frac{1}{9} \left[\frac{3}{4} \Delta q_3 + \frac{1}{4} \Delta q_8 + \Delta \Sigma \right], \quad (2.49)$$

where Δq_3 and Δq_8 are the third component of the spin triplet and the eighth component of the $SU(3)$ octet respectively. $\Delta \Sigma$ is the flavor singlet.

The first moment of $\Delta \Sigma$, which is related to the quark-antiquark spin contribution to the spin of the proton, is defined as :

$$a_o = \int_0^1 dx \Delta \Sigma \quad (2.50)$$

Now in non-relativistic case, a proton would be expected to have its spin solely contributed by all the quarks and anti-quarks and hence one might expect a_o to be ~ 1 . However, as mentioned earlier, Ellis and Jaffe [42] predicted a value of 0.59 of this contribution by taking into account the non-relativistic nature of the dynamics and neglecting the contribution from the strange quarks in $SU(3)$ framework. But the EMC measurements revealed [43] :

$$a_o \approx 0 \quad (2.51)$$

This was the first major breakthrough in the history of spin physics declaring the unexpectedly small contribution of the quark-antiquark spins to the spin of the proton. This is known as the *Spin Crisis* in the QPM.

2.2.1 Gluonic Interaction in QPM

QCD emerged as a powerful and the only theory of strong interaction that had provided a satisfactory explanation of the observed experimental results at that time by introducing the concept of *gluons* and their *interaction* with quarks inside the nucleon. Thus, the theory of QCD successfully interpreted different experimental results including the famous spin crisis and the missing nucleon momentum contribution. The original parton model completely ignores the interaction among the partons and hence the leading contribution

to the deep inelastic scattering cross section in the *naïve* parton model is $\mathcal{O}(\alpha)$ where α is the electromagnetic coupling constant. However, QCD introduces the color charge and postulates that the color interactions are a copy of the electromagnetic interactions, having α replaced by α_s , the latter being termed as the strong coupling constant introduced in chapter 1. The dynamical role of gluons leads to the further contributions such as $\mathcal{O}(\alpha\alpha_s)$ as corrections to the deep inelastic cross section. The physical meaning of this correction can be understood by picturing the quark radiating a gluon before or after it gets struck by the virtual photon as shown in the Fig. 2.7.

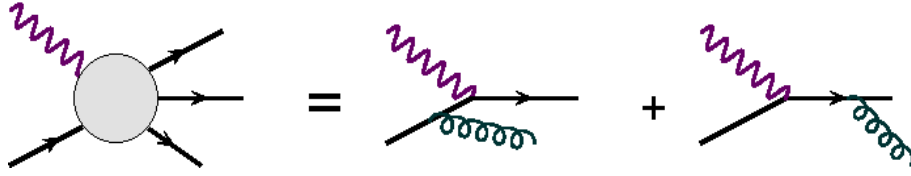


Figure 2.7: The $\mathcal{O}(\alpha\alpha_s)$ correction due to the gluon radiated by a quark.

Once the gluons are introduced in the QPM, the missing momentum contribution to the nucleon has been trivially accounted for and the spin crisis has been resolved very partially by assigning part of the contribution from the gluon spins. To be more specific, in the Bjorken limit there exists an anomalous gluonic contribution to a_o in Eq.(2.50) and hence the same can be written as :

$$a_o = \int_0^1 dx \Delta\Sigma - 3 \frac{\alpha_s(Q^2)}{2\pi} \int_0^1 dx \Delta G, \quad (2.52)$$

where the second term represents the gluon contribution ([63], [62]).

Thus, the main modifications to the original QPM in the framework of QCD involve the introduction of gluonic interactions and the contribution of the gluon polarization to $g_1(x)$. Another potential impact is the *evolution equations* which introduce a very gentle logarithmic dependence of the structure functions on Q^2 . The Q^2 evolution of the parton distribution functions is given by the Dokshitzer-Gribov-Lipatov-Altarelli-Parisi (DGLAP) equations [62], [64], [65], [66]:

$$\frac{dq(x, Q^2)}{d \ln Q^2} = \int_x^1 \frac{dx'}{x'} \left[q(x', Q^2) \cdot P_{qq}\left(\frac{x}{x'}\right) + G(x', Q^2) \cdot P_{qG}\left(\frac{x}{x'}\right) \right] \quad (2.53)$$

$$\frac{dG(x, Q^2)}{d \ln Q^2} = \int_x^1 \frac{dx'}{x'} \left[G(x', Q^2) \cdot P_{GG}\left(\frac{x}{x'}\right) + \sum_q q(x', Q^2) \cdot P_{Gq}\left(\frac{x}{x'}\right) \right], \quad (2.54)$$

where P are the *splitting functions*² calculated perturbatively. Similar equations can be found for the polarized densities $\Delta q(x, Q^2)$ and $\Delta G(x, Q^2)$.

2.3 Quark-quark Correlation Matrix in the QCD Improved QPM

The QCD improved QPM introduces the quark-quark correlation matrix³ which correlates the quarks and anti-quarks inside the nucleon. The handbag diagram of DIS process is shown in Fig. 2.8.

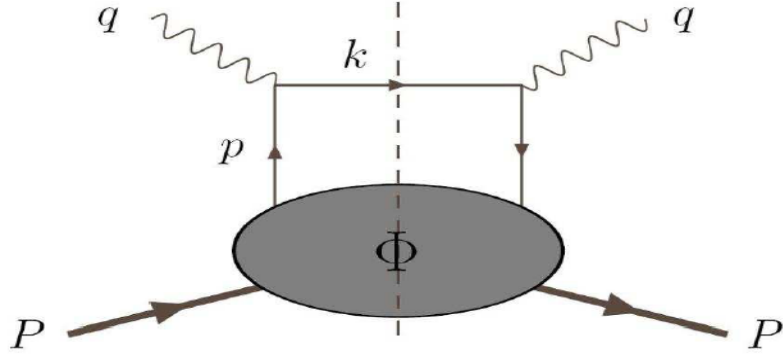


Figure 2.8: The handbag diagram for the DIS process involving the quark-quark correlation function Φ . Here, P and S are the momentum and the spin of the nucleon respectively in the initial state. q is the four momentum transfer and p represents the initial four momentum of the quark.

The hadronic tensor in this case can be expressed as [5] :

$$W_{\mu\nu} = \sum_i e_i^2 \int \frac{d^4p}{(2\pi)} \delta((p+q)^2) \text{Tr}[\Phi \gamma_\mu (\not{p} + \not{q}) \gamma_\nu], \quad (2.55)$$

where e_i is the fractional electric charge of the struck quark and γ_μ are the Dirac matrices. The matrix element Φ is called the quark-quark correlation matrix describing the quark field between the initial nucleon state $|P, S\rangle$ and the remnant $|X\rangle$, and is defined as :

$$\Phi_{i,j}(p, P, S) = \int d^4\xi e^{ip \cdot \xi} \langle P, S | \bar{\psi}_j(0) \psi_i(\xi) | P, S \rangle, \quad (2.56)$$

²A splitting function represents the probability of radiating a quark or gluon by a quark or gluon and converting into another quark or gluon. For instance, the splitting function $P_{qq'}(\frac{x}{x'})$ gives the probability that the quark q' radiates a gluon and converts to the quark q carrying a fraction $\frac{x}{x'}$ of the momentum of quark q' .

³In quantum field theory, the relation between two states can be realized through the matrix element computed by inserting a product of operators connecting the two states. The correlation matrix element, thus computed, is called the correlation function.

where the integration is performed over all possible separations ξ of the i^{th} component of the quark spinor ψ_i , i and j being the Dirac indices. The matrix Φ satisfies few relations based on the properties of hermiticity, parity and time-reversal respectively as follows [5] :

$$\Phi^\dagger(p, P, S) = \gamma^0 \Phi(p, P, S) \gamma^0 \quad (2.57)$$

$$\Phi(p, P, S) = \gamma^0 \Phi(\tilde{p}, \tilde{P}, -\tilde{S}) \gamma^0 \quad (2.58)$$

$$\Phi^*(p, P, S) = \gamma_5 C \Phi(\tilde{p}, \tilde{P}, \tilde{S}) C^\dagger \gamma_5 \quad (2.59)$$

Here $C = i\gamma^2\gamma^0$ and $\tilde{p}^\mu = (p^0, -\vec{p})$. Eq.(2.59) corresponds to the time-reversal property which is one of the most important aspect in the phenomenology of transverse polarization distributions. Now in the basis of Dirac matrices,

$$\Gamma = [\mathbf{1}, \gamma^\mu, \gamma^\mu \gamma_5, i\gamma_5, i\sigma^{\mu\nu} \gamma_5], \quad (2.60)$$

where $\sigma^{\mu\nu} = \frac{i}{2}[\gamma^\mu, \gamma^\nu]$, the correlation matrix can be, in general, decomposed as follows:

$$\Phi(p, P, S) = \frac{1}{2} \left[\mathcal{S} \mathbf{1} + \mathcal{V}_\mu \gamma^\mu + \mathcal{A}_\mu \gamma_5 \gamma^\mu + i\mathcal{P}_5 \gamma_5 + \frac{1}{2} i\mathcal{T}_{\mu\nu} \sigma^{\mu\nu} \gamma_5 \right] \quad (2.61)$$

The quantities in the above equation, i.e. the scalar \mathcal{S} , the vector \mathcal{V}_μ , the axial-vector \mathcal{A}_μ , the tensor $\mathcal{T}_{\mu\nu}$, and the pseudo-scalar \mathcal{P}_5 can be expressed in terms of p , P and S . In the following equations, the hermiticity and the time-reversal conditions have been applied :

$$\mathcal{S} = \frac{1}{2} Tr(\phi) = C_1 \quad (2.62)$$

$$\mathcal{V}^\mu = \frac{1}{2} Tr(\gamma^\mu \phi) = C_2 P^\mu + C_3 p^\mu \quad (2.63)$$

$$\mathcal{A}^\mu = \frac{1}{2} Tr(\gamma^\mu \gamma_5 \phi) = C_4 S^\mu + C_5 p \cdot S P^\mu + C_6 p \cdot S p^\mu \quad (2.64)$$

$$\mathcal{P} = \frac{1}{2i} Tr(\gamma_5 \phi) = 0 \quad (2.65)$$

$$\mathcal{T}^{\mu\nu} = \frac{1}{2i} Tr(\sigma^{\mu\nu} \gamma_5 \phi) = C_7 P^{[\mu} S^{\nu]} + C_8 p^{[\mu} S^{\nu]} + C_9 p \cdot S P^{[\mu} p^{\nu]}, \quad (2.66)$$

where the coefficients $C_i = C_i(p^2, p \cdot P)$ are real functions, owing to hermiticity. If the transverse momenta are neglected, only the vector, axial, and tensor terms remain as non-zero and Eqs.(2.63),(2.64) and (2.66) can be expressed as :

$$\mathcal{V}^\mu = \frac{1}{2} \int d^4\xi e^{ip \cdot \xi} \langle PS | \bar{\psi}(0) \gamma^\mu \psi(\xi) | PS \rangle = A_1 P^\mu \quad (2.67)$$

$$\mathcal{A}^\mu = \frac{1}{2} \int d^4\xi e^{ip \cdot \xi} \langle PS | \bar{\psi}(0) \gamma^\mu \gamma_5 \psi(\xi) | PS \rangle = \lambda_N A_2 P^\mu \quad (2.68)$$

$$\mathcal{T}^{\mu\nu} = \frac{1}{2i} \int d^4\xi e^{ip \cdot \xi} \langle PS | \bar{\psi}(0) \sigma^{\mu\nu} \gamma_5 \psi(\xi) | PS \rangle = A_3 P^{[\mu} S_{\perp}^{\nu]}, \quad (2.69)$$

where $A_i(p^2, p \cdot P)$ are real functions and $S^\mu \approx \frac{\lambda_N P^\mu}{M} + S_\perp^\mu$ is the nucleon spin with nucleon helicity λ . Now the correlation matrix can be written in the form [5] :

$$\Phi(p, P, S) = \frac{1}{2} [A_1 \not{P} + A_2 \lambda_N \gamma_5 \not{P} + A_3 \not{P} \gamma_5 \not{S}_\perp] \quad (2.70)$$

with

$$A_1 = \frac{1}{2P^+} \text{Tr}(\gamma^+ \Phi) \quad (2.71)$$

$$\lambda_N A_2 = \frac{1}{2P^+} \text{Tr}(\gamma^+ \gamma_5 \Phi) \quad (2.72)$$

$$S_\perp^i A_3 = \frac{1}{2P^+} \text{Tr}(i\sigma^{i+} \gamma_5 \Phi) = \frac{1}{2P^+} \text{Tr}(\gamma^+ \gamma^i \gamma_5 \Phi) \quad (2.73)$$

Here, P^+ is the component of the momentum⁴ of the nucleon along the light-cone axis x^+ as described in Appendix A. Integrating the amplitudes A_1 , A_2 and A_3 over p with the constraint $x = \frac{p^+}{P^+}$, the three leading-twist⁵ distribution functions can be obtained :

$$q(x) = \int \frac{d^4 p}{(2\pi)^4} A_1(p^2, p \cdot P) \delta\left(x - \frac{p^+}{P^+}\right) \quad (2.74)$$

$$\Delta q(x) = \int \frac{d^4 p}{(2\pi)^4} A_2(p^2, p \cdot P) \delta\left(x - \frac{p^+}{P^+}\right) \quad (2.75)$$

$$\delta q(x) = \int \frac{d^4 p}{(2\pi)^4} A_3(p^2, p \cdot P) \delta\left(x - \frac{p^+}{P^+}\right) \quad (2.76)$$

Then the correlation function, when integrated over the quark momentum p , can be expressed as:

$$\Phi(x) = \frac{1}{2} [q(x) \not{P} + \lambda_N \Delta q(x) \gamma_5 \not{P} + \delta q(x) \not{P} \gamma_5 \not{S}_\perp] \quad (2.77)$$

These parton distribution functions can provide a comprehensive information about the spin and momentum distributions of the quarks inside the nucleon. The first two distribution functions $q(x)$ and $\Delta q(x)$ are known to reasonable precision as mentioned earlier. The third distribution function $\delta q(x)$, which is named as the *transversity* distribution function, is the least known and only a few measurements have been dedicated to investigate this

⁴In the limit $Q^2 \rightarrow \infty$, the four momentum vector of the nucleon can be expressed in the light-cone coordinates as : $p^\mu = \left[\frac{M^2}{2P^+}, P^+, \vec{0}\right]$. See Appendix A.

⁵*Twist* is used as a parameter to represent particular effect realized in a particular experiment in the order of $\frac{1}{Q^2}$. For instance, if an observable in an experiment exhibits a behavior that is governed by $(\frac{1}{Q^2})^n$, then the *twist* of the observable is defined as $t = 2 + 2n$. The leading twist corresponds to $t=2$ which implies $n=0$. Thus, the leading twist behavior is independent of $(\frac{1}{Q^2})$. In the operator product expansion (OPE) formalism, *twist* (t) is defined as the difference between the dimension (d) and spin (s) of an operator, i.e., $t=d-s$. The extensive formal derivation of *twist* can be found in [67].

function so far. The first extraction of $\delta q(x)$ has been performed by the global fit of the data from HERMES, COMPASS and BELLE [46]. These parton distribution functions follow the following relations for the antiquarks where the anticommutation relations for the Fermion fields in the connected matrix elements have been used, i.e., ($\langle PS|\bar{\psi}(\xi)\psi(0)|PS\rangle = -\langle PS|\psi(0)\bar{\psi}(\xi)|PS\rangle$) [5]:

$$\bar{q}(x) = -q(-x) \tag{2.78}$$

$$\Delta\bar{q}(x) = \Delta q(-x) \tag{2.79}$$

$$\delta\bar{q}(x) = -\delta q(-x), \tag{2.80}$$

where $x > 0$.

2.3.1 Probabilistic Interpretation of the Distribution Function

It is worthwhile to discuss here the distribution functions as probability densities for finding the partons in a given polarization direction which carry a given momentum fraction x inside the nucleon. In the field theoretical definitions, the quark field can be decomposed into “large” and “small” components [5] :

$$\psi = \psi_+ + \psi_- \tag{2.81}$$

and $\psi_{\pm} = \frac{1}{2}\gamma^{\mp}\gamma^{\pm}\psi$. In the limit $P^+ \rightarrow \infty$, the “large” component ψ_+ dominates over the “small” components ψ_- . The probabilistic content of the distribution functions with a complete set of n intermediate states included can be expressed in terms of the following functions.

- **Unpolarized Distribution Function $q(x)$**

$$q(x) = \frac{1}{\sqrt{2}} \sum_n \delta((1-x)P^+ - P_n^+) |\langle PS|\psi_+(0)|n\rangle|^2, \tag{2.82}$$

where the summation over the n intermediate states incorporates the integration over the phase space. Thus the unpolarized distribution function gives the probability of finding an unpolarized quark with a longitudinal momentum fraction x , where $x = p^+/P^+$.

- **Helicity Distribution Function $\Delta q(x)$**

$$\Delta q(x) = \frac{1}{\sqrt{2}} \sum_n \delta((1-x)P^+ - P_n^+) \left[|\langle PS | \mathcal{P}_+ \psi_+(0) | n \rangle|^2 - |\langle PS | \mathcal{P}_- \psi_+(0) | n \rangle|^2 \right], \quad (2.83)$$

where $\mathcal{P}_\pm = \frac{1}{2}(1 \pm \gamma_5)$. The helicity distribution function gives the difference between the probability of finding a quark with momentum fraction x with its helicity in the same direction as that of the nucleon (denoted by + state) inside the nucleon and the probability of finding it with its helicity in the opposite direction as that of the nucleon (denoted by - state).

- **Transversity Distribution Function $\delta q(x)$**

$$\delta q(x) = \frac{1}{\sqrt{2}} \sum_n \delta((1-x)P^+ - P_n^+) \left[|\langle PS | \mathcal{P}_\uparrow \psi_+(0) | n \rangle|^2 - |\langle PS | \mathcal{P}_\downarrow \psi_+(0) | n \rangle|^2 \right], \quad (2.84)$$

where $\mathcal{P}_{\uparrow\downarrow} = \frac{1}{2}(1 \pm \gamma^1 \gamma_5)$. The transversity distribution function gives the difference between the probability of finding a quark with momentum fraction x with its polarization in the same direction as that of the nucleon (denoted by \uparrow state) inside the nucleon and the probability of finding it with its polarization in the opposite direction as that of the nucleon (denoted by \downarrow state). In this case, the nucleon is polarized in the trasverse direction with respect to the incoming lepton beam.

2.3.2 Vector, Axial and Tensor Charge

The integration of Eqs.(2.74), (2.75), and (2.76) over x gives the vector, axial, and tensor charges of the nucleon, respectively:

$$q = \int_0^1 [q(x) - \bar{q}(x)] dx = g_V, \quad (2.85)$$

$$\Delta q = \int_0^1 [\Delta q(x) - \Delta \bar{q}(x)] dx = g_A, \quad (2.86)$$

$$\delta q = \int_0^1 [\delta q(x) - \delta \bar{q}(x)] dx = g_T. \quad (2.87)$$

2.4 Distribution Functions with Quark-nucleon Helicity Amplitudes

The leading-twist quark distribution functions can be expressed in terms of quark-nucleon forward helicity amplitudes. In the helicity basis $[|+\rangle, |-\rangle]$, there are 16 different forward

amplitudes $\mathcal{A}_{\Lambda\lambda\Lambda'\lambda'}$ in general that can be defined where $\lambda\lambda'$ ($\Lambda\Lambda'$) are the quark (nucleon) helicities in the initial and final states. Now helicity conservation, parity invariance, and time-reversal invariance demand :

$$\Lambda + \lambda = \Lambda' + \lambda', \quad (2.88)$$

$$\mathcal{A}_{\Lambda\lambda\Lambda'\lambda'} = \mathcal{A}_{-\Lambda-\lambda-\Lambda'-\lambda'}, \quad (2.89)$$

$$\mathcal{A}_{\Lambda\lambda\Lambda'\lambda'} = \mathcal{A}_{\Lambda'\lambda'\Lambda\lambda}. \quad (2.90)$$

Thus, having imposed all the constraints, we are left with only three independent amplitudes out of the 16 : \mathcal{A}_{++++} , \mathcal{A}_{+--+} and \mathcal{A}_{+---} as shown in the Fig. 2.9.

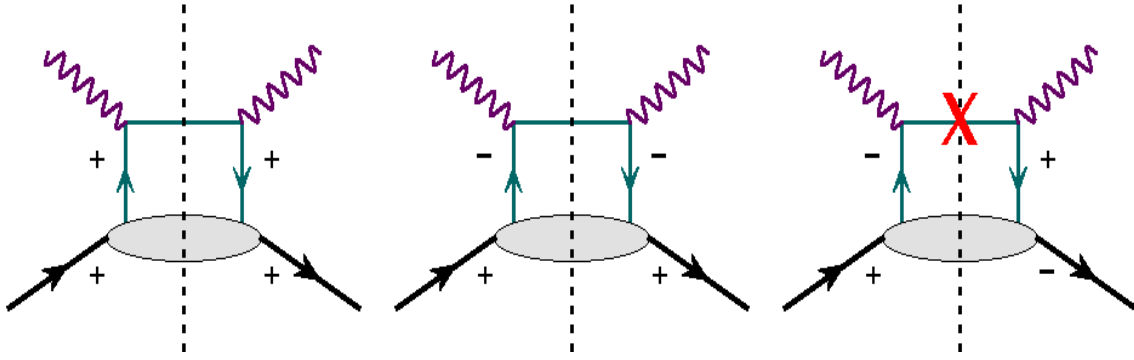


Figure 2.9: The handbag diagrams for the unpolarized distribution $q(x)$ (left), helicity distribution $\Delta q(x)$ (middle) and the transversity distribution $\delta q(x)$ (right). There are helicity flips of both quark and nucleon in case of $\delta q(x)$ and hence helicity is not conserved. In each of the diagrams, the top pair of signs (+ or -) represents the helicities of the quark and the bottom pair represents the helicities of the nucleon.

As can be seen, the first two amplitudes do not involve any quark or nucleon helicity flip. However, the last amplitude requires the helicity flip of the quark as well as the nucleon. The optical theorem (see Appendix B for details) relates these helicity amplitudes to the three leading twist distribution functions :

$$q(x) = q^+(x) + q^-(x) \sim Im(\mathcal{A}_{++++} + \mathcal{A}_{+--+}), \quad (2.91)$$

$$\Delta q(x) = q^+(x) - q^-(x) \sim Im(\mathcal{A}_{++++} - \mathcal{A}_{+--+}), \quad (2.92)$$

$$\delta q(x) \sim Im(\mathcal{A}_{+---}). \quad (2.93)$$

As mentioned above, the amplitude being off-diagonal due to the helicity flip of both the nucleon and the quark, the transversity distribution $\delta q(x)$ can not be diagonalized in the helicity basis and hence it carries no probabilistic interpretation in the helicity basis. In

order to associate a probabilistic interpretation to the transversity distribution function, it is essential to transform the helicity basis to the transversity or chirality basis, the latter being a linear combination of the former. The transversity or the chirality basis can be realized as :

$$|\uparrow\rangle = \frac{1}{2}(|+\rangle + i|-\rangle), \quad |\downarrow\rangle = \frac{1}{2}(|+\rangle - i|-\rangle). \quad (2.94)$$

In this basis, $\delta q(x)$ can be interpreted as the difference in the probabilities of finding a quark with its spin aligned along the transverse spin of the parent nucleon and with its spin anti-aligned with respect to the spin of the nucleon. Thus transversity distribution can be expressed as :

$$\delta q(x) = q^\uparrow(x) - q^\downarrow(x) \sim \text{Im}(\mathcal{A}_{\uparrow\uparrow\uparrow} - \mathcal{A}_{\uparrow\downarrow\downarrow}) \quad (2.95)$$

The helicity basis and the transversity basis can be related by means of rotation. In the relativistic regime, the Lorentz boost and rotation do not commute and hence helicity distribution and the transversity distribution are different. In addition, unlike the helicity distribution there is no transversity distribution for gluons because the gluons have integer spins and any flipping of the helicity would result in a helicity flip of 2 for the nucleons in the process which is impossible for a spin half target. However, targets with higher spin may have a helicity-flip gluon distribution. Thus the transversity distribution $\delta q(x)$ has a valence like behavior, but the Q^2 evolution of $\delta q(x)$ and $\Delta q(x)$ are different. This is shown in Fig. 2.10 and Fig. 2.11.

The Soffer Inequality

From the definitions of the three leading twist distribution functions, *viz*, $q(x) = q^+(x) + q^-(x)$, $\Delta q(x) = q^+(x) - q^-(x)$, and $\delta q(x) = q^\uparrow(x) - q^\downarrow(x)$, one can realize the following obvious bounds on these functions :

$$|\Delta q(x)| \leq q(x), \quad |\delta q(x)| \leq q(x). \quad (2.96)$$

These bounds are satisfied by the antiquarks as well. Another non-trivial bound involving all the three distribution functions together was deduced by Soffer [68]. Introducing a quark-nucleon vertex $a_{\Lambda\lambda}$ where Λ and λ are the helicities of the nucleon and the quark

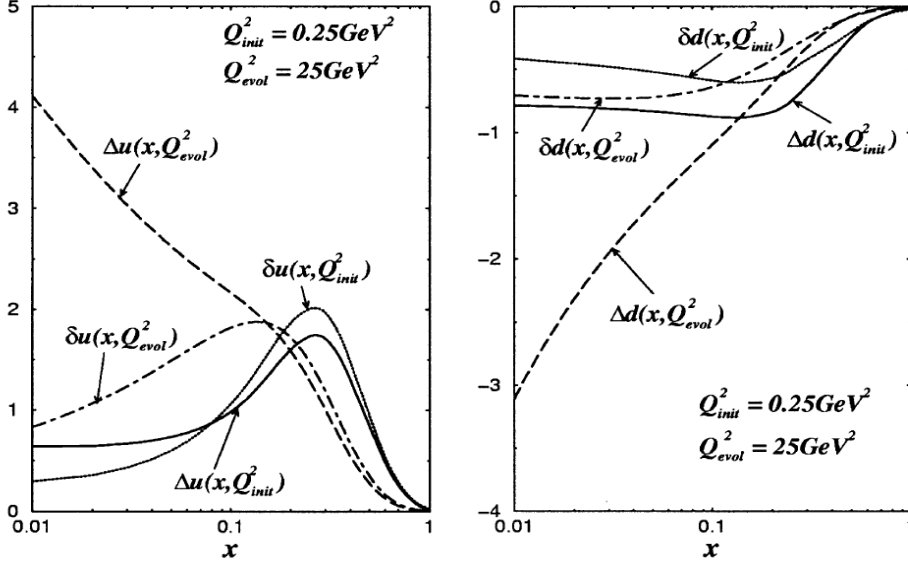


Figure 2.10: The Q^2 evolution of the transversity distribution function $\delta q(x)$ and the helicity distribution $\Delta q(x)$ for *up* and *down* quarks. This Chiral Quark Soliton Model calculation shows that for both *up* and *down* quarks, the Q^2 evolutions of the respective distributions differ in the low x region. These figures have been taken from [5].

respectively, Eqs.(2.91), (2.92) and (2.93) can be rewritten as follows [5]:

$$q(x) \sim \text{Im}(\mathcal{A}_{++,+} + \mathcal{A}_{+,-,+}) \sim \sum_X (a^*_{++} a_{++} + a^*_{+-} a_{+-}), \quad (2.97)$$

$$\Delta q(x) \sim \text{Im}(\mathcal{A}_{++,+} - \mathcal{A}_{+,-,+}) \sim \sum_X (a^*_{++} a_{++} - a^*_{+-} a_{+-}), \quad (2.98)$$

$$\delta q(x) \sim \text{Im}(\mathcal{A}_{+,-,+}) \sim \sum_X a^*_{--} a_{++} \quad (2.99)$$

Now,

$$\sum_X |a_{++} \pm a_{--}|^2 \geq 0 \quad (2.100)$$

and using parity conservation, we get,

$$\sum_X a^*_{++} a_{++} \pm \sum_X a^*_{--} a_{++} \geq 0 \quad (2.101)$$

This can be expressed in terms of the distribution function as follows :

$$q(x) + \Delta q(x) \geq 2|\delta q(x)| \quad (2.102)$$

This is called the Soffer inequality. It must be satisfied by all three leading twist distribution functions. It was very complicated to derive the inequality as the distributions involved can

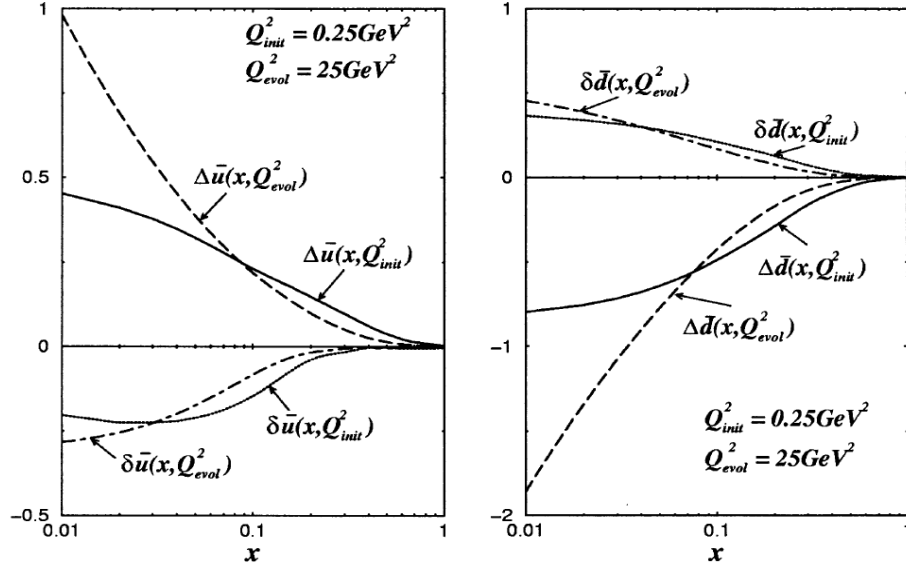


Figure 2.11: The Q^2 evolution of the transversity distribution function $\delta q(x)$ and the helicity distribution $\Delta q(x)$ for *anti-up* and *anti-down* quarks. This Chiral Quark Soliton Model calculation shows that for both *anti-up* and *anti-down* quarks, the Q^2 evolutions of the respective distributions differ in the low x region [5].

not be diagonalized in the same basis simultaneously and hence it requires the consideration of the probability amplitudes. The Soffer bound is shown in the Fig. 2.12.

2.5 Transverse Motion of Quarks : Transverse Momentum Dependent Distribution Function

The intrinsic transverse momentum of a quark can be neglected as compared to the longitudinal component since we do not deal with the final momentum of the produced hadron in the inclusive scattering process. However in semi inclusive processes, the transverse momenta of quarks $p_T^\vec{}$ can no longer be ignored as they influence the momenta of the hadrons in the final state. In general, the momentum of the quark in such a process can be expressed as :

$$p^\mu = xP^\mu + p_T^\mu \quad (2.103)$$

Here P^μ is the total longitudinal momentum of the nucleon and x is the fraction of the longitudinal momentum carried by the quark. Now if we take into consideration the transverse momenta of the quarks, additional amplitudes appear in Eqs.(2.68) and (2.69) for the

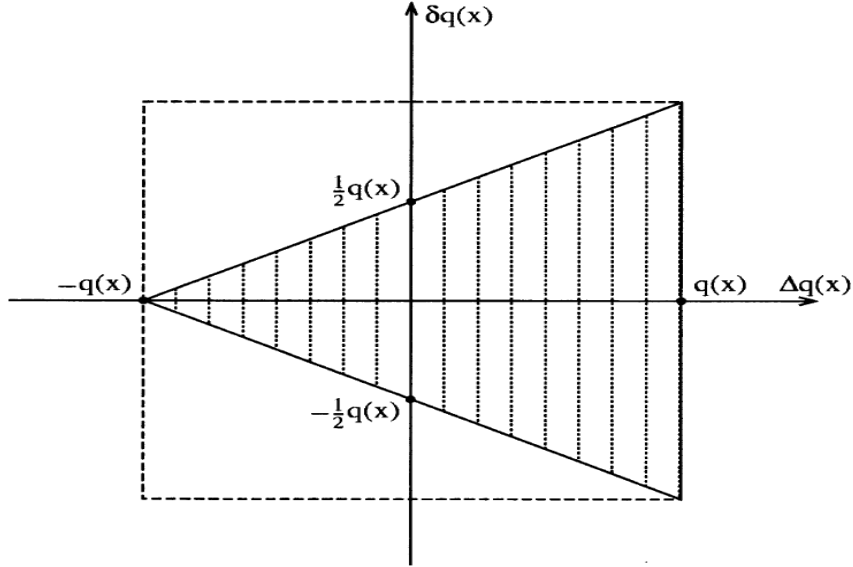


Figure 2.12: The Soffer bound for the twist-2 distribution functions [5].

axial-vector and tensor components of the correlation matrix which are described in [5]. The eight \vec{p}_T dependent distribution functions related to these amplitudes are shown in Fig. 2.13.

Integration over \vec{p}_T with the chirality and time-reversal conditions forces most of the functions to vanish except the following three :

$$q(x) = \int d^2\vec{p}_T q(x, p_T^2), \quad (2.104)$$

$$\Delta q(x) = \int d^2\vec{p}_T \Delta q(x, p_T^2), \quad (2.105)$$

$$\delta q(x) = \int d^2\vec{p}_T \left[h^q_{1T}(x, p_T^2) + \frac{p_T^2}{2M} h^{\perp q}_{1T}(x, p_T^2) \right] = \int d^2\vec{p}_T \delta q(x, p_T^2). \quad (2.106)$$

However, if time reversal invariance is not applied, two other distribution functions survive after the integration over \vec{p}_T . These are the T-odd distribution functions : *Sivers distribution function* (f_{1T}^\perp) and *Boer-Mulders function* (h_1^\perp). The *Sivers function* is related to the probability of finding an unpolarized quark in a transversely polarized nucleon whereas the *Boer-Mulders function* gives the probability of finding a transversely polarized quark in an unpolarized nucleon. The *Sivers function* f_{1T}^\perp was first proposed by Sivers [69] in order to explain the single-spin asymmetries observed in pion electroproduction in p-p scattering. f_{1T}^\perp relates the intrinsic transverse momentum of the quark to the transverse spin of the

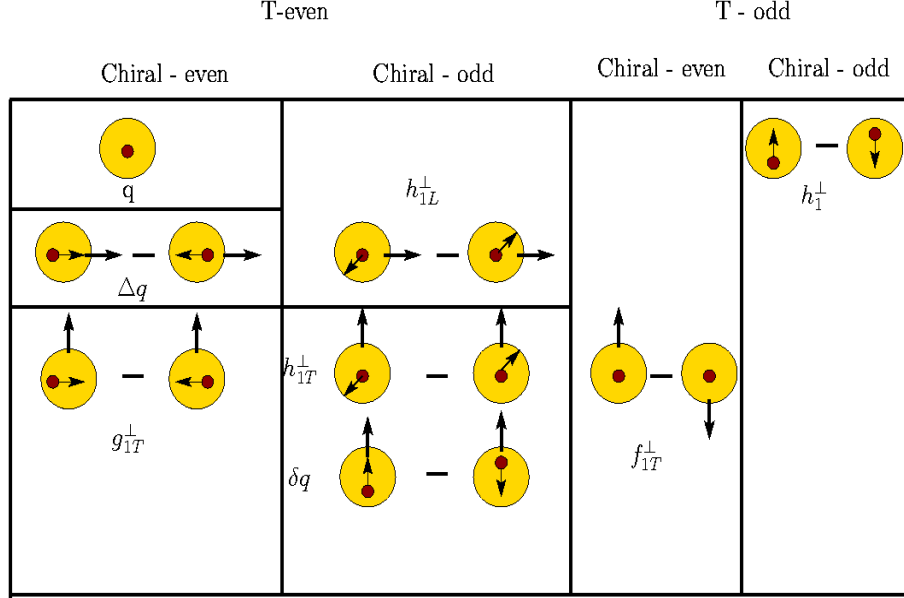


Figure 2.13: The transverse momentum dependent (TMD) parton distribution functions. Only leading twist functions are shown. The large circle represents the nucleon and the small circle depicts the quark inside it. The arrow associated with the respective nucleon and the quark signifies the spin orientation of them.

nucleon. It is expected that the non-zero *Sivers function* might signify the existence of orbital momentum of quarks inside the nucleon which could be the missing contribution to the nucleon spin [47].

2.6 The Semi-Inclusive Deep Inelastic Scattering (SIDIS) and Fragmentation Functions (FF)

The transversity distribution function can not be accessed in inclusive DIS because of its chiral-odd nature. In order to preserve chirality in the process, one has to measure another chiral-odd object together with the transversity distribution. The convolution of the chiral-odd distribution function with the fragmentation function (discussed in the next subsection) allows to access the transversity distribution function without violating any chirality conservation if the fragmentation function is known. SIDIS is one of the several ways to measure the transversity distribution function in combination with the Collins fragmentation function. In one hadron SIDIS, a final state hadron is detected in coincidence with the scattered

electron :

$$l(k) + N(P) \longrightarrow l(k') + h(P_h) + X(P_X), \quad (2.107)$$

where l is the incoming lepton with four momentum k scattered off a nucleon N with four momentum P . h is the final state hadron detected with momentum P_h and X is the undetected hadronic final state with momentum P_X . In case of SIDIS, the process of the formation of the final state hadrons has to be accounted for as an additional feature in the formalism of inclusive DIS discussed earlier. The process of formation of final state hadrons from the quarks in the deep inelastic regime is called *fragmentation* or *hadronization*. The fragmentation process occurs at low Q^2 and hence it can not be described with perturbative QCD.

The leptonic tensor in the case of SIDIS remains the same as discussed in inclusive DIS since the leptonic vertices in both cases are identical. However, the hadronic tensor gets modified because the fragmentation process comes into play. The hadronic tensor in SIDIS can be expressed as :

$$W^{\mu\nu} = \frac{1}{2M} \sum_i e_i^2 \int d^4p d^4k \delta^{(4)}(p + q - k) Tr(\Phi(p, P, S) \gamma^\mu \Delta(k, P_h) \gamma^\nu), \quad (2.108)$$

where Φ is the correlation function defined earlier and Δ is the modified correlation function which incorporates the fragmentation process:

$$\Delta_{ij}(k, P_h) = \frac{1}{(2\pi)^4} \int d^4\xi e^{ik \cdot \xi} \langle 0 | \psi_i(\xi) | P_h \rangle \langle P_h | \bar{\psi}_j(0) | 0 \rangle. \quad (2.109)$$

In analogy to the formalism followed earlier in case of the distribution function, one can decompose this new correlation function Δ in the basis of Dirac matrices which in turn results in eight fragmentation functions in leading twist. These fragmentation functions depend on the fraction of the energy carried by the outgoing hadron which is denoted by z , with $z = P \cdot P_h / P \cdot q$ and on $z^2 k_T^2$ where \vec{k}_T is the transverse momentum of the final fragmenting quark. The summation includes all spins of the detected hadrons as we are not interested in the polarization of the final hadrons. Therefore after summing over all the spins of the hadrons, only two leading twist fragmentation functions (FF) survive : the unpolarized FF $D_1^q(z, z^2 k_T^2)$ and the Collins FF $H_1^{\perp q}(z, z^2 k_T^2)$. The probabilistic interpretations of these two FFs are discussed next.

Probabilistic Interpretation of $D_1^q(z, z^2 k_T^2)$ and $H_1^{\perp q}(z, z^2 k_T^2)$:

The probabilistic interpretation of the fragmentation functions (FF) can be realized similar to the distribution functions (DF). The unpolarized FF $D_1^q(z, z^2 k_T^2)$ is the probability density that a struck quark q , having a transverse momentum \vec{k}_T , fragments into a hadron of type h which carries a momentum fraction z . The Collins FF $H_1^{\perp q}(z, z^2 k_T^2)$ represents the difference of the probability densities for the quarks with transverse spin orientations (represented by \uparrow and \downarrow) fragmenting into a hadron h . These two FFs are shown in Fig. 2.14.

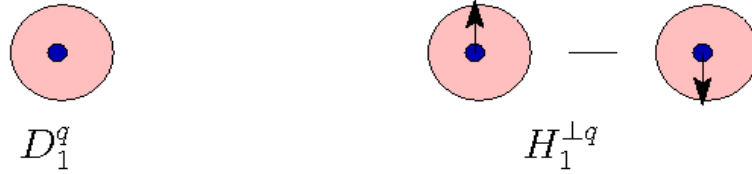


Figure 2.14: The transverse momentum dependent (TMD) fragmentation functions (twist-2). The unpolarized fragmentation function is shown in the left while the Collins fragmentation function is depicted on right. The large circle represents the unpolarized hadron produced by the fragmenting quarks which are represented by the small circle inside the large one.

The unpolarized FF $D_1^q(z, z^2 k_T^2)$ is a chiral-even and T-even function while the Collins FF $H_1^{\perp q}(z, z^2 k_T^2)$ is a chiral-odd and T-odd function. The T-odd behavior for the Collins FF can be explained by the final state interaction described in Ref. [70].

As mentioned earlier, the fragmentation process can not be described by perturbative QCD. Instead, there exist different phenomenological models in order to describe the process. The *Lund model* is one of the most successful models that has been developed which describes the existing experimental data [71], [72]. In this model, the highest energy gluons are treated as field lines which are attracted to each other due to the gluon self interaction and form a string of strong color field. The field generates a potential which increases with the distance between the quarks. In the reaction when the quark is struck by the virtual photon with enough energy, it starts getting away from the other quarks and hence the potential energy of the string increases linearly with separation. At some point, when this increasing energy surpasses the rest mass of the quark-antiquark pair, the string breaks and

creates another quark-antiquark pair. The two constituent quark and anti-quark in the new pair are connected to the initial quark by two strings. The process of breaking strings and formation of new quark-antiquark continues until a quark-antiquark pair is formed which is close to the mass of a hadron.

Considering only the three lightest quark flavors u , d , and s and applying isospin symmetry and charge conjugation, the FFs can be divided into three different categories : *favored*, *unfavored*, and *strange*. The classification is based on the flavor of the fragmenting quarks and the quark contents of the produced hadron and is given as follows:

$$F^{fav}(z, Q^2) = F_u^{\pi^+}(z, Q^2) = F_{\bar{u}}^{\pi^-}(z, Q^2) = F_d^{\pi^+}(z, Q^2) = F_d^{\pi^-}(z, Q^2), \quad (2.110)$$

$$F^{unfav}(z, Q^2) = F_u^{\pi^-}(z, Q^2) = F_{\bar{u}}^{\pi^+}(z, Q^2) = F_d^{\pi^-}(z, Q^2) = F_d^{\pi^+}(z, Q^2), \quad (2.111)$$

$$F^{strange}(z, Q^2) = F_s^{\pi^+}(z, Q^2) = F_{\bar{s}}^{\pi^-}(z, Q^2) = F_s^{\pi^-}(z, Q^2) = F_{\bar{s}}^{\pi^+}(z, Q^2). \quad (2.112)$$

Here F represents the generic FF which includes both the unpolarized and Collins FF. Similar expressions hold for charged kaons. Global analysis of the fragmentation functions for protons and inclusive charged hadrons have been done with data using single-inclusive hadron production in e^+e^- annihilation, $p - p$ collisions from RHIC, and deep inelastic lepton-proton scattering from HERMES [73].

2.7 The SIDIS Cross Section

The semi-inclusive DIS cross section of single hadron fragmentation for low transverse momentum of the hadron can be decomposed in terms of the structure functions. It can be calculated in terms of transverse-momentum-dependent (TMD) parton distributions and fragmentation functions at tree level [74]. In the derivation of the results, only one photon exchange approximation is implemented. The single hadron SIDIS process is depicted in Fig. 2.15.

The quantities are defined below:

- (\vec{k}, \vec{k}') : momenta of incoming lepton (electron in our case) and scattered lepton. They form the scattering plane.
- \vec{S}_\perp : the transverse component of the target spin vector.
- ϕ_S : azimuthal angle between \vec{S}_\perp and the scattering plane.

- \vec{P}_h : momentum of the outgoing hadron.
- $\vec{P}_{h\perp}$: transverse component of \vec{P}_h .
- ϕ_h : azimuthal angle between the scattering plane and the hadron production plane.

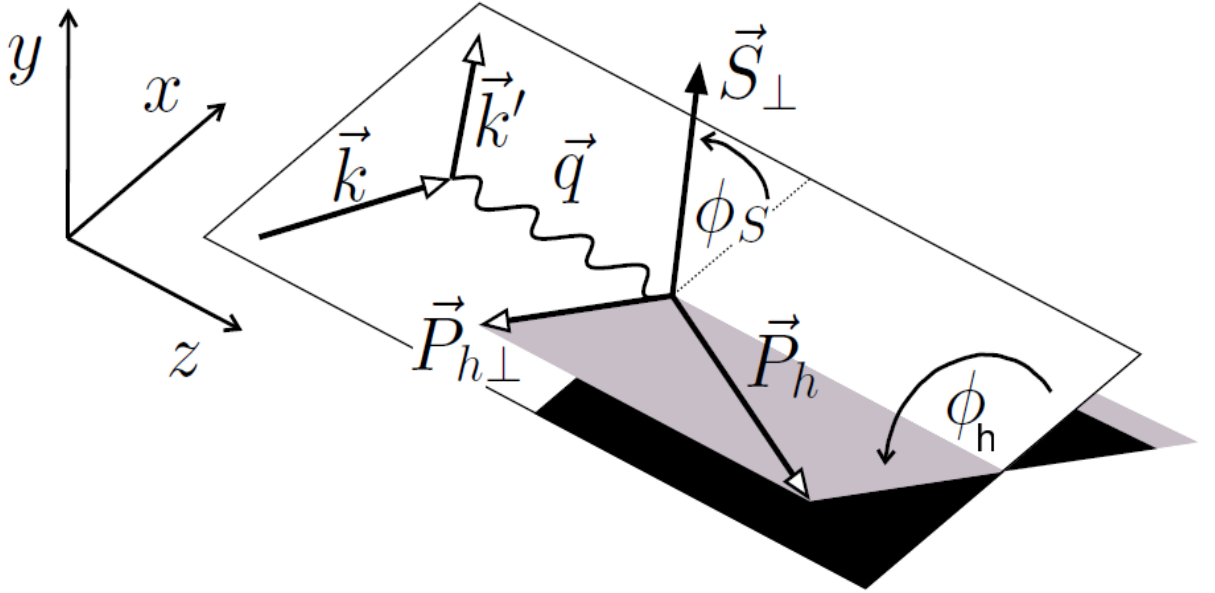


Figure 2.15: Schematic of the kinematic planes and azimuthal angles related to the transverse component of the target spin \vec{S}_\perp and the transverse component of the momentum of the produced hadron $\vec{P}_{h\perp}$.

Following the Trento conventions [75] in the target rest frame, the cross section of SIDIS process (where in this case, only the unpolarized hadrons are detected in the final state in coincidence with the scattered electrons) can be expanded in terms of a set of structure functions in a model-independent way as shown in Eq. (2.113) on the next page.

$$\begin{aligned}
\frac{d\sigma^h}{dx dy dz d\phi_S d\phi_h dP_{h\perp}^2} &= \frac{\alpha_s^2}{xyQ^2} \frac{y^2}{2(1-\epsilon)} \left(1 + \frac{\gamma^2}{2x}\right) \left[F_{UU,T} + \epsilon F_{UU,L} \right. \\
&+ \sqrt{2\epsilon(1+\epsilon)} \cos\phi_h F_{UU}^{\cos\phi_h} + \epsilon \cos(2\phi_h) F_{UU}^{\cos 2\phi_h} \\
&+ \lambda_e \sqrt{2\epsilon(1-\epsilon)} \sin\phi_h F_{LU}^{\sin\phi_h} \\
&+ S_{\parallel} \left[\sqrt{2\epsilon(1+\epsilon)} \sin\phi_h F_{UL}^{\sin\phi_h} + \epsilon \sin(2\phi_h) F_{UL}^{\sin 2\phi_h} \right] \\
&+ S_{\parallel} \lambda_e \left[\sqrt{1-\epsilon^2} F_{LL} + \sqrt{2\epsilon(1-\epsilon)} \cos\phi_h F_{LL}^{\cos\phi_h} \right] \\
&+ |S_{\perp}| \left[\sin(\phi_h - \phi_S) \left(F_{UT,T}^{\sin(\phi_h - \phi_S)} + \epsilon F_{UT,L}^{\sin(\phi_h - \phi_S)} \right) \right. \\
&+ \sin(\phi_h + \phi_S) F_{UT}^{\sin(\phi_h + \phi_S)} + \epsilon \sin(3\phi_h - \phi_S) F_{UT}^{\sin(3\phi_h - \phi_S)} \\
&+ \left. \sqrt{2\epsilon(1+\epsilon)} \sin\phi_S F_{UT}^{\sin\phi_S} + \sqrt{2\epsilon(1+\epsilon)} \sin(2\phi_h - \phi_S) F_{UT}^{\sin(2\phi_h - \phi_S)} \right] \\
&+ |S_{\perp}| \lambda_e \left[\sqrt{1-\epsilon^2} \cos(\phi_h - \phi_S) F_{LT}^{\cos(\phi_h - \phi_S)} + \sqrt{2\epsilon(1-\epsilon)} \cos\phi_S F_{LT}^{\cos\phi_S} \right. \\
&+ \left. \left. \sqrt{2\epsilon(1-\epsilon)} \cos(2\phi_h - \phi_S) F_{LT}^{\cos(2\phi_h - \phi_S)} \right] \right] \tag{2.113}
\end{aligned}$$

where α_s is the strong coupling constant and ϵ is the ratio of the longitudinal and transverse photon flux given by :

$$\epsilon = \frac{1 - y - \frac{1}{4}\gamma^2 y^2}{1 - y + \frac{1}{2}y^2 + \frac{1}{4}\gamma^2 y^2} \tag{2.114}$$

Here, $\gamma = 2Mx/Q^2$ and y is the fractional energy loss of the lepton where $y = P \cdot q / P \cdot k$. The structure functions in the above Eq.(2.113) are functions of x , Q^2 , z , and $P_{h\perp}^2$. The first subscript in F indicates the beam polarization and the second represents the respective target polarization. The third subscript signifies the polarization of the virtual photon.

Now from Eq.(2.113), one can calculate and extract the various structure functions by implementing the parametrization of the different correlators of the hadronic tensors discussed in Ref. [74].

Convolution of Distribution Functions and Fragmentation Functions

The structure functions in the above expression for the cross section can be expressed in a compact way by introducing the convolution integral and defining a unit vector $\hat{h}_\perp = P_{h_\perp}/|P_{h_\perp}|$ as follows:

$$\mathcal{C}[W, d, F] = x \sum_{q, \bar{q}} e_q^2 \int d^2\vec{p}_T d^2\vec{k}_T \delta^2 \left(\vec{p}_T - \vec{k}_T - \frac{\vec{P}_{h_\perp}}{z} \right) \cdot W(\vec{p}_T, \vec{k}_T) d_q(x, p_T^2) F_q(z, z^2 k_T^2) \quad (2.115)$$

where $W(\vec{p}_T, \vec{k}_T)$ is an arbitrary function, and $d_q(x, p_T^2)$ and $F_q(z, z^2 k_T^2)$ are the distribution function and fragmentation function respectively. The summation is over all quarks and anti-quarks. The structure functions, then, can be written as a convolution of the distribution functions and the fragmentation functions. The complete list of the results is reported in [74]. Here only a few of those mentioned are relevant to the thesis :

$$F_{UU,T} = \mathcal{C}[qD_1], \quad (2.116)$$

where q and D_1 are the unpolarized distribution function and fragmentation functions as mentioned in earlier sections and

$$F_{UU,L} = 0. \quad (2.117)$$

The Boer-Mulders distribution function h_1^\perp and the Collins fragmentation function H_1^\perp are convoluted as

$$F_{UU}^{\cos 2\phi_h} = \mathcal{C} \left[-\frac{2(\hat{h}_\perp \cdot \vec{k}_T)(\hat{h}_\perp \cdot \vec{p}_T) - \vec{k}_T \cdot \vec{p}_T}{MM_h} h_1^\perp H_1^\perp \right]. \quad (2.118)$$

The transversity distribution function δq and the Collins fragmentation function H_1^\perp are related as

$$F_{UT}^{\sin(\phi_h + \phi_S)} = \mathcal{C} \left[-\frac{\hat{h}_\perp \cdot \vec{k}_T}{M_h} \delta q H_1^\perp \right], \quad (2.119)$$

and the Siverts distribution function f_{1T}^\perp is convoluted with the unpolarized fragmentation D_1 function as

$$F_{UT}^{\sin(\phi_h - \phi_S)} = \mathcal{C}\left[-\frac{\hat{h}_\perp \cdot \vec{p}_T}{M} f_{1T}^\perp D_1\right]. \quad (2.120)$$

Other terms such as $F_{UT}^{\sin(3\phi_h - \phi_S)}$, $F_{UT}^{\sin(\phi_S)}$, $F_{UT}^{\sin(2\phi_h - \phi_S)}$, etc. have reasonably small contributions to the SIDIS cross section.

From the viewpoint our experiment in which the incoming electron beam is unpolarized and the target is transversely polarized, it is convenient to separate the SIDIS cross section into two parts :

$$\begin{aligned} d\sigma^h &\equiv d\sigma_{UU} + d\sigma_{UT} \\ &\equiv d\sigma_{UU} + (d\sigma_{UT}^{\text{Collins}} + d\sigma_{UT}^{\text{Siverts}} + d\sigma_{UT}^{\text{others}}), \end{aligned} \quad (2.121)$$

where each of the terms has the following general structure [76]:

$$d\sigma_{beam,target} = \frac{2\alpha_s^2}{sx^2y^2} \otimes \mathcal{K}(y) \otimes \mathcal{M}(\phi_h, \phi_S) \otimes \mathcal{C}[w \cdot d \cdot F]. \quad (2.122)$$

$\mathcal{K}(y)$ is a kinematic factor defined in [74] and $\mathcal{M}(\phi_h, \phi_S)$ is the angular modulation associated with the convolution \mathcal{C} depending on the *sine* and *cosine* of the azimuthal angles ϕ_h and ϕ_S . One of the two important terms we are interested in is :

$$d\sigma_{UT}^{\text{Collins}} = \frac{-2\alpha_s^2}{sx^2y^2} |\vec{S}_\perp| \mathcal{K}_C(y) \sin(\phi_h + \phi_S) \mathcal{C}\left[\frac{\hat{h}_\perp \cdot \vec{k}_T}{M_h} \delta q H_1^\perp\right] \quad (2.123)$$

Here $d\sigma_{UT}^{\text{Collins}}$ is the contribution from the convolution of the transversity distribution and the Collins fragmentation function to the SIDIS cross section modulated by $\sin(\phi_h + \phi_S)$ and the kinematic factor $\mathcal{K}_C(y)$ is defined as :

$$\mathcal{K}_C(y) = \left[1 - y - \frac{y^2\gamma^2}{4}\right] \frac{1}{1 + \gamma^2} \quad (2.124)$$

The other important contribution comes from the convolution of the Siverts distribution and the unpolarized fragmentation function modulated by $\sin(\phi_h - \phi_S)$:

$$d\sigma_{UT}^{\text{Siverts}} = \frac{-2\alpha_s^2}{sx^2y^2} |\vec{S}_\perp| \mathcal{K}_S(y) \sin(\phi_h - \phi_S) \mathcal{C}\left[\frac{\hat{h}_\perp \cdot \vec{p}_T}{M} f_{1T}^\perp D_1\right] \quad (2.125)$$

where the kinematic factor $\mathcal{K}_S(y)$ is defined as :

$$\mathcal{K}_S(y) = \left[1 - y + \frac{y^2}{2} - \frac{y^2\gamma^2}{4}\right] \frac{1}{1 + \gamma^2} \quad (2.126)$$

It is worthwhile to mention here that the contribution from the term $d\sigma_{UT}^{others}$ is modulated by $\sin(3\phi_h - \phi_S)$ and arises from the convolution of the distribution function h_{1T}^\perp and the Collins fragmentation function H_1^\perp . The distribution function h_{1T}^\perp is known as *pretzelocity* and the interpretation of the function and its analysis from the data are beyond the scope of this thesis. However, the effect of this term in our analysis was treated as a systematic uncertainty (see Appendix G).

Transverse Single Spin Asymmetry (SSA):

In order to extract the different distribution functions as well as the fragmentation functions experimentally, cross section asymmetries are measured instead of the absolute cross sections. This helps in getting rid of various systematic uncertainties which in turn makes the extraction of these functions more reliable precision. The target SSA can be defined as:

$$A_{UT} \equiv \frac{1}{|\vec{S}_T|} \frac{d\sigma_{UT}}{d\sigma_{UU}} = \frac{1}{|\vec{S}_T|} \frac{d\sigma(\phi_h, \phi_S) - d\sigma(\phi_h, \phi_S + \pi)}{d\sigma(\phi_h, \phi_S) + d\sigma(\phi_h, \phi_S + \pi)}, \quad (2.127)$$

where the target spin vector \vec{S}_T is flipped⁶ through an angle of 180° to form the cross section asymmetries. Here the modulation term $\sin(3\phi_h - \phi_S)$ in Eq.(2.113) is neglected. The experimentally measured asymmetries are approximated as a combined contribution of the Collins and Sivers asymmetries which have different angular dependencies as discussed in the previous subsection. The asymmetry can be written as:

$$A_{UT} = A_{UT}^{Collins} \sin(\phi_h + \phi_S) + A_{UT}^{Sivers} \sin(\phi_h - \phi_S), \quad (2.128)$$

where the interpretation of $A_{UT}^{Collins}$ and A_{UT}^{Sivers} as the azimuthal moments is discussed in the following section. In practice, the terms $A_{UT}^{Collins}$ and A_{UT}^{Sivers} are referred to as *Collins moment* and *Sivers moment* respectively.

2.8 The Collins and Sivers Moments

In the process of extracting the distribution and fragmentation functions via the SSAs, it is convenient to deal with the azimuthal moments. This is because one can not separate the convolution of the distribution function and the fragmentation function experimenatllly.

⁶In E06010, the asymmetry is formed by flipping the spins of the ^3He target every 20 minutes by applying an RF field to the target.

Following the published HERMES and COMPASS measurements [77], [78], [79], the Collins moment $A_{UT}^{Collins}$ and the Sivers moment A_{UT}^{Sivers} are defined as:

$$A_{UT}^{Collins} \equiv 2\langle \sin(\phi_h + \phi_S) \rangle_{UT} \cdot \mathcal{R}, \quad (2.129)$$

$$A_{UT}^{Sivers} \equiv 2\langle \sin(\phi_h - \phi_S) \rangle_{UT}, \quad (2.130)$$

where the factor \mathcal{R} is a kinematic factor which is different for HERMES and COMPASS. As for this experiment E06010, this difference is negligible, only the definitions applied to HERMES are adopted. Hence, \mathcal{R} is a function of $\mathcal{K}_C(y)$ and $\mathcal{K}_C(y)$ introduced in the previous section. The two moments can be defined in terms of the convolution of the distribution function and the fragmentation function as

$$A_{UT}^{Collins} = -|\vec{S}_T| \frac{\frac{1}{x^2 y^2} \mathcal{K}_C \int d^2 \vec{P}_{h\perp} \mathcal{C}[\frac{\hat{h}_\perp \cdot \vec{k}_T}{M_h} \delta q(x, p_T^2) H_1^\perp(z, z^2 k_T^2)]}{\frac{1}{x^2 y^2} \mathcal{K}_S \mathcal{C}[q(x) D_1(z)]} \quad (2.131)$$

$$A_{UT}^{Sivers} = -|\vec{S}_T| \frac{\frac{1}{x^2 y^2} \mathcal{K}_S \int d^2 \vec{P}_{h\perp} \mathcal{C}[\frac{\hat{h}_\perp \cdot \vec{p}_T}{M} \delta f_{1T}^\perp(x, p_T^2) D_1^\perp(z, z^2 k_T^2)]}{\frac{1}{x^2 y^2} \mathcal{K}_S \mathcal{C}[q(x) D_1(z)]} \quad (2.132)$$

In practice, the term $A_{UT}^{Collins}$ and A_{UT}^{Sivers} can be obtained directly by fitting the measured asymmetry with any of the following fitting functions:

$$A_{UT} = C \sin(\phi_h + \phi_S), \quad (2.133)$$

$$A_{UT} = S \sin(\phi_h - \phi_S), \quad (2.134)$$

$$A_{UT} = C \sin(\phi_h + \phi_S) + S \sin(\phi_h - \phi_S), \quad (2.135)$$

where C and S are the fit coefficients obtained to be identified as the Collins moment ($A_{UT}^{Collins}$) and Sivers moment (A_{UT}^{Sivers}), respectively. This simple fitting procedure has been adopted for the E06010 data where the *pretzelosity* term has not been taken into account and the extraction of these coefficients is the primary objective of the work presented in this thesis. However, for the sake of completeness, different deconvolution methods (model dependent) to extract the transversity distribution function from the experimentally measured moments are summarized below.

Deconvolution of the moments:

The convolution of the distribution and fragmentation functions in the measured moments makes it difficult to factorize and separate them because of the weight factors

$\hat{h}_\perp \cdot \vec{k}_T/M_h$ and $\hat{h}_\perp \cdot \vec{p}_T/M$ involved in the Collins and Sivers moments respectively. However, a couple of recipes are discussed in [80], [81], and [82]. Let us consider them briefly.

- **Assumption : No intrinsic transverse momentum exists for quarks:** In this case, it is assumed that the quarks do not have any intrinsic transverse momentum inside the nucleon and hence the transverse momentum of the produced hadrons with respect to the virtual photon is solely introduced in the fragmentation process. In other words, if we introduce the relation $\vec{K}_T = -z\vec{k}_T$ where \vec{K}_T and \vec{k}_T are the transverse momenta of the hadron and the fragmenting quark respectively, the convolution in the Collins moment can be disentangled and one can write :

$$\delta q(x, p_T^2) \approx \delta q(x) \frac{\delta(p_T^2)}{\pi}, \quad H_{1T}^\perp(z, K_T^2) \approx H_{1T}^\perp(z) \frac{\delta(K_T^2)}{\pi}. \quad (2.136)$$

- **Gaussian ansatz :** In this case, it is assumed that the transverse momentum exhibits a Gaussian-like behavior in case of both distribution as well as fragmentation functions. Thus one has

$$\delta q(x, p_T^2) \approx \delta q(x) \frac{e^{-\frac{p_T^2}{\langle p_T^2(x) \rangle}}}{\pi \langle p_T^2(x) \rangle}, \quad H_{1T}^\perp(z, K_T^2) \approx H_{1T}^\perp(z) \frac{e^{-\frac{K_T^2}{\langle K_T^2(z) \rangle}}}{\pi \langle K_T^2(z) \rangle}, \quad (2.137)$$

where $\langle p_T^2(x) \rangle = \frac{1}{q(x)} \int d^2\vec{p}_T p_T^2 q(x, p_T^2)$ and $\langle K_T^2(z) \rangle = \frac{1}{D_1(z)} \int d^2\vec{K}_T K_T^2 D_1(z, K_T^2)$. Then the Collins and Sivers moments can be expressed in a factorized form as follows [59]:

$$A_{UT}^{Collins} = \frac{2|\vec{S}_T|}{\sqrt{1 + \frac{z^2 \langle p_T^2(x) \rangle}{\langle K_T^2(x) \rangle}}} \frac{\frac{1}{xy^2} \mathcal{K}_C(y) \sum_{q,\bar{q}} e_q^2 \delta q(x) H^{\perp(1/2)q}(z)}{\frac{1}{xy^2} \mathcal{K}_S(y) \sum_{q,\bar{q}} e_q^2 q(x) D_1^q(z)}, \quad (2.138)$$

$$A_{UT}^{Sivers} = -\frac{2|\vec{S}_T|}{\sqrt{1 + \left[\frac{z^2 \langle p_T^2(x) \rangle}{\langle K_T^2(x) \rangle}\right]^{-1}}} \frac{\frac{1}{xy^2} \mathcal{K}_S(y) \sum_{q,\bar{q}} e_q^2 f_{1T}^{\perp(1/2)q}(x) D_1^q(z)}{\frac{1}{xy^2} \mathcal{K}_S(y) \sum_{q,\bar{q}} e_q^2 q(x) D_1^q(z)}. \quad (2.139)$$

In practice, one can avoid making any of the above assumptions and still deconvolute the integrals by implementing a weight factor $P_{h\perp}/zM_h$ and constructing $P_{h\perp}$ -weighted asymmetries. However, this requires the binning of the cross section according to the hadron transverse momentum [15]. The $P_{h\perp}$ -weighted Collins and Sivers moments are :

$$\frac{P_{h\perp}}{zM_h} A_{UT}^{Collins} \equiv 2|\vec{S}_T| \frac{\frac{1}{xy^2} \mathcal{K}_C(y) \sum_{q,\bar{q}} e_q^2 \delta q(x) H^{\perp(1)q}(z)}{\frac{1}{xy^2} \mathcal{K}_S(y) \sum_{q,\bar{q}} e_q^2 q(x) D_1^q(z)}, \quad (2.140)$$

$$\frac{P_{h\perp}}{zM} A_{UT}^{Sivers} \equiv -2|\vec{S}_T| \frac{\frac{1}{xy^2} \mathcal{K}_S(y) \sum_{q,\bar{q}} e_q^2 f_{1T}^{\perp(1)q}(x) D_1^q(z)}{\frac{1}{xy^2} \mathcal{K}_S(y) \sum_{q,\bar{q}} e_q^2 q(x) D_1^q(z)}. \quad (2.141)$$

Note that the factor $\frac{1}{xy^2}\mathcal{K}_s(y)$ in the numerator and the denominator in Eq.(2.141) may not cancel because of the independent integrations over x and y in a measurement. The factorization theorem⁷ for SIDIS at low transverse momenta in order to disentangle the distribution and fragmentation functions is reported in [83], [84].

2.9 Summary of HERMES and COMPASS Results

The results of the Collins and Sivers moments for different hadrons from the HERMES and COMPASS data on different targets are summarized in this section. The HERMES collaboration reported single spin azimuthal asymmetries in the semi-inclusive DIS lepton (27.6 GeV) scattering off a hydrogen target [85], [6]. Fig. 2.16 shows the Collins and Sivers moments extracted from the data at HERMES during the years 2002 to 2005.

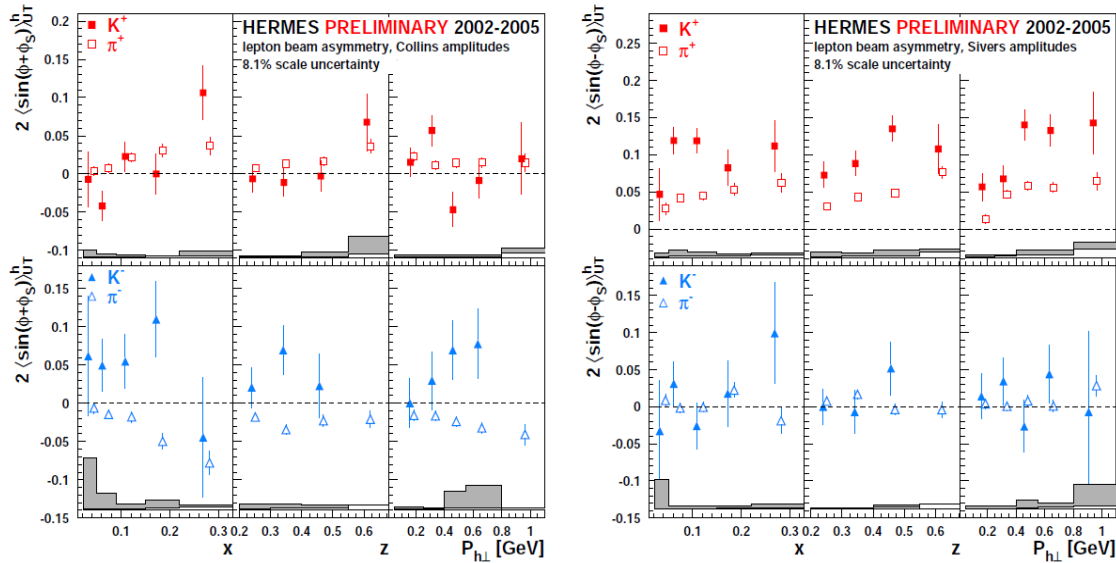


Figure 2.16: The Collins (left) and the Sivers (right) moments for the charged hadrons as a function of x , z and $P_{h\perp}$. The systematic uncertainties are represented by the shaded band [6].

The Collins moments for π^+ and π^- are different from zero and have opposite signs (positive for π^+ and negative for π^-). On the other hand, the Collins moment for K^- is

⁷A general cross section is a combination of short- and long-distance (corresponding to high Q^2 and low Q^2) behavior which can not be calculated directly in the perturbation theory. Factorization theorems, in general, allows the separation of the short distance partonic subprocesses from the long distance (low Q^2 and hence strong α_s) binding effects in a systematic way. The partonic subprocesses can be calculated within perturbative QCD and the long distance processes can be parametrized by parton distribution functions, fragmentation functions, etc.

positive while that for K^+ is comparable to zero. The Siverts moments for the positively charged hadrons are positive and zero for negatively charged hadrons.

The COMPASS collaboration also reported the Collins and Siverts azimuthal moments in the scattering of 160 GeV/c muons off a deuteron target (${}^6\text{LiD}$) as well as off a proton target (NH_3) [7], [8]. The results from the deuteron target are shown in Fig. 2.17 and Fig. 2.18.

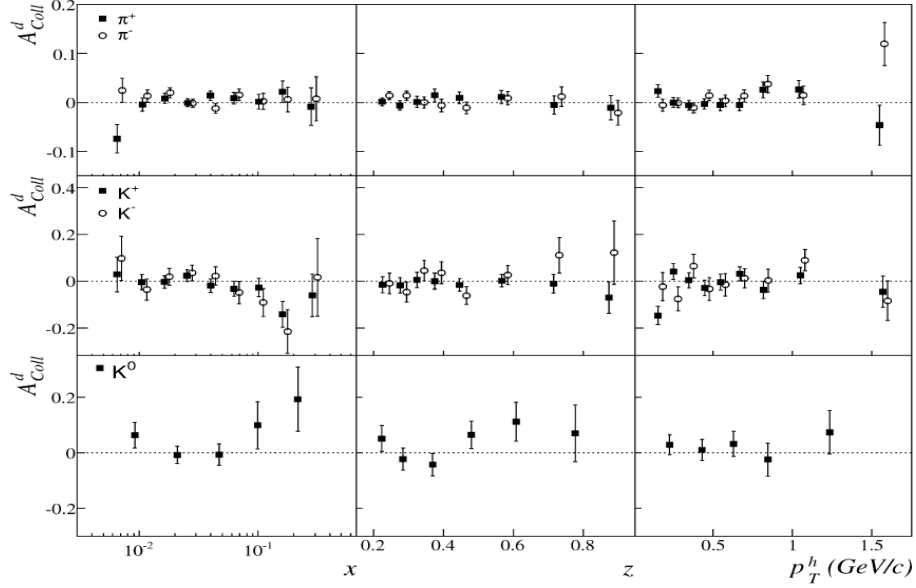


Figure 2.17: The Collins moments for the charged hadrons and K^0 as a function of x , z and P_T^h [7].

The Collins and Siverts moments for all the hadrons in this case are comparable to zero, apparently due to the cancellation of the contributions from the u and d quarks in the deuteron. Fig. 2.19 and Fig. 2.20 shows the results on the proton target which agree with the HERMES results for Collins moments in case of charged hadrons. However, unlike HERMES, the Siverts moments for the unidentified charged hadrons in this case show values comparable to zero.

The transversity experiment E06010 in Hall A at Jefferson Lab is the first experiment to measure these azimuthal moments on polarized ${}^3\text{He}$ which in turn will produce the first ever results on an effective neutron target. The results on the neutron will not only complement the existing results from HERMES and COMPASS as discussed above but may also put more constraints on flavor decomposition. The final extraction of the transversity distribu-

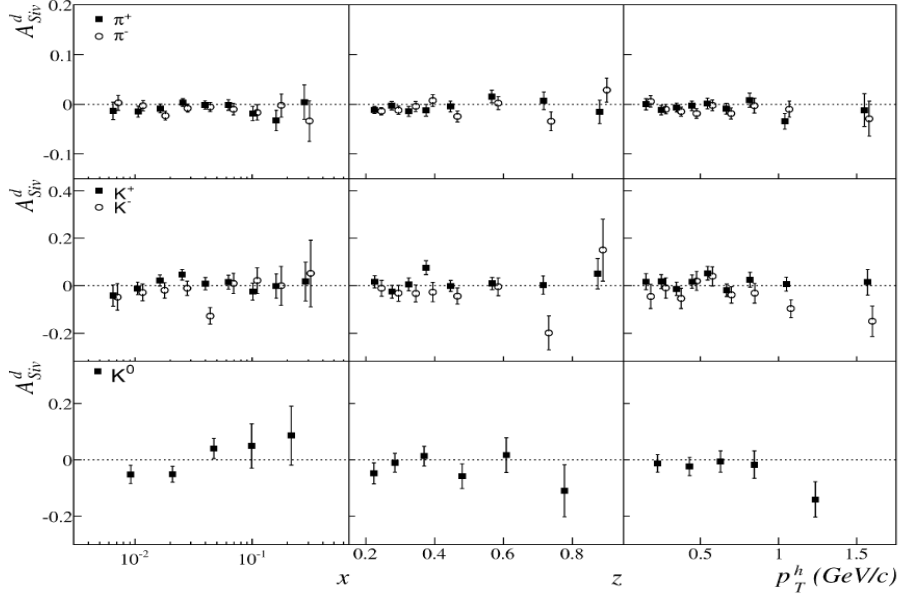


Figure 2.18: The Sivers moments for the charged hadrons and K^0 as a function of x , z and P_T^h [7].

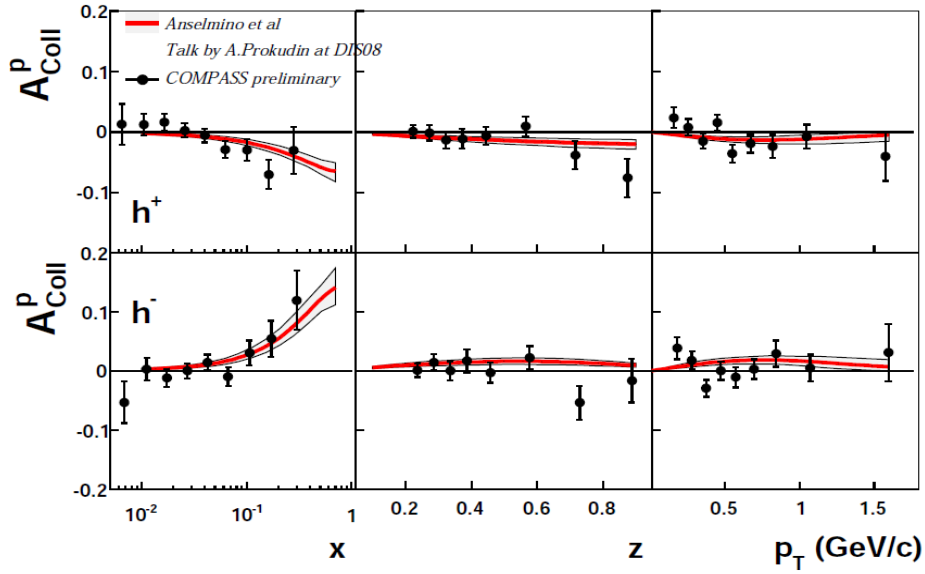


Figure 2.19: The Collins moments for the unidentified charged hadrons as a function of x , z and P_T^h [8].

tion function is beyond the scope of this thesis. The preliminary single spin asymmetries on the neutron in the SIDIS ${}^3\text{He}^\uparrow(e, e'\pi^-)X$, and the separation of the Collins and Sivers

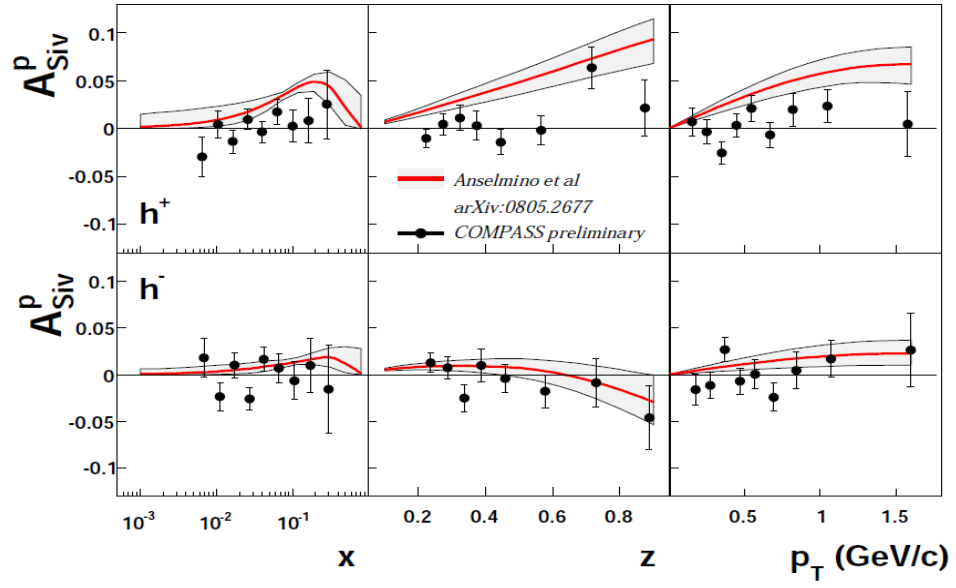


Figure 2.20: The Sivers moments for the unidentified charged hadrons as a function of x , z and P_T^h [8].

moments extracted from the measured asymmetries are presented in this work.

CHAPTER 3: THE EXPERIMENT

Experiment E06010 measured the single spin asymmetry (SSA) on a transversely polarized ^3He target in the deep inelastic region. The incoming electron beam was scattered off a polarized target and the scattered electrons were detected in the BigBite spectrometer coincident with the hadrons detected in the left high resolution spectrometer (LHRS). The hadrons produced and detected in the scattering included pions, kaons, and protons. The experiment was dedicated to measure the asymmetries of both pions and kaons. The focus of this thesis is mostly on pion asymmetries, especially on π^- mesons. In this chapter, different detector packages in both the BigBite spectrometer and the LHRS as well as the beam line components will be described.

3.1 Overview of CEBAF

Jefferson Laboratory is situated in Newport News, Virginia. Its superconducting radio frequency (srf) Continuous Electron Beam Accelerator Facility (CEBAF) provides a multi-GeV continuous wave electron beam quite efficiently for all the nuclear experiments. The aerial view of the CEBAF complex is shown in Fig. 3.1.



Figure 3.1: The CEBAF aerial view in Newport News. The three experimental Halls are also shown [9].

The accelerator consists of an injector and two anti-parallel linear accelerators (linacs) linked by nine recirculation beam lines for up to five passes. The schematic diagram of the accelerator is shown in Fig. 3.2. The two arcs (east and west) consist of the above mentioned recirculation beam lines giving rise to the “racetrack” shape of the accelerator.

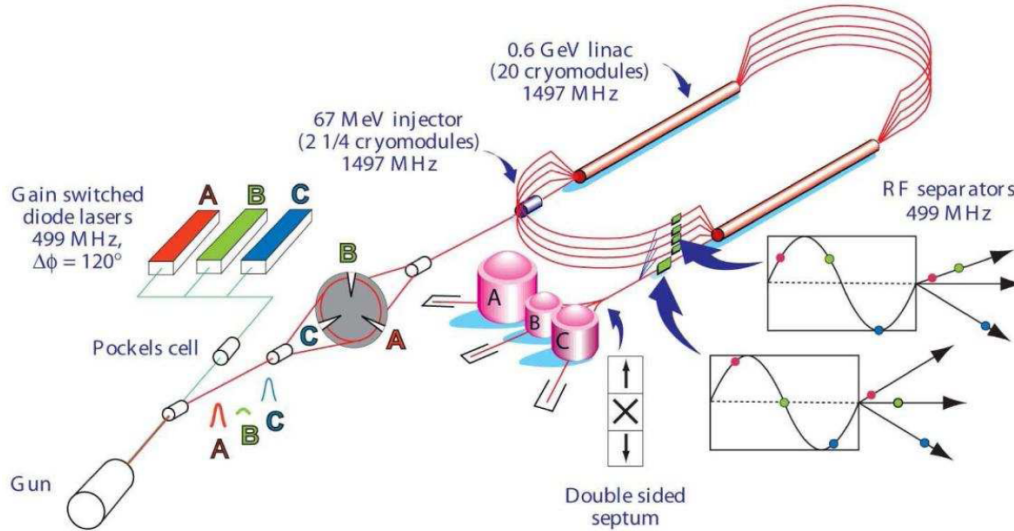


Figure 3.2: Schematic of the accelerator and its components. Reproduced from [10].

The basic principle of the operation of different components are summarized as follows:

- The Injector is the “injection point” of the electron beam into the accelerator. The electrons produced at the polarized electron source (discussed in the next section) have an energy almost equal to 0.1 MeV. The injector contains 18 acceleration cavities, each giving 2.5 MeV to an electron. Thus, the electrons leaving the injector actually have an energy of about 45 MeV.
- The North and the South linacs have 20 cryomodules. Each of the cryomodules has 8 cavities. Thus, each linac has 160 cavities lined up in such a way that the 45 MeV electrons entering into those cavities gain energy up to 500 MeV at the output each time they pass through. Fig. 3.3 shows a cavity based on a design developed at Cornell University. It operates at a frequency of 1497 MHz. More details can be found in [86]. The cavities are placed in liquid helium produced at the Central Helium Liquefier (CHL). The CHL is a large refrigerator which keeps the helium at about 2.2 K and

sends cold helium at a pressure of 2.8 atm to the cryomodules in the linacs.

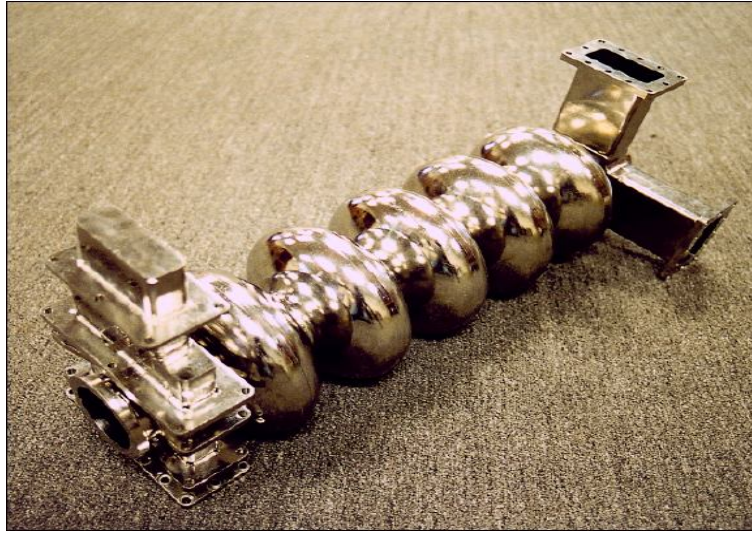


Figure 3.3: A typical RF cavity.

- The East and the West arcs are the components of the accelerator that consist of thousands of electromagnets which bend and focus the electron beam connecting the two linacs. Each arc has a spreader and a combiner. This is extremely important because the electrons in the linacs have different energies depending upon how many times they have travelled through the linacs. Now when it comes to bending in the arcs, the more energy the electron has, the more difficult it is to bend when it passes through the magnet. Hence, all the electrons are separated by the magnet depending on the energy such that the electrons having lowest energy are bent most and are guided into the topmost pipe and the electrons having largest energy almost move undeviated along the pipe near the floor. As a result, each of the pipes have electrons with only one specific energy. On the other hand, all the electrons having five different energies are combined back into one pipe in the recombiner by another magnet located at the exit of an arc so that they all again pass through the linac together.

3.1.1 Polarized Electron Source

The CEBAF at Jefferson Laboratory has been dedicated to conduct high-precision nuclear physics involving electromagnetic interactions that requires highly polarized electron beams, often at high average currents. The continuous wave (cw) electron beam has a small emit-

tance ($\epsilon < 1$ mm-mrad) and a very low energy spread ($\frac{\Delta E}{E_{rms}} < 2 \times 10^{-5}$)¹ [87]. GaAs-based semiconductor photocathodes are used to produce the polarized electrons via the process of photoemission by shining circularly polarized laser light on them. This cathode is actually built on a GaAs substrate, different layers of which are shown in Fig. 3.4.

The top layer of pure GaAs is grown on a layer of GaAs_{0.72}P_{0.28}. The lattice constant of GaAs_{0.72}P_{0.28} is smaller than that of GaAs [88]. This lattice constant for the strained GaAs_{1-x}P_x (in general) can be adjusted by varying the phosphorus fraction x . The shorter lattice spacing of GaAs_{0.72}P_{0.28} forces the natural spacing of pure GaAs to shrink and hence, a strain is created in the topmost layer. The resulting biaxial compressive strain within the GaAs layer lifts the degeneracy in the $P_{3/2}$ level of the electrons in the valence band. In other words, this strain induces an energy gap between the sub-levels of the $P_{3/2}$ electrons as shown. The electrons in the $P_{3/2}, m_{3/2}(P_{-3/2}, m_{-3/2})$ valence band can be excited to $S_{1/2}, m_{1/2}(S_{-1/2}, m_{-1/2})$ level in the conduction band only when a left (right) circularly polarized laser with the proper wavelength is incident on the conduction band. This is because the energy gap between the two sub-levels of the $P_{3/2}$ created by the strain is large enough so that the laser light can not excite the transitions from the two $m=1/2$ and $m=-1/2$ states. Hence, if the polarization of the laser light has the same sign of circular polarization (helicity +1 or -1), all the electrons that diffuse to the surface and escape are either from $S_{1/2}, m_{1/2}$ or $S_{-1/2}, m_{-1/2}$ state depending on the helicity sign. As a result, one could expect almost 100 polarized electrons coming out of the GaAs crystal.

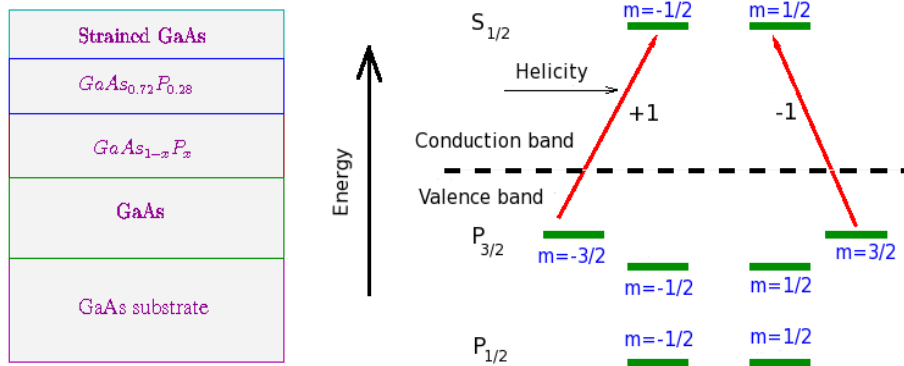


Figure 3.4: Different layers of GaAs and the degenerate states available for optical pumping.

¹ E_{rms} is the root mean square value of the energy of the continuous electron beam.

3.2 Beamline

The Hall A beamline has a number of components that serve very effectively to transport the electron beam onto the target as well as to measure and monitor the different essential parameters of the beam. The basic beamline components include a Compton polarimeter and a Møller polarimeter to measure the polarization of the electron beam, two Beam Current Monitors (BCM) to measure the beam current, a raster (pair of dipoles) to control the beam spot on the target, an “eP” device to measure the energy of the beam, and couple of Beam Position Monitors (BPM) to measure the position of the beam on the target. These important components in the beamline will be discussed in the following subsections.

3.2.1 Beam Energy

The energy of the electron beam is one of the basic characteristics that needs to be measured as accurately as possible. There are two independent methods usually employed to measure the absolute energy. These are:

1. Arc energy measurement.
2. “eP” energy measurement.

However, during the transversity experiment, the beam energy was measured with Arc energy method only. The “eP” energy method was not employed and hence will not be discussed here.

The Arc Energy Measurement

This method, originally developed by P. Vernin *et al.* [89], basically measures the bend angle of the electron beam through a precisely known magnetic dipole field in the arc section. Eight dipole magnets are used to bend the beam by an angle of 34.3° . The basic concept that governs this method is the deviation of a moving charged particle in a magnetic field. One can write the momentum of the charged particle (electron in this case) as a function of the deflection angle and the magnetic field integral as follows:

$$P = k \frac{\int \vec{B} \cdot d\vec{l}}{\theta}, \quad (3.1)$$

where θ is the deflection angle of the electron in radians, $d\vec{l}$ is the path length traversed by the electron, $k= 0.299792 \text{ GeV}\cdot\text{rad}\frac{T^{-1}\text{m}^{-1}}{c}$ and the $\int \vec{B} \cdot d\vec{l}$ is the field integral in T·m [12]. Two measurements need to be performed simultaneously. One is to measure the field integral of the dipoles in the arc and the other one is to determine the actual bend angle of the arc.

The field integral measurement is done based on a dipole magnet that sits outside the arc which is called as the “9th magnet” or “reference magnet”. This is because all the eight dipoles are located in the vacuum and those can not be probed directly. Hence, the 9th dipole magnet was constructed, identical to the others and wired in series (hence the same current flow). This dipole is instrumented with a Hall probe scanner that can be moved through the field gap and the field can be measured directly. The assumption that the 3 m dipole responds identically to the other ones was directly tested after its construction [90].

The bend angle is measured by a set of wire scanners. As shown in Fig. 3.5, there are two pairs of wire scanners at the entrance (upstream) of the arc and at the exit (downstream) of the arc, respectively.

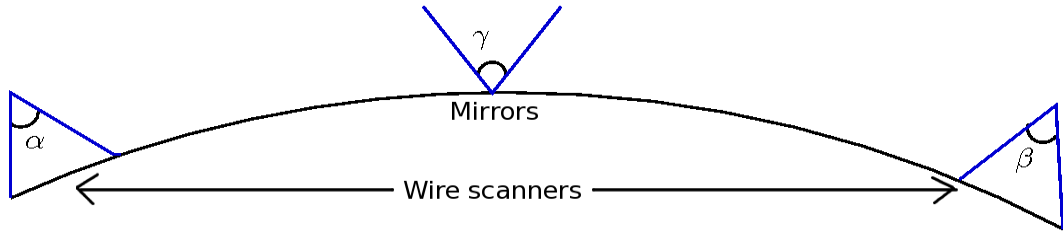


Figure 3.5: Schematic of the complete angle measurement in the arc energy method. The wire scanners and the mirrors in the middle of the arc are shown with their respective angles.

All the wires are vertical to the beam line and they are moved horizontally across the beam line. When the beam hits the wire, the current generated by the scattered particles off the wire is measured and the horizontal beam profile is observed. Both the profiles at the entrance and at the exit are compared and the horizontal beam angles α and β are determined. Finally, the auto collimation technique [89] allows the measurement of the total bend angle by placing two mirrors facing opposite to each other at the middle of the arc

Table 3.1: The Arc measurement result during E06-010. The corresponding result from the Tiefenbach method is also shown.

date	Arc measurement result \pm stat. \pm sys.	Tiefenbach result \pm sys
11/17/2008	$(5889.4 \pm 0.5 \pm 1)$ MeV	(5891.3 ± 2.5) MeV

and keeping the angle γ constant all the time. Hence, the total bend angle is $\theta = \alpha + \beta + \gamma$.

Both the Arc Energy method and the “eP” Energy method have an accuracy of $\frac{\Delta E}{E} \sim 2 \times 10^{-4}$. There was only one Arc energy measurement performed during the experiment with 6 μ A cw beam in the dispersive mode. Most of the time, the beam energy was monitored by the Tiefenbach method. The *Tiefenbach* method is usually employed for a continuous monitoring of the beam energy. It calculates the value of the incoming beam energy by using the Hall A arc field integral values and the arc beam position monitors and records it into the data stream continuously. Frequent calibrations are done for this method with the Arc method.

3.2.2 Beam Current

The beam current (charge) in Hall A is measured with a Beam Current Monitor (BCM) that is located 25 m upstream of the target in the beam line. The Beam Current Monitor system consists of an Unser monitor which is a Parametric Current Transformer (PCT), two rf cavities, the electronics, and a data acquisition (DAQ) system. The BCM system set up is shown in Fig. 3.6. The cavities and the Unser monitor are enclosed in a box so that they can be isolated from any other magnetic field as well as any temperature variations.

The two cavities perform a relative beam current measurement. The measurement with the rf cavities is relative because the output of these are not exactly the beam current but a voltage that is proportional to the beam current. These cavities are made of stainless steel and have dimensions of 15.48 cm in diameter and 15.24 cm in length. They are located before and after the Unser (PRT) monitor along the beamline. Each of the cavities has a magnetic field probe used to couple the beam signal out of the cavity. The cavities are tuned to the resonant frequency of 1.497 GHz. The electron beam passing through each cavity excites the TM_{010} mode at this frequency and it is picked up by a coaxial antennae running along the outer shell coupled to the cavity. The output signal determined by the

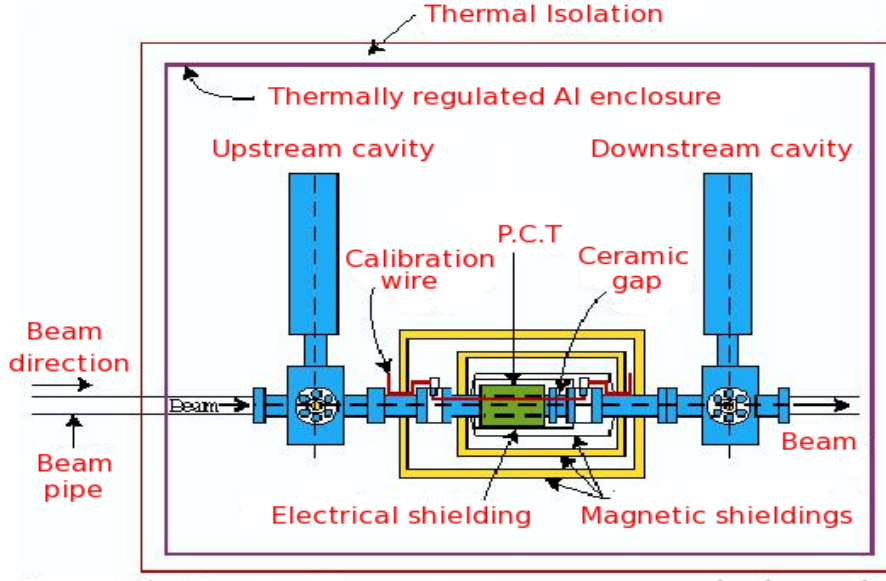


Figure 3.6: The BCM system reproduced from [11].

probe is proportional to the Q factor of the cavity. The Q factor is defined as

$$Q = \frac{Ef}{P}, \quad (3.2)$$

where E is the total energy stored in the cavity, f is the resonant frequency and P is the total dissipated power. The Q values of these cavities are ~ 3000 . The signals produced in the cavities are transmitted to the electronics. The voltage of the signal is proportional to the beam current. This measurement of the beam current by the cavities is calibrated with the Unser monitor which performs an absolute measurement of the beam current. The details of the working principle of the Unser monitor can be found in [91], [92]. The processing of the output signal by the data acquisition is summarized below:

Electronics and DAQ

The basic process of operation of the BCMs can be summarized in the following steps.

- The output signal of each rf cavity is fed into a Down-converter where it gets split into two parts: *the sampled part* and *the integrated part*.
- *The sampled part* is then fed into a high precision digital multimeter (DMM) and *the integrated part* is sent to an RMS-to-DC converter as shown in Fig. 3.7.

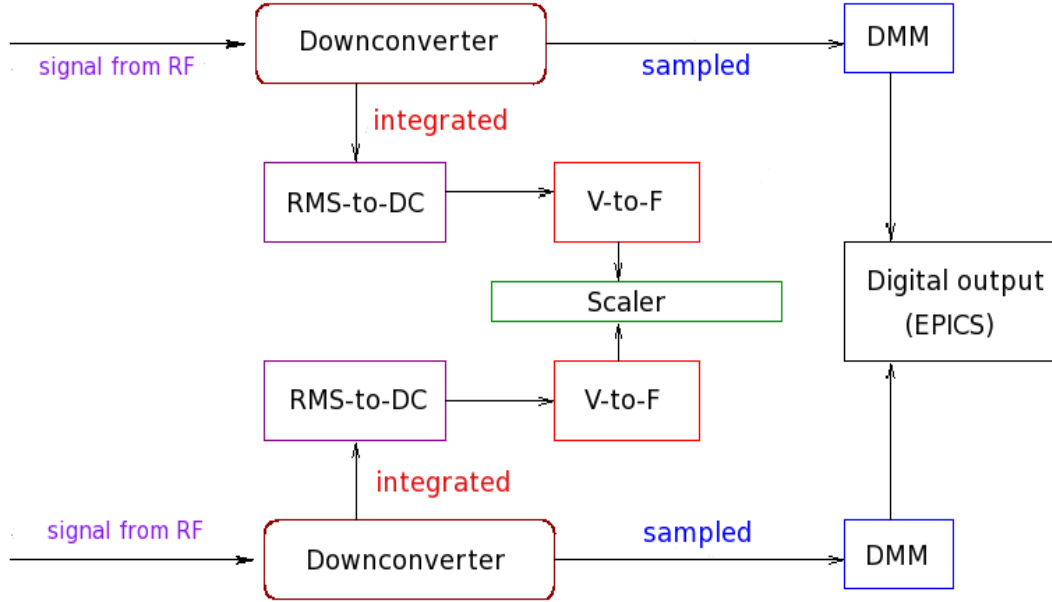


Figure 3.7: The electronics in the BCM system.

- The DMM output is a digital signal produced every second, which is the root-mean-square (RMS) of the input sampled signal. In other words, this output signal from the DMM is proportional to the average beam current over each second and is sent to the computer through GPIB ports.
- The output of the RMS-to-DC converter which is now an analog DC voltage is fed into a voltage-to-frequency converter (V-to-F). The output frequency is proportional to the input DC voltage and is sent to a Fastbus scaler which is read by the DAQ system. Thus, the output voltage and hence the frequency is proportional to the beam current which is read by the scaler.

The detailed description can be found in [93]. It is worthwhile to mention here that the analog DC voltage from the RMS-to-DC converter is a non-linear function of beam current for small currents below $5 \mu\text{A}$. Hence, amplifiers with gain $\times 3$ and $\times 10$ are used to overcome the effect and as a result, there are 3 signals coming out of each BCM. They are amplified by a factor of 1 (the original signal), 3 and 10. Therefore, a set of six signals from the two cavities (named as U1,U3,U10,D1,D3,D10) are sent to the scalers. U stands for Upstream, D stands for Downstream, and the numbers represent the respective gain factors. The calibration of the scaler signals are done with standard procedures. With these BCMs in

the Hall, usually the charge for a real production run in any physics experiment can be measured down to $1 \mu\text{A}$ within 0.5% accuracy [12].

3.2.3 Beam Position

Precise measurement of the position of the beam on the target is extremely crucial in any experiment. The Hall A beamline has two Beam Position Monitors (BPM) located at distances 7.524 m and 1.286 m upstream of the target which measure the position and the direction of the beam on the target. The monitor that is closer to the target is referred to as BPMB and the one further away from the target is referred to as BPMA. Each BPM has a 4-wire antenna at $\pm 45^\circ$ relative to the Hall horizontal and vertical directions tuned to 1.497 GHz RF frequency as shown in Fig. 3.8. The calibration is performed with the wire scanners or the superharps². The superharps are located at 7.353 m and 1.122 m upstream of the target close to the BPMs.

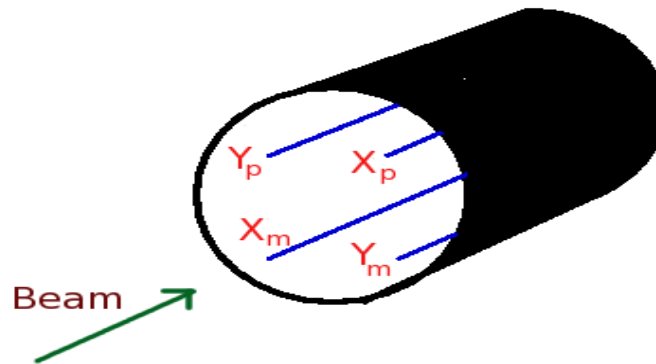


Figure 3.8: The beam position monitors.

The technique used to determine the relative position of the beam with the BPMs is known as “difference over sum” technique. It is based on the comparison of the two induced signals in the two opposite antennae when the electron beam passes through. The position

²The superharps consist of three wires. The orientation of the wires is such that one of them are vertical and the other two make angles $\pm 45^\circ$ with respect to the vertical one. During measurement, the wires are scanned across the beamline. Thus, the electrons hitting the wires create showers of particles which are detected resulting in the determination of the position of the wires and hence the beam.

of the beam on the target can be computed using the following equations:

$$X_b = \kappa_X \cdot (18.87mm) \cdot \frac{(X_p - \alpha_X \cdot X_m)}{(X_p + \alpha_X \cdot X_m)}, \quad (3.3)$$

$$Y_b = \kappa_Y \cdot (18.87mm) \cdot \frac{(Y_p - \alpha_Y \cdot Y_m)}{(Y_p + \alpha_Y \cdot Y_m)}, \quad (3.4)$$

where κ_X , κ_Y are absolute conversion factors, α_x , α_Y are relative gains and X_p, X_m, Y_p, Y_m are the offset subtracted signals from the four wires. These signals are proportional to the beam current and inversely proportional to the distance between the wires and the beam. The relative position can be determined to within 100 microns for currents greater than $1\mu\text{A}$. The details can be found in [94].

The Raster

In order to prevent the target from being overheated locally by the high intensity incident beam, the electron beam is rastered³ on the target. This is essential because of the fact that our target cell is made of thin glass containing high pressure ^3He gas. The raster is a pair of horizontal(X) and vertical(Y) air core magnetic dipoles located at a distance of 23 m upstream of the target center. Two modes, *viz*, the sinusoidal modulation mode and the amplitude modulation mode can be used. In the sinusoidal mode, a sine wave of ~ 18.3 KHz drives both the X and Y magnets. There exists a relative phase difference of 90° between X and Y magnet sine waves and they do not produce a closed Lissajous figure. The amplitude of both the waves remain constant. With the beam rastered on the target in both vertical and horizontal directions, a uniform energy deposition of the beam on the target cell is achieved.

3.3 Beam Polarization

The electron beam can have a wide range of energy and intensity. Two methods of beam polarization measurement are usually implemented in Hall A. One method uses the basic process of Compton scattering (Compton Polarimeter) and the other is based on Møller scattering (Møller Polarimeter). The former is mainly used for the medium to high beam energies and high beam intensities whereas the latter is mostly useful for low to medium beam energies and low beam intensities. Both will be discussed in the following subsections.

³The term *rastered* is used to describe the fact that the electron beam coming on to the target is projected in such a way that the original diameter of the beam ($\sim 100 \mu\text{m}$) is enlarged to $\sim (2-3)$ mm on the target.

3.3.1 Compton Polarimeter

The Compton polarimeter is used to measure the longitudinal polarization of the high intensity electron beam having energy range of 3 to 6 GeV that is injected into Hall A. The measurement is basically based on the Compton effect discovered by Arthur Holly Compton. The effect is the electromagnetic interaction between electrons and photons which results in the electron recoiling with part of the given energy and a photon with the rest of the energy being emitted in a different direction with respect to the incident direction.

In Hall A, the polarization of the beam is one of the essential parameters that needs to be measured as accurately as possible without affecting the data taking process of the experiment. Unlike the Møller measurement (discussed in the next subsection), the Compton measurement is non-invasive. In this measurement, the polarized electron beam is deviated from the main beamline and is guided in such a way that it is scattered off circularly polarized photons (from a 240 mW infra-red laser operating at 1064 nm wavelength). The cross sections of the polarized electrons scattered off polarized photons as a function of their energy and the scattering angle can be accurately calculated. The cross sections are different for the electrons scattered off the photons with the helicity states parallel to the photons and for those whose helicity states are opposite to those of the photons. If we denote the cross section of the electrons with parallel orientations with respect to the photons by σ_+ and the anti-parallel orientations by σ_- , then the theoretical asymmetry or the analyzing power of the process can be defined as

$$A_{th} = \frac{\sigma_+ - \sigma_-}{\sigma_+ + \sigma_-}. \quad (3.5)$$

Now the orientation of the electron spin in the beam (or the helicity) is flipped by an angle of 180° at a rate of 30 Hz. If N_+ and N_- represent the number of events in two opposite helicity states of the electrons, then the experimental asymmetry can be written as

$$A_{exp} = \frac{N_+ - N_-}{N_+ + N_-}, \quad (3.6)$$

where the events signify the count rates normalized to the beam intensity. Then the polarization of the electron beam can be evaluated by the following equation with the known polarization P_γ of the photons:

$$P_{beam} = \frac{A_{exp}}{P_\gamma A_{th}}. \quad (3.7)$$

More details of the calculations and the procedures can be found in [12].

The Hall A Compton polarimeter is located at the entrance of the hall. It consists of a magnetic chicane, a Fabry-Perot cavity serving as a photon target housed on an optics table, an electron detector, and a photon detector. A schematic of the Compton polarimeter is shown in Fig. 3.9.

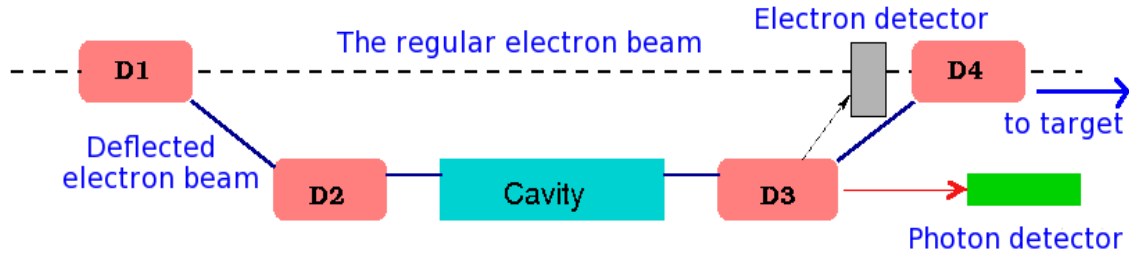


Figure 3.9: Schematic of the Compton polarimetry set up.

The magnetic chicane has four dipoles D1, D2, D3, and D4 that can deliver a magnetic field up to 1.5 T. (D1,D2) deviate the original electron beam vertically down and guide it to pass through the optical cavity so that it can interact with the photon beam at the center of the cavity. This point is the Compton Interaction Point (CIP). Then (D3,D4) deflect the scattered electrons vertically up and guide to the original beamline and hence to the Hall A target. The photon source is a 240 mW CW Nd:YAG laser beam at wavelength 1064 nm. This laser beam is then amplified by a resonant Fabry-Perot cavity which is 85 cm long. It uses two high-finesse mirrors to amplify the incoming beam. By locking the laser frequency to that of the cavity by a feedback mechanism, an amplification factor of 7300 is achieved which corresponds to a photon beam power of 1680 W inside the cavity [12]. A rotatable quarter wave plate is used to control the circular polarization of the photon beam. The photon polarization is typically $\sim 99\%$. The photon detector is an electromagnetic calorimeter which detects the Compton backscattered photons and it consists of PbWO_4 crystals ($2\text{ cm} \times 2\text{ cm} \times 23\text{ cm}$). The electron detector has four silicon strip planes, each containing twelve strips.

It is essential for the electron beam and the photon beam to have the relative crossing angle very small. The fields of the dipoles are varied to adjust the electron beam vertically so that the CIP is at the center of the cavity. Data are recorded once the Compton luminosity is maximized. Either single electrons, single photons, or the coincidences can be used as a trigger for the data acquisition. The positions of the scattered electrons in the electron detector and the energy of the backscattered photons in the photon detector give the energy of the Compton events.

3.3.2 Møller Polarimeter

A Møller polarimeter is used to measure the polarization of the electron beam at low intensities. This method is invasive and it is usually effective only for low beam energies (up to ~ 4 GeV). The method uses the Møller scattering of polarized electrons from the beam off polarized atomic electrons. The reaction is given by:

$$e^- + e^- \longrightarrow e^- + e^- . \quad (3.8)$$

The cross section of this process is a function of the beam and the target polarizations and can be expressed as

$$\sigma \propto (1 + \sum_{i=x,y,z} (A_{ii} \cdot P_i^t \cdot P_i^b)), \quad (3.9)$$

where P^t is the target polarization, P^b is the beam polarization, A is the analyzing power and $i = x, y, z$ are the projections of the polarizations. Now assuming that the beam is along the z -axis and the $x - z$ plane is the scattering plane, the analyzing power can be defined as [93]

$$A_{xx} = -\frac{\sin^4 \theta_{CM}}{(3 + \cos^2 \theta_{CM})^2}, \quad (3.10)$$

$$A_{yy} = -A_{xx}, \quad (3.11)$$

$$A_{zz} = -\frac{\sin^2 \theta_{CM} \cdot (7 + \cos^2 \theta_{CM})}{(3 + \cos^2 \theta_{CM})^2}. \quad (3.12)$$

As we can see, the analyzing power is a function of the scattering angle θ_{CM} in the center of mass frame and independent of the beam energy. The maximum analyzing power $A_{zz}^{max} = 7/9$ at $\theta_{CM} = 90^\circ$ for longitudinal polarization of the beam. The transverse components give rise to small asymmetries and hence a low analyzing power as can be seen from

the above equations.

The Møller polarimeter consists of a polarized target, a magnetic channel with three quadrupoles and a dipole, and a detector made of lead glass and scintillators. The schematic is shown in the Fig. 3.10.

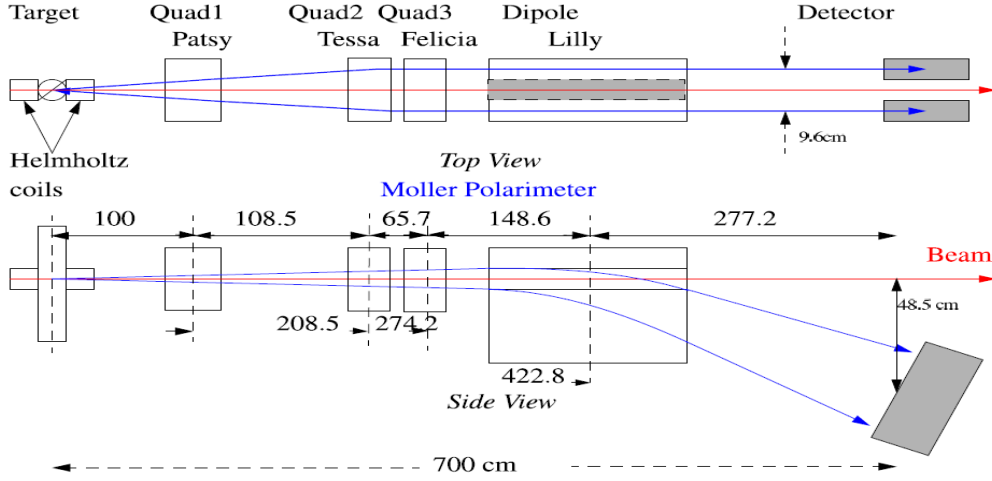


Figure 3.10: Schematic of the Møller polarimeter reproduced from [10].

The polarized electron target for the Møller polarimeter is located 17.5 m upstream of the Hall A target. It consists of 5 ferromagnetic foils on a sliding rail. Two of foils are made of Fe and the rest are made of supermendur alloy [93]. The target is saturated magnetically along the beam by two external Helmholtz coils which produce a field of 350 G. In the ferromagnetic coil, about 2 electrons/atom can be polarized giving rise to average electron polarization of $\sim 8\%$. As the foils can be rotated from 20° to 160° with respect to the beam, the effective polarization of the target can be written as

$$P^t = P^f \cdot \cos\theta_t, \quad (3.13)$$

where P^f is the polarization of the foil derived from special magnetization measurements of the foil samples oriented at an angle θ_t with respect to the beamline. The angle is measured using a scale on the target holder.

The electron pairs produced in the scattering process are deflected by a spectrometer (three quadrupole and one dipole magnets) towards the detector system within a certain

kinematic range. The azimuthal acceptance is restricted by a collimator in front of the dipole and the acceptance in θ_{CM} is limited by the magnetic field strength of the dipole as well as the vertical dimensions of the detector system. Usually the Møller Polarimeter detects scattered electron pairs in the range $75^\circ < \theta_{CM} < 105^\circ$. The Møller detector has two identical modules placed symmetrically about a vertical plane containing the beam axis [12]. The coincidence events are detected and the longitudinal beam polarization is determined as

$$P_z^b = \frac{N_+ - N_-}{N_+ + N_-} \cdot \frac{1}{Pf \cdot \cos\theta_t \cdot \langle A_{zz} \rangle}, \quad (3.14)$$

where N_+ and N_- are the counting rates with two opposite orientations (180° relative angle) of the beam and target polarizations. The analyzing power $\langle A_{zz} \rangle$ can be computed by a Monte-Carlo calculation of the spectrometer acceptance and is about 0.76. This invasive measurement can provide a statistical accuracy of about 0.2% and the systematic errors in the measurement can be neglected.

Møller beam polarization results:

A series of Møller measurements were performed during the experiment E06-010. The results are summarized in Table 3.2 and plotted in Fig. 3.11 [95]. In addition, the Compton polarimeter was used to monitor the polarization of the beam continuously during the data taking. However, the Compton polarimeter was not working properly due to some technical issues. Hence, only the results from the Møller measurements were used in different stages of data analysis.

Hall A Detector Package:

In E06010, the hadrons (pions, kaons, and protons) were detected in coincidence with the scattered electrons. The standard Hall A High Resolution Spectrometer (LHRS) was used to detect and separate different hadrons while the BigBite spectrometer was used to detect the scattered electrons. The LHRS was placed at an angle of 16° to the left with respect to the incoming electron beam and the BigBite was sitting at an angle of 30° to the beam right. Both spectrometers consist of different detectors to perform various operations. The detector packages and their working principle in each of the spectrometers are discussed in

Table 3.2: The Møller polarization measurement results during E06-010.

date	Møller results \pm stat. \pm sys. [%]
11/02/2008	$88.41 \pm 0.22 \pm 0.02$
11/12/2008	$-74.94 \pm 0.14 \pm 0.03$
11/02/2008	$-74.46 \pm 0.11 \pm 0.03$
11/02/2008	$-74.22 \pm 0.17 \pm 0.03$
11/02/2008	$80.97 \pm 0.19 \pm 0.03$
11/02/2008	$-54.16 \pm 0.20 \pm 0.03$
11/02/2008	$-79.16 \pm 0.16 \pm 0.03$
11/02/2008	$-80.00 \pm 0.18 \pm 0.03$
11/02/2008	$-81.12 \pm 0.15 \pm 0.02$
11/02/2008	$-79.01 \pm 0.13 \pm 0.02$
11/02/2008	$-75.84 \pm 0.16 \pm 0.02$

the following sections.

3.4 Hall A Left High Resolution Spectrometer (LHRS)

The Left High Resolution Spectrometer (LHRS) is one of the two identical standard Hall A spectrometers that are designed to do high precision and high resolution experiments. Both the right and the left spectrometers share the same design and characteristics. Only the LHRS was used in the experiment to detect pions and kaons, and therefore only the LHRS is described here. The original requirements behind the design of the spectrometer and its associated instrumentation are to achieve an accuracy of $\sim 10^{-4}$ in the determination of the relative particle momenta and ~ 0.1 mr for the scattering angle. With the present design of the spectrometers, many experiments have been performed with great success and the physics goal of an absolute accuracy of $\sim 1\%$ has been achieved as planned in the Hall [93].

3.4.1 LHRS Design and Characteristics

The central momentum of LHRS is 4 GeV/c with a vertical bending plane and a 45° bending angle. The structure consists of two superconducting quadrupoles(QQ), then a 6.6 m long dipole (D) followed by a third superconducting quadrupole(Q). This structure is sometimes denoted as DDQD magnet configuration. The second and the third quadrupoles are identical in design and construction because they both have similar field and size requirements. The layout of the LHRS is shown in Fig. 3.12 and the important characteristics are summarized

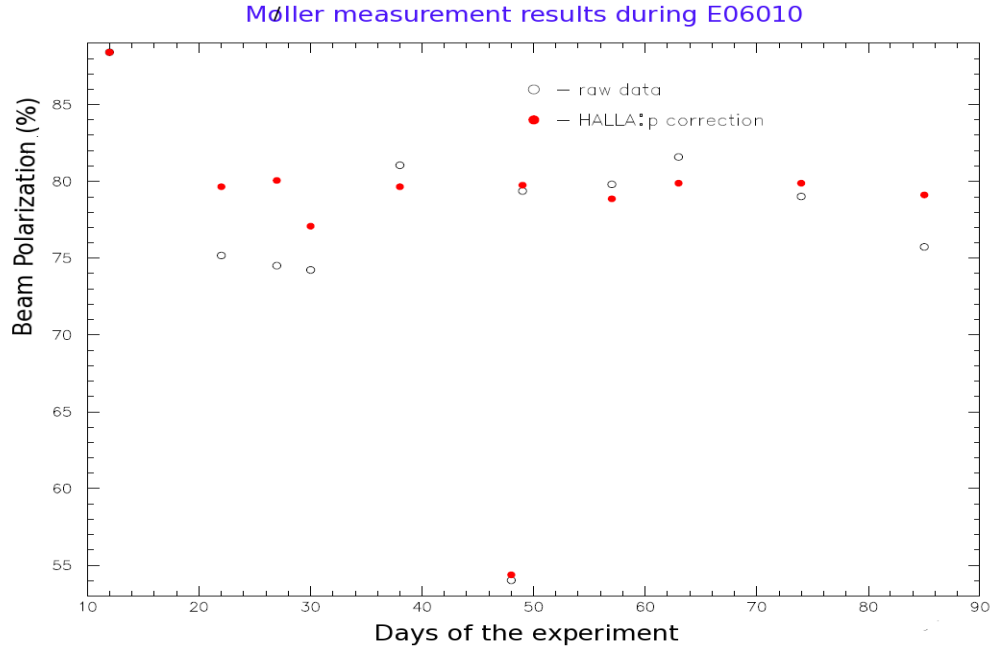


Figure 3.11: The Møller measurement results during E06010.

Table 3.3: LHRS characteristics

Configuration	QQDQ
Optical Length	23.4 m
Bending Angle	45°
Momentum range P	0.3-4.0 GeV/c
Momentum acceptance	$-4.5\% < \frac{\delta p}{p} < +4.5\%$
Momentum resolution	1×10^{-4}
Angular range	12.5°-150°
Horizontal angular acceptance	± 30 mrad
Vertical angular acceptance	± 60 mrad
Horizontal angular resolution	0.5 mrad
Vertical angular resolution	1.0 mrad
(Solid angle) $\frac{\delta p}{p}=0, y_o=0$	6msr

in Table 3.3. The details can be found in Refs. [12], [93].

3.4.2 Detector Package

The detector package of the LHRS is located inside a Shield Hut(SH) at the end of the spectrometer magnet assembly. The shield hut protects the detectors and the data acqui-

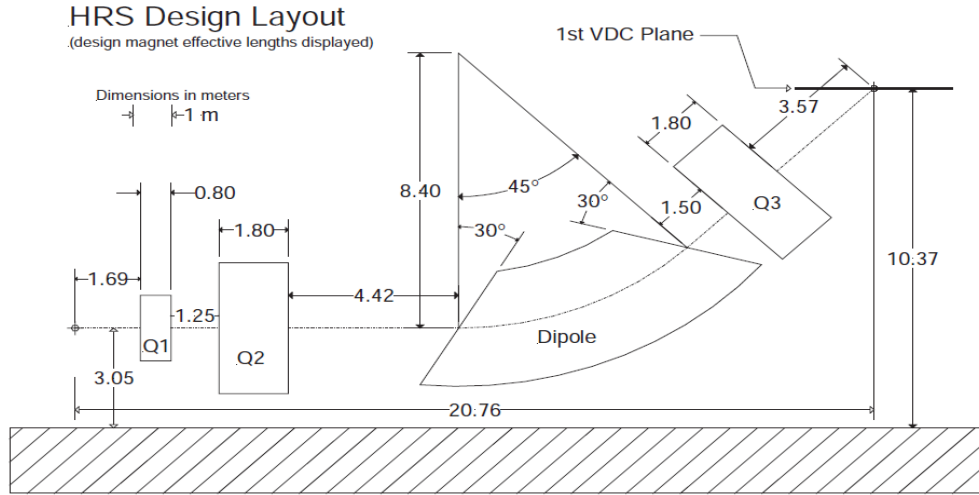


Figure 3.12: The schematic of the LHRs showing the geometrical configuration of the QQDQ layout. The first VDC plane is also shown [12].

sition(DAQ) electronics from the radiation background in the Hall. The detector package for the transversity experiment consists of the following detector components:

- A pair of Vertical Drift Chambers (VDC) to provide information about the tracking.
- Two Scintillator Planes (S1 and S2m) to provide the timing information and the main trigger.
- An Aerogel Čerenkov and a Gas Čerenkov for particle identification.
- Two sets of Lead-Glass counters (Pion-Rejector1 and Pion-Rejector2) to provide additional information about particle identification.
- A RICH detector for particle identification. This is a special Čerenkov counter used in the experiment to separate pions and kaons. Its not a standard part of the detector package.

Fig. 3.13 shows a schematic diagram of the detector package from the side. The individual detectors are installed on a retractable frame. Thus, if needed for repair or reconfiguration, each of them can be moved out of the SH. The DAQ electronics are also mounted on the same frame.

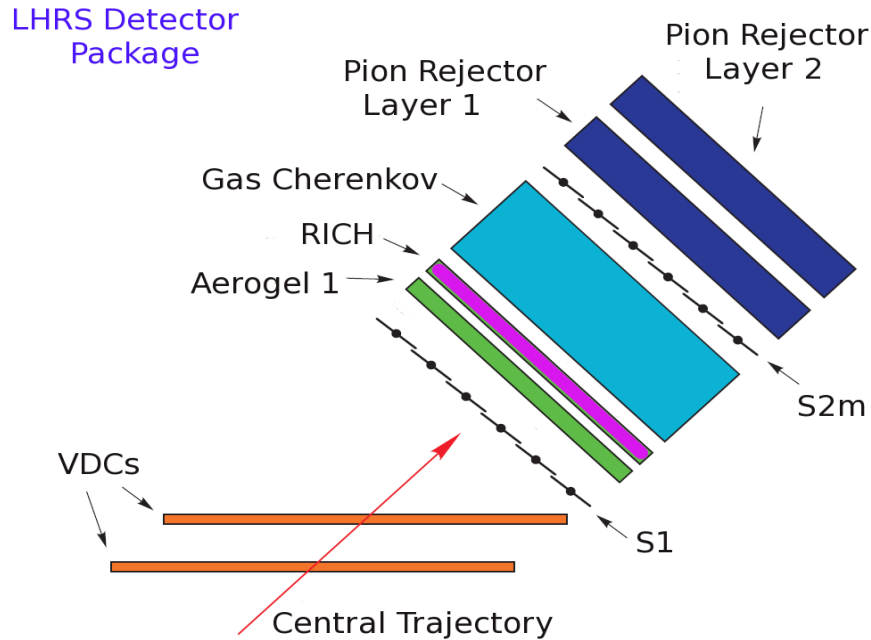


Figure 3.13: The layout of the detector packages in the LHRs [13].

3.4.3 Vertical Drift Chambers (VDCs)

Design and Characteristics

The Vertical Drift Chambers are used to provide information about the tracking of the scattered particles. There are two VDCs in each spectrometers which determine the position and track of a scattered particle. Each of these two VDCs is composed of two wire planes in the standard UV configuration. The wires in the U and V planes are perpendicular to each other and lie in the laboratory horizontal plane. Both the planes are oriented at 45° with respect to the nominal particle trajectory. The distance between the two VDC planes is 335 mm and the separation between each pair of U and V planes is 26 mm as shown the Fig. 3.14. There are a total of 368 sense wires in each plane, spaced 4.24 mm apart [12]. The wires are made of Au-plated tungsten. The VDCs are constructed and placed in such a way that the lower VDC is positioned to coincide with the spectrometer focal plane and the second VDC is located above it (as shown in the figure) to enable precise angular reconstruction of the particle trajectories [96].

The operation of the VDCs during the data taking is based on four subsystems: the gas system, the high voltage, the low voltage and the readout system. The chamber gas is provided by the Hall A Wire-chamber Gas System(HAWGS). The gas supplied to the VDCs is a mixture of (62%/38% by weight) argone and ethane with a flow rate of 10 liter/hour [96]. There are three high voltage planes at about -4 kV in each VDC, one is in the middle of the U and V planes and the other two are on the two opposite sides (top and bottom). High voltage is provided by a single channel of a Bertan 377N HV power supply. All these subsystems are well explained in [93].

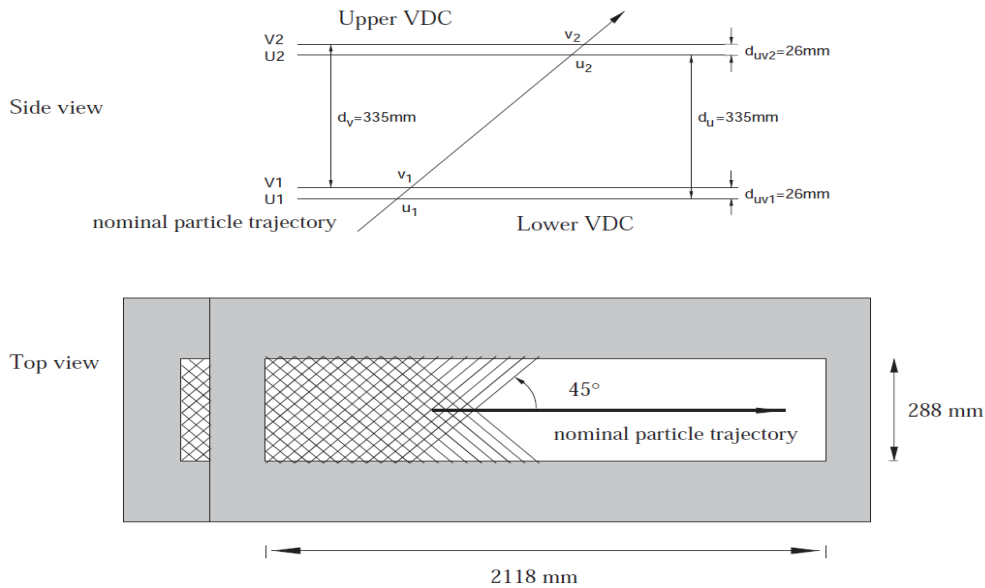


Figure 3.14: Schematic diagram of the LHRV VDC planes. Reproduced from [12].

Basic Principle and Theory

The basic principle which governs the operation of the drift chambers is based on the ionization of the gas molecules in the chambers and the drift of the electrons in an electric field. When a charged particle travels through the gas in the chamber, it transfers energy to the gas by ionizing its molecules and atoms. The mean rate of energy loss of the traversing

charged particle is given by the Bethe-Bloch equation:

$$\frac{dE}{dx} = \frac{4\pi N_o Z^2 e^4}{mv^2} \left(\frac{Z}{A} \right) \left[\ln \left(\frac{2mv^2}{I(1-\beta^2)} \right) - \beta^2 \right], \quad (3.15)$$

where v is the velocity of the particle, $\beta = \frac{v}{c}$, E is the energy of the particle, x is the distance travelled by the particle, e is the charge of an electron, m is the rest mass, Z is the atomic number, A is the mass number and N_o is the number density.

The energy loss of the particles to the gas results in the production of electrons and ions along its trajectory. This is called the primary ionization. These electrons then are accelerated towards the wires by the electric field via a geodesic path which is the path traversed in the least time by the electrons. The electric field inside the chamber is constant through most of the drift area except near the sense wires where it becomes almost like a purely radial ($1/r$) field. The electrons drift along the field lines with almost constant drift velocity ($\sim 50 \mu\text{m/ns}$). But in the very close proximity of the sense wires, they suddenly enter into a field region where the field increases rapidly. Hence the electrons in this region acquire enough energy to produce secondary electrons which create an avalanche effect. This effect eventually creates a signal in the sense wire and it is detected by the electronics.

The VDCs feature a five cell design as shown in Fig. 3.15. This means that a particle with a track at the nominal angle of 45° with respect to the laboratory horizontal plane fires five wires. On the other hand, the particles having an extreme angle (52°) track fire only three.

The fired wires are read out with TDCs (Time-to-Digital converters). The TDCs are operated in common stop mode and hence a larger TDC signal corresponds to shorter drift time. Since the drift velocity is known, the drift distance from the trajectory of the particle to each fired wire can be extracted from the TDC readouts. Thus the trajectory of a particle can be reconstructed by combining all the drift distances from all the fired wires together. A position resolution of $\sigma_{x(y)} \sim 100 \mu\text{m}$ and an angular resolution of $\sigma_{\theta(\phi)} \sim 0.5 \text{ mrad}$ were achieved in the focal plane.

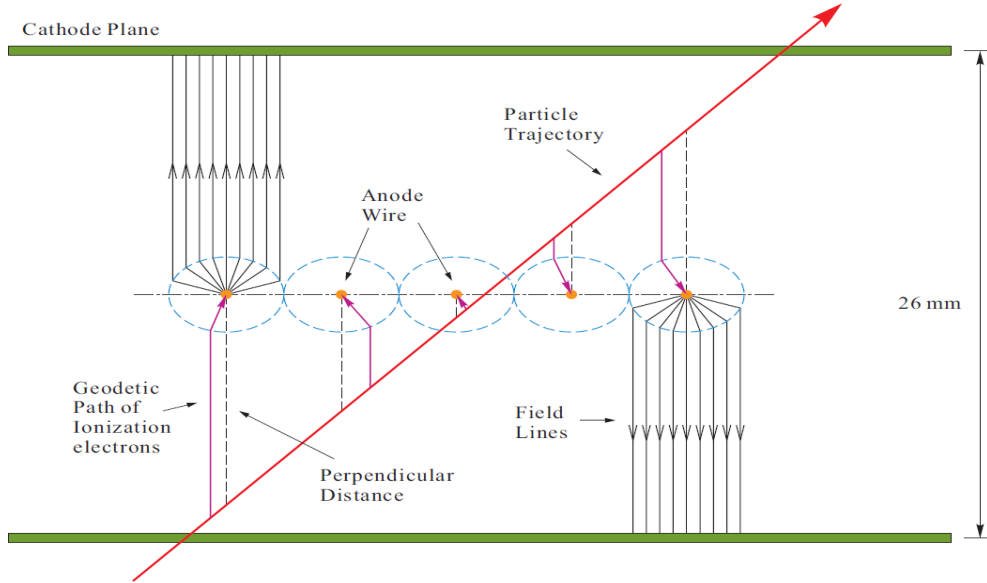


Figure 3.15: The 5-cell configuration in LHRs VDCs [13].

3.4.4 Lead-Glass Counters

Two sets of lead glass counters are used for particle identification. Those are typically called the pion rejector layer 1 and layer 2. Together with an Aerogel and a Gas Čerenkov detector, the pion rejector helps in separating the electrons from the pions in the LHRs. In our case, since we wanted to distinguish pions from the electrons as efficiently as possible, these lead-glass counters provided useful particle identification. Among the GeV/c charged particles passing through the lead glass counters, only the electrons develop electromagnetic showers while the heavy hadrons can not develop as strongly as the electrons because of their comparatively longer mean free path. The energy deposited by the particles in the counters is used to identify different particles since the signal in the counters is linearly proportional to the energy deposition. In our case, we have two distributions of energy: *low ADC signals for hadrons* and *high ADC signals for electrons*.

The construction of both layers of the pion rejector is the same. Each layer consists of 17 short blocks and 17 long blocks of lead glass, forming a 2(transverse) \times 17(dispersive) array. This is shown in Fig. 3.16. Thus, both the layers are composed of 34 blocks and each has dimensions of 14.5 cm \times 14.5 cm \times 30(35) cm. The gap between two blocks in the first

layer is covered by the block in the second layer, and vice versa as shown in Fig. 3.16.

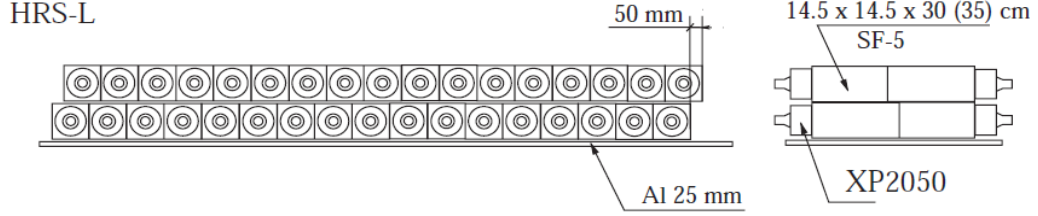


Figure 3.16: Pion Receptor: Layer1 and Layer2. Reproduced from [12].

3.4.5 Gas Čerenkov Counter

The Gas Čerenkov counter in the LHRs is one of the most efficient particle identification detectors used to select or reject the electrons from other particles. In our case, the Gas Čerenkov counter was used to reject the detected electrons which were treated as the largest background in the detected hadron samples. The gas Čerenkov detector is filled with CO_2 at atmospheric pressure and is mounted between the Aerogel detector and the S2m scintillator plane.

A threshold gas Čerenkov detector is based on the principle of Čerenkov radiation. When a high energy charged particle moves in a medium of refractive index n with a velocity v higher than that of light in the same medium, *i.e.* $\beta > \frac{1}{n}$, a characteristic electromagnetic radiation is emitted. This is called the Čerenkov radiation and the phenomenon is termed as Čerenkov effect. The radiation propagates in a direction forming an angle θ with the path of the charged particle given by:

$$\cos(\theta) = \frac{1}{\beta n}, \quad (3.16)$$

where β is the ratio of the particle velocity to that of light in vacuum [97].

The reason the high energetic particle emits Čerenkov light is that when the particle passes through the medium, it momentarily polarizes the atoms along its track, making them electric dipoles. Now once the particle has passed, this polarized state collapses and each atom emits Čerenkov radiation. If the velocity of the charged particle v is lower than that of light, the dipoles created by it are arranged symmetrically around the particle's path. This makes the polarization perfectly symmetrical which results in zero net dipole

moment and hence no radiation. But if $v > c/n$, this polarization is no longer symmetrical and hence the net non-vanishing dipole moment leads to the emission of Čerenkov radiation.

The refractive index of the CO₂ gas used in the detector is 1.00041 which gives a threshold momentum of ~ 17 MeV/c for electrons and 4.8 GeV/c for pions. Therefore, for the designated momentum range $0.30 \sim 4.0$ GeV/c in the LHRS, only electrons can emit Čerenkov radiation and generate an ADC signal.

The gas Čerenkov detector has 10 spherical mirrors positioned in a 2(horizontal) \times 5(vertical) array. Each of the mirrors has a radius of curvature of 90 cm and is coupled to a PMT which is placed at a distance of 45 cm from the mirror. As a result, the parallel rays of incident light emitted by the electrons are approximately focused onto the PMT after reflection. Then the PMT converts the incident light to an electronic signal and the signal is then sent to an ADC attached to it. The summation of all the ADC signals gives the information about the total amount of light emitted by the particle.

Although pions do not have the threshold momentum to produce any Čerenkov light in the detector, they can still interact with the atoms in the medium and create secondary or δ electrons. Then those electrons can emit Čerenkov light and produce signals in the ADCs. But the δ electrons do not move in the same direction as the scattered electrons and hence the emitted light is not efficiently collected by the mirrors. These summed ADC signals for the δ electrons are mostly single photo-electron peaks. On the other hand, the Čerenkov light emitted by the scattered electrons corresponds to the multi photo-electron peak in the ADC signals. The number of photo-electrons in each PMT determines the efficiency of the separation of the single photo-electron peak from the multi photo-electron peak and hence the PID quality of the detector. During the experiment, the average number of photo-electrons for each PMT was ~ 6 . The PID efficiency analysis will be discussed in chapter 5.

3.4.6 Aerogel Čerenkov Counter A1

A1 is one of the Aerogel diffusion type counters that is used for the particle identification which is based on the detection of Čerenkov radiation as discussed in the previous subsection.

A1 has 24 PMTs (Burle 8854). The aerogel radiator used in A1 is 9 cm thick and it has a refractive index of 1.015 which results in a threshold of 2.84 GeV/c for kaons and a threshold of 0.803 GeV/c for pions. Hence, during the normal operation with the LHRS momentum between 0.42 - 2.8 GeV/c, pions fire the A1 and kaons do not. A schematic diagram of the A1 counter is shown in the Fig. 3.17.

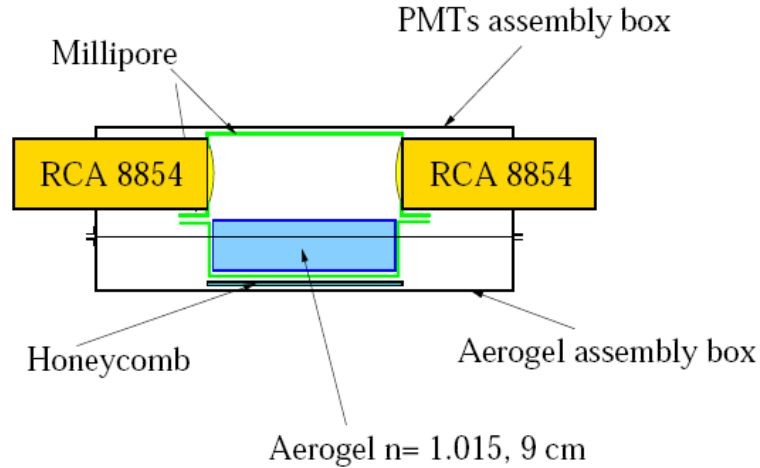


Figure 3.17: Schematic of the A1 counter.

In the experiment, A1 was used to select the pions and to reject the kaons which produced the single photo electron peak in the ADC spectrum at the channel 100 (after calibration).

3.4.7 RICH Detector

The Hall A Ring Imaging Čerenkov (RICH) detector was mainly used in this experiment to identify kaons, pions, and protons. Using the RICH detector in addition to Time of Flight (TOF) to distinguish between pions and kaons helped tremendously in this experiment. The RICH detector was placed between the Aerogel and the Gas Čerenkov detector in the detector hut. The basic design of the RICH detector is identical to the CERN Alice HMPID detector [93]. But it has been modified to accommodate different specific requirements for different experiments. It has a proximity focussing geometry and it does not have any mirrors which makes the detector compact (total length less than 50 cm) and relatively thin ($18\%X_0$). The working principle of the adopted RICH detector in the experiment is

shown in the Fig. 3.18.

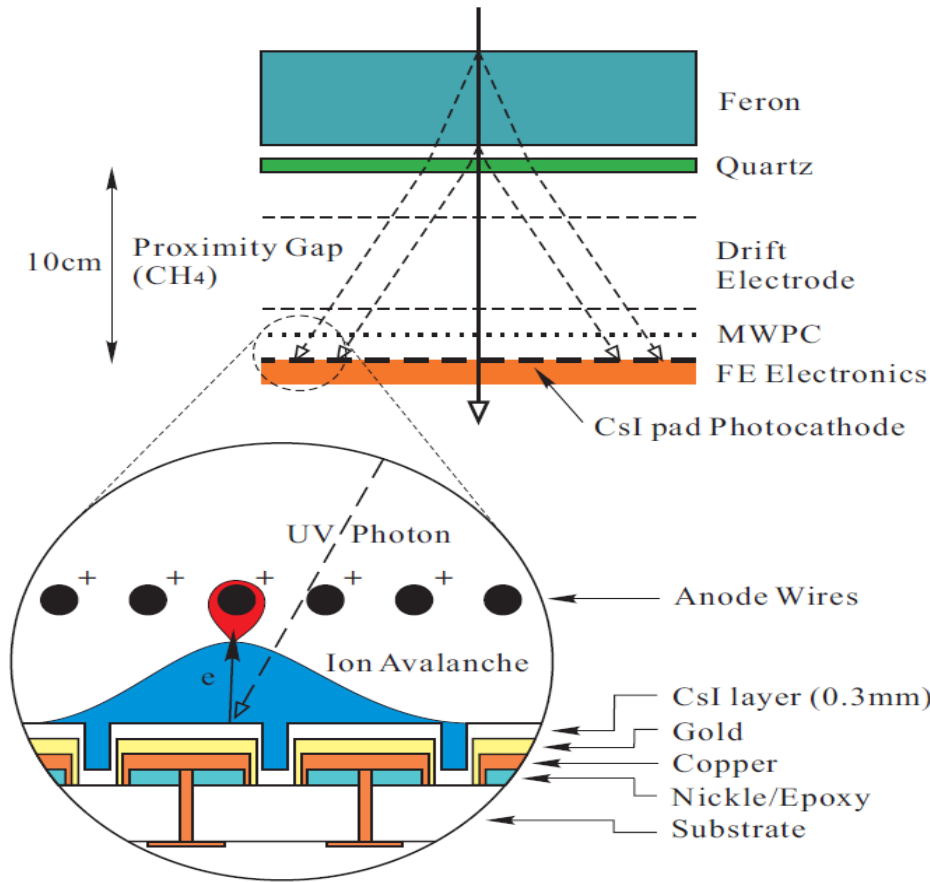


Figure 3.18: The RICH detector working principle [13].

When a charged particle traverses through the liquid freon, it emits Čerenkov radiation. The 1.5 cm thick liquid radiator is housed in a vessel made of NEOCERAM on all sides except the exit window. NEOCERAM is a glass-ceramic material with mechanical and thermal properties almost identical to quartz. The exit window is made of 0.5 cm thick pure quartz. The use of a liquid radiator has been imposed by the momentum range (around 2 GeV/c) of the particles to be identified. The Čerenkov photons, emitted along a conical surface, are refracted by the freon-quartz-methane interfaces and strike a pad plane after traveling a proximity gap of 10 cm filled with methane.

The pad plane is covered by a thin substrate of CsI which acts as a photon converter. An electric field of ~ 2100 V/2 mm is produced between the pad plane and an anode wire

plane in front of the pads which accelerates the emitted photo-electrons, thus forming a multi-wire proportional chamber (MWPC). During the operation, the anode wires collect the avalanche of the electrons while the counterpart ions are collected by a cluster of pads, each of which is connected to the input channel of a multiplexed sample-and-hold electronics module, housed on the back of the pad plane. Then finally the cluster of pads hit by the photons should be scattered around a ring (ellipse) while one cluster coming from the charged particle track should be located in the central region of the ring. The secondary electrons produced by the ionization of the counting gas by the charged particles in the proximity gap are prevented from reaching the MWPC by a drift electrode. This electrode is positioned close to the quartz window and its operating voltage is about 250 V. The MWPC of the RICH detector has to be operated with pure methane to achieve the designed performance.

An upgrade of the HallA standard RICH was done as a requirement of the transversity experiment. Since this experiment measures $2.4(\pm 5\%)\text{GeV}/c$ π^\pm and K^\pm mesons single spin asymmetries and due to the fact that the pion production is large with respect to kaons, but the asymmetries are of the same order, a $\pi : K$ rejection of 10^{-3} was required. The upgrade basically involved the extension of the photon detection surface which improved the photon collection and at the same time permitted to increase the proximity gap and consequently the angular distribution. The new upgraded version used in the experiment has a net surface area which is 1.65 times larger than the previous one. The larger photon detection plane permitted a longer proximity gap (from 100 to 175 mm) and therefore a smaller overall angle reconstruction error [98].

3.4.8 S1 and S2m Scintillator Planes

There are two scintillator planes in the LHRS in the standard detector configuration, *viz.*, S1 and S2m. These planes are used to form various triggers specific to the requirements of the experiment and they also provide timing information which is quite important for particle identification.

The S1 scintillator plane consists of six paddles, each with an active area of $29.5\text{ cm} \times 35.5\text{ cm}$. Each of the paddles is viewed by a 2" photomultiplier tube (Burle 8575) on each

end. The S1 paddles are installed at a small angle with respect to the S1-plane and overlap by 10 mm. The S2m scintillator plane consists of sixteen paddles, each of them having a dimensions of 17" \times 5.5" \times 2" thick. But the paddles do not overlap unlike the S1 plane. The timing resolution per plane is approximately 0.30 ns (σ). A schematic diagram of the scintillator is shown in Fig. 3.19.

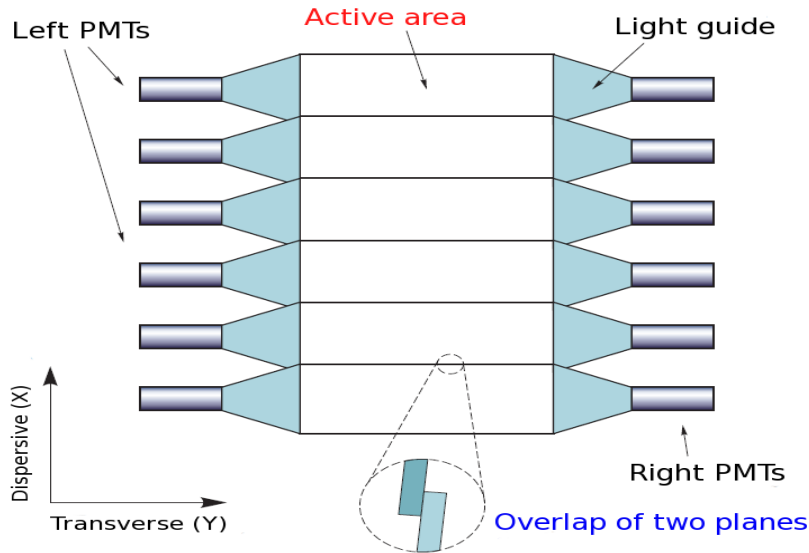


Figure 3.19: A schematic of the S1 scintillators for reference. S2m has the same structure except it has 16 paddles and the paddles do not overlap. This figure is reproduced from [13].

During the experiment, S1 and S2m were used for the trigger formation. However, the right PMT signals in S2m were treated as the reference for all the timing information. This will be discussed in the trigger section later. All the time-of-flight and coincidence timing calibrations were performed with respect to the timing information from the S2m.

3.5 The BigBite Spectrometer

The BigBite spectrometer was used to detect the scattered electrons coincident with the hadrons detected in the left high resolution spectrometer (LHRS). The BigBite detector package was placed at a forward angle of 30° to the right with respect to the incoming beam. It is a large momentum, non-focusing spectrometer and it consists of a large dipole magnet and a detector assembly. During the experiment, the dipole magnet was driven by full current to produce a maximum field of 1.2 T.

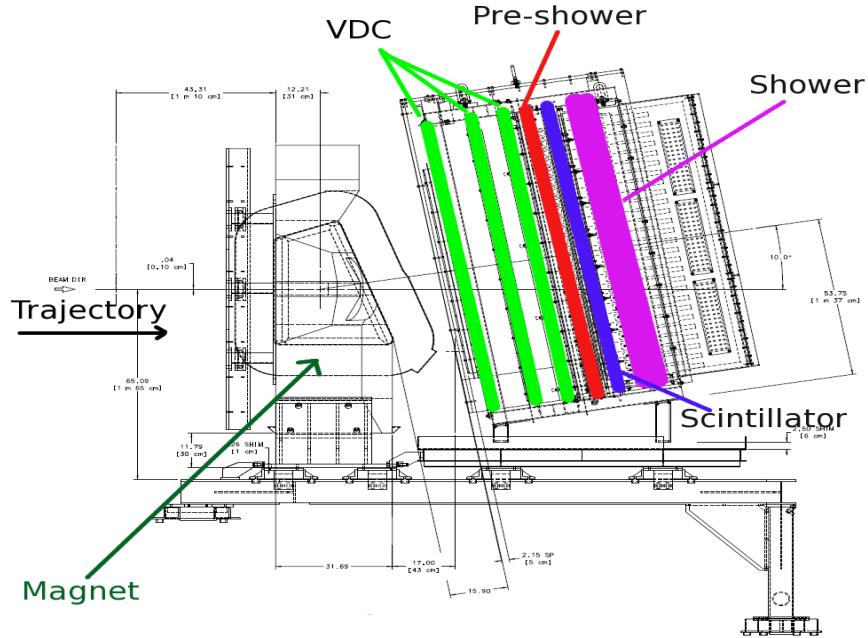


Figure 3.20: The schematic of the BigBite spectrometer package [14].

The detector assembly consisted of three multi-wire drift chambers, a gas Čerenkov detector, a scintillator plane, and two lead glass calorimeters known as shower and preshower. The BigBite spectrometer detector package is shown in Fig. 3.20. The gas Čerenkov in the BigBite spectrometer was not used in the transversity experiment and will not be discussed here.

3.5.1 Multi-Wire Drift Chambers

The multi-wire drift chambers contained three different sets of wire chambers which were ~ 35 cm apart from each other. Each of these had U-U', V-V' and X-X' planes which provided a very high spacial resolution of $180 \mu\text{m}$. The orientation of the U, V and X planes is shown in the Fig. 3.21.

The U and V wires were at $\pm 30^\circ$ with respect to the X wires which were horizontal. Each chamber had sense wires ($20 \mu\text{m}$ in diameter) which were 1 cm apart from each other and had a field-shaping wire in between. As typical for drift chambers, the wire planes were surrounded by cathode planes. The distance between a cathode plane and the wire planes was about 3 mm whereas the wire planes were 6 mm apart. The chambers were filled with

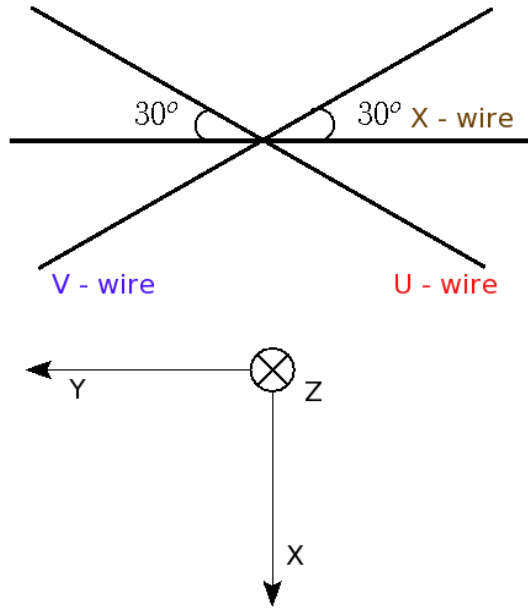


Figure 3.21: The orientation of the U, V and X planes in MWDC.

an equal mixture of argone and ethane, kept slightly above atmospheric pressure [10].

The working principle of the drift chambers is the same as explained in the earlier section for the LHRS. The electrons produced in the ionization of the gas mixture by a charged particle traversing through it triggered the sense wires. The wires were set to some definite potential difference and hence the generated charges drifted towards the wires, creating the electrical signals which were then sent to a discriminator and were read out by a time-to-digital converter (TDC).

3.5.2 Scintillators

A plane of 13 scintillator paddles was installed in between the preshower and the shower detectors to provide the timing information. The scintillators had a timing resolution of ~ 300 ps and each of them was attached to two photomultiplier tubes at each end. The signal from each photomultiplier tube was sent to an ADC and a TDC through an amplifier. The timing resolution was used to reconstruct the time of the electron at the drift plane when it was associated with the track of the electron. The timing resolution was very crucial for this coincidence experiment as a part of particle identification. When combined with the left spectrometer resolution of ~ 130 ps, the BigBite resolution of ~ 300 ps gave a coincidence timing window of ~ 450 ps which helped achieving a clean separation of the real coincidence

pions and electrons from the kaons in the left spectrometer. The detailed analysis of the coincidence-time-of-flight will be discussed in chapter 5.

3.5.3 Shower and Preshower Detectors

The shower and preshower detectors in the BigBite detector assembly were used for particle identification as well as to form one of the triggers for the electrons. The preshower was located at a distance of 0.85 m from the first drift chamber plane and consisted of 54 lead glass blocks arranged in 2 columns and 27 rows. Each block had a dimension of 35 cm \times 8.5 cm. The shower had 189 lead glass blocks, each having a dimension of 8.5 cm \times 8.5 cm. They were arranged in 7 columns and 27 rows at a distance of 1 m from the first drift chamber plane. A schematic diagram of the shower and preshower detector is shown in the Fig. 3.22.

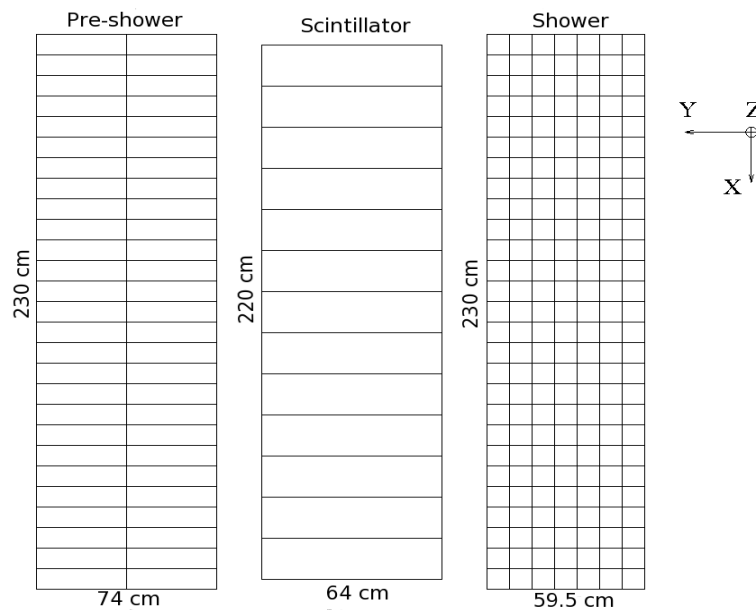


Figure 3.22: Schematic of preshower and shower blocks. The scintillators are also shown.

The electromagnetic shower produced by a particle entering the lead glass block generated Čerenkov light which was collected by the photomultiplier tube attached to it. Then the signal was sent to an ADC after having it passed through an amplifier. Another copy was sent to a set of summing modules. A copy of the summed output was then sent to an ADC and another copy was sent to a TDC through a discriminator. The amplitude of the summed signal was roughly linearly proportional to the energy of the particle. The

combination of the shower and preshower signals gave an energy resolution of $\sim 8\%$ of the total energy.

3.6 Hall A Data Acquisition System (DAQ)

The data acquisition (DAQ) systems in Hall A use CODA developed by the data acquisition group at Jefferson Lab. CODA stands for *CEBAF On-line Data Acquisition system* which is a toolkit of distributed software components from which data-acquisition systems of varying degrees of complexity can be implemented [12]. The DAQ system also includes the hardware elements such as front-end Fastbus and VME digitization devices (ADCs, TDCs, scalers), single board VME computers, a mass storage tape silo (MSS), etc., along with the other software components. The trigger supervisor is a customized support module developed at Jefferson Lab which will be discussed in the next section. The most important custom software components are the read-out controller (ROC) which runs on front-end crates, the event builder (EB) and the event recorder (ER) which run on a Linux workstation, the event transfer (ET) system which allows the distributed access to the data online and the Run Control process, which allows the users to control the data taking, changing the CODA configurations, etc.

Fig. 3.23 shows an example of a CODA configuration. Using various combinations of the ROCs, different CODA configurations can be realized as per the requirement of the specific experiment. The trigger supervisor digitizes the signals from the different detectors and reads out the crate by executing a set of C routines (known as CODA readout list). The data from the crates are collected and put into structured CODA events by the EB which are then recorded as a CODA file on disk by the ER. The transfer of the data among different components is achieved via the ET library.

3.7 Trigger Formation and Electronics

The formation of different triggers generated from the detectors and the related electronics are the essential parts of the DAQ. The trigger supervisor (TS) and the triggers related to the Left High Resolution Spectrometer (LHRS) and the BigBite spectrometer are discussed in this section. More details can be found in [15].

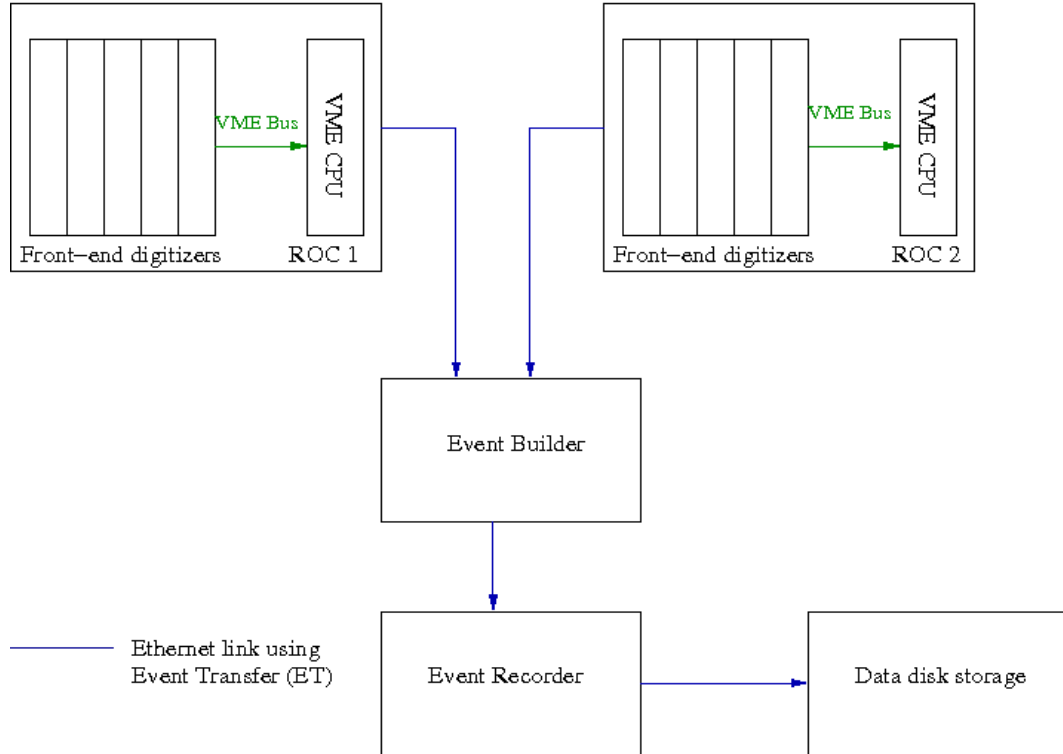


Figure 3.23: The general flow chart of the CODA configuration [15].

The Trigger Supervisor (TS) :

This is the central part of the data acquisition process during the experiment which connects the ROCs and the triggering system. The hardware contains a 9U multi-functional VME board and several ECL inputs. There are 8 input channels to accept the triggers named T1 to T8. Once multiple triggers are accepted and pre-scaled, the TS generates a signal known as L1A (*level-1 accept*) which is used for gating and timing the front-end electronics. The status of the ROCs is monitored by the TS so that during the processing of the data by the ROCs, no additional trigger is accepted by the TS, thus making the data acquisition and the trigger system perfectly synchronized.

The Trigger Electronics for LHRS :

The main trigger in the LHRS was formed by requiring that both the S1 and S2m scintillator paddles have a hit, i.e. one paddle in S1 and one paddle in S2m have a hit on both sides.

In other words, both the left and right PMTs in each paddle should have a signal to fulfill the requirement for the trigger formation. This is known as T3 trigger and the right side PMT signal of the S2m scintillator paddle serves as a reference for this trigger. Another trigger, T4, can also be formed, in general, which requires two out of three detectors have a hit. In this case, in addition to S1 and S2m, the Gas Čerenkov serves as the third detector. This was not used in E06010 and hence will not be discussed here. The gates for the ADCs and TDCs were generated using the L1A signal and the S2m PMT signals with the retiming circuit [15]. The TDCs in the S1 and S2m scintillators were common-start single hit LeCroy 1875 TDCs with a timing resolution of 50 ps. The trigger diagram for the LHRS is shown in Fig. 3.24.

The Trigger Electronics for BigBite :

The BigBite spectrometer was used as an electron arm and it contained the preshower and shower blocks as described in the earlier sections to select the electrons. The trigger was formed to select the electrons by measuring the total energy deposited by the particles in the preshower and shower blocks. The total energy deposited by a particle in the preshower and shower detectors was determined by forming a total hardware sum (TSUM) of the two overlapping rows of the preshower and shower detectors as shown in Fig. 3.25.

4 blocks (2×2) in the preshower detector and 14 blocks (2×7) in the shower detector were considered for the deposition of energy. The summation of the energy deposition was done separately for both these detectors using LeCroy 428F modules (preshower) and custom built summing modules (shower) and then the “sum signals” from both were combined together to form the TSUM. This TSUM signal (analogue signal) which is proportional to the total energy deposited by the particle was then sent to a discriminator. The threshold of the discriminator could be adjusted following the experimental requirement to form the trigger. This trigger was called the T1 trigger. Fig. 3.26 shows a schematic diagram of the electronics for the triggers formed in BigBite spectrometer.

There were other triggers formed in the BigBite spectrometer to satisfy various requirements for parasitic experiments that ran along with the E06010. Those are listed in Table 3.4 along with the main triggers.

The TDCs used in the scintillators were common-stop multi hit F1 TDCs with a resolu-

Table 3.4: The different triggers formed during the experiment. T1, T3 and T5 are the relevant ones.

Trigger Type	Description
T1	BigBite lead-glass (low threshold)
T2	BigBite Gas Čerenkov
T3	LHRS singles (S1 AND S2m)
T4	LHRS (S1/S2m/Gas Čerenkov) efficiency
T5	Coincidence (BigBite T1 AND LHRS T3)
T6	BigBite lead-glass (high threshold)
T7	BigBite Gas Čerenkov and lead-glass overlap
T8	Pulser (1024 Hz clock)

tion of 60 ps. LeCroy 1881 ADCs were used to read all the PMT signals in the calorimeter and the scintillators. The ADC gate width was ~ 240 ns.

Coincidence Trigger :

The coincidence trigger T5 formed by the overlapping of T1 and T3 triggers in time described above was the most important trigger for this experiment. The experiment was devoted to detect the hadrons in the LHRS that were coincident with the scattered electrons detected in BigBite. Hence in order to form the coincidence trigger, the exact trigger formation time and the time-of-flight of the detected particle in both the spectrometers had to be determined. Once the trigger formation time and the time-of-flight information are known, T1 and T3 triggers were forced to overlap by adjusting the cable delays in both of them. The T5 trigger logic and the relative timing diagram of all the triggers are shown in Fig. 3.27 and Fig. 3.28.

3.8 Scaler and Dead Time Measurement

Scalers were used to count the raw signals from the PMTs on different detectors as well as from the Beam Current Monitors (BCM), thus providing various information regarding the raw rates for different types of triggers and beam current. The detailed information about the scalers is reported in [15]. For this experiment, five scalers were configured depending upon the helicity states of the incoming electron beam and the target spin. Out

of them, four scalers were gated as $(++)$, $(+-)$, $(-,+)$, and $(--)$ where the first quantity in the parentheses is the target spin state and the second one is the beam helicity. The last one was not gated by any beam or target helicity and termed as ungated scaler. All these five scalers were also gated with the run period i.e. they counted only when the run was started and stopped counting as soon as the run was terminated. The run gate was obtained from the trigger supervisor. All these signals were finally sent to the control bit on an SIS3800 scaler for gating purpose and they were read out from the server by VME.

The scalers were used to determine the dead time during the data taking process. Two kinds of dead time were realized in practice : *electronic dead time (EDT)* which occurred in the front end electronics due to high rate of data taking and *DAQ dead time* which was due to the DAQ electronics. During the process of data acquisition, the trigger supervisor was always synchronized with the ROCs and hence it only accepted triggers when the ROCs were not busy handling the signals. However, during the period when the ROCs processed the data which was between $300 \mu\text{s}$ to $500 \mu\text{s}$ there were a lot of events ignored by the trigger supervisor. Those events were lost due to the waiting period of the trigger supervisor and had to be corrected for in the data analysis.

The electronic dead time was measured by sending a pulser of 12.5 Hz to the front-end electronics and comparing the number of pulses recorded by the DAQ and the number of pulses originally sent. The electronic dead time was reasonably small as compared to the DAQ dead time. The DAQ dead time can be expressed as:

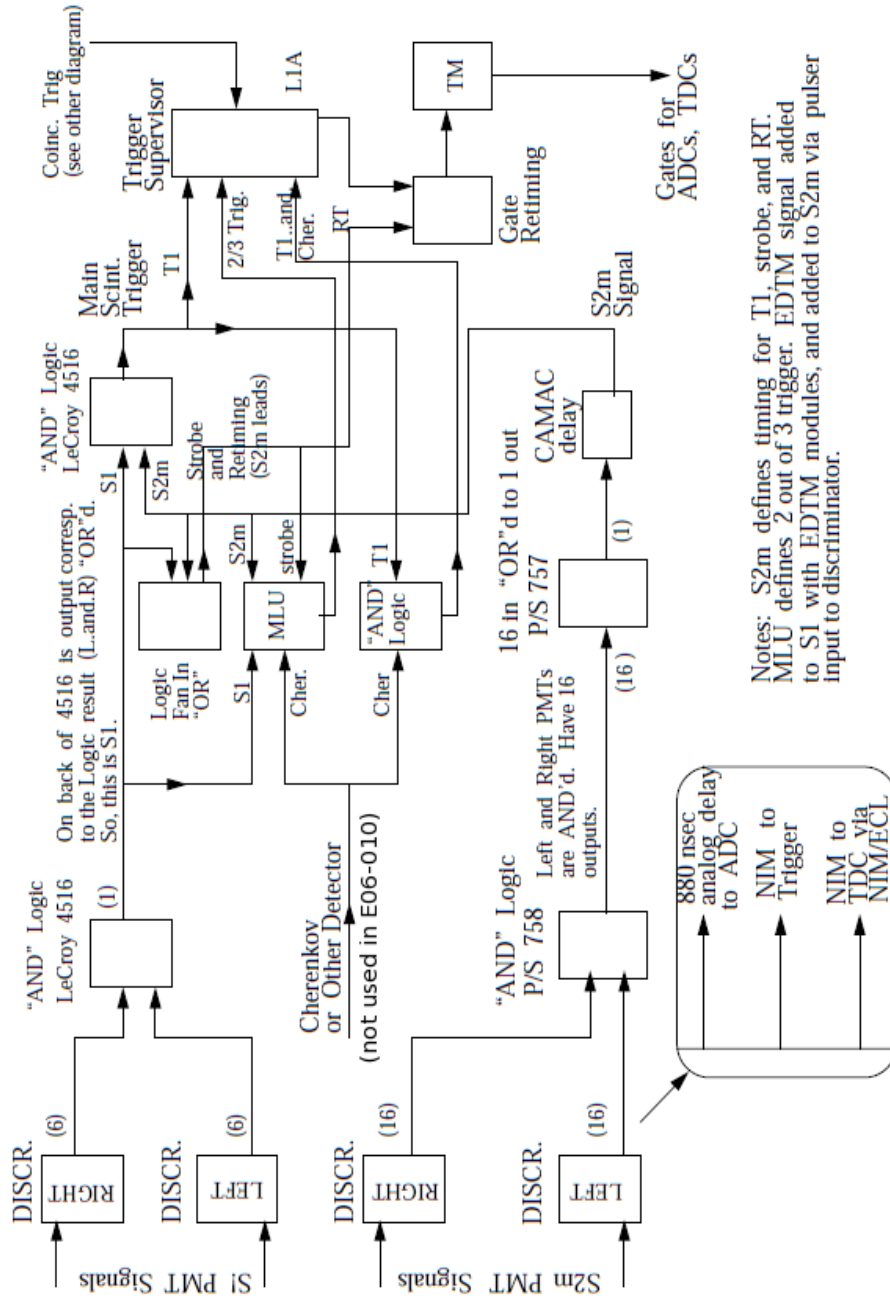
$$DT = 1 - \frac{p \times n_r}{n_t}, \quad (3.17)$$

where the quantities are defined as follows:

- n_r = number of events recorded by a particular trigger
- n_t = total number of events occurred due to the respective trigger
- p = pre-scale factor for the trigger

Figure 3.24: Schematic of the trigger electronics in LHRS [16].

Single Arm Trigger Logic



Notes: S2m defines timing for T1, strobe, and RT.
MLU defines 2 out of 3 trigger. EDTM signal added to S1 with EDTM modules, and added to S2m via pulser input to discriminator.

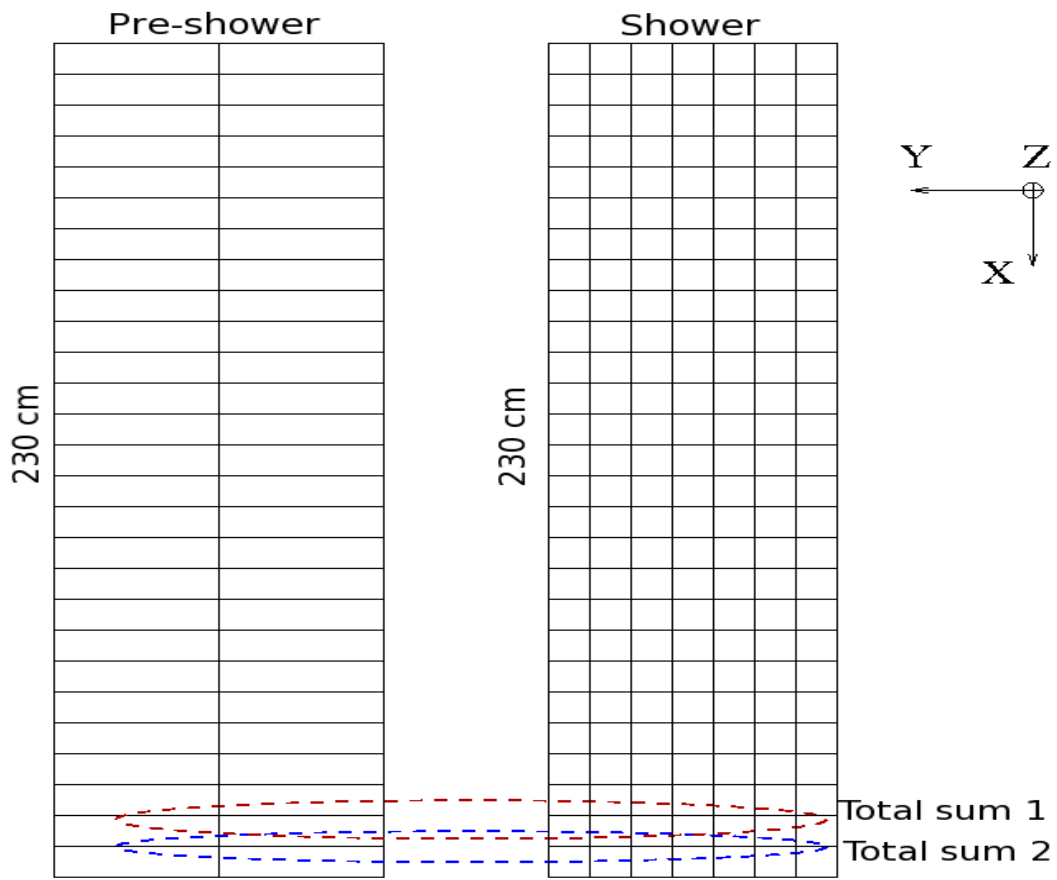
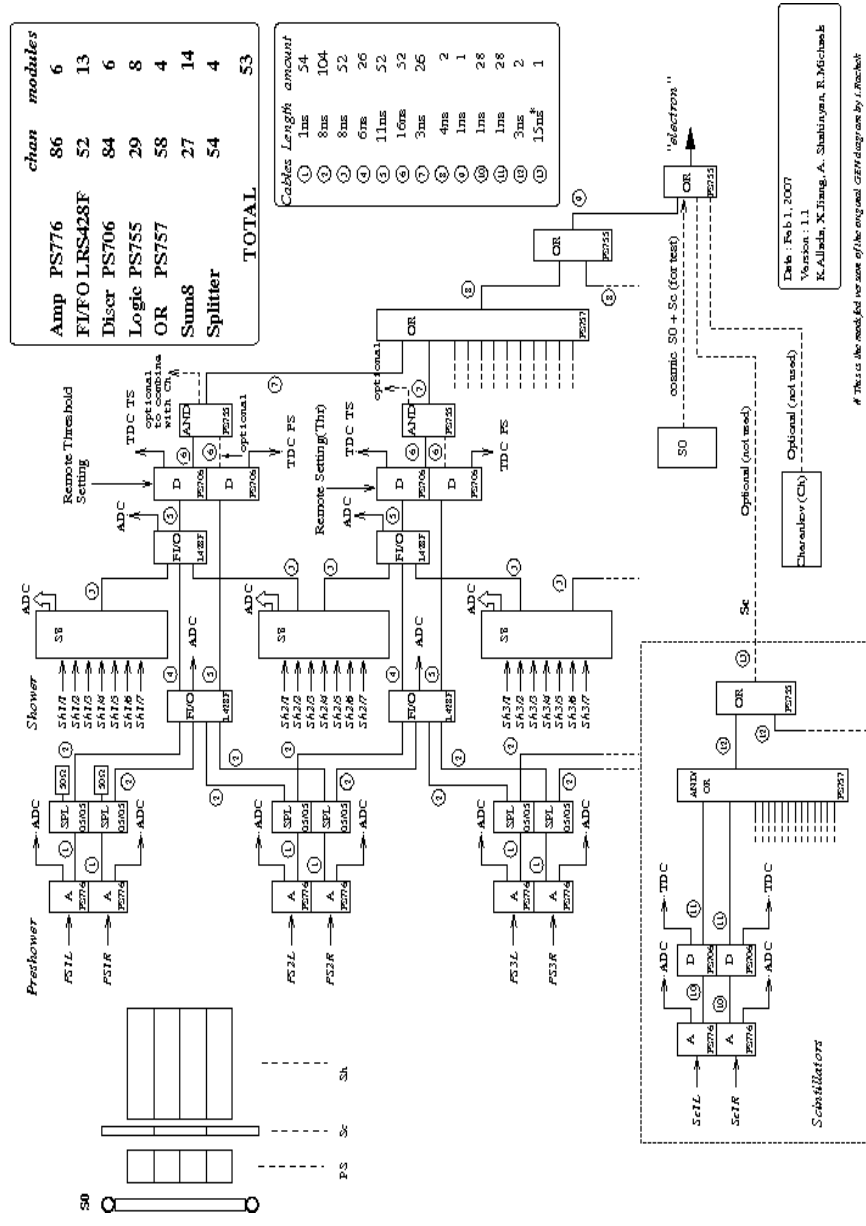


Figure 3.25: The preshower and shower energy sum formation for the trigger in BigBite [15].

Figure 3.26: A schematic of the trigger electronics in BigBite [15]
 BigBite Trigger Logic for Hall A Transversity (E06-010) Experiment



Date: Feb 1, 2007
 Version: 1.1
 K. Akhida, X. Jiang, A. Shaheen, R. M. Schaeck

* This is the modified version of the original CERN design by J. M. Schaeck

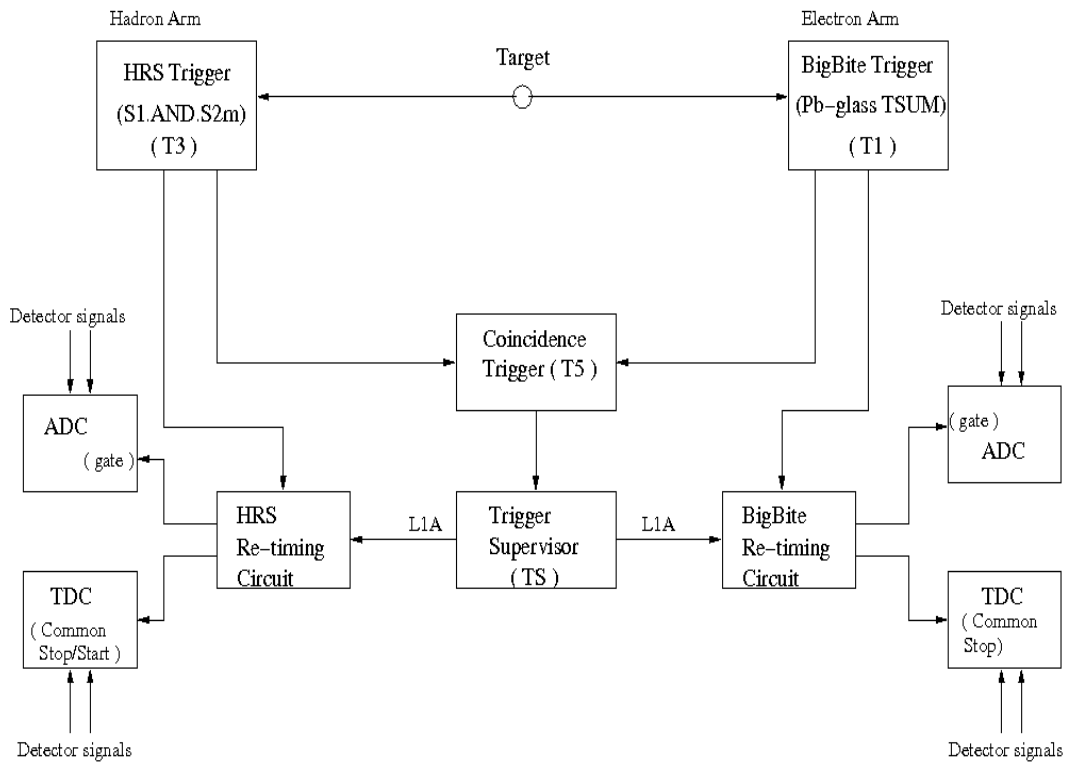


Figure 3.27: Schematic of the coincidence trigger logic [15].

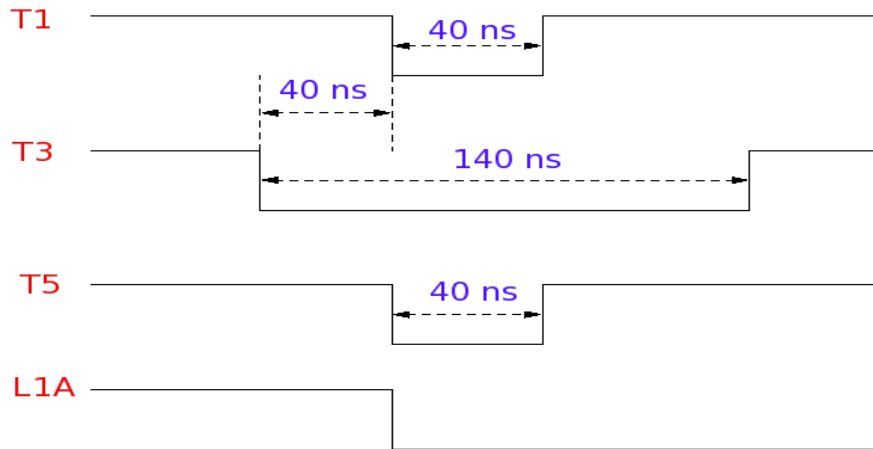


Figure 3.28: The relative timing scheme of the triggers used in E06010. The timing of the T5 is given by the leading edge of T1 [15].

CHAPTER 4: THE POLARIZED ^3He TARGET

This chapter is dedicated to the description of the polarized ^3He target used in experiment E06010 in Hall A at Jefferson Lab. Several other experiments had used a polarized ^3He target as an effective neutron target in Hall A before. The basic principle of optical pumping to polarize the ^3He atoms, the experimental setup of the target system, different polarimetry techniques to measure the polarization, and the polarization analysis are presented in this chapter.

4.1 Polarized ^3He Nuclei As An Effective Neutron Target

Experiment E06010 aimed at measuring single spin asymmetries (SSA) on a transversely polarized neutron target and ideally we needed a collection of polarized neutrons. However, the half-life of a free neutron is very short¹ which would unfortunately make our measurement practically impossible. Hence, the polarized ^3He target serves as a substitute for a polarized neutron target. Deuteron can also be used as a neutron target. However, since the deuteron contains one proton and one neutron, the neutron polarization is more diluted by the proton as compared to the ^3He nucleus. The ^3He nucleus has two protons and one neutron of which the two protons cancel their spins in the ground state most of the time ($\sim 90\%$) which corresponds to the S -state as shown in Fig. 4.1 and effectively the ^3He nucleus behaves as a single neutron. Thus, in the ground state, the S -state is the most favorable state among the other two S' and D -states² as shown in the Fig. 4.1.

A polarized ^3He target has been used at SLAC, in the HERMES experiment at DESY, at MAMI, and at Jefferson Lab to study the spin structure functions of the neutron. Our experiment E06010 also used a polarized ^3He target successfully to study the SSA on the neutron with the objective to explore the quarks' *transversity distribution* by looking at the Collins and Sivers contribution to the SSAs.

¹The half-life of a free neutron is $(878.5 \pm 0.7_{stat} \pm 0.3_{sys} \text{ s})$ [99]. This is the most recent result on neutron lifetime measurement using gravitationally trapped ultracold neutrons (UCN). The number is quoted from the Particle Data Book (PDB).

²In addition to the S -state which is the space-symmetric state, S' and D -states exist due to the spin dependence of the nucleon-nucleon potential and the tensor force in the nuclear Hamiltonian, respectively. However, they have only a few percent probability as shown in the figure.

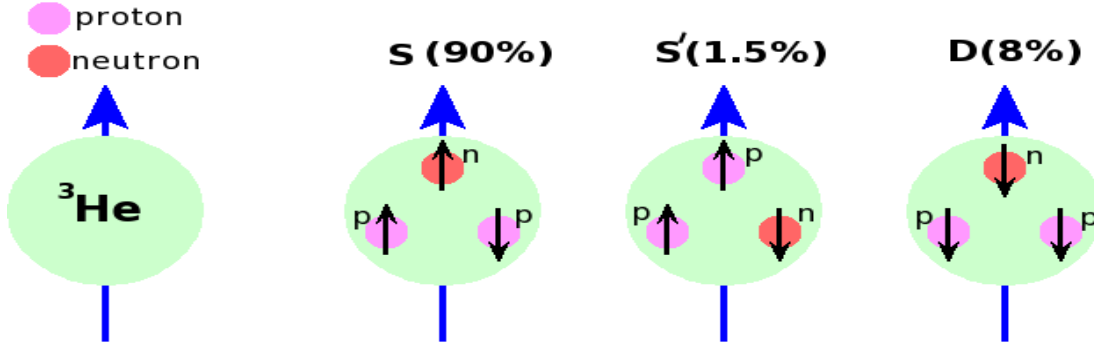


Figure 4.1: Different ground state wave functions of ${}^3\text{He}$. The pink circle represents a proton and the red circle represents a neutron.

4.2 Basic Principle

Consider a sample of N ${}^3\text{He}$ nuclei in an external magnetic field. Now if N^\uparrow is the number of spins aligned parallel to the direction of the magnetic field and N^\downarrow is the number of spins aligned anti-parallel to the field, then the vector polarization is defined as

$$P = \frac{N^\uparrow - N^\downarrow}{N}. \quad (4.1)$$

There are two hyper-polarization methods that have been used to polarize ${}^3\text{He}$. One is metastability-exchange optical pumping [100], [101] and the other one is spin-exchange optical pumping [102]. The spin-exchange optical pumping scheme is used in Hall A to polarize the ${}^3\text{He}$ gas.

4.2.1 Optical Pumping

Spin-exchange optical pumping was used to polarize the atoms of ${}^3\text{He}$. The atoms are polarized in a two-step process. First, electrons in Rb atoms are polarized by optical pumping and then these polarized electrons transfer the polarization to the ${}^3\text{He}$ nuclei via spin-exchange collisions. A pure³ ${}^3\text{He}$ gas cell contains only Rb atoms and a small amount of N_2 ⁴ in addition to the ${}^3\text{He}$. Experiment E02013 was the first experiment in Hall A that used a hybrid cell which contains potassium (K) in addition to Rb, N_2 and ${}^3\text{He}$ in order to

³The word *pure* is used to refer to the ${}^3\text{He}$ cell which contains Rb and N_2 with the ${}^3\text{He}$ gas. However, to enhance the process of optical pumping by making the spin exchange between the alkali atoms and the inert gas nuclei more efficient, potassium (K) was added in addition to the ${}^3\text{He}$ gas in the cell. Thus, the ${}^3\text{He}$ cells containing K atoms are termed as *hybrid* cells.

⁴A small amount of N_2 is added to the ${}^3\text{He}$ cell in order to quench any unpolarized light during the process of optical pumping.

make the spin-exchange process faster and more efficient. E06010 used three hybrid cells during the process of data taking. In case of a hybrid cell, Rb is optically pumped and the polarization of the Rb atoms is transferred to the K atoms via spin-exchange collisions. Then the polarized K atoms in turn transfer the polarization to the ^3He nuclei. This spin-exchange via K is much faster than the Rb- ^3He exchange. The details of this process will be presented in the later sections.

We use 795 nm diode lasers to polarize the electrons in the Rb atoms. Rb has one electron in its outermost $5S_{1/2}$ shell. The ground state Hamiltonian for Rb in an external magnetic field \vec{B} applied along the z -direction can be written as [103]:

$$H = A_g \vec{I} \cdot \vec{S} + g_s \mu_B S_z B_z - \frac{\mu_I}{I} I_z B_z, \quad (4.2)$$

where the term $A_g \vec{I} \cdot \vec{S}$ describes the coupling between the electron spin \vec{S} and the nuclear spin \vec{I} of the alkali atoms, A_g being the isotropic magnetic-dipole coupling coefficient. The second term $g_s \mu_B S_z B_z$ describes the magnetic-dipole coupling between the electron spin \vec{S} and the external magnetic field \vec{B} where $g_s=2.00232$ for the electron and the Bohr magneton $\mu_B = 5.7884 \times 10^{-11}$ MeV/T. The last term is the magnetic-dipole coupling between the nuclear spin \vec{I} and the static magnetic field \vec{B} where μ_I is the nuclear magnetic moment which is 4.26426×10^{-12} MeV/T for ^{85}Rb . $I = 5/2$ for ^{85}Rb and $I = 3/2$ for ^{87}Rb . Now the expectation value of the Hamiltonian in Eq.(4.2) is given by the eigenstate $|F, m_F\rangle$ where F is the total angular momentum quantum number of the state defined as $\vec{F} = \vec{I} + \vec{S}$. In a magnetic field, F splits into $2F+1$ sub-levels denoted by $m_F = m_I + m_S$ with $m_I = -I, -I+1, \dots, I-1, I$, $m_S = -S, -S+1, \dots, S-1, S$, and $m_F = -F, -F+1, \dots, F-1, F$. Hence,

$$H|F, m_F\rangle = E(F, m_F)|F, m_F\rangle. \quad (4.3)$$

For the ground state, the total angular momentum of the electron $\vec{J} = \vec{S}$ as the orbital angular momentum \vec{L} is zero. Since $S=1/2$ in this case, $m_S = m_J = \pm 1/2$.

Fig. 4.2 shows the process of optical pumping where the Rb atoms are exposed to circularly polarized laser light of wavelength 795 nm which corresponds to the $5S_{1/2} \rightarrow 5P_{1/2}$ transition known as D_1 transition. Depending on the helicity of the photon absorbed, the electrons finally populate the $m_F = 3$ or $m_F = -3$ sub-level of the $5S_{1/2}$ state as shown in Fig. 4.2.

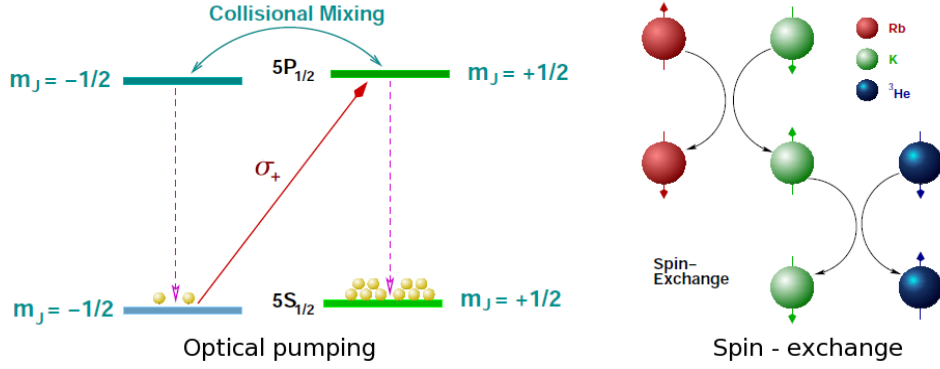
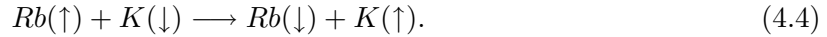


Figure 4.2: The process of optical pumping (left) and the polarization transfer from Rb to K and K to ^3He via spin exchange (right) [10].

4.2.2 The Spin Exchange

As mentioned in the previous subsection, the polarization of the alkali atoms is transferred to the ^3He nuclei via the spin exchange process which is a collisional transfer process between the two atoms. In a “hybrid” spin exchange process, a simple spin exchange collision between a Rb atom and a K atom transfers the polarization of Rb atoms to K atoms and then another subsequent spin exchange collision between the K atoms and the ^3He nuclei transfers the polarization to the ^3He nuclei. A simple spin-exchange collision between the two $S_{1/2}$ Rb and K atoms can be expressed as follows [104]:



This equation represents how the Rb spin which was $up(\uparrow)$ before collision is transferred to the K spin which was $down(\downarrow)$ so that after the collisional exchange, the K spin is $up(\uparrow)$ and the Rb spin is $down(\downarrow)$. The interaction potential, in this case, is of the form [104]:

$$V(r) = V_o(r) + S_{Rb} \cdot S_K V_1(r), \quad (4.5)$$

where S_{Rb} and S_K are the spin operators of Rb and K atoms, respectively. Now this potential is of order electron-volts because of the electrostatic nature of the spin-exchange interaction forces. But the most important observation is even if the atoms exchange their individual spins during collision, the total spin of the colliding pair is always conserved [104]. The next consecutive process of the spin exchange mechanism in the hybrid cell is the binary

collisional transfer of polarization between the K atoms and the nuclei of the inert gas atoms (^3He). The spin dependent interaction between an alkali atom and an inert gas atom can be written as [88]:

$$V(\vec{R}) = \gamma(R)\vec{N} \cdot \vec{S} + A(R)\vec{I} \cdot \vec{S}, \quad (4.6)$$

where R is the inter-atomic separation. The first term describes the interaction between the electron spin \vec{S} and the rotational angular momentum \vec{N} of the K- ^3He system. The second term stands for the hyperfine interaction between \vec{S} and the inert gas nuclear spin \vec{I} . It is worth mentioning here that in the collision process, van der Waals molecules are produced which live until they are broken apart by a subsequent collision. This can be the main relaxation mechanism. But since gas pressure used for optical pumping is very high, most of the molecules break up before they depolarize the nucleus. Hence, this effect can be neglected [103].

4.2.3 More On Hybrid Spin-Exchange and Polarization of ^3He

Hybrid Spin-Exchange Optical Pumping⁵ (HSEOP) has the advantage over pure alkali Spin-Exchange Optical Pumping (SEOP) that it transfers the polarization of the alkali atoms to ^3He with much greater efficiency. The spin exchange collisions between K and ^3He atoms transfer the angular momentum to the ^3He much more quickly and efficiently than the collisions between Rb and ^3He atoms. For any SEOP process, two types of efficiencies are relevant.

- **Photon efficiency (η_γ):** It is defined as the number of ^3He nuclei polarized by each photon that is absorbed.
- **Spin-exchange efficiency (η_{SE}):** It is defined as the ratio at which the polarization is transferred to the ^3He nuclei to the rate at which it is depolarized through different collisions by the alkali atoms present in the cell.

In case of HSEOP, measurements of both η_γ and η_{SE} revealed that there is an order-of-magnitude SEOP improvement for K-Rb- ^3He as compared to Rb- ^3He . At typical densities of 10^{14} cm^{-3} , the K-Rb spin-exchange rate is $10^5/\text{s}$ which is much greater than the typical

⁵The Spin -Exchange Optical Pumping (SEOP) in case of a hybrid cell involving the K atoms are termed as Hybrid Spin-Exchange Optical Pumping.

500/s alkali spin-relaxation rates in ^3He cells. The equation governing the rate of change of ^3He polarization $P_{^3\text{He}}$ can be written as [105]:

$$\frac{dP_{^3\text{He}}}{dt} = \gamma_{SE}(P_A - P_{^3\text{He}}) - \gamma_{^3\text{He}}P_{^3\text{He}}, \quad (4.7)$$

where $\gamma_{SE} = k_K[K] + k_{Rb}[Rb]$ is the spin-exchange rate, k_K and k_{Rb} are the spin-exchange rate coefficients, $[K]$ and $[Rb]$ are the densities of K and Rb, respectively. P_A is the electron spin polarization for K and Rb. In spin-temperature equilibrium, K and Rb have equal electron spin polarization [104], [106]. The depolarization rate of ^3He in other processes is denoted by $\gamma_{^3\text{He}}$. For a normal non-hybrid cell, the spin relaxation rate of Rb is dominated by three different collisional transfer processes: the transfer of spin angular momentum of Rb to the rotational angular momentum of other Rb atoms, ^3He atoms, and N_2 atoms. It is to be noted that a very small amount of nitrogen is always added to the ^3He gas to absorb any unpolarized photon that is emitted from the decay of the electrons in the Rb or K atoms from the excited state during the pumping process. The total spin relaxation rate of Rb can be expressed as

$$\Gamma_{Rb} = k_{Rb-^3\text{He}}[^3\text{He}] + k_{Rb-\text{N}_2}[\text{N}_2] + k_{Rb-Rb}[Rb], \quad (4.8)$$

where the coefficient $k_{Rb-^3\text{He}}$ represents the spin relaxation rate constant for collisions between the Rb atoms and the ^3He nuclei and so on. $[^3\text{He}]$, $[\text{N}_2]$ and $[Rb]$ denote the densities of ^3He , N_2 , and Rb respectively [107]. The relaxation due to the collision of Rb atoms with the cell wall is negligible [108]. In case of the hybrid spin exchange process, the spin relaxation of K atoms is also dominated by K-K, K-Rb, and K- ^3He collisions, diffusion losses at the wall being small [105]. In the presence of rapid K-Rb spin exchange, the effective spin relaxation rate of Rb increases from Γ_{Rb} to Γ'_{Rb} given by

$$\Gamma'_{Rb} = \Gamma_{Rb} + \Omega\Gamma_K + q_{K-Rb}[K], \quad (4.9)$$

where $\Omega = [K]/[Rb]$, Γ_K is the total relaxation rate of K and $q_{K-Rb}[K]$ is the K-Rb loss rate. Usually under our conditions, this K-Rb loss rate is negligible.

The spin exchange efficiency that is responsible for the effectiveness of the evaluation of the hybrid pumping is

$$\eta_{SE} = \frac{\gamma_{SE}[^3\text{He}]}{[Rb]\Gamma'_{Rb}} = \frac{(k_{Rb} + \Omega k_K)[^3\text{He}]}{\Gamma_{Rb} + \Omega\Gamma_K + q_{K-Rb}[K]}. \quad (4.10)$$

Table 4.1: A few useful parameters associated with a typical hybrid cell and the spin exchange process. Most of these quantities are explained in [1]. T represents the temperature in Kelvin. The densities of ^3He , N_2 , and alkali atoms are typical values at our working temperature of 230°C .

Relevant quantities	Experimental values/expressions
Density of ^3He ($[^3\text{He}]$)	$\sim 10^{20} \text{ cm}^{-3}$
Density of alkali ($[\text{Rb}], [\text{K}]$)	$\sim 10^{14} \text{ cm}^{-3}$
Density of N_2 ($[\text{N}_2]$)	$\sim 10^{18} \text{ cm}^{-3}$
Spin exchange rate coefficient, k_K	$5.5 \times 10^{-20} \text{ cm}^{-3}/\text{s}$
Spin exchange rate coefficient, k_{Rb}	$6.8 \times 10^{-20} \text{ cm}^{-3}/\text{s}$
Spin relaxation rate constant, k_{Rb-Rb}	$4.2 \times 10^{-13} \text{ cm}^{-3}/\text{s}$
Spin relaxation rate constant, $k_{Rb-^3\text{He}}$	$1.0 \times 10^{-29} T^{4.259} \text{ cm}^{-3}/\text{s}$
Spin relaxation rate constant, k_{Rb-N_2}	$1.3 \times 10^{-25} T^3 \text{ cm}^{-3}/\text{s}$
Spin relaxation rate constant, k_{K-K}	$9.6 \times 10^{-14} \text{ cm}^{-3}/\text{s}$
Spin relaxation rate constant, $k_{K-^3\text{He}}$	$5.5 \times 10^{-20} + 5.8 \times 10^{-31} T^{4.259} \text{ cm}^{-3}/\text{s}$
Spin relaxation rate constant, k_{Rb-N_2}	$7.0 \times 10^{-26} T^3 \text{ cm}^{-3}/\text{s}$
Spin relaxation rate constant, q_{K-Rb}	$2.2 \times 10^{-13} \text{ cm}^{-3}/\text{s}$

Studies have shown that even with $\Omega \sim 1$, considerable improvements could be achieved in terms of hybrid exchange. In our experiment, all the three cells used had $\Omega \sim 5$. Table 4.1 summarizes the values of different quantities explained above that are typical to a hybrid cell and the hybrid spin exchange process. A typical measure of the efficiency of the spin exchange process is a *spin-up* time of the polarization of the ^3He atoms. The *spin up* time is defined as the amount of time the ^3He atoms require to reach the equilibrium polarization. A typical *spin up* time for a hybrid cell used in E06010 was ~ 4 hours as shown in Fig. 4.3.

4.3 The Target System

The target system for the transversity experiment was by far the most complicated system in the history of polarized ^3He experiments in Hall A. The system was mainly composed of three pairs of Helmholtz coils, two pairs of RF coils, the oven with three pairs of pick up coils, the ^3He cell, the target ladder with an empty target cell, reference target cell, and an optics target (7 carbon foils and 1 BeO foil) as well as two pairs of target chamber pick up coils. A heater system together with an air flow system acted as an integral part of the target system to maintain the desired temperature of 230°C inside the oven. Also there are two additional pairs of magnet coils to correct for any magnetic field gradient in the target

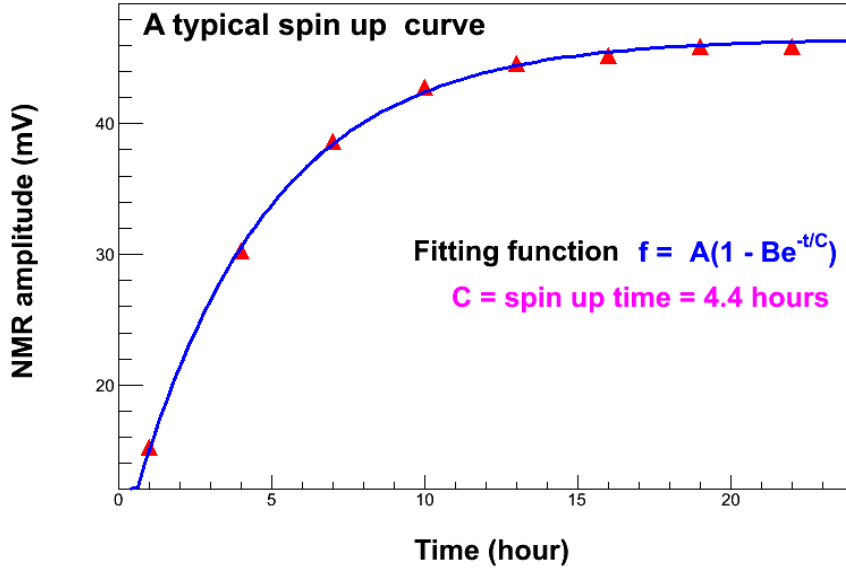


Figure 4.3: A typical spin up curve for one of the hybrid cells used in E06010. The fitting function is $A(1 - Be^{-t/C})$ where the fitting parameter A represents the expected maximum value of the NMR amplitude and C represents the spin up time. B is irrelevant to our measurement. In the plot, $A = 46.53 \pm 0.08 \text{ mV}$ and $C = 4.42 \pm 0.04 \text{ hours}$.

region. However, during the experiment those coils were not used as the field gradient was already very small.

4.3.1 The ^3He Cell

All the cells used in the experiment were hybrid cells. The cells were blown at Princeton by Mike Souza and filled at the University of Virginia and the College of William and Mary. Since E06010 required to have polarized ^3He in both vertical and transverse directions⁶, special consideration was taken to make the “seals”⁷ of these cells so that we could access both the pumping directions on the cell without hitting the “seals” by the powerful lasers. A name “90 degree pull off” was given to each of these cells in order to differentiate them from the other cells used for pumping in the longitudinal (along the direction of the in-

⁶Vertical and transverse directions are defined with respect to the horizontal plane which contains the incoming electron beam through the center of the hall, the center being the center of the target. This means when the direction is referred to as *vertical*, it represents that the ^3He spins are aligned vertically upwards or downwards with respect to the horizontal plane along the incoming beam. On the other hand, the direction *horizontal* refers to the ^3He spins aligned perpendicular to the incoming beam but in the hall plane.

⁷The special procedure of sealing the glass cell and detaching it from the rest of the glass blowing equipments results in a slightly deformed extension which looks like a little tail coming out of the spherical cell. This portion of the cell is sometimes termed as the “pull off” of the cell. The “pull off” is about 3 to 4 cm long.

Table 4.2: The respective numbers are from the University of Virginia and the College of William and Mary database. V_p is the volume of the pumping chamber, V_t is the volume of the target chamber, and V_{tt} is the volume of the transfer tube.

Name	Filled at	V_p	V_t	V_{tt} (cm^3)	Fill Density	Lifetime (hours)
Astral	UVA	164.92	79.47	6.77	8.08	40
Maureen	W/M	180.75	89.05	4.15	7.23	26
Brady	UVA	169.27	74.57	5.98	7.87	31

coming electron beam) direction. A schematic diagram of the cell dimensions as well as its orientation with respect to the Hall A coordinate system is shown in Fig. 4.4. The main characteristics of the cells used in this experiment are summarized in Table 4.2.

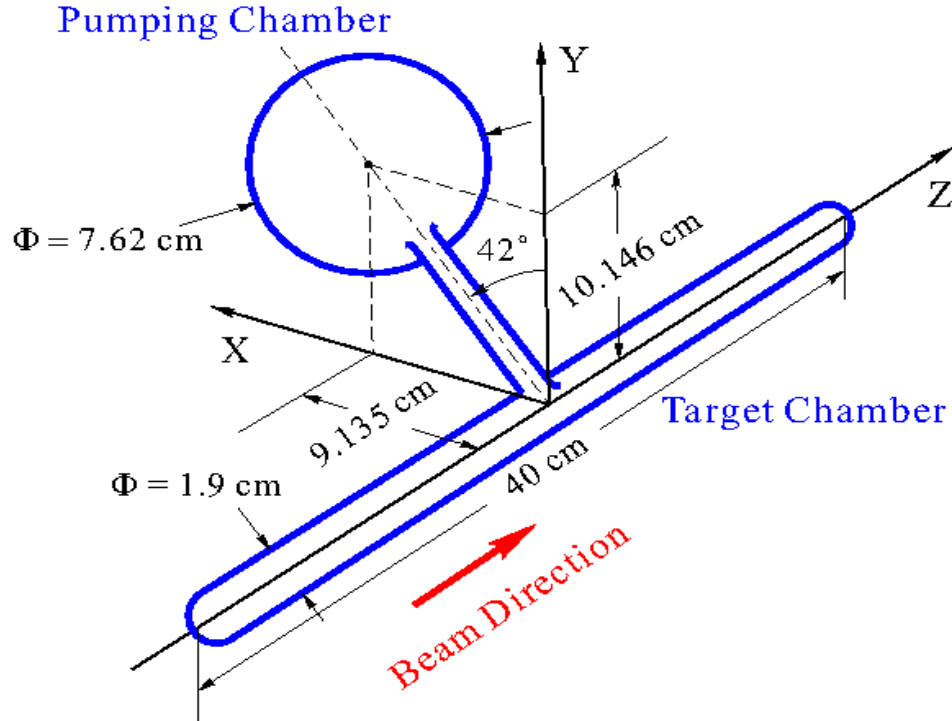


Figure 4.4: Orientation of the hybrid cell in the Hall A coordinate system. The pumping chamber and a part of the transfer tube are inside the oven which is not shown here.

Each of these cells had a pumping chamber of 3 inches in diameter and a target chamber of ~ 2 cm in diameter. The pumping chamber and the target chamber are connected through a 5 to 6 cm long transfer tube. Typically aluminosilicate glass (GE180) is used to make these cells. All the quantities in Table 4.2 were measured at the University of Virginia and

the College of William and Mary. In addition to those numbers, the material of the glass, the thickness of the cell windows and the cell walls, the length of the transfer tube and the ratio of the K to Rb atom densities are extremely important quantities for polarimetry as well as the radiative correction analysis.

4.3.2 Target Ladder

A target ladder is mounted on the oven which has five different target positions. The positions are shown in the Fig. 4.5 and described below:

- **Polarized ^3He target cell position**

This position was for the polarized ^3He cell which was used for the main production data in the experiment. The cell was glued to the bottom plate of the oven with RTV⁸. This could be replaced by a water cell at times. The water cell was used for the calibration of the polarization measurement in the ^3He cell discussed later in the polarimetry section.

- **A solid BeO target in line with seven Carbon foils**

This position was for the alignment of the beam on the target by tuning the beam positions and for optics calibration of the detectors. The beryllium oxide (BeO) foil was used to make the beam spot easily visible so that a correct beam position on the target could be achieved.

- **A “hole” target**

This was just the central carbon foil but extended in height with a hole in it. This was also used for finer alignment.

- **An empty target position**

This position was mostly used for beam tuning and also during the Møller measurement. It contained *no target* and thus this position allowed the incoming beam to pass without any obstacles in its path.

- **A reference cell position**

This position was for different calibration processes such as the elastic calibration, the

⁸RTV is a special kind of glue that can be used at high temperatures.

detector calibration, other background studies, etc. The reference cell was filled with either nitrogen, hydrogen or helium-3 in accordance with the purpose of the studies.

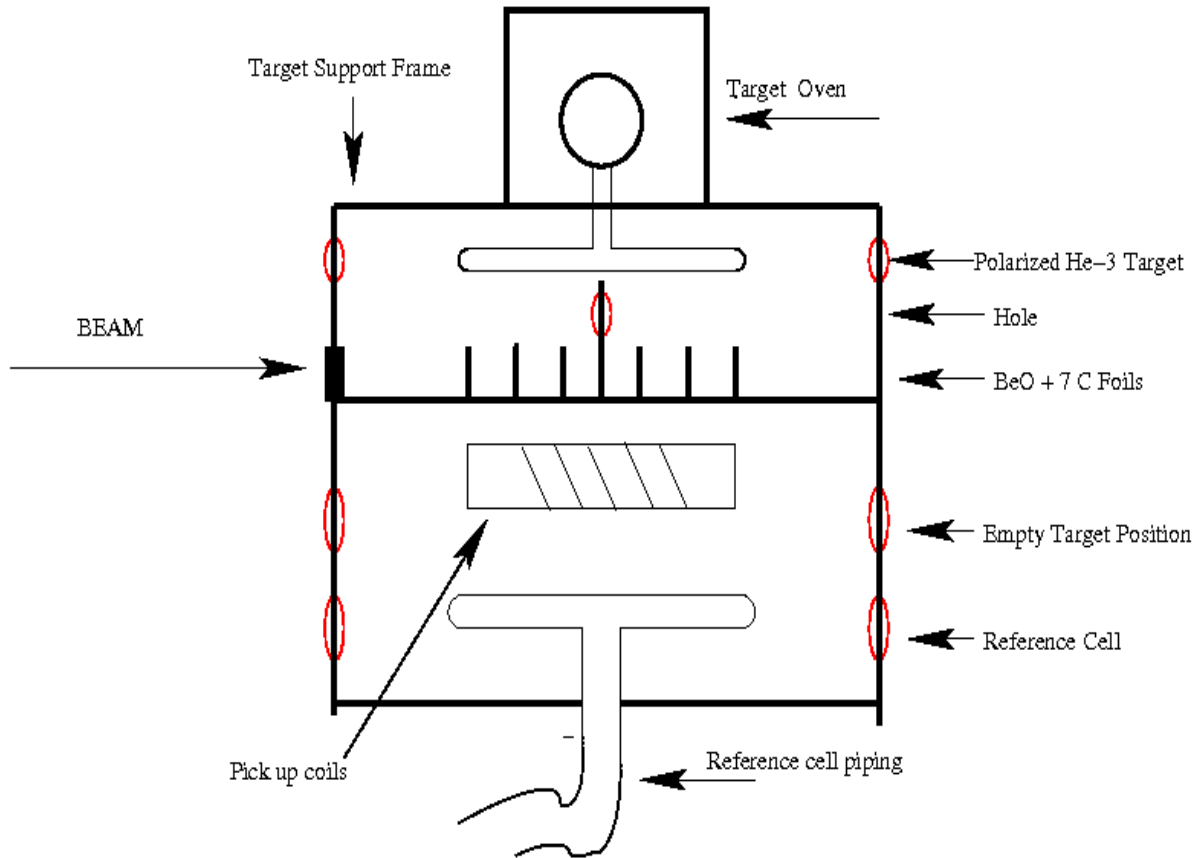


Figure 4.5: Schematic diagram of the target ladder system.

The target ladder could be moved vertically to different positions using a stepper-motor-driven motion control system. It had a limit switch at each position and the motion was controlled remotely via EPICS from the counting house. The pick up coil position shown in the schematic is the position between the two pairs of pick up coils. The target was lowered to this position to do the NMR measurements.

4.3.3 Oven, Heater, and Airflow System

The oven used in the experiment was made of a material called CS85. It had an inlet and an outlet for the circulation of compressed air. Since the pumping chamber was in the oven and it had to be kept at 230°C to evaporate potassium in the ^3He cell, the air blown into

the oven must be hot enough to maintain a stable temperature. In order to accomplish this, pressurized, dry, and filtered air provided by a compressor in Hall A was allowed to pass through two heaters. One heater was controlled by a variac in the hall and the other one was controlled by a PID feedback electronic control chassis. The hot air in the oven exited through an exhaust pipe. Both the inlet and the outlet piping were enclosed in a tube that supported the oven and was wrapped with insulation material. A Resistive Temperature Device (RTD) was attached inside the oven to read the inside temperature and a thermocouple was inserted inside the insulation material near the second heater to measure the temperature of the hot air going into the oven. Throughout the experiment, our oven temperature was kept stable at 230° with a PID system that was able to restrict any temperature fluctuations within 2°C .

4.3.4 Holding Field Set Up

Three pairs of Helmholtz coils were used in the experiment to produce the magnetic fields in three mutually orthogonal directions. Two pairs of horizontal Helmholtz coils were used to produce the desired magnetic field in the two horizontal directions, *viz*, the longitudinal field along the beam direction and the transverse field perpendicular to the beam direction but in the horizontal plane⁹. The third pair of Helmholtz coils was the largest one which encompassed the other two and was used to produce the vertical field. A schematic diagram of the Helmholtz coils system is shown in the Fig. 4.6. Table 4.3 shows the basic characteristics of the three pairs of Helmholtz coils.

Table 4.3: Dimensions of the Helmholtz coils used in the experiment to produce the magnetic field holding the spins of the ^3He spins.

Coil	Inner diameter (m)	Number of turns	Resistance (Ω)
Small	1.27	256	3
Large	1.45	272	3
Vertical	1.83	355	4.4

The horizontal pairs of coils were powered by two KEPCO BOP 36-12D power supplies

⁹Specifically as explained earlier, the *Transverse* refers to a direction which is either right or left to the incoming electron beam at an angle 90° but lies in the horizontal plane. *Longitudinal* refers to the direction in the horizontal plane along the incoming electron beam (i.e. the relative angle with respect to the beam is either 0° or 180°).

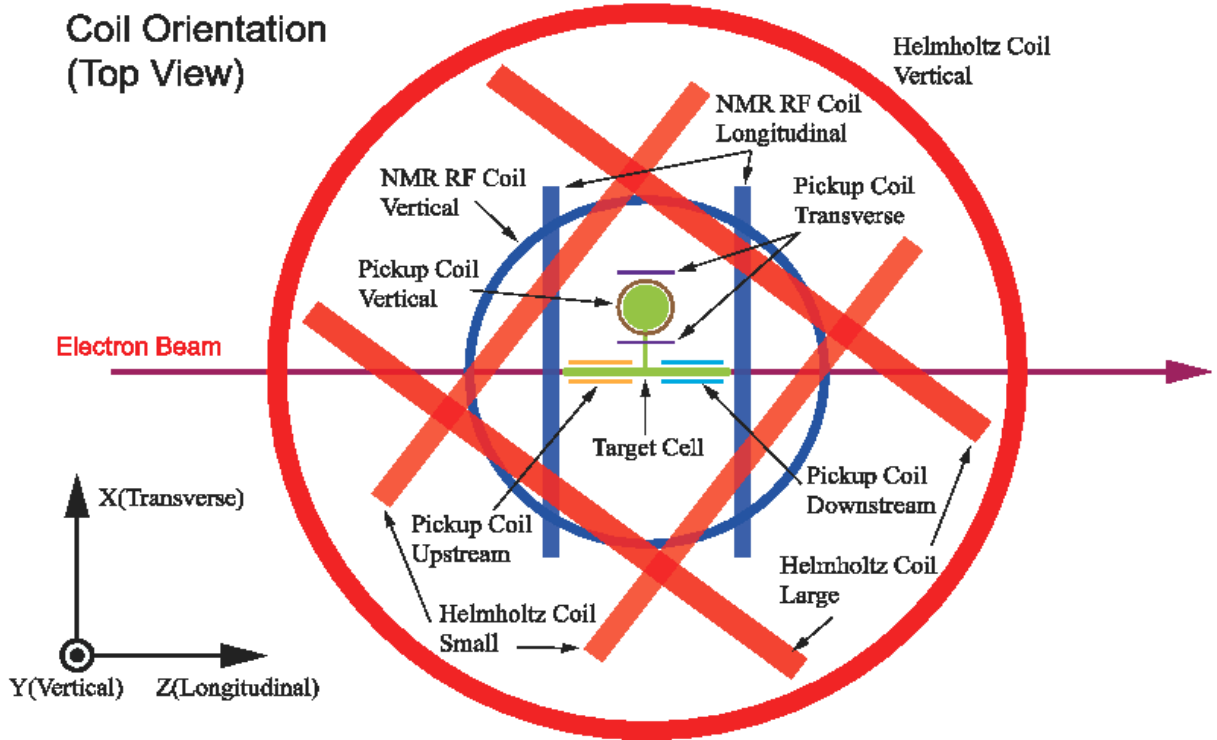


Figure 4.6: Schematic diagram of the Helmholtz coil system used in E06010 in Hall A. The RF coils and the pick up coils are also shown [9].

while an Agilent 6675A supply was used to power up the vertical pair. The current settings for these three pairs of coils throughout the experiment are shown in Table 4.4.

Table 4.4: Current settings for the three pairs of Helmholtz coils. \vec{B} stands for the holding magnetic field direction, I_S for the current in the small coils, I_L for the current in the large coils, and I_V for the current in the vertical coils. The small and the large coils are the two pairs used to produce the field in horizontal directions. The typical magnitude of the magnetic field generated in any of these two directions is 25 Gauss.

\vec{B}	I_S (A)	I_L (A)	I_V (A)
Transverse	6.234	-4.621	0.712
Vertical	0.329	-0.358	14.093

4.4 Laser and Polarizing Optics

4.4.1 Laser and Optical Fibers

In the past years, all the polarized ^3He experiments in Hall A used Fiber Array Package (FAP) systems to optically pump and polarize the ^3He atoms. For the first time in Hall A, the FAP systems were replaced by COMET lasers in this experiment. Three COMET lasers were used during the experiment. The difference between the COMET (sometimes referred to as Narrow Bandwidth) lasers and the FAP lasers is the narrow wavelength linewidth (~ 0.2 nm) of the COMET laser as compared to the 2 nm linewidth of a FAP system. As a result, there is a dramatic increase in the absorption of the laser light by the Rb atoms in the hybrid cells and a larger polarization of the ^3He atoms could be achieved in a shorter period of time. With these three COMET lasers, a maximum polarization of $\sim 72\%$ could be estimated during the production and because of this high maximum polarization, $\sim 62\%$ in beam polarization (with spin flips included) was achieved during the experiment. The currents and the corresponding powers of the COMET lasers used in the experiment are listed in the Table 4.5.

Table 4.5: The laser parameters used throughout the experiment. It is important to mention here that the diode temperatures were adjusted a few times during the experiment. They were more or less consistent with the numbers listed.

Lasers	Current (A)	Power (W)	Diode Temperature ($^{\circ}\text{C}$)
COMET1	35.0	25	26
COMET2	34.0	25	20
COMET3	35.9	25	25

The lasers were installed and interlocked in the laser building behind the counting house on the accelerator site at Jefferson Lab. The fiber coming out of each COMET control unit was connected to a 75 m long fiber that ran from the laser building to the hall. Then the 75 m long fiber was connected to a 5-to-1 combiner. A 5-to-1 combiner has five separate fibers as inputs and one output. During the entire period of production data taking, we used three lasers at a time for one particular pumping direction. Three 75 m fibers were connected to one 5 to 1 combiner. A typical power loss in such a 75 m long fiber was $\sim 6\%$.

4.4.2 Optics

The laser light coming out of the 5-to-1 combiner had to be aligned in order to focus the light on the ^3He cell in such a way that the diameter of the spot is approximately equal to the diameter of the cell. In other words, in order to make the polarization process efficient, it was essential to converge the laser light into the cell uniformly and *wasting* as little light as possible. This was achieved with our optics assembly where various optical components were placed and aligned accordingly. The unpolarized laser light was allowed to pass through the same optics components so that either a left or a right circularly polarized light could be available at the output of the optics assembly. The circularly polarized light, when focused to a spot of ~ 3 inches in diameter on the cell, was absorbed by the Rb atoms in the cell. A very good alignment of the optics was quite essential in order to achieve a very high polarization of the ^3He atoms.

Three optics lines were installed and aligned in the optics enclosure in the hall. The transverse and the vertical lines were used for the transversity experiment E06010 and the longitudinal line was used for other experiments. The setup of the optics components is shown in the Fig. 4.7.

A brief description of the optics components

Unpolarized laser light with a wavelength of 795 nm from the three outputs of the combiner was incident on the first lens L1. The focal length of L1 was 75 mm. L1 focused the three spots at its focal point. But after the focal point, the spots started to diverge again. Another lens, L2, of focal length 750 mm was placed in such a way that the spots incident on the lens were within the diameter but still reasonably separated and could be clearly visible. Then the beam splitter was used to separate S and P waves from the incident unpolarized light coming out of L2. The S wave was allowed to pass through the quarter wave plate Q1 and reflect back from mirror M1 and pass through Q1 again. Thus, after getting reflected from M1 and passing through Q1 twice, the S wave became a P wave and passed through the beam splitter again. On the other hand, the P wave now was incident on the mirror M2. Now both P waves passed through two quarter wave plates Q2 and Q3 so that the linearly polarized P waves became circularly polarized. The quarter wave plates were cali-

brated to proper angles so that the linearly polarized P waves, when passed through them, would become circularly polarized in the same direction (either left circularly polarized or right circularly polarized). The last two components in the path were the mirrors MB1 and MB2. Each of them had a diameter of 6 inches. The two circularly polarized waves now were incident on MB1 at an angle of 45° . The reflected waves were also incident on MB2 at an angle of 45° . The relative orientation of the big mirrors was important in order to preserve the polarizations of both waves. The final spot size of the laser light on the cell was mostly influenced by L1. A simulation was performed well ahead of the experiment to determine the distances between different optics components and the focal lengths of the lenses used.

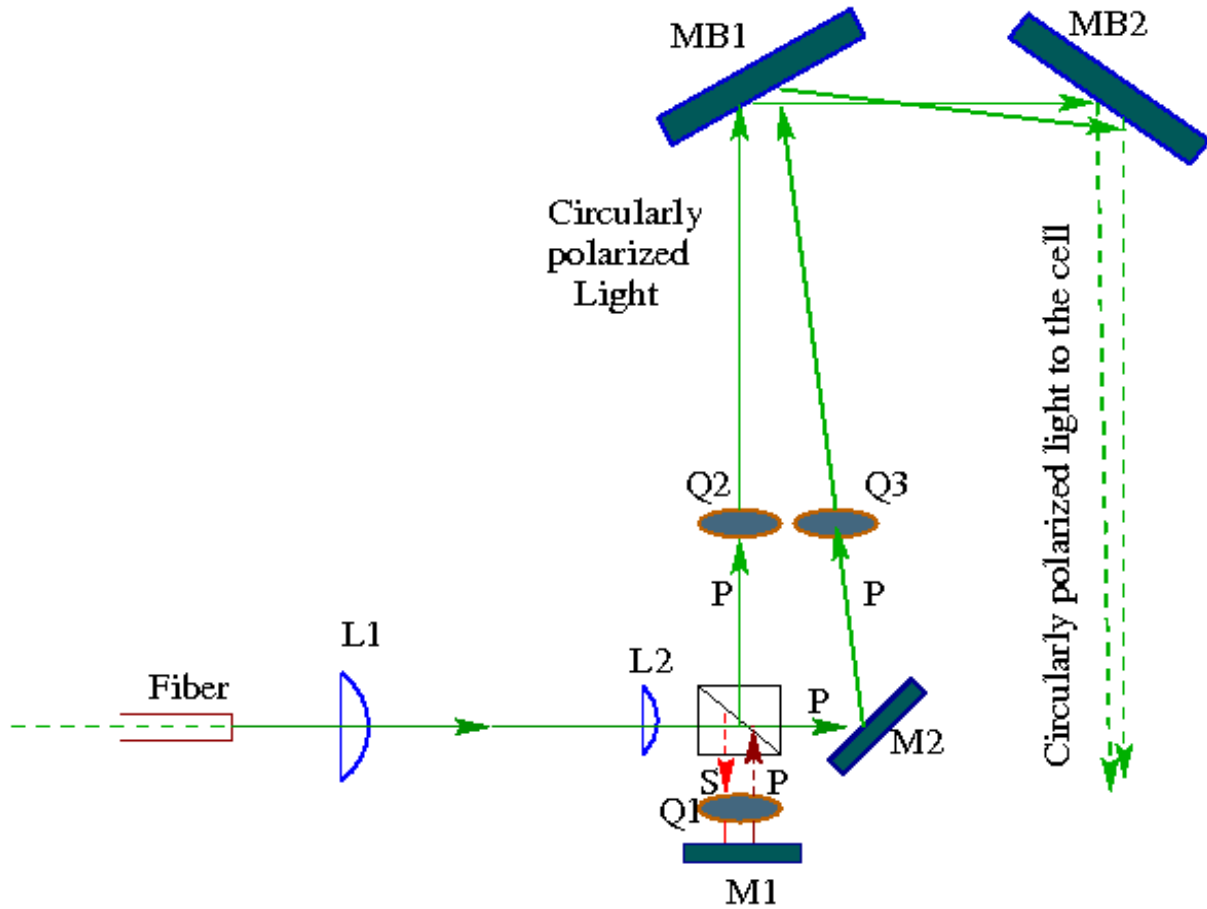


Figure 4.7: Schematic diagram of the optics setup. This setup was for the vertical pumping. For the transverse pumping, another mirror was attached to the oven not shown in the figure. The reflected light from the big mirror MB2, in this case, was incident on that mirror mounted on the oven. The rest of the setup was the same.

4.5 Polarimetry

Two polarimetry techniques were employed during E06010 to measure the polarization of the ^3He atoms. Nuclear Magnetic Resonance (NMR) was used frequently to measure and monitor the polarization of ^3He . Since during the experiment the spins of the ^3He nuclei were reversed every 20 minutes, an NMR measurement was performed during every flip. Therefore, the polarization was determined and recorded every 20 minutes. However, NMR is a relative measurement and hence an absolute method, Electron Paramagnetic Resonance (EPR), was used to calibrate the NMR measurements. In addition to the EPR measurements, two water NMR measurements were performed as well to cross check our polarimetry. The EPR measurements were performed on the pumping chamber and the water NMR was performed on the target chamber. Both these methods measure the absolute ^3He polarization and will be discussed in the following subsections.

4.5.1 Nuclear Magnetic Resonance (NMR)

Nuclear magnetic resonance (NMR) is a phenomenon that is observed when a nucleus of an atom with non zero spin is in a static magnetic field and is subjected to another oscillating magnetic field. It utilizes the principle of Adiabatic Fast Passage (AFP) which is described below.

Principle of NMR-AFP

Let us consider a free particle with spin \vec{I} and magnetic moment \vec{M} in a magnetic field \vec{H}_0 . According to classical theory of electromagnetism, the torque $\vec{\tau}$ experienced by the particle is given by

$$\vec{\tau} = \vec{M} \times \vec{H}_0. \quad (4.11)$$

We know that torque is the rate of change of angular momentum. Hence, one can write,

$$\vec{\tau} = \hbar \frac{d\vec{I}}{dt}. \quad (4.12)$$

The magnetic moment \vec{M} can be written in terms of spin as

$$\vec{M} = \gamma \hbar \vec{I}, \quad (4.13)$$

where γ is the gyro-magnetic ratio. Combining Eqs.(4.11), (4.12), and (4.13), we get:

$$\vec{M} \times \vec{H}_0 = \hbar \frac{d\vec{I}}{dt} \quad (4.14)$$

$$\implies \vec{M} \times \vec{H}_0 = \frac{1}{\gamma} \frac{d\vec{M}}{dt} \quad (4.15)$$

$$\implies \frac{d\vec{M}}{dt} = \gamma \vec{M} \times \vec{H}_0. \quad (4.16)$$

Now this equation is in the inertial or laboratory frame of reference. To simplify, let us consider a rotating frame of reference, S' , rotating with an angular velocity $\vec{\omega}$ with respect to the laboratory frame. Then the relation of the rate of change of the magnetic moment between these two frames can be written as:

$$\frac{d\vec{M}}{dt} = \frac{\partial \vec{M}}{\partial t} + \vec{\omega} \times \vec{M}, \quad (4.17)$$

where the term $\frac{d\vec{M}}{dt}$ represents the rate of change of \vec{M} in the laboratory frame and the term $\frac{\partial \vec{M}}{\partial t}$ represents the rate of change in the rotating frame. Now combining Eq.(4.16) and Eq.(4.17), we can write the motion of the magnetic moment in the rotating frame S' as:

$$\frac{\partial \vec{M}}{\partial t} = \gamma \vec{M} \times \vec{H}_0 - \vec{\omega} \times \vec{M} \quad (4.18)$$

$$\implies \frac{\partial \vec{M}}{\partial t} = \gamma \vec{M} \times \left(\vec{H}_0 + \frac{\vec{\omega}}{\gamma} \right). \quad (4.19)$$

Now if we compare Eq.(4.16) and Eq.(4.19), we see that in the rotating frame S' , the original holding field \vec{H}_0 is replaced by an effective field \vec{H}_e given by

$$\vec{H}_e = \vec{H}_0 + \frac{\vec{\omega}}{\gamma}. \quad (4.20)$$

Let us consider our system when we do an NMR measurement. There were two holding field configurations, *viz*, the vertical and the transverse directions. Here, only the vertical configuration is considered where the holding field \vec{H}_0 was along the x-axis¹⁰. Now if we choose a rotating frame with an angular velocity $\vec{\omega} = -\gamma \vec{H}_0$, the effective field \vec{H}_e vanishes and hence magnetic moment becomes a constant of motion. This frequency is called the *Larmour frequency*. In order to perform an AFP process during the measurement, an RF field was applied in the longitudinal \hat{k} direction (which was along the beam direction). If

¹⁰If we define a coordinate system (x,y,z) with the corresponding unit vectors (i, j, k), the incoming electron beam is along the z-axis while the x and y axes represent the vertical and transverse directions, respectively.

we denote the RF field by $\vec{H}_{rf} = H_{rf} \cos(\omega t) \hat{k}$, the effective field in the rotating frame can be written as,

$$\vec{H}_e = (H_0 + \frac{\omega}{\gamma}) \hat{i} + H_{rf} \hat{k}, \quad (4.21)$$

where ω is the precession frequency of the rotating frame. Note that ω is not necessarily equal to the *Larmour frequency*.

During the measurement, the RF was swept from 77 kHz to 85 kHz through the resonance at $\omega_0 = 81$ kHz and back. The sweep rate was 4 kHz/s to satisfy the AFP conditions. The Adiabatic Fast Passage conditions have two requirements. The change in the frequency and hence the passage of the spins through the resonance should be fast enough so that the spins do not have time to relax during the sweep (*fast condition*) and slow enough compared to ω_0 so that the spins can follow the sweep (*adiabatic condition*). The AFP condition for the frequency sweep NMR is derived in Ref. [10] and can be expressed as:

$$\frac{|\gamma H_{rf}|}{T_2} \ll |\dot{\omega}| \ll \gamma^2 H_{rf}^2. \quad (4.22)$$

where T_2 is the transverse ^3He spin relaxation time, $\gamma = 3.24$ kHz/G is the gyromagnetic ratio for ^3He and H_{rf} is the amplitude of the RF field. For field sweep NMR where the holding field is swept and the frequency is kept constant, the usual AFP condition requires a sweep rate of 1.2 G/s. In this case, the holding field is swept from 25 G to 32 G and then back with the resonance at 28 G which corresponds to a transition frequency of 91 kHz. During the experiment, field sweep NMR was done a few times as part of our calibration process. This allowed us to compare the pumping chamber polarization with the target chamber polarization.

Electronics and measurement procedure

Most of our NMR measurements were frequency sweep NMR measurements in the pumping chamber and were calibrated with EPR measurements. Since we flipped the spins of the target every 20 minutes by performing frequency sweep NMR, we actually monitored the polarization in the pumping chamber every 20 minutes throughout the experiment. The advantage was that no extra NMR measurements were needed to be performed frequently unlike the previous polarized ^3He experiments.

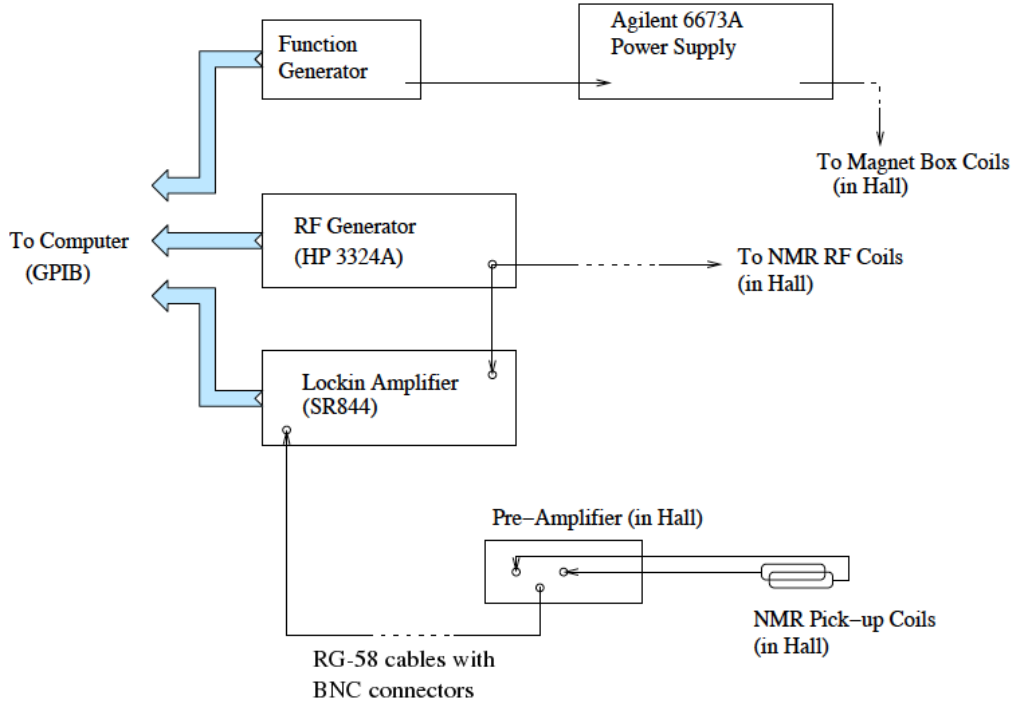


Figure 4.8: The electronic set up for the NMR measurements. The figure is reproduced from [10].

The electronics set up for the NMR measurements is shown in the Fig. 4.8. The power supplies for the holding field provided the necessary currents into the Helmholtz coils to maintain a constant field. While keeping the holding field constant at 25 G, an RF function generator, HP 3324A, swept the frequency from 77 kHz to 85 kHz at the rate of 4 kHz/s. During the sweep, the spins follow the frequency and move from being aligned to anti-aligned or vice versa with respect to the holding field. The spins, when passing through resonance, change the flux through a pair of pick up coils which were mounted on the oven (there were three pairs of pick up coils on the pumping chamber for three different configurations and two pairs of pick up coils fixed along the target chamber). This change in flux then induces an electromotive force and a signal is generated in the pick-up coils. Then the signals from both pick up coils were sent into low-noise pre-amplifier inputs (input A and input B) of an SR620 and the output (A-B) was then connected to the input of a lock-in amplifier (Model SR844). It was essential at the beginning of the experiment to adjust all the five pairs of pick-up coils in such a way that, when connected and the output (A-B) subtracted, the real signal was added and the noise got subtracted. The Helmholtz coils,

the RF coils, and the pick-up coils have to be orthogonal to each other in order to perform the NMR measurement and obtain a signal from the pick-up coils. Once the signal from the pick-up coils through the pre-amplifier was sent to the lock-in amplifier, and then the signal was read by a computer via a GPIB interface.

A typical frequency sweep NMR signal is shown in the Fig. 4.9. The height of the signal from the lock-in amplifier is proportional to the transverse component of the magnetization of ^3He and hence the polarization. The signal is fitted to the square root of a Lorentzian function :

$$S \propto \frac{\omega_1}{\sqrt{(\omega - \omega_0)^2 + \omega_1^2}}, \quad (4.23)$$

where ω_0 is the Larmour frequency, ω is the frequency of the RF field and ω_1 is related to the width of the peak and the magnitude of the RF field.

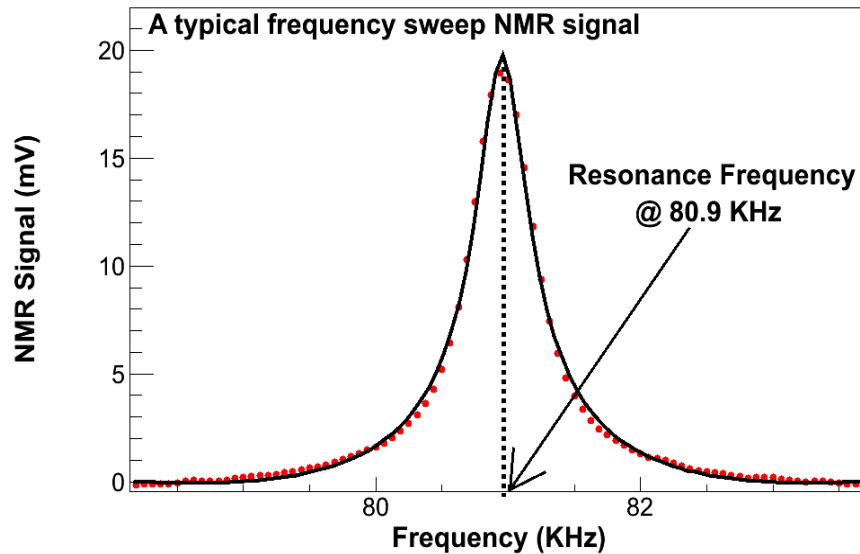


Figure 4.9: NMR frequency sweep signal fitted to the square root of a Lorentzian function.

4.5.2 Electron Paramagnetic Resonance (EPR)

Theory

Electron Paramagnetic Resonance (EPR) measures the splitting of different energy levels of an atom in the presence of an external magnetic field due to the Zeeman effect. Using

EPR on the alkali atoms which are present in the ^3He cell, the absolute polarization of ^3He can be extracted. The high pressure hybrid ^3He cell contains some amount of Rb and K. The ratio of Rb to K densities in the cells used in the experiment was 5:1. For an alkali atom, the eigenstates of the total angular momentum can be written as (defined earlier)

$$\vec{F} = \vec{I} + \vec{S}, \quad (4.24)$$

where \vec{I} is the nuclear spin and \vec{S} is the electron spin of the alkali atom. For ^{85}Rb , $I=5/2$ and $S=1/2$ and for ^{39}K , $I=3/2$ and $S=1/2$. In presence of the holding field \vec{B} , F splits into $(2F+1)$ sub-states. For ^{85}Rb , $F=2,3$ and for ^{39}K , $F=1,2$. In case of ^{85}Rb , the $F=3$ state splits into 7 sub-states while for ^{39}K , the $F=2$ state splits into 5 sub-states in the presence of \vec{B} . When we shine circularly polarized laser of 795 nm wavelength on the cell, the light gets absorbed by the Rb atoms in all the sub-states of the lower $S_{1/2}$ level and as a result, the atoms get excited to the higher $P_{1/2}$ level. For example, for right circularly polarized laser light, the atoms in the sub-state $m_F=-3$ of $S_{1/2}$ absorb the incident light and get excited to the sub-state $m_F=-2$ of $P_{1/2}$. This excitation process is restricted by the selection rule $\Delta m_F=+1$ for absorption. However, the selection rule for emission $\Delta m_F=+1, -1, 0$ allows the atoms in the $m_F=-2$ of $P_{1/2}$ to decay into $m_F=-3, -2, -1$ of $S_{1/2}$ as shown in Fig. 4.10. The probabilities of the decay process can be determined by the Clebsch-Gordon coefficients. Consequently, the number of atoms now present in the $m_F=-3$ sub-state of $S_{1/2}$ is less than the original number, before the absorption of light. Now this process takes place through all the m_F sub-states in the $S_{1/2}$ state and eventually, all the atoms are polarized in the $m_F=+3$ sub-state. Even though the atoms in the $m_F=+3$ sub-state of $P_{1/2}$ can decay into both $m_F=+2$ and $m_F=+3$ sub-states of $S_{1/2}$, the atoms which decay into $m_F=+2$ sub-state immediately absorb the laser light and get excited back to the $m_F=+3$ sub-state of the $P_{1/2}$ state due to the continuous pumping of laser in the cell. The Zeeman splitting between the $m_F=+3$ and $m_F=+2$ state of $S_{1/2}$ describes the corresponding EPR frequency for Rb. On the other hand, if the laser light is left circularly polarized, then the EPR frequency would correspond to the Zeeman splitting between the $m_F=-3$ and the $m_F=-2$ state of the $S_{1/2}$ state. Similarly for K, the splitting between $m_F=+2$ and $m_F=+1$ (for right circularly polarized light) and the splitting between $m_F=-2$ and $m_F=-1$ (for left circularly polarized light) describe the EPR frequency. This EPR frequency is not only affected by the applied external field \vec{B} , but also by the Rb- ^3He (K- ^3He in case of K) spin

exchange interaction as well as the small magnetic field generated by the polarization of ^3He .

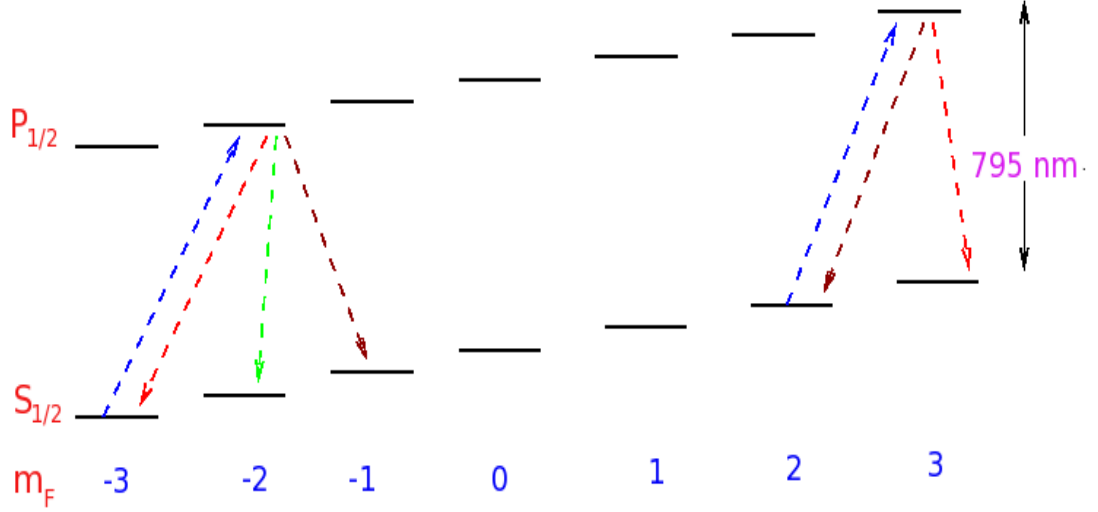


Figure 4.10: The splitting of the $S_{1/2}$ and $P_{1/2}$ states of Rb into sub-states in the presence of an external magnetic field. The absorption and the emission of the 795 nm laser light are also shown for a few selected transitions.

If we look at the Hamiltonian of the alkali atoms (Rb or K) in a magnetic \vec{B} , it consists of three parts given by Eq. (4.25).

$$\mathcal{H} = 2\pi\hbar A \vec{I} \cdot \vec{S} + \vec{S} \cdot \vec{B} + \vec{I} \cdot \vec{B}, \quad (4.25)$$

where the different terms are given as follows:

- $2\pi\hbar A \vec{I} \cdot \vec{S}$: Contribution due to the hyperfine interaction between the alkali nucleus and the electron.
- $\vec{S} \cdot \vec{B}$: Contribution due to the Zeeman splitting of the electron energy levels.
- $\vec{I} \cdot \vec{B}$: Contribution due to the Zeeman splitting of the nuclear energy levels.

Here A is the alkali hyperfine splitting frequency, \vec{B} is the total magnetic field, \vec{I} is the alkali nuclear spin and \vec{S} is the alkali electronic spin. The eigenvalues of this Hamiltonian are given by the Breit-Rabi formula [109]:

$$E_{F=I\pm 1/2, M} = \frac{-A(I+1/2)}{2(2I+1)} - g_I \mu_N B M \pm \frac{A(I+1/2)}{2} \left(1 + \frac{4M}{2I+1} x + x^2\right)^{1/2}, \quad (4.26)$$

where $x = \frac{\omega}{2\pi A(I+1/2)}$ and $\omega = \frac{2\mu B}{\hbar}$.

Now as the variation of the EPR frequency, ν_{EPR} , for the respective alkali atom with respect

to \vec{B} is small, the change $\Delta\nu_{EPR}$ can be approximated by the equation:

$$\Delta\nu_{EPR} = \frac{d\nu_{EPR}}{dB} \Delta B, \quad (4.27)$$

where $\frac{d\nu_{EPR}}{dB}$ can be calculated from Eq. (4.26). $\Delta\nu_{EPR}$ is in fact a combination of three terms which can be written as:

$$\Delta\nu_{EPR} = \Delta\nu_{SE} + \Delta\nu_{He} + \Delta\nu_B, \quad (4.28)$$

where $\Delta\nu_{SE}$ is the contribution from the alkali- ^3He spin exchange, $\Delta\nu_{He}$ is the contribution from the classical magnetic field created by the polarized ^3He atoms and $\Delta\nu_B$ is the contribution from the magnetic holding field. Since we flip the ^3He spins while doing the measurement, the contribution from the holding field cancels. This is because of the fact that when the ^3He spins are parallel to the holding field \vec{B} , a very small additional magnetic field, $\Delta\vec{B}$, arises from the ^3He spins which are aligned along \vec{B} . Thus the effective field in this case is $\vec{B} + \Delta\vec{B}$. When the ^3He spins are flipped by 180° , they are aligned anti-parallel to the field \vec{B} and in this case, the effective field becomes $\vec{B} - \Delta\vec{B}$. Hence, there remains no effect of the holding field once the difference between these two states is taken. One can now write Eq. (4.27) in terms of the respective magnetic field components as follows:

$$\Delta\nu_{EPR} = \frac{d\nu_{EPR}}{dB} [\Delta B_{SE} + \Delta B_{He}]. \quad (4.29)$$

The term ΔB_{SE} corresponds to the small effective magnetic field that comes from the very short but frequent spin exchange collisions between the alkali atoms and the ^3He atoms and it can be written as:

$$\Delta B_{SE} = (2K_{He}\hbar/T_{He}g_e\mu_B) \langle \vec{K} \rangle, \quad (4.30)$$

where K_{He} is the frequency shift parameter, $1/T_{He}$ is the alkali- ^3He spin exchange rate per alkali atom, $g_e=2.000232$, $\mu_B=5.7884 \times 10^{-11}\text{MeV/T}$ and $\langle \vec{K} \rangle$ is the average ^3He nuclear spin.

The term ΔB_{He} corresponds to the classical magnetic field produced by the bulk magnetization of the polarized ^3He gas. The size of the classical magnetic field is dependent on the geometry of the target cell. It can be expressed as:

$$\Delta B_{He} = \frac{C\eta_{He}\mu_{He} \langle \vec{K} \rangle}{K}, \quad (4.31)$$

where C is the dimensionless factor that depends on the geometry of the cell, η_{He} is the density of ^3He , $\mu_{He}=6.706984 \times 10^{-14}\text{MeV/T}$, and $\langle \vec{K} \rangle = P_{He}$ is the polarization of ^3He in the cell. Combining Eqs. (4.29), (4.30), and (4.31), one can write:

$$\Delta\nu_{EPR} = \frac{8\pi}{3} \frac{d\nu_{EPR}}{dB} \kappa_0 \mu_{He} \eta_{He} P_{He}, \quad (4.32)$$

where $\kappa_o \equiv \kappa_0(T) = \kappa_{00}(T_{ref}) + \kappa_{0T}(T - T_{ref})$ is a dimensionless constant that parametrizes the spin-exchange “effective” field. This is the biggest source of systematic error in the polarization measurement. There have been a few measurements dedicated to determine κ_0 at different temperatures. These measurements are reported in Refs. [110], [111], [112]. Each of these measurements was primarily dominated by the systematic effects due to the uncertainties in temperature, density of the alkali atoms and the polarization measurements of ^3He atoms. However, the highest temperature at which one of these measurements was performed was $\sim 172^\circ\text{C}$ [112]. In order to determine the value of κ_0 at our working temperature, we had to rely on a linear extrapolation of the measured values at a lower temperature ($T_{ref} = 100^\circ\text{C}$). Hence, the extrapolation to a temperature of $\sim 250^\circ\text{C}$ results in larger uncertainties in the determination of κ_0 .

Electronics and measurement procedure

Basically the EPR system consists of the following components:

In the Hall:

- The EPR RF coil mounted on the oven.
- The EPR lens and fiber assembly mounted on the oven.
- The Photodiode and the Rb D2 filter assembly.
- The EPR RF amplifier.

In the Counting House:

- The EPR RF function generator HP/Agilent E4400B.
- The EPR frequency counter SR 620.
- The Lock-in amplifier EGG 745.
- The PI feedback box constructed by the University of Kentucky.
- The function generator DS345.

The setup is shown in the Fig. 4.11.

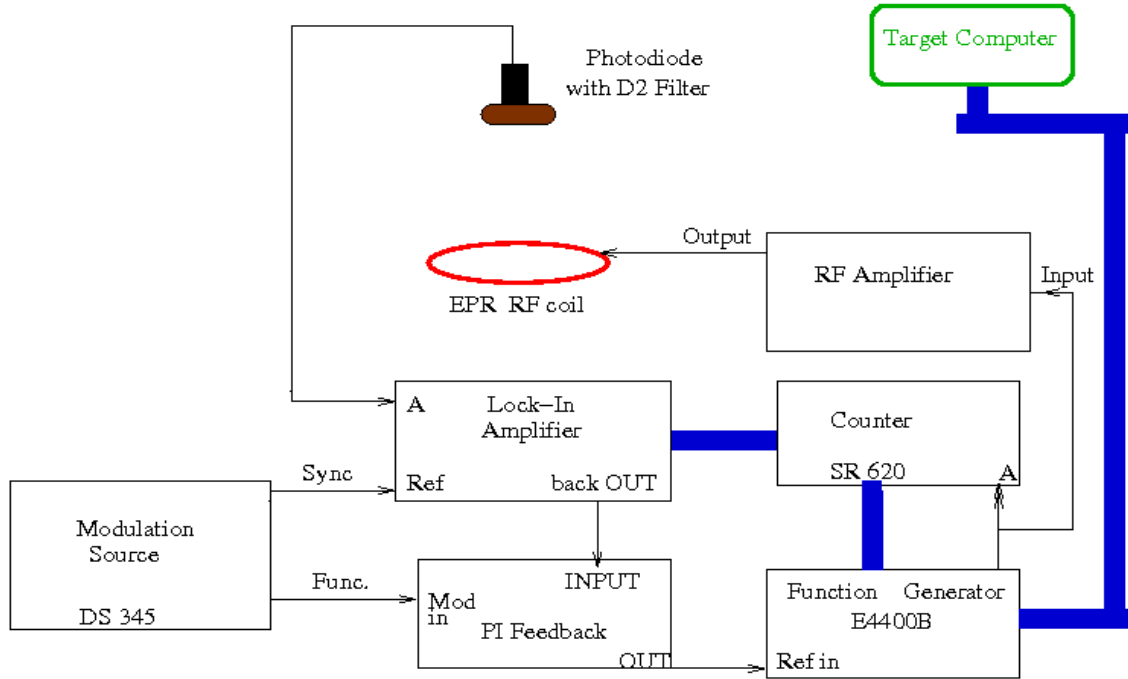


Figure 4.11: Schematic diagram of the EPR setup in the experiment. The blue connections correspond to the GPIB controls and the arrows represent the connections with the BNC cables.

The EPR transition is excited by a frequency modulated RF signal which is sent from the function generator into a small coil located inside the oven and near the top of the pumping cell. The frequency of the signal corresponds to the energy difference between the two sub-states $m_F = -2$ and $m_F = -1$ or $m_F = +2$ and $m_F = +1$ of the $F=2$ states of K as mentioned earlier. For $\Delta m_F = -2 \rightarrow -1$, the resonance frequency is ~ 19 MHz and for $\Delta m_F = +2 \rightarrow +1$, the frequency is 16 MHz in a holding field of 25 G. Note that this happens in ground state of the K-atom. Now as described earlier in the theory section, the Rb atoms continuously absorb circularly polarized laser light and get excited from the $S_{1/2}$ state to the $P_{1/2}$ state. Finally all the polarized Rb atoms accumulate in the $m_F = -3$ or $m_F = +3$ sub-state of the $S_{1/2}$ state. When we perform EPR measurement on Rb, i.e., if the RF signal matches the frequency difference between the two m_F sub-states of Rb atom, the polarized Rb atoms in $m_F = +3(-2)$ are de-excited to $m_F = +2(-3)$. Then these atoms again absorb laser light and get excited to the $P_{1/2}$ state. Performing EPR on K causes some depolarization of the K atoms by the RF probe. However, the atoms re-polarized very quickly by K-Rb spin exchange, thus depolarizing Rb.

During the depolarization of Rb and then re-absorption of the laser light, there is an increase in the photons emitted from the $P_{1/2}$ to $S_{1/2}$ (D1) transition (795 nm). But due to the thermal mixing between the $P_{1/2}$ and $P_{3/2}$ energy states and sometimes collisional mixing with the N_2 atoms present in the cell, the atoms in the $P_{1/2}$ state can mix with the $P_{3/2}$ state. Then those atoms decay from $P_{3/2}$ state to $S_{1/2}$ state which corresponds to the D2 transition (780 nm). The amount of D1 and D2 fluorescence is essentially the same. But the D1 light is suppressed by the large background of the laser light and hence we detect the emitted D2 light with a photodiode. In order to filter the D2 light from the D1, two D2 filters were attached to the face of the photodiode. Further, the light was focused by a lens system mounted on the oven and guided by a 10 m long fiber. The other end of the fiber was attached to the filter and photodiode assembly. Hence the signal detected in the photodiode after mainly consisted of D2 light, but there are still some amount of D1 light that got detected.

This D2 signal consists of a DC component and an AC component. The DC part is present because of the fact that some amount of D2 light also reaches the photodiode which comes from the parts of the cell that are minimally effected by the EPR RF excitation coil. The EPR de-excitation is very small in this case and hence, the alkali polarization is not changing drastically. The AC component, on the other hand, is at the modulation frequency of the RF coil and is detected in the lock-in amplifier. When this component is plotted against the central frequency of the EPR excitation, the lineshape looks like the derivative of a Lorentzian function as shown in Fig. 4.12.

To get a good or optimal EPR frequency lineshape signal, various parameters in the lock-in amplifier, the modulator, and the function generator had to be adjusted. The most commonly used parameters throughout the measurements are listed below.

The Lock-in Amplifier

- Time constant: 1 ms
- Sensitivity: 500 μV
- AC gain: Highest possible value without overloading the amplifier.
- Input limit and DR are associated with AC gain

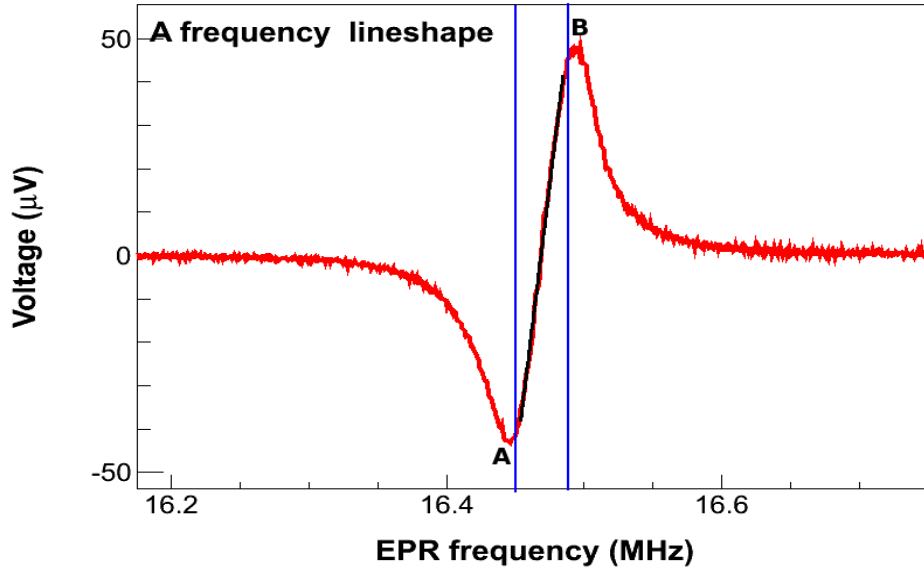


Figure 4.12: A typical EPR frequency lineshape spectrum recorded in the lock-in amplifier. The blue lines show the region where the frequency needs to be locked with the feedback mechanism discussed in the text. The region between point A and point B is fitted with a first order polynomial in order to determine the slope. The range of the fit is ~ 50 kHz.

RF Function Generator HP E4400B :

- Amplitude: -10 dB to 2 dB depending on the signal
- FM deviation: 50 kHz to 100 kHz depending on the strength of the signal and the range of frequencies we would like to have when the ^3He spins are flipped

Modulation source DS345 :

- Frequency: 200 kHz
- Amplitude: $1.5 V_{PP}$
- Function: sine wave
- Sweep/Modulation: LIN SWP

Once a good FM lineshape is obtained, the Proportional Integral (PI) feedback circuit comes into play which is the most important part in the EPR measurement. The PI feedback parameters which lock the EPR transition are entirely dependent on the lineshape.

The slope of the frequency sweep lineshape (shown in Fig. 4.12) is called the “feedback slope” and determines the gain of the PI feedback box and is in the units of $\frac{\mu V}{kHz}$. This relates the EPR resonance frequency to the drive voltage of the sensing electronics and thus the analog signal from the lock-in amplifier is converted into a frequency correction that is applied to the central frequency of the RF generator. The feedback process will be described in the next subsection.

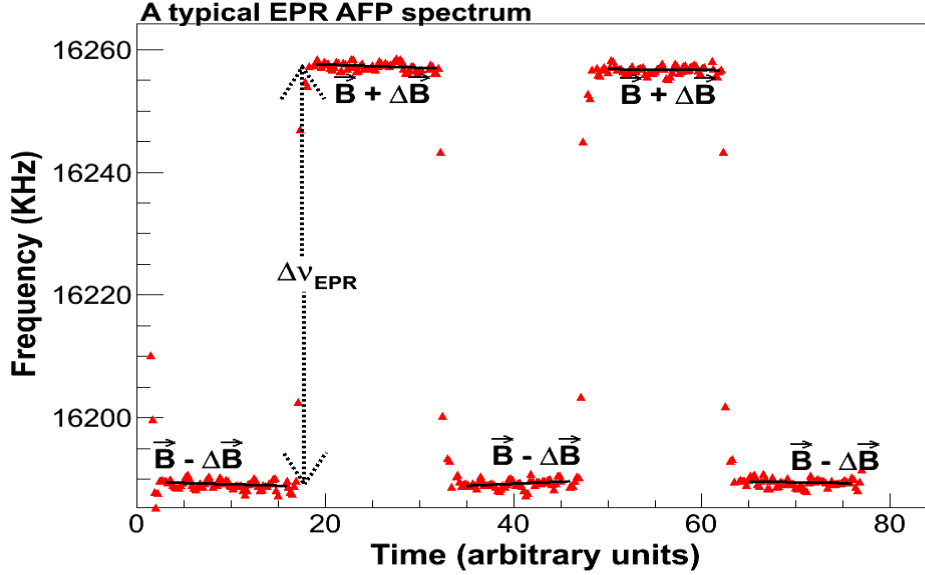


Figure 4.13: A typical EPR AFP spectrum. $\vec{B} + \Delta\vec{B}$ ($\vec{B} - \Delta\vec{B}$) corresponds to the state when the magnetic field generated by ^3He is parallel (anti-parallel) to the holding field.

Once the EPR frequency signal is locked with the proper PI gains, the frequency reading in a counter is recorded as a function of time. The ^3He spins are then flipped twice with respect to the main holding field using the NMR frequency sweep AFP technique. This is called EPR AFP. The difference in the two frequencies corresponding to the two opposite ^3He spin states is proportional to the “effective field” to first order. As explained earlier, this “effective field” is partially generated by the polarization of the ^3He atoms. One can measure very precisely the absolute polarization of the ^3He gas by just measuring the difference in the EPR frequencies. A typical EPR AFP spectrum is shown in the Fig. 4.13. The difference between the frequencies in the two states ($\vec{B} + \Delta\vec{B}$ and $\vec{B} - \Delta\vec{B}$), denoted by $\Delta\nu_{EPR}$, is proportional to the ^3He polarization. Note that when the field generated by the ^3He , i.e. $\Delta\vec{B}$ is parallel to the holding field \vec{B} , the ^3He spins are actually anti-parallel

to \vec{B} because the magnetic moment of ^3He is negative and hence, its polarization has an opposite sign.

The Proportional-Integral (PI) feedback circuit

The PI feedback circuit is in fact the heart of the EPR measurement. It is the gain of this circuit that determines how well we can lock the EPR frequency and hence, the calibration of the PI box was an integral part of the process. A PI box constructed by the University of Kentucky was used in this experiment. It was built by the electronics group in the Department of Physics and Astronomy at the University of Kentucky. The circuit diagram of the box is shown in Fig. 4.14.

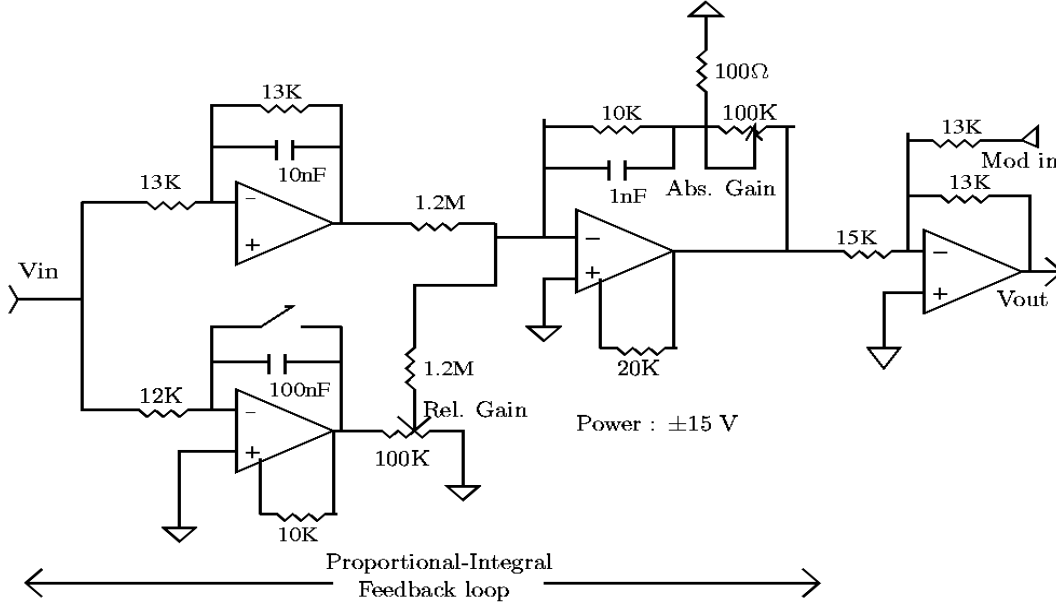


Figure 4.14: EPR PI feedback circuit used in the experiment.

The master EPR feedback equation can be written as [113]:

$$\frac{\Delta V_{FM}}{\Delta \nu_{FM}} \times \frac{10V}{\text{Lock-in Sensitivity}} \times G_P \times 2 \times G_{HP} \times \frac{\nu_{dev}}{1V_{PP}} \leq 1 \quad (4.33)$$

where the different parameters are defined as follows:

- $\frac{\Delta V_{FM}}{\Delta \nu_{FM}}$ is the slope of the differentiated “FM sweep” lineshape explained earlier.
- G_P is the absolute gain of the PI circuit.
- G_{HP} is the gain of the RF function generator. Basically, it is a response of the generator

in terms of the conversion between the frequency and the output voltage which can be measured easily.

- ν_{dev} is the FM deviation of the function generator. Usually it is specified as per 1 V peak to peak voltage, therefore $1 V_{PP}$ is explicitly put in the equation.

Usually the total gain of such a circuit is between 0 and 1. The slope $\frac{\Delta\nu_{FM}}{\Delta V_{FM}}$ depends on G_{HP} and ν_{dev} . Hence, when we actually measure the slope of the lineshape, these two factors are actually accounted for already. Also in practice, we require the total gain of the PI circuit to be -0.5 . The negative sign is because of the nature of the feedback circuit. Now the master equation can be written as:

$$m_{FM} \times \frac{10V}{Lock - in Sensitivity} \times G_P = -0.5 \quad (4.34)$$

where m_{FM} is the slope of the fit to the region in the lineshape spectrum shown in Fig. 4.12.

The calibration of the PI box involved determining the absolute gain of the circuit by putting a constant voltage from the function generator as an input and measuring the corresponding output voltage. The box has two regulators in the front panel. One regulates the absolute gain and the other controls the integration gain. We measured the gain of the circuit for a constant input voltage as function of the regulator positions which actually have numbers from 1 to 10. Then the data were fitted to a first order polynomial so that we could write

$$G_P = m \cdot n + C, \quad (4.35)$$

where m is the slope of the fit, C is the offset parameter and n is the regulator position.

Using Eq.(4.34) in Eq.(4.35),

$$m_{FM} \times \frac{10V}{Lock - in Sensitivity} \times (m \cdot n + C) = -0.5 \quad (4.36)$$

The FM lineshape slope determines m_{FM} . Then Eq.(4.36) yields the feedback gain and hence the corresponding regulator position for the absolute gain in the PI box can be determined. Thus, setting the proper absolute gain of the feedback circuit, the EPR frequency can be locked. Our calibration of the PI box was good enough so that almost all the EPR measurements performed during the experiment were quite stable with the absolute gain

determined by Eq.(4.36). However, it was not possible to calibrate the PI box for the integration gain. But most of time, it turned out that the integration regulator positions 1 and 1.5 were reasonable positions to set the desired integration gain for the circuit.

4.6 Polarimetry Analysis and Results

During the experiment, approximately ten EPR measurements were performed for each of the ^3He cells (Astral, Maureen, and Brady). We calibrated each EPR AFP flip with the corresponding NMR sweep during the measurement and used that calibration constant for our regular polarization measurement via frequency sweep NMR every 20 minutes. The calibration constant is the ratio of the polarization number from the EPR frequency shift to the corresponding NMR signal height and is usually expressed in $\%/mV$. The calibration procedure will be discussed later.

4.6.1 EPR Analysis

The extraction of the absolute polarization of the ^3He atoms from an EPR measurement can be performed in two ways. The *direct method* evaluates directly the absolute holding field at each frequency state and uses the magnetization of the ^3He spins to extract the polarization. The *derivative method*, on the other hand, uses the frequency difference between the two states (original and flipped) of the ^3He spins and the derivative of the frequency with respect to the holding field to calculate the polarization. Both methods were used for the analysis to cross check the polarization number and they were quite consistent. The methods are discussed in more detail below.

The direct method extraction

The Breit-Rabi formula yields the energies of different states in an alkali atom. The situation becomes simpler when we deal with the transitions involving the *edge states*¹¹. Since we performed EPR on potassium only, the transitions between the *edge states* correspond to either $m_F=1\rightarrow 2$ or $m_F=-1\rightarrow -2$. These are termed *end transitions*. In this case, the

¹¹The two m_F sub-states having the highest or lowest energies of any S or P state in an atom are called the *edge states*.

frequency of an *end transition* has the following simpler form [113]:

$$\nu_{\pm} = \left(\frac{g_S \mu_B}{-2} - \frac{1}{2} g_I \mu_N \right) \frac{B}{h} \pm \frac{\nu_{hfs}}{2} \left[1 - \sqrt{1 \pm 2 \left(\frac{2I-1}{[I]} \right) x + x^2} \right], \quad (4.37)$$

where the parameters are as follows¹²:

- frequency ν_{\pm} where \pm refers to the *edge state* $m_F = \pm(I + \frac{1}{2})$ in the *end transition*
- electron g-factor $g_S = -2.002319304372$
- g-factor $g_I = +0.26097$
- Bohr magneton $\mu_B = 9.27400095 \times 10^{-24} \text{JT}^{-1}$
- magnetic moment $\mu_N = +0.39146$
- ground state hyperfine splitting frequency $\nu_{hfs} = 461.719 \text{ MHz}$
- holding field: B
- $x = (g_I \mu_N - g_S \mu_B) \frac{B}{h \nu_{hfs}}$

Because of the slightly simpler form of Eq.(4.37) and due to the fact that it has only one square root term, one can invert the equation to get the field as a function of frequency.

The field corresponding to a particular frequency is therefore:

$$B(\nu) = (-b - s\sqrt{b^2 - 4c})/2, \quad (4.38)$$

where s is called the “shift” parameter which determines the sign of $B(\nu)$. It has a value equal to $+1$ if the EPR AFP spectrum has a “HAT” shape and -1 if the spectrum has a “WELL” structure. The details of about the “shift” parameter s can be found in [113]. The spectrum shown in Fig. 4.13 is an EPR AFP spectrum which has a “HAT” shape. b and c are called Breit-Rabi b -coefficient and c -coefficient, respectively, and they are defined as follows:

$$b = - \frac{\left[g_S \mu_B \left(\frac{h\nu_{hfs}}{2I+1} - sh\nu \right) - g_I \mu_N \left(\frac{2Ih\nu_{hfs}}{2I+1} - sh\nu \right) \right]}{sg_S g_I \mu_B \mu_N}, \quad (4.39)$$

$$c = [sh\nu(h\nu_{hfs} - sh\nu)]/g_S g_I \mu_B \mu_I. \quad (4.40)$$

In the analysis, we fit a straight line to each of the spin states and extrapolate the fit to a frequency where the transition or the flip occurs. Usually the spectrum looks very stable and one could fit a constant assuming that the deviation of the frequency from the mean value is small as a function of time. If we denote the transition point frequencies in each ³He

¹²In ν_{hfs}, hfs corresponds to the *Hyperfine Splitting*.

spin state as ν_1 and ν_2 for the first AFP in the spectrum, we can calculate the corresponding magnetic fields B_1 and B_2 from Eq. (4.38). Now the difference $\Delta B=B_1-B_2$ can be related to the magnetization of ^3He as:

$$M_{He} = \frac{\Delta B}{(2/3)\mu_0\kappa_0}, \quad (4.41)$$

where $\mu_0 = 4\pi \times 10^{-7} \text{ N/A}^2$ is the permeability of free space and $\kappa_0=4.269+0.00864\times\text{T}$ as explained earlier. Finally taking into consideration the absolute density of the ^3He atoms in the cell, the absolute polarization can be extracted by simply using the following equation :

$$P = \frac{M_{He}}{\rho\mu_{He}}, \quad (4.42)$$

where P is the polarization, ρ is the density, and $\mu_{He}= 1.07\times 10^{-26} \text{ J/T}$.

The derivative method extraction

This method utilizes the low field frequency derivative with respect to field expansion, i.e. $\frac{d\nu}{dB}$ to extract the polarization P according to the equation:

$$P = \frac{\Delta\nu}{\frac{d\nu}{dB} \frac{8\pi}{3} \kappa_0 \mu_{He} \rho}, \quad (4.43)$$

where $\Delta\nu = \nu_1 - \nu_2$ and the rest of the parameters were explained before. The derivative of the frequency with respect to the field is:

$$\frac{d\nu}{dB} = \mp \frac{g_I\mu_N}{h} + \frac{g_I\mu_N - g_S\mu_B}{2h[I]} \left[\frac{2m_F + [I]x}{\sqrt{1 + \frac{4m_F}{[I]}x + x^2}} - \frac{2m_F - 2 + [I]x}{\sqrt{1 + \frac{4(m_F-1)}{[I]}x + x^2}} \right] \quad (4.44)$$

The derivative can be expanded in terms of x (defined earlier) at low field and to fifth order in the field, it can be expressed as :

$$\frac{d\nu_{\pm}}{dB} = \frac{(g_I\mu_N - g_S\mu_B)}{h[I]} \sum_{n=0}^5 b_n \frac{x^n}{[I]^n}, \quad (4.45)$$

where $[I]=2I+1$ and b are the coefficients of expansion which are functions of $[I]$ and m_F . The detailed calculation can be found in [114]. Here the first six coefficients are listed for the end transitions that we used in our analysis.

$$b_0 = 1 \pm \mathcal{O}(10^{-3}), \quad (4.46)$$

$$b_1 = \mp 4I, \quad (4.47)$$

$$b_2 = 6I(2I - 1), \quad (4.48)$$

$$b_3 = \mp 8I(4I^2 - 6I + 1), \quad (4.49)$$

$$b_4 = 10I(2I - 1)(4I^2 - 10I + 1), \quad (4.50)$$

$$b_5 = \mp 12I(16I^4 - 80I^3 + 80I^2 - 20I + 1), \quad (4.51)$$

where \pm refers to the *edge state* $m_F = \pm(I + 1/2)$ involved in the transition.

As mentioned earlier, approximately 10 EPR measurements were performed for each of the three cells during the entire period of production data taking. Each of them was analyzed using both procedures mentioned above and they were very consistent with each other. Fig. 4.15 shows the polarization results for all the measurements with transverse and vertical directions of optical pumping. The measurements with larger statistical error bars involved larger statistical fluctuations in the alkali Zeeman splitting frequency which correspond to a weaker PI lock of the frequency. Most of the measurements were within a statistical uncertainty of 2%.

Calibration of the NMR signal with EPR

Each frequency sweep NMR signal in the pumping chamber was calibrated with EPR. Since the spins of the ^3He nuclei were flipped every 20 minutes, a corresponding NMR signal was obtained every 20 minutes and, using the EPR calibration, a polarization number could be obtained every 20 minutes. Fig. 4.16 shows the relation between an NMR and an EPR AFP spectrum used to determine the calibration constants.

As can be seen from Fig. 4.16, when the spins of the ^3He atoms are flipped, say, from state A to state B, an NMR signal of amplitude S_1 is obtained. From the frequency shift $\Delta\nu_1$ between the states A and B, an absolute ^3He polarization number P_1 is determined by using Eq.(4.43) after fitting the data points in each state with a first order polynomial. Then a calibration constant is evaluated by taking the ratio of the polarization number to the NMR signal height as follows:

$$C_1 = \frac{P_1}{S_1} \quad (4.52)$$

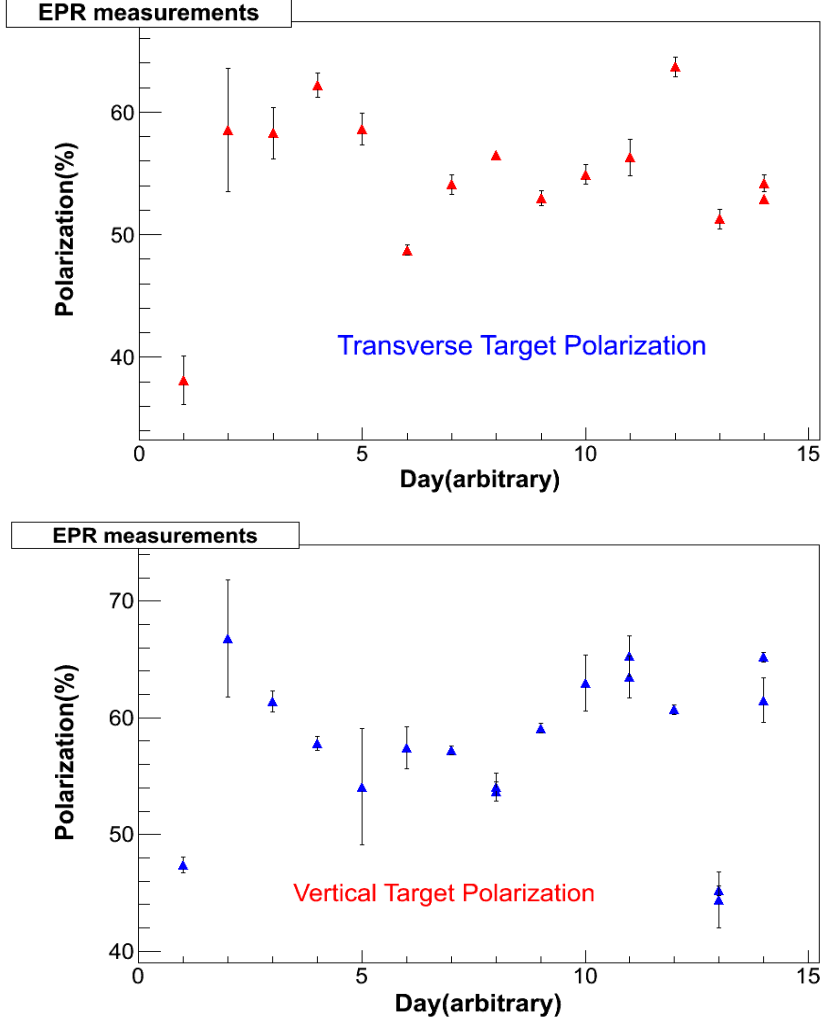


Figure 4.15: The polarization results from the all the EPR measurements for all the cells in the transverse (top) and the vertical (bottom) target polarization configuration. The polarization numbers are determined using the direct extraction method.

Similarly, when the ^3He spins are flipped back from state B to state A, another calibration constant is evaluated :

$$C_2 = \frac{P_2}{S_2} \quad (4.53)$$

Thus, the final calibration constant is the average of C_1 and C_2 . In general, if there are n number of flips involved in the EPR measurement, the calibration constant can be written as :

$$C = \frac{1}{n} \sum_{i=1}^n C_i \quad (4.54)$$

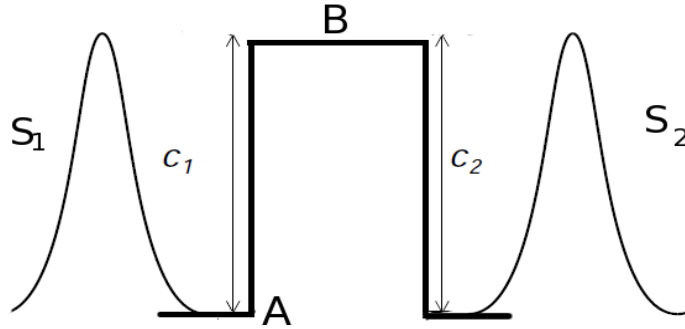


Figure 4.16: The EPR AFP spectrum and the corresponding NMR signals for each ^3He spin flip during AFP.

In practice, we used two sets of calibration constants corresponding to *sweep up* and *sweep down* signals. For instance in Fig. 4.16, the transition of state A to state B occurs through the NMR process when the ^3He spins are flipped by sweeping the RF frequency from 77 kHz to 85 kHz (*sweep up*). This results in the calibration constant C_1 . Then, the calibration constant C_2 corresponds to the NMR process when the ^3He spins are flipped back by sweeping the RF frequency from 85 kHz to 77 kHz (*sweep down*) and hence to the transition of state B to state A. In practice, C_1 and C_2 are slightly different. The calibration constants are shown in Fig. 4.17. All the internal temperature corrections, density corrections etc. are included in the analysis.

4.6.2 Water NMR Calibration

An NMR signal from a water sample can be used to calibrate the ^3He signal in the target chamber. A target cell was filled with water (natural water) to perform the NMR calibration. The ^3He cell was replaced by the water cell in the oven and during the experiment only one water NMR calibration was performed trying to keep the same environment as in case of the ^3He measurements. The reason water NMR is usually used as a calibration is that the thermal polarization of the protons in water can be calculated precisely in a given magnetic field at a given temperature. The thermal polarization of protons can be expressed as:

$$P = \tanh\left(\frac{\mu_p B}{k_B T}\right), \quad (4.55)$$

where T is the temperature of the water sample in Kelvin (K), $\mu_p = 8.79 \times 10^{-14}$ MeV/T is the magnetic moment of protons in water and B is the magnitude of the applied magnetic

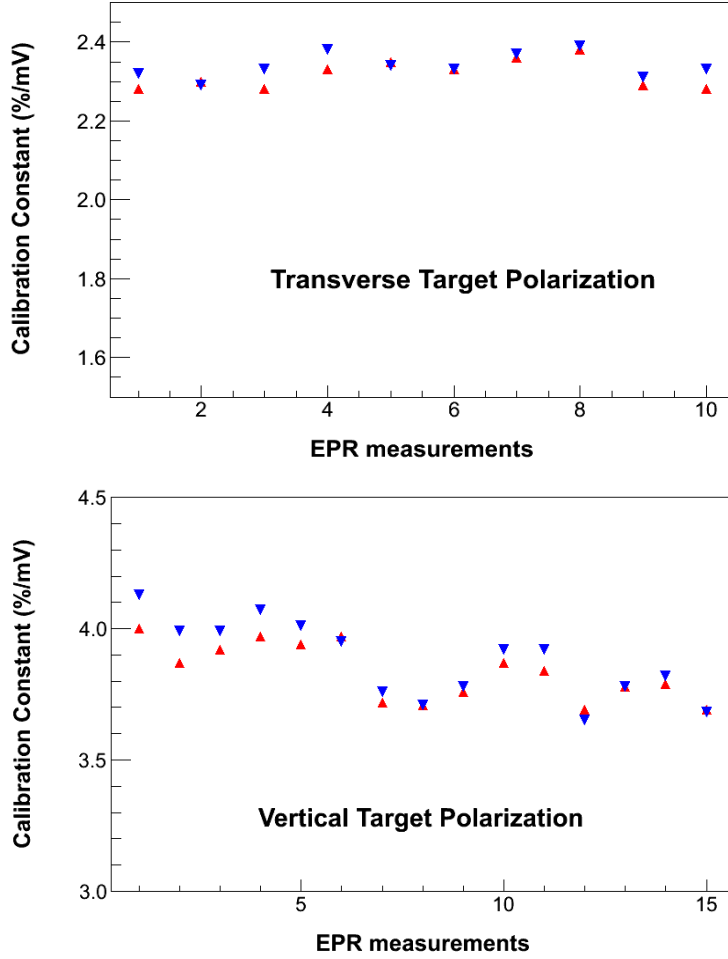


Figure 4.17: The calibration constants from the EPR measurements for the transverse and vertical target polarizations. The red points correspond to the constants determined from the *sweep up* signals and the blue points correspond to the constants from the *sweep down* signals.

holding field. The AFP condition for the water sample is different from the usual polarized ^3He sample. The applied RF field (H_1) and the gyromagnetic ratio (γ) of the sample are related by the following equation :

$$H_1 = \frac{2\pi f}{\gamma}, \quad (4.56)$$

where f is the applied frequency and γ for the proton is 26.75 kHz/G which gives a resonance field of 21.3G at a frequency of 91 kHz. Hence in practice, unlike the range in ^3He NMR, the holding field was swept from 18 G to 25 G for the water calibration. The NMR signal from the water sample is usually of the order of a few tens of micro volt which is very

tiny as compared to the usual ^3He signal. A typical signal of the water NMR calibration during the experiment is shown in Fig. 4.18. It was extremely important to realize a reasonable signal-to-noise ratio. This was done by adjusting the pick-up coils in such a way that any residual RF field could be removed by cancelling the components through both the coils. In addition, since the polarization of the protons remains constant for every sweep, one can take advantage of doing the measurements thousands of times and averaging all of them. During our measurement, we performed 2000 sweeps which resulted in a reasonable signal-to-noise ratio and a statistical uncertainty of less than 1% was achieved.

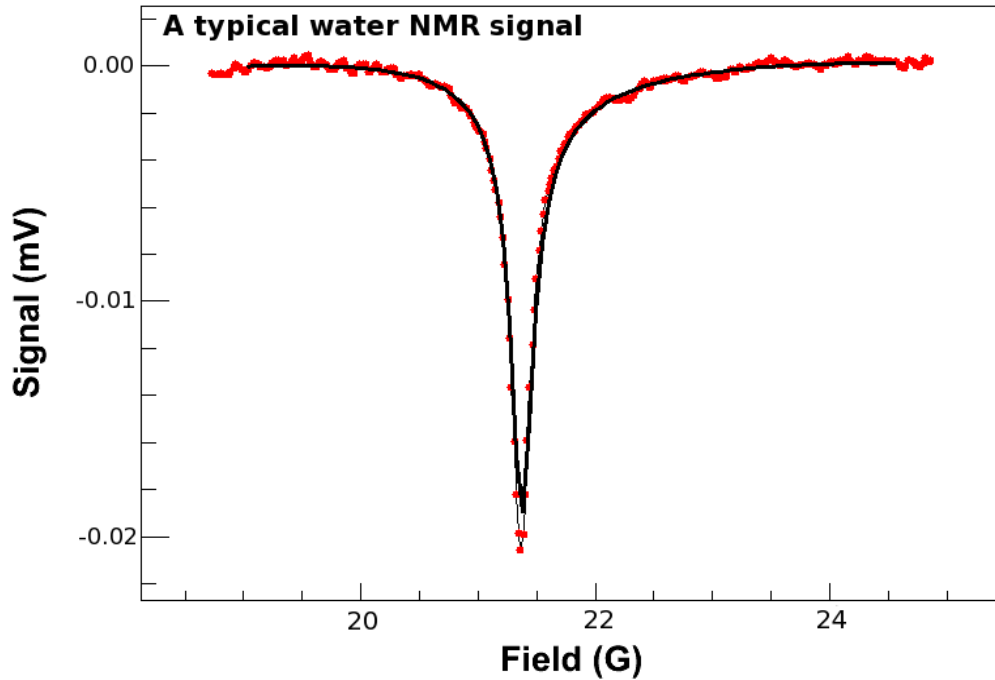


Figure 4.18: A typical water NMR signal (2000 sweeps).

Basic Formalism : The Bloch Equations

One of the interesting properties of water signal is that the relaxation times of water, T_1 and T_2 , are comparable to the sweep time of the NMR measurement. T_1 and T_2 are the longitudinal relaxation time and the transverse relaxation time, respectively. The relaxation during the sweep influences the shape and the height of the water NMR signal which de-

depends on the direction of the magnetic field sweep in addition to the sweep speed. The Bloch equations describe the time evolution of the thermal polarization of water $\vec{P}(P_x, P_y, P_z)$ in a rotating frame $(\hat{x}, \hat{y}, \hat{z})$, when a constant holding field H along the \hat{z} axis and an RF field H_1 along the \hat{x} axis are applied [107]:

$$\frac{dP_x(t)}{dt} = \gamma[H(t) - H_0]P_y(t) - \frac{1}{T_2}P_x(t) + \frac{1}{T_2}\chi H_1, \quad (4.57)$$

$$\frac{dP_y(t)}{dt} = -\gamma[H(t) - H_0]P_x(t) - \frac{1}{T_2}P_y(t) + \chi H_1 P_z(t), \quad (4.58)$$

$$\frac{dP_z(t)}{dt} = -\gamma H_1 P_y(t) - \frac{1}{T_1}P_z(t) + \frac{1}{T_1}\chi H(t), \quad (4.59)$$

where the definitions of the various terms are listed below:

- $H_0 = 21.3$ G is the resonance field for an RF of 91 kHz
- H_1 is the RF field at frequency 91 kHz (The amplitude of the RF field was ~ 90 mG.)
- $H(t) = H_0 + \alpha t$ where $\alpha = 1.2$ G/s is the ramping speed of the holding field.
- $\gamma = 26.75$ kHz/G is the gyromagnetic ratio of the proton.
- $\chi = \frac{\mu_p}{k_B T}$ is the magnetic susceptibility of the proton.
- T_1 is the longitudinal relaxation time in seconds.
- T_2 is the transverse relaxation time in seconds.

This set of differential equations does not have any analytical solutions, but they can be solved numerically with the initial conditions requiring that each of the first derivatives in the time evolution to be at zero when the sweep starts (steady-state conditions). The set of the above equations can be reduced to a single equation if one assumes that both the relaxation times are equal, i.e., if $T_1 = T_2$. This leads to the fact that an effective polarization P_{eff} can be defined along the effective field \vec{H}_{eff} in the rotating frame as follows:

$$P_{eff} = k\sqrt{P_x^2 + P_y^2 + P_z^2}, \quad (4.60)$$

where $k = \pm 1$. The time evolution of P_{eff} can be expressed as :

$$\frac{dP_{eff}(t)}{dt} = \frac{1}{T_1}[P_{eff} - P_{eq}(t)], \quad (4.61)$$

where $P_{eq}(t)$ is defined as :

$$P_{eq}(t) = \chi \frac{H_1^2 + \alpha t(H_o + \alpha t)}{\sqrt{H_1^2 + \alpha^2 t^2}} \quad (4.62)$$

The solution of the differential equation is given by :

$$P_{eff}(t) = \exp^{-(t-t_i)/T_1} \left[P_{eq}(t_i) + \frac{1}{T_1} \int_{t_i}^t \exp^{(u-t_i)/T_1} P_{eq}(u) du \right] \quad (4.63)$$

which has no analytical representation. However, by expanding the exponential term and the square root term within the integral and keeping the terms only up to third order, one can reduce the expression for P_{eff} to an analytical form which can be used to fit the water NMR signal. After fitting the signal, a calibration constant C_w can be obtained and the polarization of the ^3He atoms is then related to the calibration constant as follows:

$$P_{3He} = C_w \cdot S_{3He}, \quad (4.64)$$

where S_{3He} is the signal height of the ^3He NMR.

4.7 Magnetic Field Direction Measurement

Experiment E06010 requires to have ^3He spins polarized in two orthogonal directions, *viz*, the vertical and the transverse directions. It was extremely important to know the direction of the applied magnetic field in the target region in order to make sure that the field in any of the two directions is not affected by the unwanted field components in any arbitrary directions during the process of data taking and hence, it was necessary to know the field direction to a level of at least 0.5° . Two different types of compasses were used to determine the holding field direction. The transverse field was defined as the applied magnetic field that was in the horizontal plane but perpendicular to the incoming electron beam (the electron beam lies in the horizontal plane passing through the center of the target and the center of the target coincided with the center of the hall plane) while the vertical field was the magnetic field perpendicular with respect to the horizontal plane. The transverse field direction was measured by a dipole magnet which was a 40 cm long iron bar covering the target length and was named longitudinal compass. The vertical field direction was measured by a vertical compass which was a floating device in air with a magnetic cylinder and an optical encoder attached to it. This device was developed in the Department of Physics and Astronomy at the University of Kentucky and was used for the first time in

this experiment. Schematic diagrams of both compasses are shown in Fig. 4.19 and Fig. 4.20.

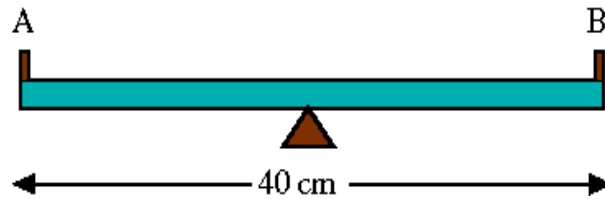


Figure 4.19: The 40 cm longitudinal compass. During the measurements, point A and B were surveyed by the survey group.

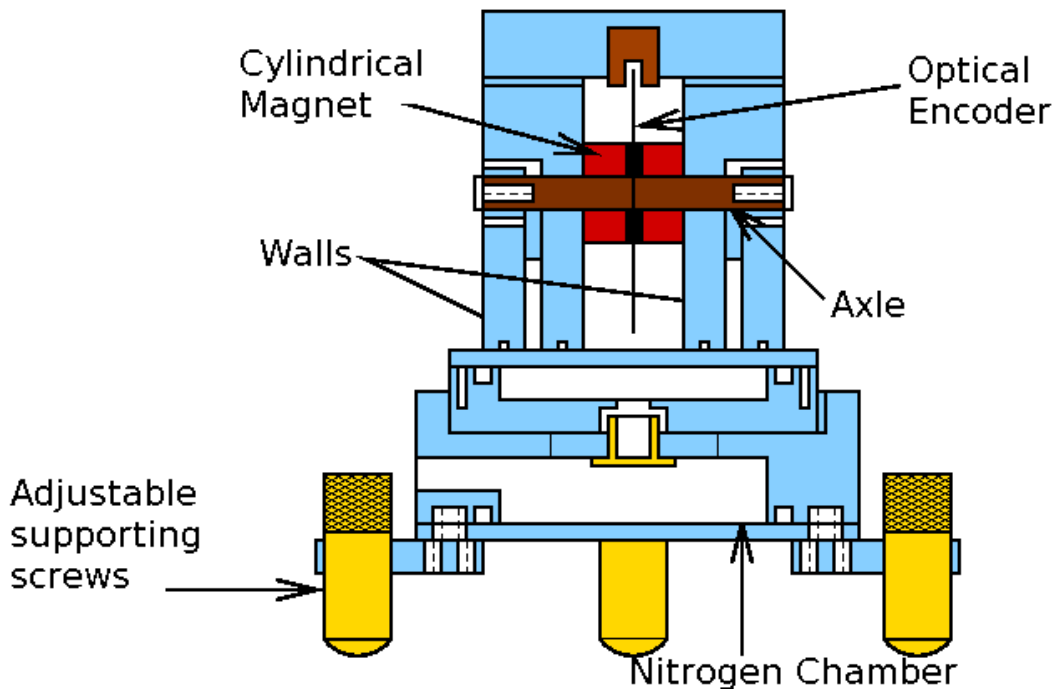


Figure 4.20: The side view of the vertical compass assembly. This figure is obtained from Ref. [17].

The measurement procedure with the longitudinal compass was very straight forward and done by the survey group at Jefferson Lab. The device was placed exactly at the height of the polarized ^3He target and was surveyed for different values of the two Helmholtz coil currents which produced the transverse magnetic field. Measurements were performed both with the BigBite spectrometer field turned on and off. Once the surveyed angles were analyzed with the corresponding currents in the coils, the correct values of the currents in the two Helmholtz coils to achieve the proper direction of the transverse field can be solved for. Here the details of the analysis of the longitudinal compass will not be presented. Instead,

the analysis and the measurement procedure of the vertical compass is presented in the following subsection.

The Vertical Compass

The vertical compass is an air floating device. There are holes in the bottom stand as well as the bottom of each of the pieces that hold the magnetic cylinder. We used nitrogen instead of air in order to improve stability. Nitrogen was blown into the system through the inlet as shown in Fig. 4.20 and eventually the magnetic cylinder was made to float since there were holes evenly distributed on the bottom plate as well as the bottom of each of the side pieces. We found two optimum settings for the nitrogen flow based on a trial and error method. The first one was for the optimum floatation of the bottom disk and the second one was the floatation of the magnetic cylinder. An optical encoder was attached to the magnetic cylinder and it was read by a computer once connected through a USB system. The procedure of the measurement was as follows :

- The whole system was placed on a platform at the center of the target. The platform was designed in such a way that the compass, when placed on it, was at the height of the target and the center of the magnetic cylinder coincided with the center of the target in the hall coordinate system.
- We took out the top piece of the system having the encoder, leaving the bottom stand on the platform. Then the bottom stand was leveled up to a precision of $\frac{1}{100000}^{th}$ of an inch. Once leveled, the top part was placed on the stand.
- Nitrogen was allowed to flow into the system very slowly. In order to find an optimum floatation point for the disk, the disk was rotated slowly at each nitrogen flow setting until a frictionless oscillation of the disk was observed. Thus, after a few iterations, the bottom disk was clamped down once the optimum floatation point was reached for the disk of the system. This was the first optimum nitrogen flow setting.
- Once the bottom disk was clamped down, the nitrogen flow was adjusted further to have the magnetic cylinder floating this time. This was again a similar trial and error process which involved the rotation of the cylinder slowly by hand and looking into

the value of the encoder reading if it came back to the original value once released. This was the second optimum setting for the flow.

- Once we had our compass floating, the vertical magnetic field was turned on and the value of the encoder reading was noted (N_1).
- With the same nitrogen flow on, the clamps were removed and the disk was rotated 180° and was clamped again. The reading of the encoder was noted (N_2).
- The angle of the field direction corresponding to the applied current to the vertical Helmholtz coil was then given by :

$$\theta = 90 - (N_1 - N_2) \times \frac{0.09}{2}, \quad (4.65)$$

where 0.09 was the resolution of the encoder disk and θ is in degrees.

- We repeated the measurements for three different sets of current values (0 A, 8A, and 16 A) in the vertical Helmholtz coil.
- Once the measurements were done at the center, the whole procedure was repeated placing the compass ± 20 cm from the center to measure the field directions at the upstream and downstream ends of the target.

Analysis Formalism and Results

There were three pairs of Helmholtz coils in the target system. The *horizontal pairs* were used to produce the field in transverse and longitudinal directions and the *vertical pair* was used to produce the field in vertical direction. Let us define a few quantities in order to define the angle of the resultant magnetic field in the vertical direction as shown in the Fig. 4.21.

- B_l is the resultant field produced by the large horizontal Helmholtz coils together with the magnetic field produced by the BigBite magnet. If I_l is the current in the large coils, I_B is the current in the BigBite magnet and E_l is the Earth's magnetic

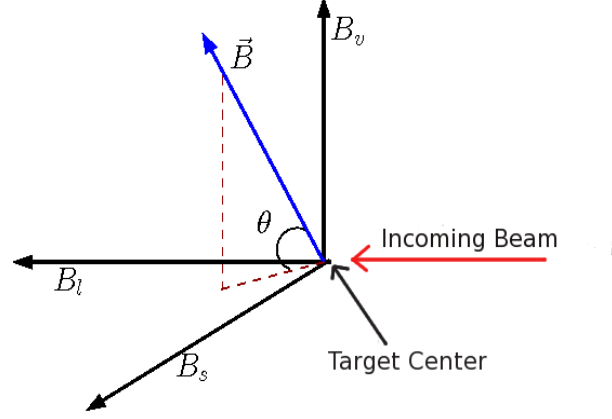


Figure 4.21: Definition of the vertical angle θ with respect to the incoming beam.

field component or any other ambient fields along the respective direction, B_l can be written as

$$B_l = a_l \cdot I_l + E_l + a_{lB} \cdot I_B, \quad (4.66)$$

where a_l and a_{lB} are the respective coefficients relating the currents and the generated magnetic fields. This is one of the *in-plane* resultant magnetic fields.

- B_s is the resultant field produced by the small horizontal Helmholtz coils together with the magnetic field produced by the BigBite magnet. If I_s is the current in the small coils, B_s can be written as

$$B_s = a_s \cdot I_s + E_s + a_{sB} \cdot I_B, \quad (4.67)$$

where a_s and a_{sB} are the respective coefficients relating the currents and the generated magnetic fields with E_s and I_B defined above. This is the second *in-plane* resultant magnetic field.

- B_v is the resultant field produced by the vertical Helmholtz coils together with the magnetic field produced by the BigBite magnet. If I_v is the current in the vertical coils, B_v can be written as

$$B_v = a_v \cdot I_v + E_v + a_{vB} \cdot I_B, \quad (4.68)$$

where a_v and a_{vB} are defined as above. This is the vertical *out-of-plane* resultant magnetic field.

- If θ is the angle between the resultant magnetic field produced by all the three pairs of Helmholtz coils and the horizontal plane as shown in Fig. 4.21, then θ can be expressed as:

$$\begin{aligned}
\tan\theta &= \frac{B_v}{\sqrt{B_s^2 + B_l^2}} \\
&= \frac{a_v \cdot I_v + E_v + a_{vB} \cdot I_B}{\sqrt{(a_s \cdot I_s + E_s + a_{sB} \cdot I_B)^2 + (a_l \cdot I_l + E_l + a_{lB} \cdot I_B)^2}} \\
&= \frac{K(I_v + A + B \cdot I_B)}{\sqrt{(I_s + C + D \cdot I_B)^2 + R^2(I_l + E + F \cdot I_B)^2}}, \tag{4.69}
\end{aligned}$$

where $K = \frac{a_v}{a_s}$, $A = \frac{E_v}{a_v}$, $B = \frac{a_{vB}}{a_v}$, $C = \frac{E_s}{a_s}$, $D = \frac{a_{sB}}{a_s}$, $E = \frac{E_l}{a_l}$, $F = \frac{a_{lB}}{a_l}$ and $R = \frac{a_l}{a_s}$. The goal of the analysis was to evaluate the parameters K, A, B, R, C, D, E, and F by fitting the different data points for each target position¹³ with Eq.(4.69). However, the parameters R, C, D, E and F could already be obtained from the longitudinal compass data with a similar fitting procedure and used as inputs to the analysis of vertical compass data. Once all these parameters were obtained, the exact combination of current values in the three pairs of coils could be calculated in order to achieve a vertical field.

Fig. 4.22 shows a sample plot of the vertical angles as a function of vertical coil currents when the compass was placed at the center of the target. Two sets of data points were taken with the BigBite magnetic field turned on and off as shown in the figure.

Table 4.6 summarizes the measurements of the field at the center of the target. The

Table 4.6: Data were taken with three sets of current settings in the vertical coil. $\theta_{BB=0}$ represents the measured angle when the BigBite magnetic field was off while $\theta_{BB=1}$ represents the angle when the BigBite magnetic field was on.

I_v (A)	$\theta_{BB=0}(\circ)$	$\theta_{BB=1}(\circ)$
0	0.45	1.98
8	21.33	23.62
16	37.53	40.14

effect of the BigBite magnetic field at the center of the target is clearly visible from the table.

¹³Three positions along the target cell were considered for the measurements. Two of them were near the target end caps on both sides (upstream and downstream) and one was at the center which was the most crucial one.

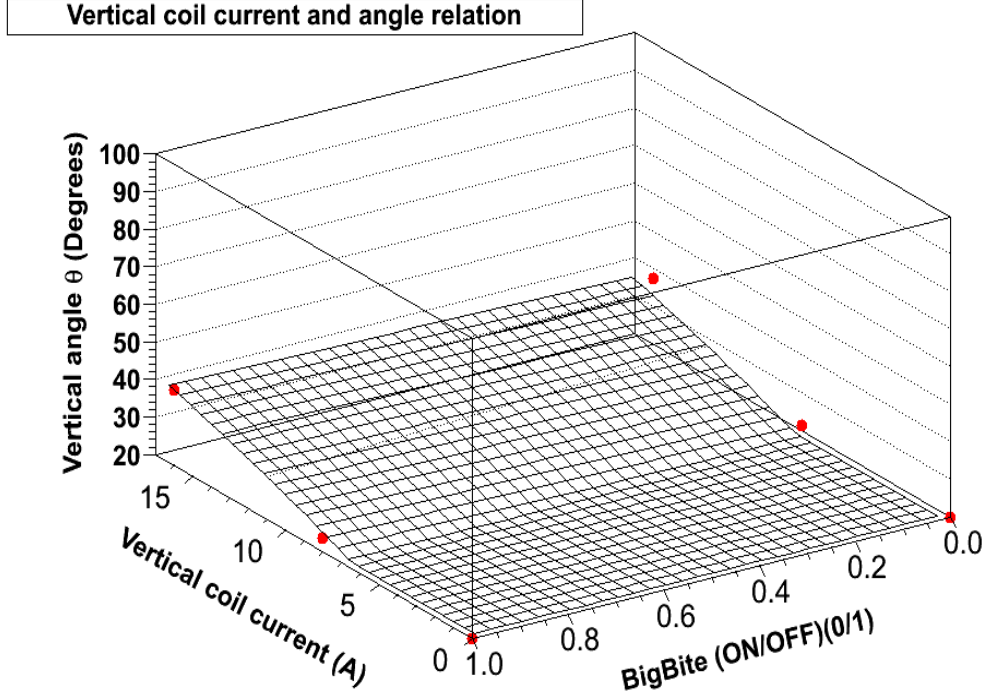


Figure 4.22: The direction of the vertical field as a function of vertical coil current with the BigBite magnetic field turned on and off.

For all our measurements when the BigBite magnetic field was on, the current setting in the magnet was 710 A which was the same current we applied during our whole production data taking period. The quality of the fit of Eq.(4.69) to the data points is shown in Fig. 4.23 with a chi-squared of ~ 1.1 .

The final equation for the desired vertical angle as a function of all the currents in all the three pairs of coils at the center of the target can be written as :

$$\tan(\theta_{center}) = 0.549299 \cdot \frac{I_v + 0.712}{\sqrt{(I_s + 0.424)^2 + 0.9614(I_l - 0.409)^2}}, \quad (4.70)$$

where the numbers are the values of the fitted parameters (as in Eq.(4.69)). Table 4.7 lists all the values.

Similar equations were obtained for the upstream and downstream positions as well:

$$\tan\theta_{up} = 0.539 \cdot \frac{I_v + 0.806}{\sqrt{(I_s + 0.392)^2 + 0.9644(I_l - 0.367)^2}}, \quad (4.71)$$

$$\tan\theta_{down} = 0.545 \cdot \frac{I_v + 0.781}{\sqrt{(I_s + 0.477)^2 + 0.9606(I_l - 0.448)^2}}. \quad (4.72)$$

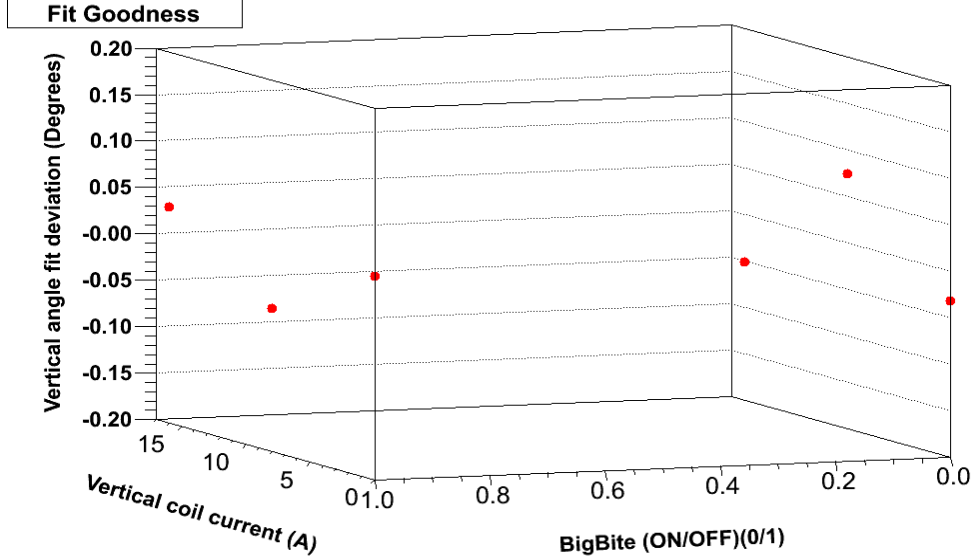


Figure 4.23: The deviation of the measured vertical angle and the angle determined from the fit.

Table 4.7: The fitting parameters from the Eq.(4.69) for the center position.

K	0.549 ± 0.005
(A+B)	0.712 ± 0.10
R^2	0.9614 ± 0.13
(E+F)	-0.409 ± 0.21
(C+D)	0.424 ± 0.20

Finally, by solving these equations, the currents in all the three coils are determined to achieve a vertical angle of 90° out of plane with respect to the electron beam. The currents in all the three coils determined for the experiment are listed in the Table 4.8 and the precision of the angle measurements was better than 0.3° . However, since the currents in the large and small coils were slightly different for different positions, only the values at the target center were considered as the final setting of currents for the production data taking.

Table 4.8: The final values of the currents in all the three Helmholtz coils for a vertical magnetic field in E06010.

Position	I_v (A)	I_l (A)	I_s (A)
Center	16	0.409	-0.424
Upstream	16	0.368	-0.392
Downstream	16	0.448	-0.477

4.8 Target Spin Flip System

One of the most important aspects of experiment E06010 was the target spin flip system which ensured the flipping of the ^3He spins very reliably every 20 minutes during the experiment to reduce systematic uncertainties. The system not only successfully flipped the spins of ^3He and read the current spin state back, but also sent information about the flipping to the main DAQ system. Here only a summary of the spin flip system structure and its operation is presented. The details of the system can be found on the wikipedia page of experiment E06010 [115].

Basic structure of the system

- **User Interface:** The user interface was a Lab view based environment which allowed the user to control the whole system by taking the various inputs and displaying and confirming the resulting status. It was the control panel of the system.
- **Core:** This part of the system was the heart of the whole spin flip system. It generated and induced the spin flip in the target system in the Hall. Once the spins were flipped, this part of the system was used to collect the information back and send the response to the user interface as well as to the main DAQ system. It also acted as a feedback control system in case of any malfunctioning and allowed the user to respond quickly without losing any vital information.
- **Flip Confirmation:** Basically it was a part of the core structure which collected the NMR signal during the spin flip and sent it back to the lock-in amplifier through the pick-up coils. Then it processed the signal and sent the information about the current spin state to the system manager which again was monitored by the user interface.
- **System Failure Monitor:** This allowed the constant monitoring of the different essential components of the system while in operation. The most important components were the rotatable quarter wave plates of the polarization optics in the hall. When the ^3He spins were flipped by 180° , the polarization of the incoming lasers to the cell also needed to be reversed. In order to do that, all the quarter wave plates that ensured the circular polarization of the lasers had to be rotated by 90° during the flip so that once the spins got flipped, the lasers would pump the reversed spins in the correct

direction. All the quarter wave plates were well calibrated before the experiment and were assigned specific numbers corresponding to specific angles related to a particular circular polarization of the lasers. All the quarter wave plates were monitored with each spin flip during the experiment.

Another important aspect of the spin flip system was the logic electronics for the target spin signal formation. The target logic electronics was an independent system which extracted the information of the spin flip and the spin state from the NMR measurement irrespective of the status of the target computer system. The idea was to keep track of the spin state for each event in the data taking process. The spin state was inserted into the main DAQ system independent of the target control system in the computer itself. It was read by ADCs and treated as a target spin flag for each event. It also formed the gates for the scalars. The signal distribution scheme is shown in Fig. 4.24 and the structure of the system is shown in Fig. 4.25.

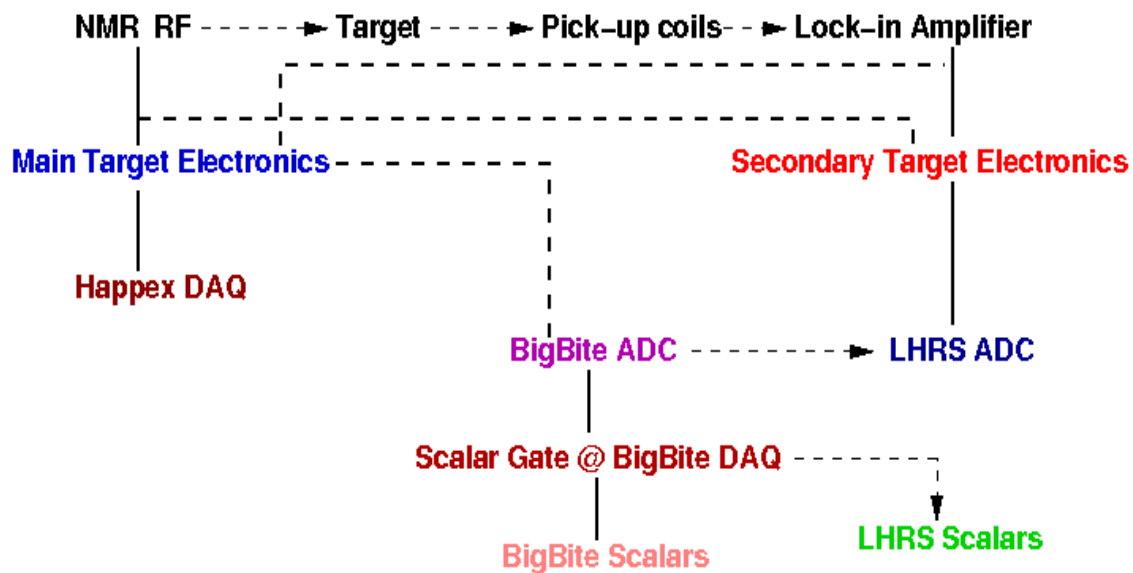


Figure 4.24: Schematic diagram of the spin flip distribution scheme.

Spin Flip System Diagram

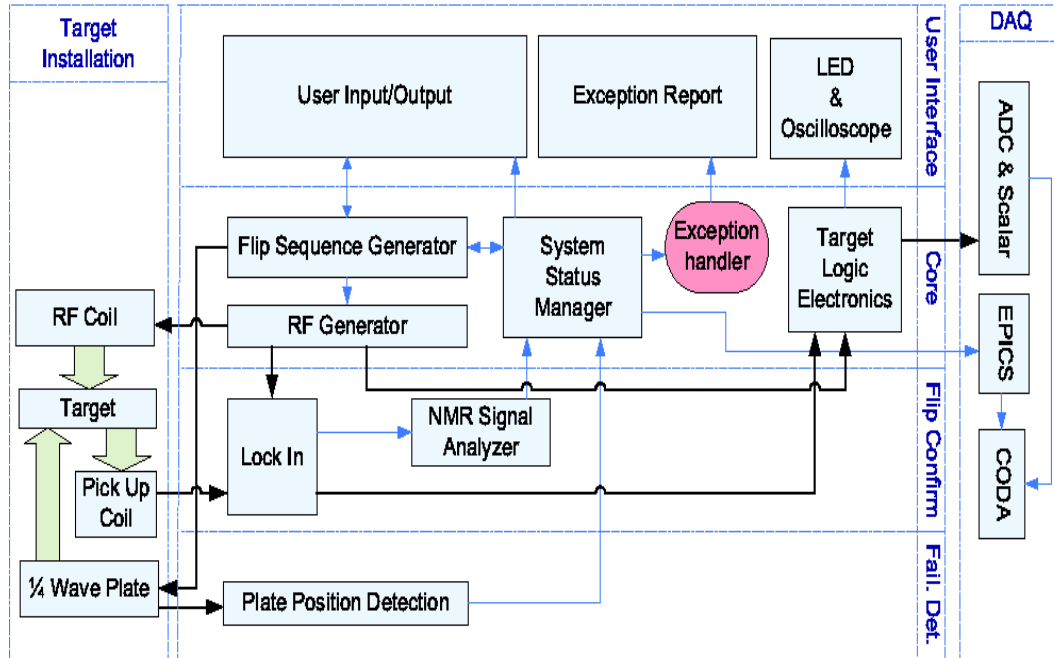


Figure 4.25: Schematic diagram of the spin flip system structure.

Copyright © Chiranjib Dutta 2010

CHAPTER 5: DATA ANALYSIS

In this chapter, analysis details of the production data are presented. The calibrations of different detectors in both the Left High Resolution Spectrometer (LHRS) and the BigBite spectrometer are discussed.

5.1 Left High Resolution Spectrometer (LHRS) Calibrations

The LHRS consists of different detector packages as discussed in chapter 3. The detector packages include two vertical drift chambers (VDCs), an Aerogel Gas Čerenkov detector (A1), a Gas Čerenkov detector (GC), a Ring Imaging Čerenkov detector (RICH), two scintillator planes (S1 and S2m) and two layers of lead-glass counters (PR1 and PR2, PR standing for Pion Rejector). The detector packages are designed to perform various functions in the characterization of the charged particles passing through the spectrometer such as tracking of the particles, time-of-flight and coincidence time determination, trigger formation to activate the data acquisition, etc. Therefore, in order to understand the performance of the detectors and to facilitate the analysis of the final physics asymmetries, it is very important to perform a very careful calibration of the detectors. In the following subsections, the calibration procedures are summarized.

5.1.1 Vertical Drift Chambers (VDC)

The working principle of a VDC is explained in chapter 3. The typical drift time spectrum of a wire plane is shown in the Fig. 5.1 where the drift times of all the wires in a plane are plotted in terms of Time-to-Digital Converter¹ (TDC) channels.

The TDCs were operated in common-stop mode and hence the large TDC values correspond to the short drift times. The various regions in the spectrum can be understood as follows:

- **Region A** : This is a region that corresponds to the particles having larger trajectory angles and hence are further away from the drift cell around the sense wires.
- **Region B** : This region has all the field lines parallel and hence the drift velocity of the electrons is constant.

¹A Time-to-Digital Converter (TDC) is a device that converts a signal of pulses into a digital representation of the time of arrival of that signal.

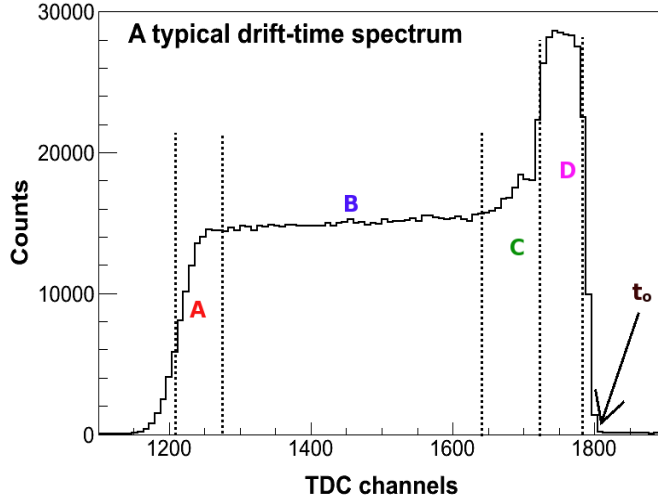


Figure 5.1: A drift-time spectrum of a VDC plane.

- **Region C** : In this region, the field lines begin to change from parallel to quasi-radial closer to the sense wires and as a result, the probability of detecting a particle begins to increase.
- **Region D** : This region corresponds to a region very close to the sense wires where the drift velocity of the electrons increases drastically and probability of detecting a particle is maximal.

In order to compare and use the drift time spectra from all the wires in a plane, a reference timing t_0 for all the wires had to be defined so that the various timing offsets due to variable cable lengths and signal processing times for different wires could be eliminated. The calibration procedure, thus, involved the determination of t_0 for each wire in the plane and matching each of them to one common reference point. t_0 for each wire was determined by differentiating the region of short drift times around channel 1800 numerically and looking for the maximum slope. Once the maximum slope was calculated, it was extrapolated to the channel axis and the point of intersection of the extrapolation and the axis was determined as shown in Fig. 5.1. Each of the four planes in the two VDCs was calibrated and the reference t_0 was determined. This corresponds to 0 ns in the corrected timing spectrum shown in Fig. 5.2.

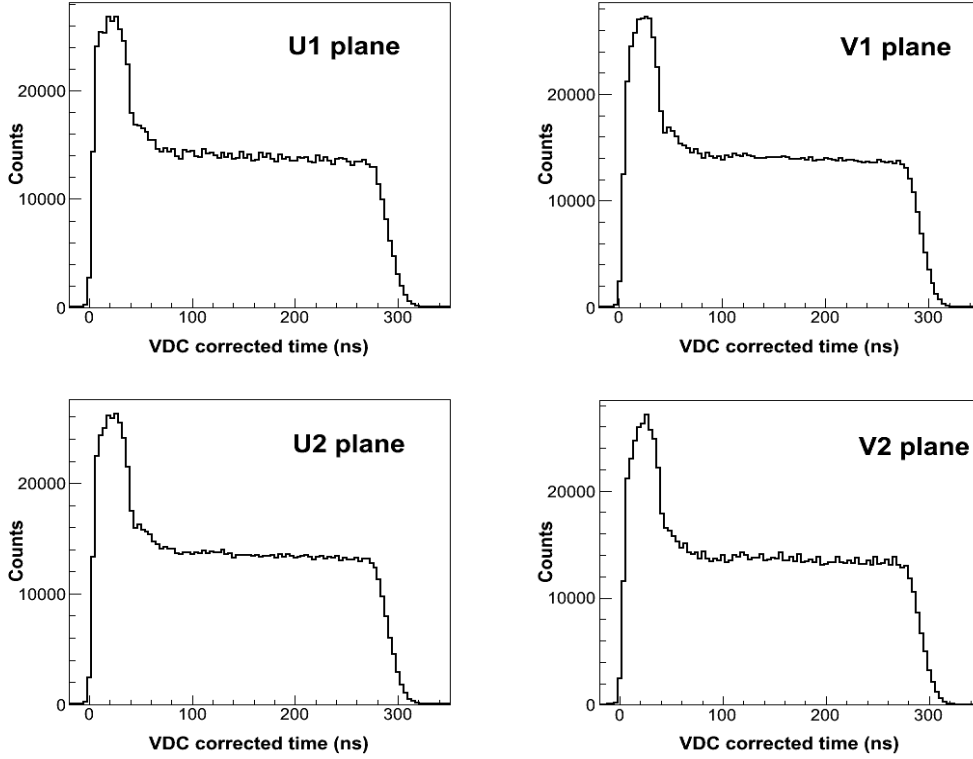


Figure 5.2: The corrected timing spectra of the four VDC planes after calibration.

5.1.2 Gas Čerenkov (GC)

The GC in the LHRS consists of 10 mirrors, each coupled to a photomultiplier tube² (PMT). The signal was extracted from an Analog-to-Digital Converter³ (ADC) and the TDC connected to each PMT. The electrons fire the GC while the pions and the kaons do not have enough momenta⁴ to produce Čerenkov radiation and hence they can not trigger the ADCs. However, the pions and the kaons can produce secondary electrons by interacting with other atoms in the gas which in turn can emit Čerenkov light. But this kind of radiation has arbitrary directions as the secondary electrons do not move in any preferred direction and hence the light is collected very inefficiently by the mirrors. This kind of secondary radiation

²A photomultiplier tube (PMT) is a detector which is very sensitive to light in the ultraviolet, visible and near-infrared ranges of the electromagnetic spectrum. It immensely multiplies the current produced by the incident light and hence it is very useful when the incident flux of light is very low. The working principle is based on the *photoelectric effect*.

³An Analog-to-Digital Converter (ADC) is a device which converts a continuous analog signal to a discrete digital signal.

⁴As discussed in chapter 3 in the Gas Čerenkov section, the particles inside the gas should have a minimum momentum to produce Čerenkov radiation.

triggers the ADCs and produces signals which can be misinterpreted as primary electrons produced in the reaction. However, the signals generated by these secondary electrons are very small and correspond to low ADC channels. Such a signal is not part of the main signal generated in the ADCs and is called Single Photo Electron (SPE) peak. The calibration of the GC involved aligning the single photo-electron peaks in all of the ADCs to a certain value so that the secondary electrons generated from the hadrons can be separated from the primary electrons. Thus, calibration of the Gas Čerenkov allows clear identification of hadrons which helps in rejecting the primary electrons in the LHRS.

For our experiment, we chose the channel 200 of each ADC for the SPE peak. The SPE peak in each ADC spectrum was fitted with a Gaussian profile and the mean value of the distribution was determined. Then a correction coefficient was calculated which is defined by $C=200/N$, where N is the mean value of the distribution. Thus, 10 different coefficients were determined from the fits and finally implemented in the database. The calibration of the GC was quite straightforward and each of the ADCs was aligned to the channel 200 for the SPE peak by just multiplying the existing SPE peak channel with the correction coefficient. It was very important to distinguish the SPE peak from the main electron peak in the ADC sum spectrum so that only the primary electrons could be chosen or rejected in our case and not the electrons induced by any other particles like pions and kaons. A typical ADC sum cut of less than 250 channels was applied to our data in the final analysis to get rid of the background particles. Figure 5.3 on the next page shows the calibrated sum of the GC ADCs and Fig. 5.4 shows the aligned SPE for all the PMTs after calibration.

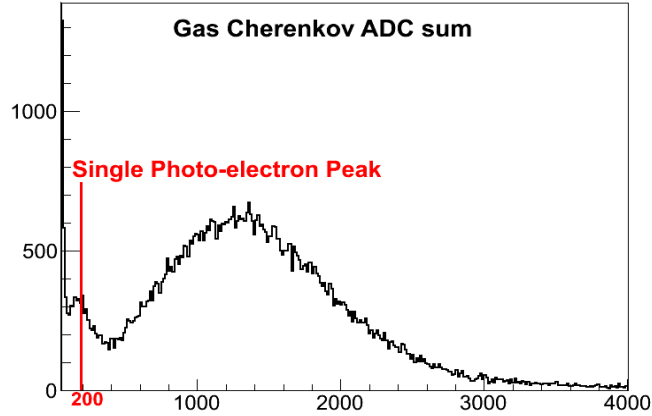


Figure 5.3: The Gas Čerenkov ADC sum spectrum after calibration.

5.1.3 Aerogel Čerenkov (A1)

The calibration procedure for the A1 was exactly the same as for the GC. In the case of A1, both electrons and pions can trigger the ADCs, but not kaons or protons. Hence, the single photo-electron (SPE) peaks produced in this case were mostly from kaons and protons (for positive LHRS polarity). There were 24 PMTs and all the SPEs were aligned to the ADC channel of 100. Figure 5.5 shows the A1 ADC sum spectrum after the calibration.

5.1.4 Lead-Glass Counter (Pion Rejector)

There were two layers of lead-glass counters as described in chapter 3 which were used as particle identification detectors. The energy deposition by the hadrons corresponded to the lower value of the ADC channel while that of the electrons corresponded to the higher ADC value. During the calibration, all the pion peaks in the ADCs for both layers were aligned to channel 100. The clear separation of pions and electrons in the energy over momentum plot (E/p spectrum) is shown in the Fig. 5.6. After calibration, a cut less than 0.6 in E/p was used in the final analysis to choose the pions.

5.1.5 Scintillator (S2m)

There were two scintillator planes, *viz*, S1 and S2m in the LHRS. Both were used to form the triggers however, only S2m was used as a reference for determining the timing of the events. Therefore calibrations were done only for S2m. There were 16 scintillator paddles

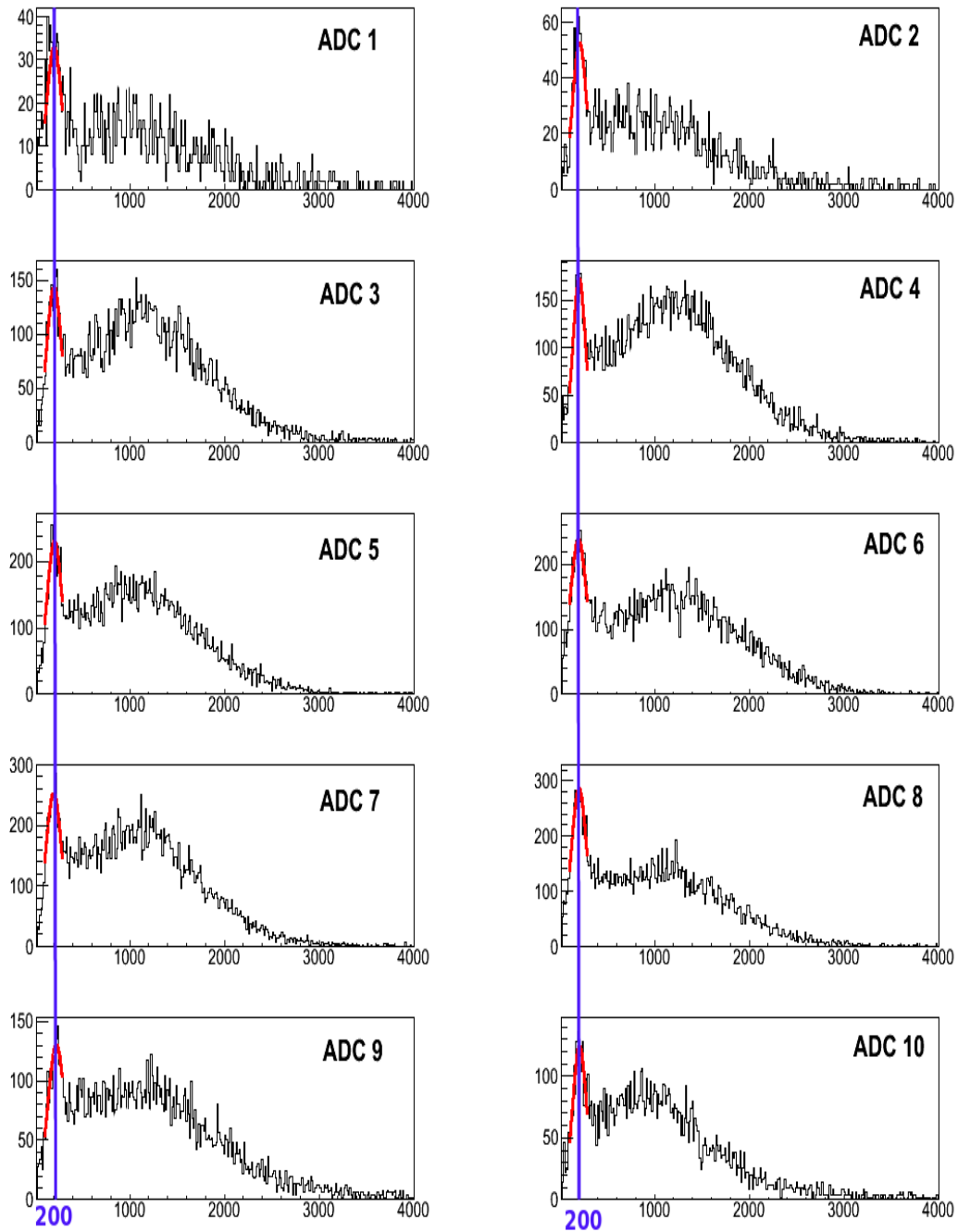


Figure 5.4: All 10 ADC spectra for the Gas Čerenkov after calibration.

in S2m having a PMT on each side. The calibration procedure involved determining the different timing offsets of the scintillator paddles and aligning them to a particular TDC channel. The timing of an event in any scintillator paddle can be expressed by the following two sets of equations corresponding to the two PMTs:

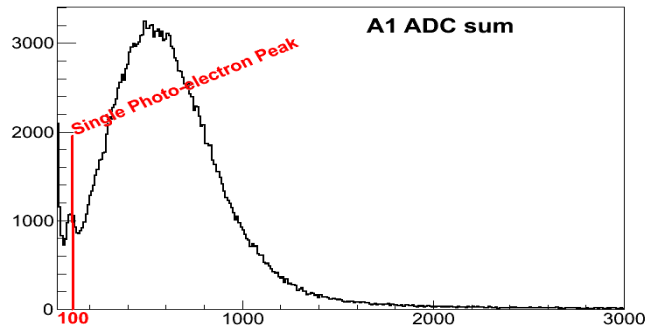


Figure 5.5: The A1 Čerenkov detector ADC sum spectrum after calibration.

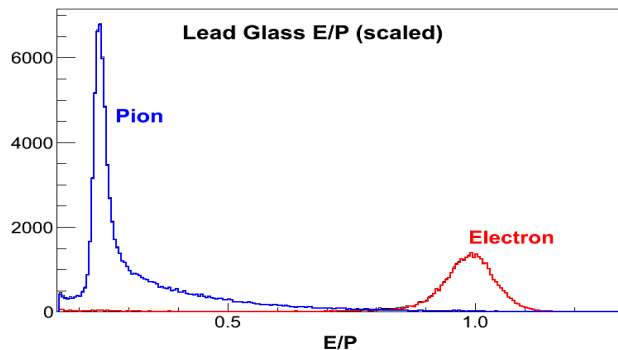


Figure 5.6: The Lead-glass counter E/p spectrum after calibration.

$$T_L = T_0 + \frac{l}{2c_n} - \frac{y}{c_n} + T_{Ltw}, \quad (5.1)$$

$$T_R = T_0 + \frac{l}{2c_n} + \frac{y}{c_n} + T_{Rtw}, \quad (5.2)$$

where L and R correspond to the left and right PMTs. c_n is the speed of light in the scintillator material and $T_{Ltw/Rtw}$ is the timewalk effect correction term for the left (right) PMT. Figure 5.7 shows the basic diagram of particles (in our case we chose electrons) passing through two adjacent scintillator paddles.

There were two steps to calibrate the paddles. First, the left and right PMTs were aligned independently. In one case, the difference between the corrected times of the left PMTs for adjacent paddles were plotted and TDC offsets were determined. In the second case, the same procedure was applied for corrected times of the right PMTs for adjacent paddles. Scintillator paddle # 7 which was in the middle of the detector plane, was used

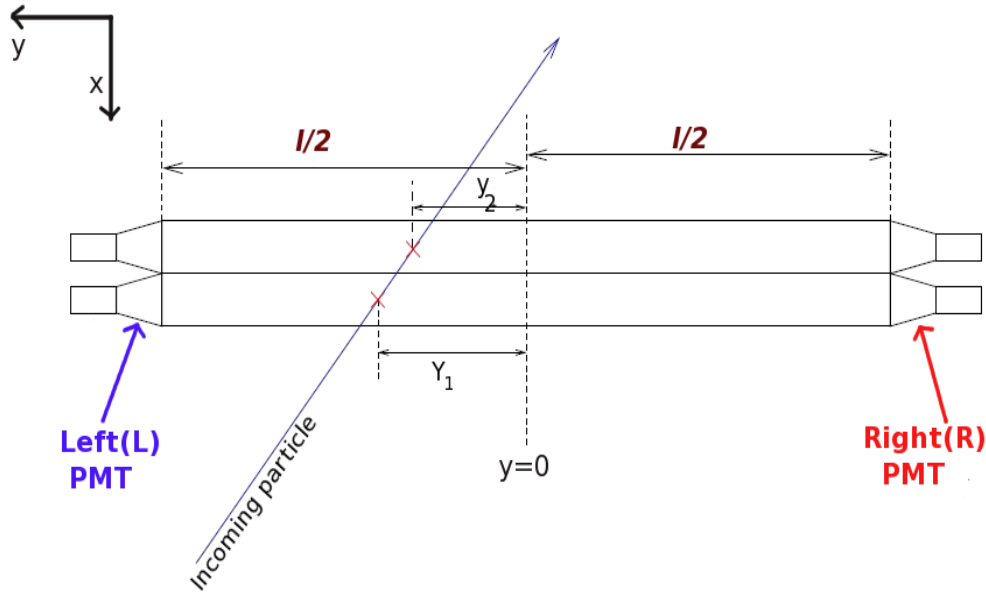


Figure 5.7: The incoming particle hitting the two adjacent paddles in the S2m.

as a reference for these alignments. Once determined, the offsets were put into the LHRS databases for S2m and checked after replaying the data. This was an iterative process and two, three iterations were implemented for finer adjustments.

The next step involved plotting the difference between the left and right time average of adjacent paddles along with the left and right time difference. This shifted the time differences of the paddles to an arbitrary value. They did not have to have a value close to zero as long as they all were aligned within a few tens of picoseconds. More discussions on the timing offset calibrations and the timewalk effect corrections are presented in the coincidence time calibration section.

5.2 BigBite Spectrometer

The BigBite spectrometer consists of three wire chambers for the track and momentum reconstruction of the particles, a preshower detector and a shower detector for particle identification and formation of the trigger, and a scintillator plane between the preshower and shower detectors. A Gas Čerenkov detector was inserted in front of the preshower detector, but due to some technical issues it was not used for more than 95% of the running period and hence will not be discussed here. The BigBite detector package was not a stan-

standard detector package in Hall A as a result of which the calibration procedure involved in this case was more rigorous and extensive as compared to the LHRS. Moreover, the environment in the spectrometer was much noisier than the standard clean LHRS environment. The calibration of the wire chambers and the preshower and shower detectors are presented here. Details of these calibration procedures and results can be found in [18], [15].

5.2.1 BigBite Multi Wire Drift Chamber (MWDC)

The BigBite spectrometer had three wire chambers each having six wire planes as described in chapter 3. Overall more than 3200 wires in the chambers were used for track reconstruction in the transversity experiment. The calibration procedure for the MWDCs involved four parts which are summarized as follows:

- Detector Channel Map Check:** Since the wire chambers had a huge number of wires as mentioned above and each of them was connected to a TDC channel which gave the timing information of the wire hit, a correct correspondence of the wires and the TDC channels was crucial for the DAQ system. A detector channel map was formed to serve this purpose. During the reconstruction of tracks, the TDC channels were projected to the corresponding wires in the wire planes. Thus, the first part of the calibration involved examining the detector map with the experimental data where various problems related to different incorrect channel mapping could be identified. With a perfect detector map, the distribution of the wire hit in a plane should be very smooth as shown in the Fig. 5.8.
- t_0 calibration:** The basic purpose of the t_0 calibration was the same as discussed in the case of the LHRS. In the case of the BigBite spectrometer, the MWDCs were associated with a DAQ which recorded the time difference between the signal from a particular wire reaching the TDC (t_{signal}) and the signal of the trigger from the calorimeter arriving at the TDC ($t_{trigger}$). Taking into account the trigger time-walk correction which was of the order of a few nanoseconds, the drift time of the electrons in the chamber (t_{drift}) and the time of hit of the particles in the chamber (t_{hit}) can be expressed in relation to t_{signal} as follows [18]:

$$t_{signal} - t_{trigger} - t_{timewalk} \equiv t_{drift} - t_{hit} + t_0, \quad (5.3)$$

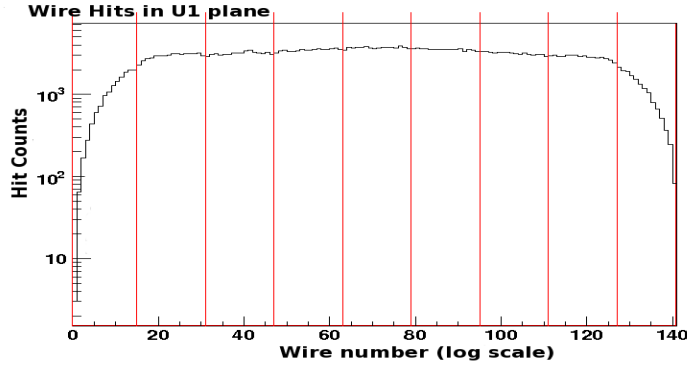


Figure 5.8: A typical distribution of the wire hits in the U1 plane in the first chamber in E06010. The separation of different read-out amplifier cards are represented by the red lines [18].

where t_0 is the time offset related to the difference in time between the signal in the wire (which is hit) takes to reach the TDC and the time that the trigger signal takes to reach the respective TDC. The quantity $(t_{drift} - t_{hit})$ represents the real drift time of the particle detected. t_0 was determined the same way as in the LHRS, i.e., by identifying the rising edge or the maximum slope of the drift time spectrum near the edge as shown in Fig. 5.9.

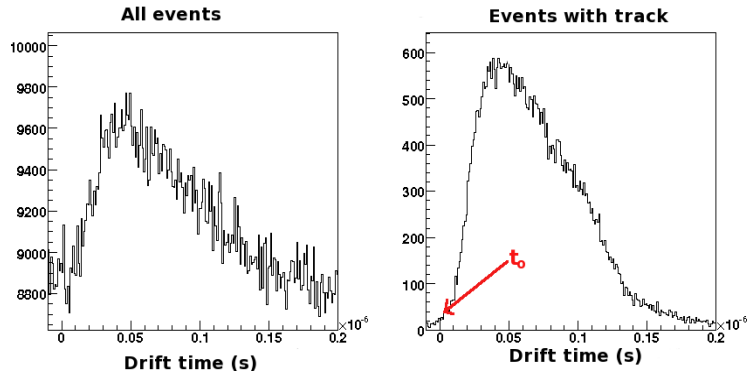


Figure 5.9: The drift time spectrum in the X -plane of the second chamber. The left plot shows the spectrum for all the events and the right plot shows the drift time for the particles for which a valid track was reconstructed. t_0 is also shown [18].

- **Drift Distance to Drift Time Conversion:** The drift distance is defined as the distance of the reconstructed track from the wire hit position. The function that converts the drift distance to drift time was parametrized by several polynomial functions

through the entire drift time window.

- **Wire Position Calibration:** In order to reconstruct a track precisely, the positions of the wires needed to be known to great accuracy and this was achieved by combining the knowledge from the survey report with the calibration of the track residual [18].

The calibration of the MWDC was an iterative process and few iterations had to be performed in each step to achieve a good resolution and hence a precise track and momentum reconstruction. The final spatial resolution achieved after very cautious calibration was better than 200 μm .

5.2.2 Preshower/Shower Detector

The preshower and shower detectors in the BigBite spectrometer were made of lead-glass blocks as described in chapter 3. The preshower detector had 54 blocks while the shower detector consisted of 189 blocks. These were used to perform the particle identification as well as to form the trigger in the spectrometer. The working principle of these preshower and shower blocks is based on the total energy deposition of the particle passing through them which is approximately proportional to the sum of the cluster amplitudes found in the individual blocks. Hence, in order to perform the energy loss determination and track matching precisely, both the preshower and the shower had to be calibrated to a known energy of the incident particle. One of the best options in our experiment was acquiring calibration data using the elastic reaction $\text{H}(e,e')\text{X}$. Two different incident beam energies, *viz*, $E_0 = 1.231 \text{ GeV}$ and $E_0 = 2.306 \text{ GeV}$ were used in combination with an H_2 target. The entire calibration procedure involved two processes that used the shower cluster reconstruction. The details can be found in [15]. Here a summary of the procedure is presented:

- **Preliminary calibration with cosmic rays:** The preshower and shower detectors were gain matched using cosmic rays for a rough alignment of the ADC amplitudes by adjusting the high voltages on the PMTs at the beginning of the experiment. Two scintillators were mounted on the top and at the bottom of the detectors and a trigger was set up for the cosmic rays passing vertically through the constituent blocks. There were two PMTs attached to each of the scintillators and hence a logical AND of the four PMTs formed the trigger. The cosmic rays, which were primarily muons, passing vertically through the blocks generated energy loss peaks in the ADCs which were then

aligned by adjusting the high voltages through a number of iterations. The ADCs in the preshower were aligned to channel 240 and those of the shower were aligned to channel 120.

- **Elastic calibration:** The calibration of the preshower and shower detectors using elastic data involved determining the coefficients C_j in Eq.(5.4) for every block (e.g. the j^{th} block) which actually transforms the pedestal subtracted ADC amplitudes to the energy deposition E_j by the following equation :

$$E_j = C_j(A_j - P_j), \quad (5.4)$$

where A_j and P_j are the raw ADC amplitude and the pedestal of the j^{th} block. Now the coefficient C_j was determined by the linear minimization of the quantity χ^2 for n elastic events which is defined as :

$$\chi^2 = \sum_{k=1}^n \left[E^k - \sum_{j=0}^M C_j A_j - P_j^k \right]^2, \quad (5.5)$$

where E^k is the energy of the k^{th} scattered electron from the tracking and M represents the total number of blocks. Requiring $\frac{\partial \chi^2}{\partial C_j} = 0$, a set of linear equations were obtained in matrix form [15]. Solving these equations, the coefficient C_j for the j^{th} block was calculated. Elastic data with beam energies $E_0 = 1.231$ GeV and $E_0 = 2.306$ GeV were used for this calibration. The scattered electrons had a momentum range of 0.8 GeV to 2.0 GeV of which the elastic events were selected by placing a cut on the momentum vs. scattered angle plot choosing the elastic section. One set of calibration constants was sufficient for the experiment as there was only one momentum setting for the BigBite spectrometer. An energy resolution of $\sim 8\%$ was achieved after the calibration as shown in the Fig. 5.10.

5.2.3 Scintillator Plane

The BigBite spectrometer contained a scintillator plane consisting of 13 scintillator paddles which was used for the timing information of the events. However, it was not used to form any triggers. The calibration of the scintillators was done exactly the same way as that of S2m in the LHRS using the *two-adjacent bar hit* method. The other corrections such as time-walk effect and more on the time offset will be discussed in the coincidence timing calibration section.

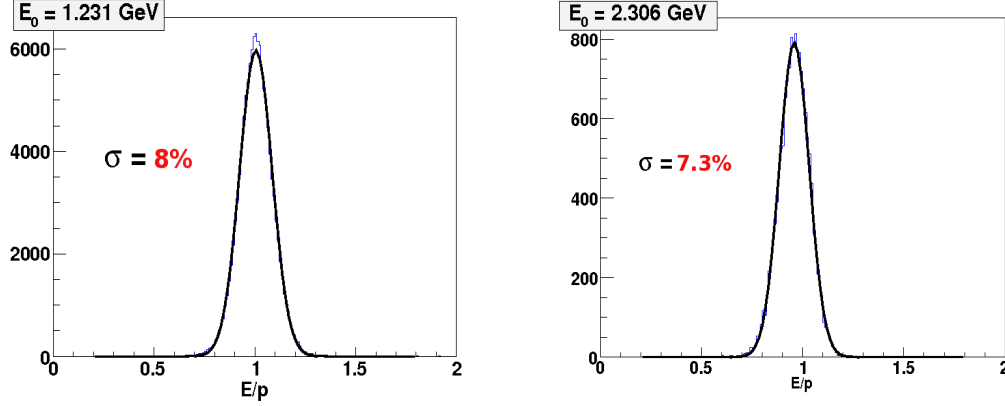


Figure 5.10: $\frac{E}{p}$ for the electrons in the preshower and shower detectors for two different incident beam energies. E is the total energy deposited by the electron having momentum p .

5.3 Detector Efficiency Study

The detector efficiency study includes the particle identification efficiencies of different detector packages with respect to the various cuts applied in the analysis. This was done extensively for each of the particle identification detectors. The efficiency study was very important in order to select the hadrons in the LHRS and the electrons in the BigBite as effectively as possible since the experiment was statistically limited. Hence proper and efficient cuts on different detectors were essential. The particle identification efficiencies for the detectors are presented in the following.

5.3.1 Gas Čerenkov (GC) Efficiency in the LHRS

The GC detector in the LHRS was used to reject electrons which were the largest background in the detection of hadrons (pions and kaons). A GC cut efficiency study was performed in order to find an efficient rejection of the electrons and at the same time to have a reasonable detection efficiency for pions and kaons. The rejection efficiencies of the electrons and the detection efficiencies of the hadrons were evaluated with different cuts on the GC detector ADC sum spectra. Once the calibrations of the GC detector and the lead-glass counters were done, the lead-glass counters were used to determine the efficiency of the GC. Two kinds of efficiencies can be defined as follows :

- **Electron rejection efficiency:** To determine the electron rejection efficiency, a very tight two dimensional graphical cut was applied to choose the electrons in the lead

glass counters. Figure 5.11 shows the energy in lead glass layer 1 vs. energy in layer 2 and the graphical cut sections. Let N_e denote the number of electrons chosen in the graphical cut A. Then this cut was used in the GC detector ADC sum spectrum to find the number of electrons triggered by the cut. Let this number be represented by N_{gce} . Then the electron rejection efficiency can be defined as :

$$\varepsilon_R = 1 - \frac{N_{gce}}{N_e} \quad (5.6)$$

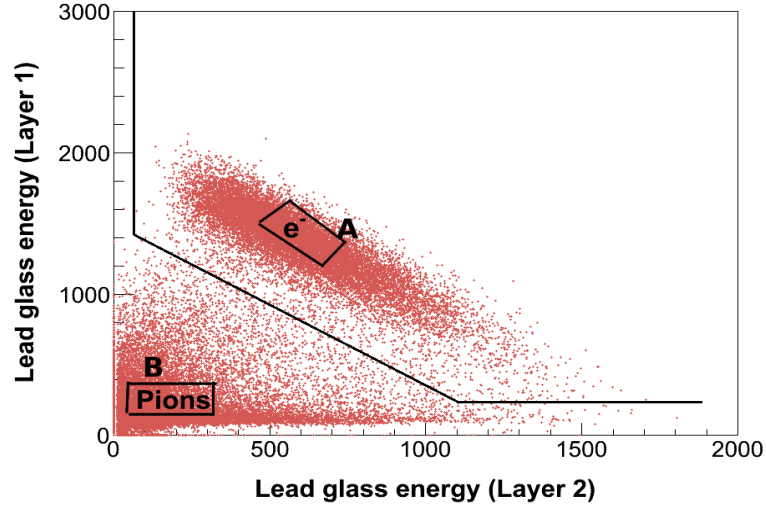


Figure 5.11: The lead glass layer 1 and layer 2 energies. The graphical cuts used in the analysis are also shown.

- **Pion detection efficiency:** To determine the pion rejection efficiency, a very tight two dimensional graphical cut was applied to choose the pions in the lead glass counters as shown in Fig. 5.11. Let N_{pion} denote the number of pions chosen in the graphical cut B. Then this cut was used in the GC detector ADC sum spectrum to see the number of pions triggered by the cut. Let this number be represented by N_{gcpi} . The pion detection efficiency can be defined as :

$$\varepsilon_D = \frac{N_{gcpi}}{N_{pion}} \quad (5.7)$$

The typical response of the Gas Čerenkov detector to the cuts applied in the lead glass counters is shown in Fig. 5.12.

ε_R and ε_D were determined for different cuts in the GC detector ADC sum spectrum as shown in Fig. 5.13. Here a cut >150 on the Aerogel Čerenkov detector ADC sum was

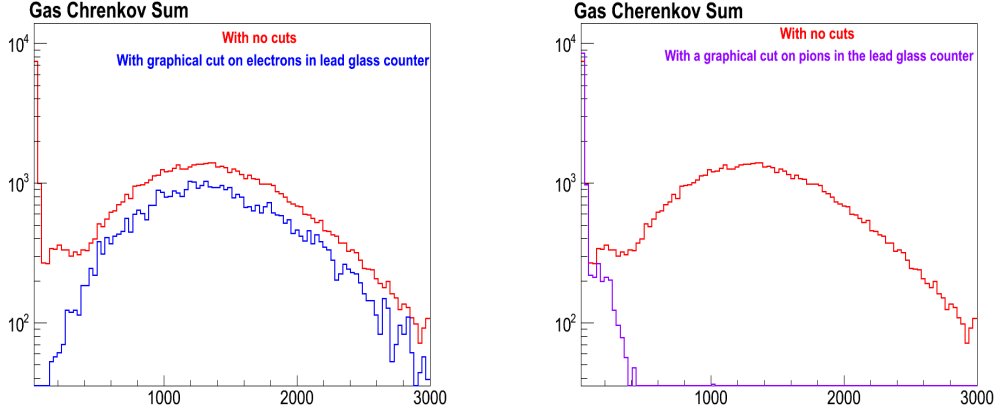


Figure 5.12: The Gas Čerenkov detector response to the lead glass counter cuts. The left figure shows the comparison of a typical GC spectrum and a GC spectrum triggered by the electrons chosen in the lead glass counters. The right figure shows a comparison of a typical GC spectrum and a GC spectrum triggered by the pions chosen in the lead glass counters.

applied. Fig. 5.14 shows the same analysis except no Aerogel cut was applied. The pion detection efficiency increased as the Aerogel cut was removed while the electron rejection remained almost the same. In our final analysis of the physics asymmetries, a GC detector cut <250 was applied on the ADC sum, the single photo-electron peak being at channel 200. The efficiencies are summarized in the Table 5.1:

Table 5.1: Gas Čerenkov detector efficiencies with the standard cut on the ADC sum (<250).

A1 cut	$\varepsilon_R(\%)$	$\varepsilon_D(\%)$
No A1 cut	98.7	96.8
A1 >150	98.8	90.3

5.3.2 Lead Glass Counter Efficiency

The lead glass counters, commonly known as the pion-rejector, were used as an additional particle identification detector to choose the pions and reject the electrons in the LHRS. Similar to the GC detector efficiency analysis, the pion rejector efficiency was determined by treating the GC as a reference. The two types of efficiencies are defined as follows :

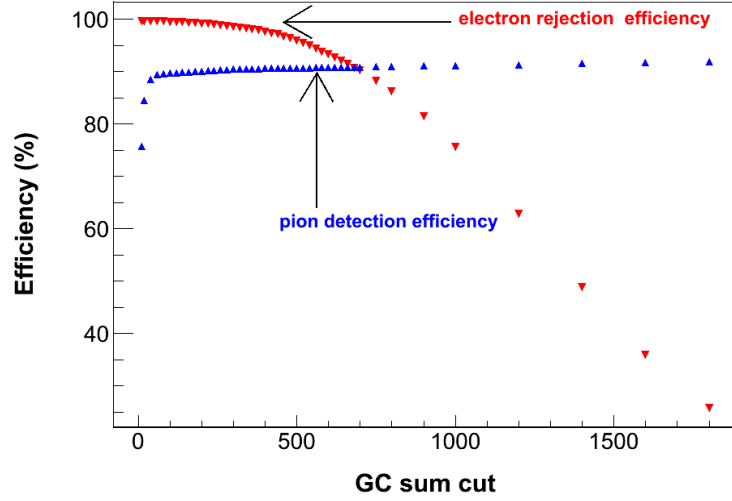


Figure 5.13: The Gas Čerenkov detector efficiencies with the standard Aerogel ADC sum cut > 150 .

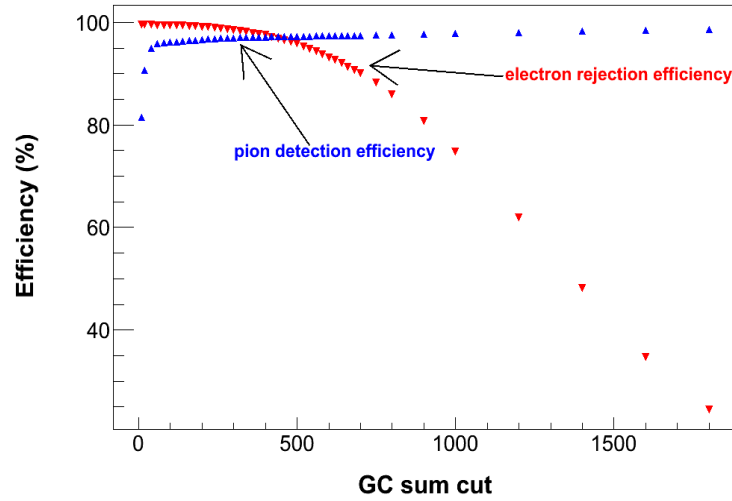


Figure 5.14: The Gas Čerenkov detector efficiencies without any Aerogel detector ADC sum cut.

- **Electron rejection efficiency** : The electron rejection efficiency, analogous to Eq.(5.6), is defined as :

$$\varepsilon_R = 1 - \frac{N_{pre}}{N_e}, \quad (5.8)$$

where N_e is the number of electrons chosen after putting a tight cut on the GC detector ADC sum spectrum (>1100) and N_{pre} is the number of electrons triggered

by the same cut in the pion rejector $\frac{E}{p}$ spectrum.

- **Pion detection efficiency** : The pion detection efficiency, analogous to Eq.(5.7) is defined as :

$$\varepsilon_D = \frac{N_{prpi}}{N_{pion}}, \quad (5.9)$$

where N_{pion} is the number of pions chosen after putting a tight cut on the GC detector ADC sum spectrum (<200) and N_{prpi} is the number of pions triggered by the same cut in the pion rejector $\frac{E}{p}$ spectrum.

Both ε_R and ε_D were determined for various cuts in the pion rejector $\frac{E}{p}$ spectrum as shown in Fig. 5.15. A cut <0.60 was chosen as a standard cut for our final analysis to select the pions in the pion rejector. The efficiencies corresponding to that cut are summarized in the following Table 5.2:

Table 5.2: Lead glass detector efficiencies with the standard cut on $\frac{E}{p} < 0.6$.

A1 cut	$\varepsilon_R(\%)$	$\varepsilon_D(\%)$
No A1 cut	95.2	98.6
A1>150	96	98.6

The typical response of the lead glass counters to cuts on the Gas Čerenkov is shown in Fig. 5.16 and Fig. 5.17.

5.3.3 Aerogel (A1) Efficiency

The Aerogel Čerenkov detector was used to separate pions from kaons. In addition to A1, the coincidence-time-of flight and the RICH detector were used for particle identification of pions and kaons. The coincidence-time-of-flight spectrum was taken as a reference to study the efficiency of A1 detector. In this study, a cut of ± 0.5 ns was applied to the pion peak as shown in the Fig. 5.18 and the the number of pions triggered by that cut in the A1 detector ADC sum spectrum was calculated for various cuts. The pion detection efficiency is then defined as :

$$\varepsilon_D = \frac{N_{A1}}{N_{pion}} \quad (5.10)$$

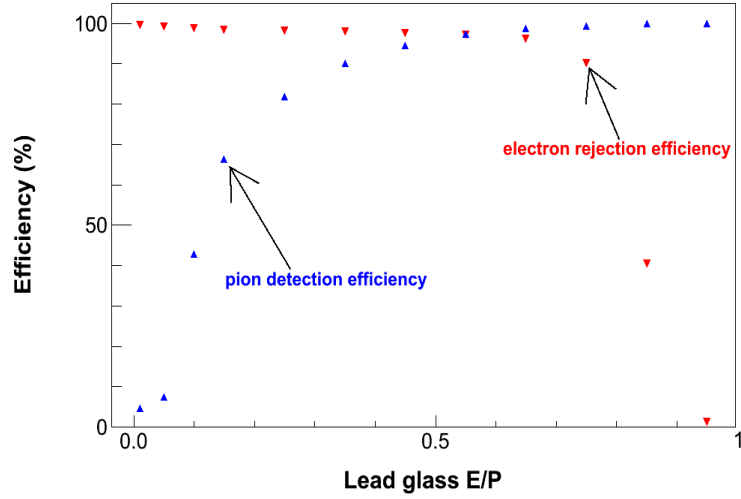


Figure 5.15: The lead glass counter efficiencies with a standard Aerogel detector ADC sum cut >150 .

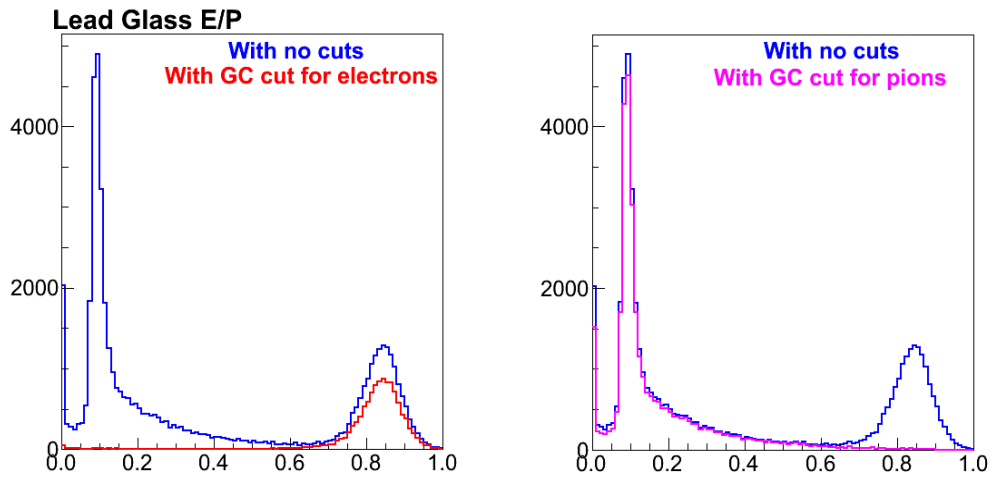


Figure 5.16: $\frac{E}{p}$ spectra of the lead-glass counter with different GC detector cuts.

where N_{pion} is the number of pions selected in the coincidence spectrum (variable CT.pi.t) and N_{A1} is the number of pions triggered by the respective cut in A1. The pion detection efficiencies of A1 detector are shown in Fig. 5.19 as a function of the cuts on the ADC sum for both polarities of the LHRS. A cut of an ADC sum >150 for A1 detector was chosen as the standard cut for the final analysis to choose the pions. The pion detection efficiency ε_D was $\sim 98\%$.

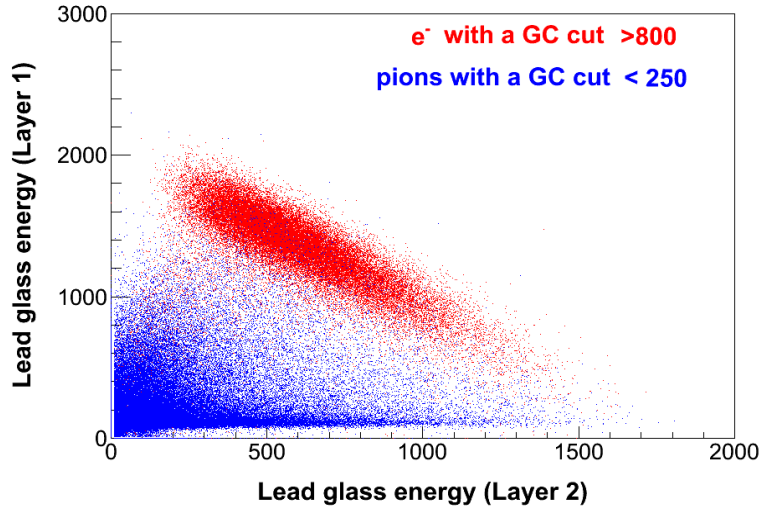


Figure 5.17: The energy of lead glass layer 1 vs. the energy of layer 2 with different GC detector cuts.

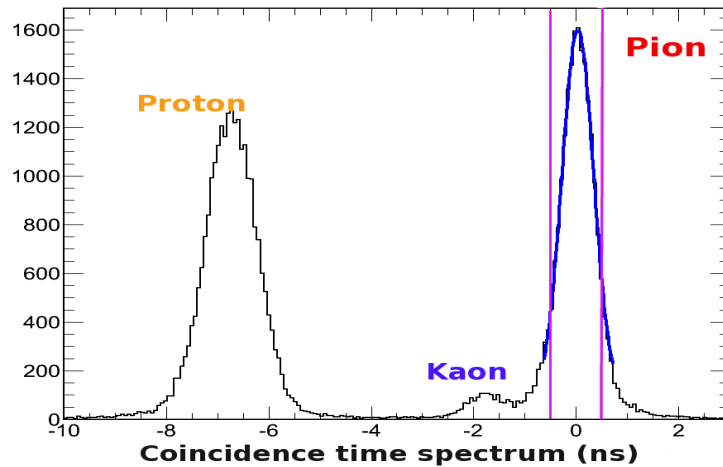


Figure 5.18: The (e' , π) coincidence time spectrum. The pink lines show the cut region to select coincidence pions. This plot corresponds to the coincidence spectrum for the hadrons when the LHRS polarity was positive and hence, there is a proton peak on the left, ~ 7 ns away from the pion peak.

Along with this detector efficiency study, a contamination study was also performed in both the LHRS and the BigBite spectrometer which is discussed in the following section.

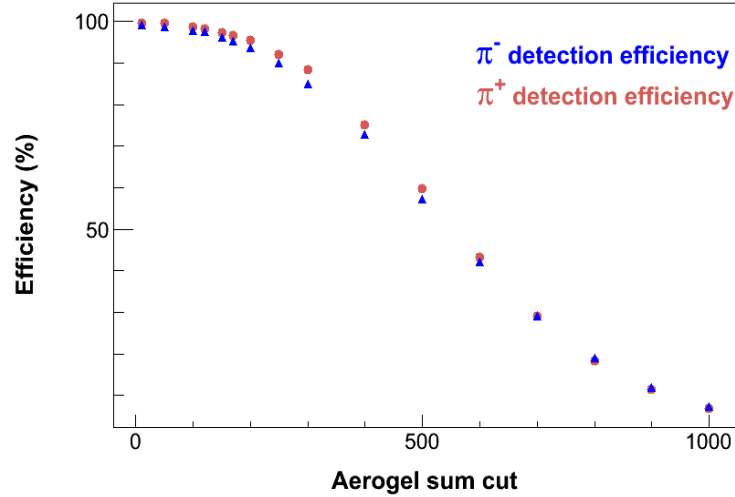


Figure 5.19: The A1 detector pion detection efficiencies as a function of ADC sum cuts.

5.4 LHRS Contamination Study

Different types of contamination studies were performed as part of the data analysis. During the experiment, the data taking process was divided equally using the two polarities of the LHRS : negative and positive. In the negative polarity mode, the electrons were the largest background to the hadrons (pions and kaons) and in the positive polarity mode, the protons were the largest background. In addition, the hadron identification process treated the kaons as contamination to the pions and vice versa. In this section, a different contamination analysis will be discussed. The analysis presented here involves only the standard detector cuts described in the earlier sections which were applied in all the physics analyses.

5.4.1 Electron Contamination to Pions

In order to determine the electron contamination to pions, the Gas Čerenkov detector and the lead glass counters were used in the analysis and the contamination in both detectors were combined to get the resultant contamination in the LHRS with negative polarity. In the analysis, both T3 (LHRS singles) and T5 (coincidence) events were treated separately.

Electron contamination in the Gas Čerenkov detector

In order to determine the contamination of electrons to the pions in the Gas Čerenkov detector (GC) using the standard cut (ADC sum <250), an electron sample in the lead

glass counter was chosen with an $\frac{E}{p}$ cut >0.6 and a standard Aerogel detector ADC sum cut >150 . The GC sum is plotted in a histogram, say $hGC(4000, 0, 4000)$, with the cuts mentioned above where the first number in the parentheses is the bin number and the second and the third represent the minimum and maximum of the range. Then a number N_{GC} can be defined such that :

$$N_{GC} = \int_0^{250} (hGC)dx, \quad (5.11)$$

where the bins (x) 0 to 250 are integrated in the histogram⁵. Another histogram with the reconstructed vertex is generated, say $h2(1, -0.2, 0.2)$ with the same set of cuts applied to histogram hGC and the total number of events (N) in the histogram is obtained.

Then, the electron contamination to the pion sample in the Gas Čerenkov detector with the ADC sum cut < 250 is defined as :

$$[\alpha_{e^- \rightarrow \pi^-}]_{T3} = \frac{N_{GC}}{N}, \quad (5.12)$$

$$[\alpha_{e^- \rightarrow \pi^-}]_{T5} = \frac{N_{GC}}{N}, \quad (5.13)$$

where T3 and T5 correspond to the respective triggers for which the events were chosen. It was found in our experiment with all the standard cuts, $[\alpha_{e^- \rightarrow \pi^-}]_{T3} = 0.013$ and $[\alpha_{e^- \rightarrow \pi^-}]_{T5} = 0.028$.

Electron contamination in the Lead glass counters

In order to determine the contamination of electrons to the pions in the lead glass counters using the standard cut ($\frac{E}{p} < 0.6$), an electron sample in the Gas Čerenkov detector was chosen with an ADC sum cut >250 and a standard Aerogel ADC sum cut >150 . The lead glass $\frac{E}{p}$ is plotted in a histogram, say $hLG(120, 0, 1.2)$, with the cuts mentioned above where the first number in the parentheses is the bin number and the second and the third represent the minimum and maximum of the range as explained in the case of the GC. Then a number N_{LG} can be defined such that :

$$N_{LG} = \int_0^{60} (hLG)dx \quad (5.14)$$

⁵The integration is done over the bins in the histogram. The histogram is binned in such a way that each bin contains one ADC channel.

Similar to the case of GC, a normalization number N is obtained from a histogram with the reconstructed vertex using the same cuts applied to hLG. Then, the electron contamination to the pion sample in the lead glass counters with $\frac{E}{p}$ cut < 0.6 is defined as :

$$[\beta_{e^- \rightarrow \pi^-}]_{T3} = \frac{N_{LG}}{N}, \quad (5.15)$$

$$[\beta_{e^- \rightarrow \pi^-}]_{T5} = \frac{N_{LG}}{N} \quad (5.16)$$

In E06010, the values of $[\beta_{e^- \rightarrow \pi^-}]_{T3}$ and $[\beta_{e^- \rightarrow \pi^-}]_{T5}$ were found out to be 0.03 and 0.06, respectively.

Hence, using both detectors together, the final contamination of the electrons to the pions in the LHRS can be expressed as :

$$[\gamma_{e^- \rightarrow \pi^-}]_{T3} = [\alpha_{e^- \rightarrow \pi^-}]_{T3} \times [\beta_{e^- \rightarrow \pi^-}]_{T3} = 0.0004, \quad (5.17)$$

$$[\gamma_{e^- \rightarrow \pi^-}]_{T5} = [\alpha_{e^- \rightarrow \pi^-}]_{T5} \times [\beta_{e^- \rightarrow \pi^-}]_{T5} = 0.0016 \quad (5.18)$$

5.4.2 Pion Contamination to Electrons

Similar to the electron contamination study to pions, the Gas Čerenkov detector and lead glass counters were used to determine the pion contamination to the electrons in the LHRS. The same procedure was employed in this case except different cuts were applied to the detectors to choose pions instead of electrons in the reference detector. The final contamination of the pions to electrons in LHRS can be expressed as :

$$[\gamma_{\pi^- \rightarrow e^-}]_{T3} = [\alpha_{\pi^- \rightarrow e^-}]_{T3} \times [\beta_{\pi^- \rightarrow e^-}]_{T3} = 0.0002, \quad (5.19)$$

$$[\gamma_{\pi^- \rightarrow e^-}]_{T5} = [\alpha_{\pi^- \rightarrow e^-}]_{T5} \times [\beta_{\pi^- \rightarrow e^-}]_{T5} = 0.0002, \quad (5.20)$$

where α (β) is the pion contamination to the electrons in the Gas Čerenkov (Lead-glass) detector⁶.

5.5 BigBite Optics

The BigBite optics module can be used to reconstruct the particle (electrons, negative pions, etc.) kinematics information when it leaves the target. Two beam energy settings ($E_0=1.230$ GeV and $E_0=2.396$ GeV) were used to perform the calibrations. The optics

⁶ $[\alpha_{\pi^- \rightarrow e^-}]_{T3} = 0.013$, $[\alpha_{\pi^- \rightarrow e^-}]_{T5} = 0.009$, $[\beta_{\pi^- \rightarrow e^-}]_{T3} = 0.020$ and $[\beta_{\pi^- \rightarrow e^-}]_{T5} = 0.023$

data quality were further checked with beam energy of 5.892 GeV. The vertex reconstruction was done with multi-foil carbon targets. The exact positions of the foils were known from a survey report which were used as a reference. On the other hand, the momentum reconstruction was done using the elastic $H(e, e')X$ scattering while a sieve slit plate was put in front of the magnet for the angular reconstruction.

The first order BigBite optics model treated the BigBite spectrometer as a perfect dipole magnet. The first order momentum is defined as [18] :

$$p = L \left[2 \cdot \sin\phi \cdot \tan\left(\frac{\theta}{2}\right) \right]^{-1}, \quad (5.21)$$

where L is the distance travelled by the scattered particle inside the magnetic field \vec{B} , θ is the bending angle for the particle in a plane perpendicular to \vec{B} , and ϕ is the angle between \vec{B} and the momentum p . The vertex reconstruction, the angle reconstruction, and the momentum reconstruction procedures are summarized below. Details can be found in [18].

- **Vertex reconstruction :** The vertex reconstruction was done taking into account the higher order correction terms and their dependences on the hit position, direction, and the bend angle of the reconstructed tracks with momentum reconstruction in the three dimensional phase space. The final vertex reconstruction is shown in Fig. 5.20 The resolutions are ~ 1 cm at a momentum of 0.95 GeV/c and ~ 0.77 cm at a momentum of 1.2 GeV/c.
- **Angle reconstruction :** The angle reconstruction was done by putting a sieve slit plate (1.5 inches thick) in front of the magnet and reconstructing the hole pattern in it by connecting the final vertex reconstruction and the hypothetical middle point in the BigBite optics model. A vertical bending plane was assumed to exist in the middle of the BigBite magnet and the reconstructed track from the wire chamber would have an interception point in the middle plane. In other words, the reconstructed track would cross the plane at some point and then it gets bent. This point is termed as the hypothetical middle point. Fig. 5.21 shows the sieve slit pattern after the first order correction (left), after the addition of the offsets (middle) and after the higher order corrections (right). The red points show the real sieve slit holes and the black points are the reconstructed ones. Details can be found in [18].

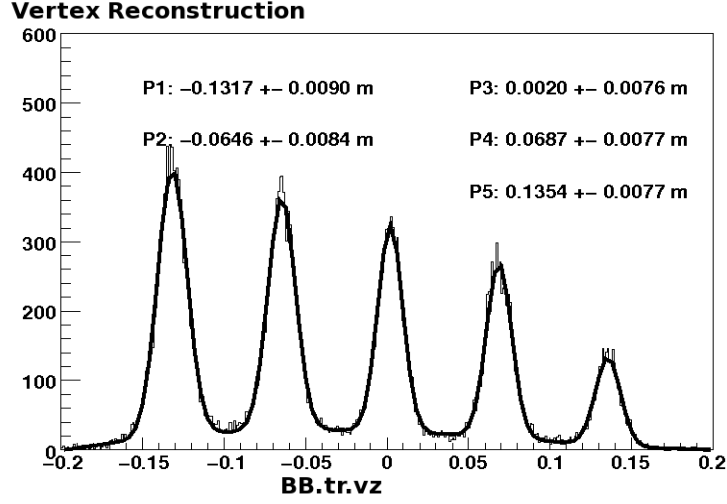


Figure 5.20: The BigBite vertex reconstruction at a momentum of 1.2 GeV/c.

- **Momentum reconstruction :** The momentum calibration range of the BigBite spectrometer (0.8 GeV/c to 2.2 GeV/c) was covered by the two elastic energy settings as mentioned earlier. The detailed procedure of the calibration can be found in [18]. One of the important steps involved in this procedure was the energy loss effect for both the beam and the scattered electrons while traveling through different materials along the path. The energy loss can be approximated by the following equation :

$$\frac{p_{loss}}{p_0} = 0.492 \cdot \exp\left(-\frac{L}{X_0}\right), \quad (5.22)$$

where L is thickness of the material traversed by the electron with initial momentum p_0 and X_0 is the radiation length. The factor 0.492 is obtained by comparing the average value and the peak value of the Landau distribution of the energy loss. Taking into account all the energy loss effects and selecting the elastic electrons, the momentum was reconstructed to first order as follows:

$$p^{(1)} = z_0 \cdot p^{(1)} + z_1 + z_2 \cdot tr_x + \frac{z_3}{\theta}, \quad (5.23)$$

where z_0 , z_1 , z_2 and z_3 are functions of the middle point positions [18] and tr_x is the hit position in the first VDC plane. A momentum resolution of $\sim 1\%$ for the entire momentum range was achieved as shown in Fig. 5.22.

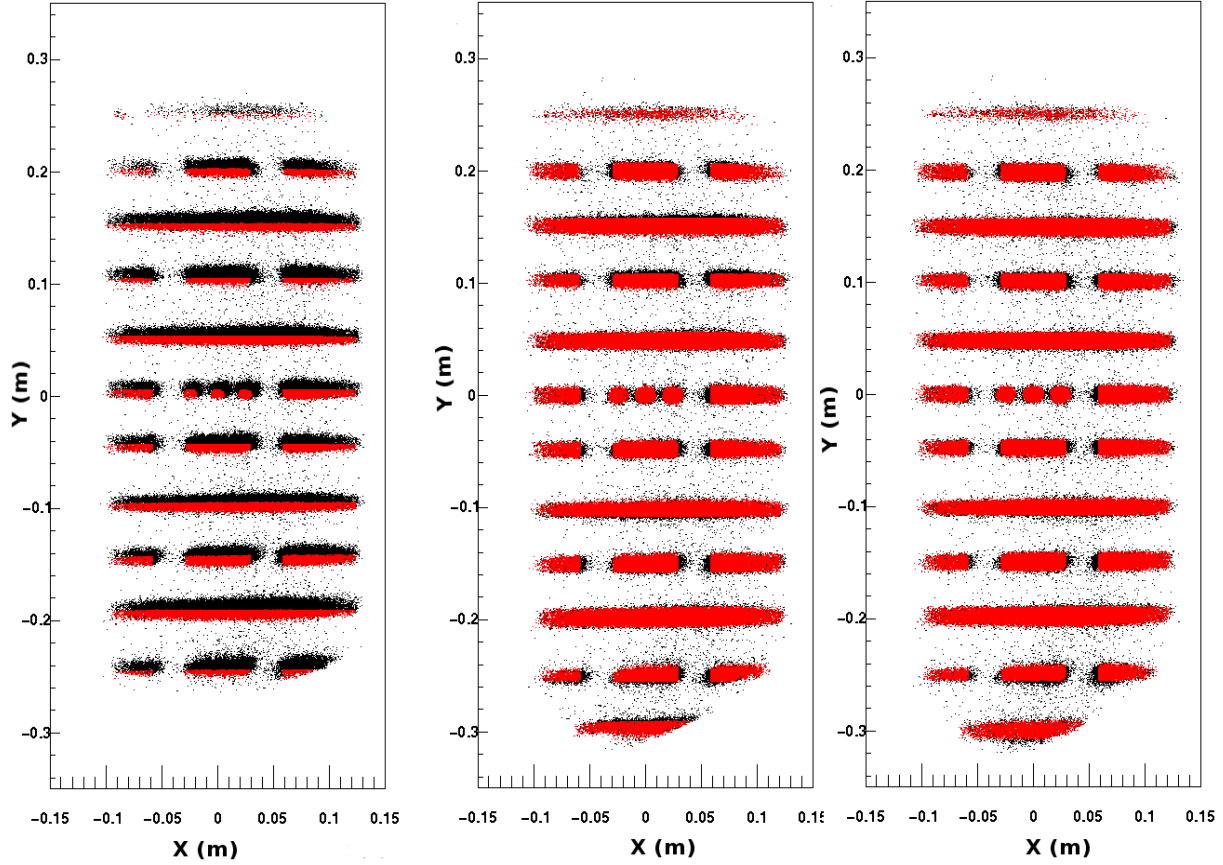


Figure 5.21: The reconstructed sieve plate with different correction terms [18].

5.6 LHRS Optics Calibration

The scattered particles entering the LHRS acceptance need to be reconstructed to the target very carefully to make sure that they come from the reaction vertex. The goal of the optics calibration involved the calibration of the following optics variables that can be defined for a fixed beam position (x, y) :

- θ_{tg} and ϕ_{tg} : These two out-of-plane and in-plane angles determine the angular information of the Semi-inclusive Deep Inelastic Scattering (SIDIS) hadrons and the angular separation of the asymmetries involved.
- y_{tg} and z_{react} : y_{tg} is the position of the reaction point in the LHRS frame and z_{react} is the reconstructed vertex point. These are essential for the vertex coincidence

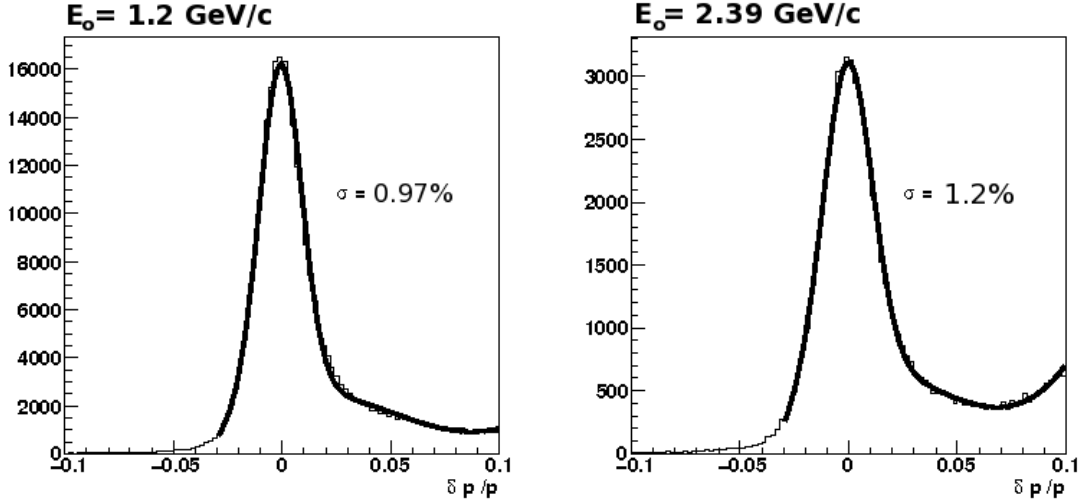


Figure 5.22: The BigBite spectrometer momentum reconstructions at beam energies of 1.200 GeV/c and 2.396 GeV/c.

condition with the BigBite spectrometer to suppress random coincidence background.

- δ_{tg} : δ_{tg} is the momentum fraction $\frac{dp}{p}$ which is important in the elastic asymmetry studies and pressure curve analyses for better background subtraction as will be discussed later.

Similar to the BigBite optics study, the multi-foil carbon target (7 foils termed “optics target”) was used for the optics calibration. Data were taken with a sieve slit plate placed at the entrance of the LHRS similar to the BigBite optics calibration. In addition, elastic reference cell runs of ^3He , H_2 , and N_2 gases were used for different calibrations. A new optimization routine was developed [19] and implemented using MINUIT⁷. The details of the calibration procedure can be found in Refs. [19] and [117]. Here a brief summary of the process is presented:

- **Vertex reconstruction** : The reaction vertex z_{react} was calibrated with reference to the carbon foil positions from the survey report. Fig. 5.23 shows how well the carbon foil peaks were reconstructed as compared to their actual positions. The average resolution was ~ 6 mm. The reaction vertices for the LHRS and the BigBite agree to a level of 1 cm (1σ) for the coincidence case.

⁷Minimization tool available in the ROOT [116] software package.

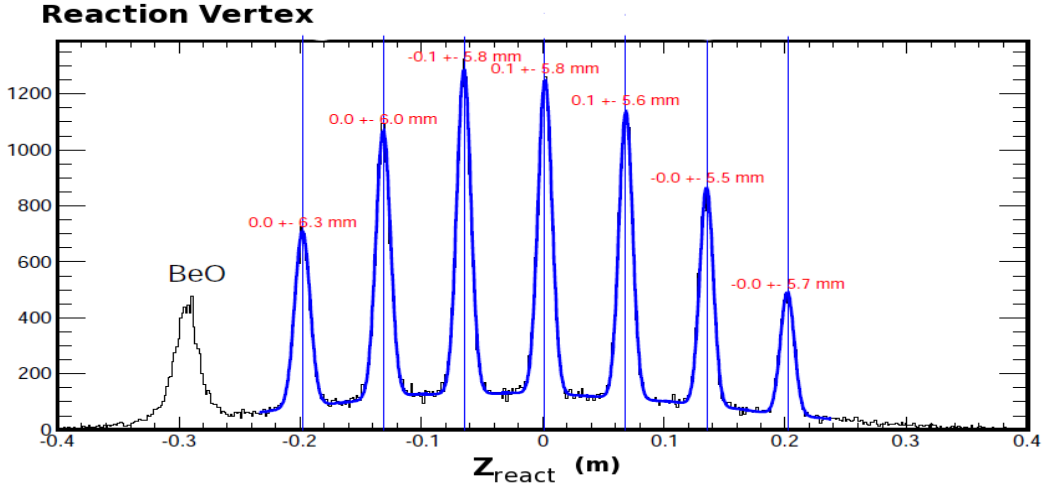


Figure 5.23: The z-component of the LHRs reaction vertex: each of the carbon foil peaks was fitted and compared to the actual position from the survey report.

- **Angle reconstruction** : Similar to the BigBite optics analysis, the carbon foil runs with the sieve slit plate inserted in front of the LHRs entrance were used to calibrate the angles. The angles θ_{tg} and ϕ_{tg} were optimized by minimizing the difference between the calculated angle and the actual one from the survey report. The final reconstruction of the sieve pattern is shown in Fig. 5.24.
- **Momentum reconstruction** : The momentum calibration was done using a similar set of runs as used in case of angle reconstruction. The full momentum range of the LHRs was covered by moving the carbon elastic peak across the focal plane in a momentum scan, called δ -scan: $\frac{dp}{p_0} = 0\%$, $\pm 2\%$ and $\pm 4\%$. For each momentum setting, the carbon ground state or a specific excited state was selected. The resolution achieved was better than 0.05%.

5.7 Coincidence Time-of-Flight

E06010 measured Single Target Spin Asymmetries of the final state hadrons which were detected in the LHRs coincident with the electrons detected in the BigBite spectrometer. The coincidence times of detecting different types of hadrons and electrons are different and can be used as a powerful particle identification technique to separate different types of hadrons in the LHRs. In our case, the hadrons include pions and kaons which can be

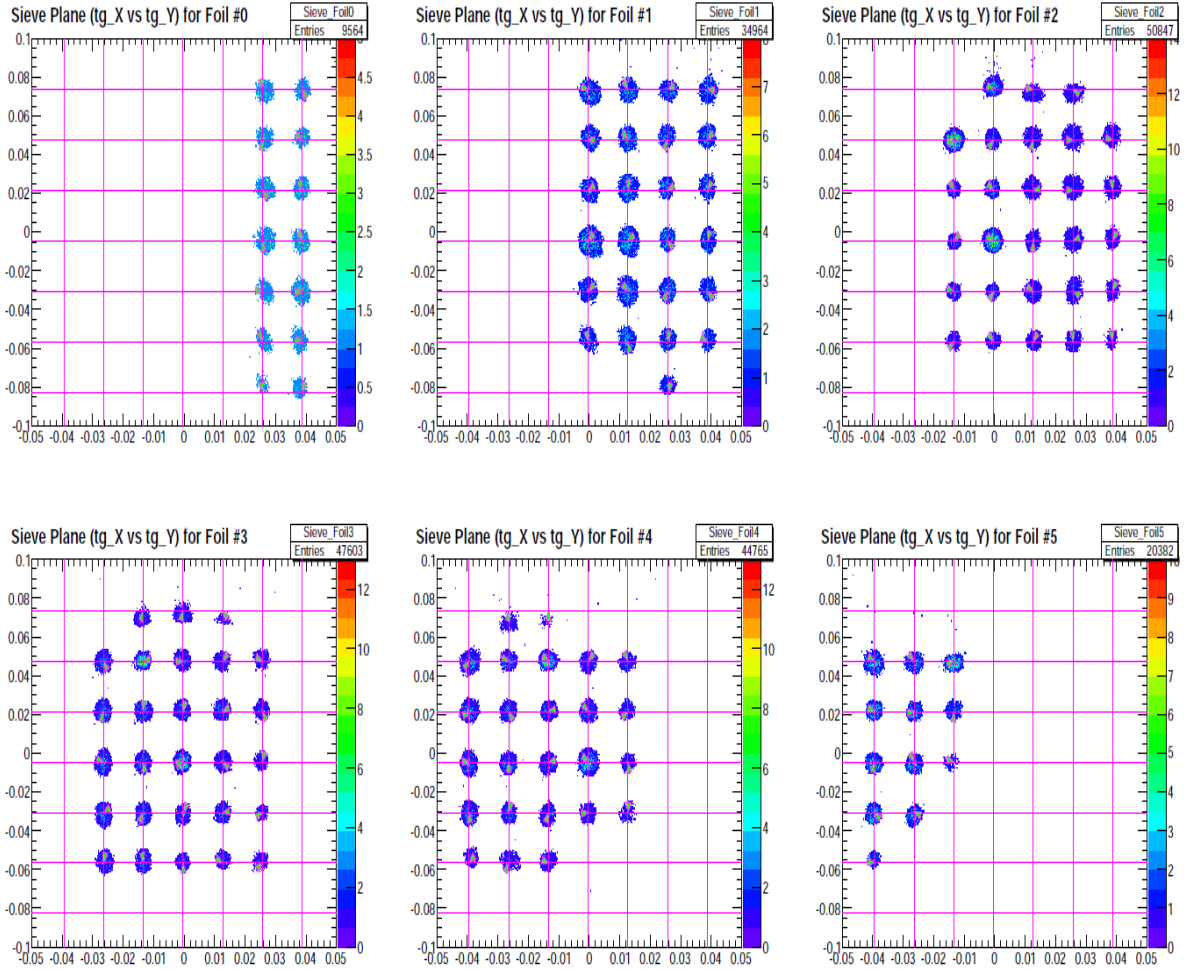


Figure 5.24: The reconstructed LHRs sieve slit plate.

identified using the coincidence time-of-flight technique in addition to the other particle identification detectors such as the Aerogel gas Čerenkov and the RICH detector. In order to implement this method to identify hadrons that were coincident with the electrons, both the two spectrometers had to be calibrated independently and in this section, a detailed analysis of the calibrations is presented.

Basic Formalism:

The coincidence time (CT) between the two spectrometers (LHRs and BigBite) is defined as the time difference between the two particles are created in the reaction at the vertex. If a pion is generated and detected in the LHRs at a time T_{pion} and an electron is generated

and detected in the BigBite spectrometer at a time T_e , then the coincidence time is defined as

$$CT = T_{pion} - T_e - C, \quad (5.24)$$

where C is a constant which includes various timing offsets and triggers for both spectrometers. The calibration for each detector involves determining and extracting the different quantities in the above equation. As such, it is obvious that for a perfect system, the CT spectrum should show a sharp peak at $CT = 0$ which implies that if for instance, a pion and an electron are generated at the same time in the scattering reaction, the CT spectrum for these two particles would have a peak at 0 with the proper offsets (C) corrected. Now for different types of hadrons in the final state, the CT spectrum should show multiple peaks at different timing locations. For example, if we calibrate the pion-electron CT spectrum to be peaked at 0 ns, the kaon-electron or the proton-electron CT peak would be separated by specific time from 0 ns depending on the time-of-flight of the kaon or proton. To be specific, in our case the CT spectrum shows the peak of the kaon-electron coincidence separated by ~ 1.8 ns and that of the proton-electron coincidence separated by ~ 6 ns relative to the pion-electron peak. Thus, the CT calibration involves the alignment of the pion-electron CT peak to 0 ns as well as minimizing the width of the peak which not only improves the hadron particle identification in the LHRS, but also greatly reduces the random coincidence background.

In the analysis, the CT between the LHRS and BigBite is defined as:

$$CT = RF_{LHRS} - RF_{BigBite} - \Delta_{trigger}, \quad (5.25)$$

where $RF_{LHRS/BigBite}$ is defined as the amount of time between a vertex reaction and single arm trigger, and $\Delta_{trigger}$ is the time difference between the two single arm triggers. The $RF_{LHRS/BigBite}$ includes contributions from the following factors:

- **Time-of-flight** : The amount of time the particle takes from the reaction vertex to reach the detector timing plane (in our case, the S2m scintillator plane) depends on the path length of the particle to reach a certain detector from the target.

- **Response time:** This includes the detector timing response, cable delay, electronic processing delay, etc.
- Time difference between the detector timing signal and the trigger signal. These values were recorded using high resolution TDCs (50 ps for the LHRS and 60 ps for BigBite).

In the analysis, $RF_{LHRS/BigBite}$ is defined in terms of the beam radio frequency (RF) signal relative to the single arm trigger and it has a structure of sharp (Gaussian like) peaks every 2 ns. Each peak is a beam bunch separated by 2 ns. The $RF_{LHRS/BigBite}$ is calibrated separately for each arm by minimizing the width of these peaks (beam bunches).

5.7.1 LHRS Timing Calibration

In the LHRS, the time reference was defined by the S2m scintillators. The 2 ns RF structure of the beam bunch was used as a reference for the entire analysis and it can be defined as

$$RF_{LHRS} = t_{RF} - \frac{(t_L + t_R)}{2} + \frac{Pathlength}{c}, \quad (5.26)$$

where t_{RF} is the RF signal recorded in the TDCs relative to the single arm trigger, $t_{L/R}$ is the time of a hit recorded in the left/right TDCs corrected for time offsets and timewalk (see below) and $Pathlength$ is the corrected pathlength of the particle in the LHRS determined from the target vertex to the S2m scintillator plane. As can be seen from the above equation, various corrections have to be implemented in order to minimize the timing resolution to a level of a few hundred picoseconds in the RF structure. In the following subsections, each of the corrections will be discussed in detail.

Pathlength correction

The LHRS pathlength can be expressed in general as:

$$L = L_0 + a1 \cdot x + a2 \cdot x^2 + a3 \cdot \theta + a4 \cdot \theta^2 + a5 \cdot y + a6 \cdot y^2 + a7 \cdot \phi + a8 \cdot \phi^2, \quad (5.27)$$

where the variables x , θ , y and ϕ are the coordinates of the particle in the TRANSPORT convention as described in Ref. [12]. L_0 is the constant term which is the distance from the vertex to the S2m scintillator plane and is measured to be 25.7 m. It is worth mentioning here that the dependences of the pathlength on x and θ were relevant upto second order

while the dependences on y and ϕ could be ignored in the analysis as they were negligibly small. However, the above equation can be expressed up to any order for all the variables including the cross terms depending on the kinematic settings as well as the requirements of the experiment. The terms up to second order are only specific to our experiment. The objective of the pathlength calibration was to determine the coefficients ($a1$ to $a8$) by looking at the dependences of the quantity RF_{LHRS} on all the variables mentioned above.

Two methods were used to determine these dependences of the RF on different variables. One was to look at the RF as a function of θ first since the dependence on θ was the strongest of all. Once fitted with a second order polynomial and corrected for it, the RF was then plotted as a function of x . Then it was fitted again with a second order polynomial for x and corrected. Thus, once both θ and x were corrected for, there remained a very little to do as the dependences on y and ϕ were really small and could be neglected. The other method involved the minimization of the width of the RF structure by varying all the parameters (x, θ, y and ϕ) together. A MINUIT based code was written specifically for this analysis. Both methods were reasonably consistent with each other and only x and θ corrections were applied finally. No corrections were applied to y and ϕ . Figure 5.25 and Fig. 5.26 show the RF structure before and after the pathlength corrections as a function of x, θ, y and ϕ . Note that each of the corrected plots are with all the corrections applied and not with the individual correction for each term.

Time offset calibration and timewalk correction

Consider Eq.(5.26) where we have two terms t_L and t_R corresponding to the corrected times of a hit at a particular paddle on both the left and right sides (TDCs). These can be defined as follows:

$$t_L = t_{L.raw} - t_{L.off} - t_{L.tw}, \quad (5.28)$$

$$t_R = t_{R.raw} - t_{R.off} - t_{R.tw}, \quad (5.29)$$

where $t_{L.raw(R.raw)}$ is the raw time recorded by the left(right) TDC, $t_{L.off(R.off)}$ is the offset corresponding to left(right) TDC and $t_{L.tw(R.tw)}$ is the timewalk correction to the left(right) TDC. All these corrections were applied to each paddle separately for both left and right photomultiplier tubes (PMTs) each of which was connected to an ADC and a TDC.

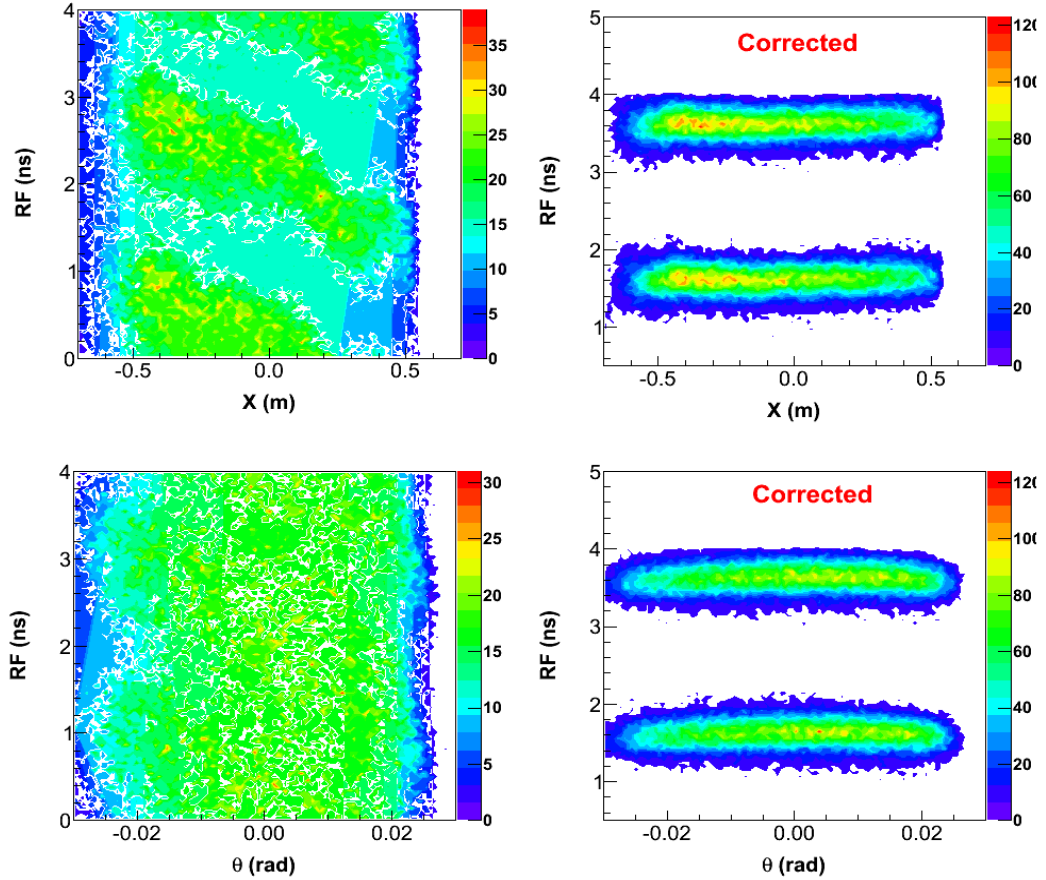


Figure 5.25: The x and θ dependences of RF without (left) and with (right) pathlength corrections.

The time offset calibration of each paddle in the S2m plane involved making corrections to the raw time measured by the TDC for the different hit positions along the bar and for different cable length delays. The corrections were done to both TDCs in each paddle, i.e., the offsets were determined separately for left and right TDCs. For the offset calibration, only those events were chosen which fire two adjacent bars together. We called those events *two-bar-hit events* with tight ADC cuts. The alignment of the time offsets of the paddles in S2m as well as the aligned projections of the x positions of the tracks in the paddles are shown in Fig. 5.27.

The timewalk effect is caused by the dependence of the TDC signals on the ADC amplitudes. A large ADC amplitude and a small ADC amplitude have TDC signals at different times and there is a linear dependence of the TDC signals on the ADC amplitudes. This effect is of the order of a few picoseconds (20 ps to 30 ps). The timewalk is defined as

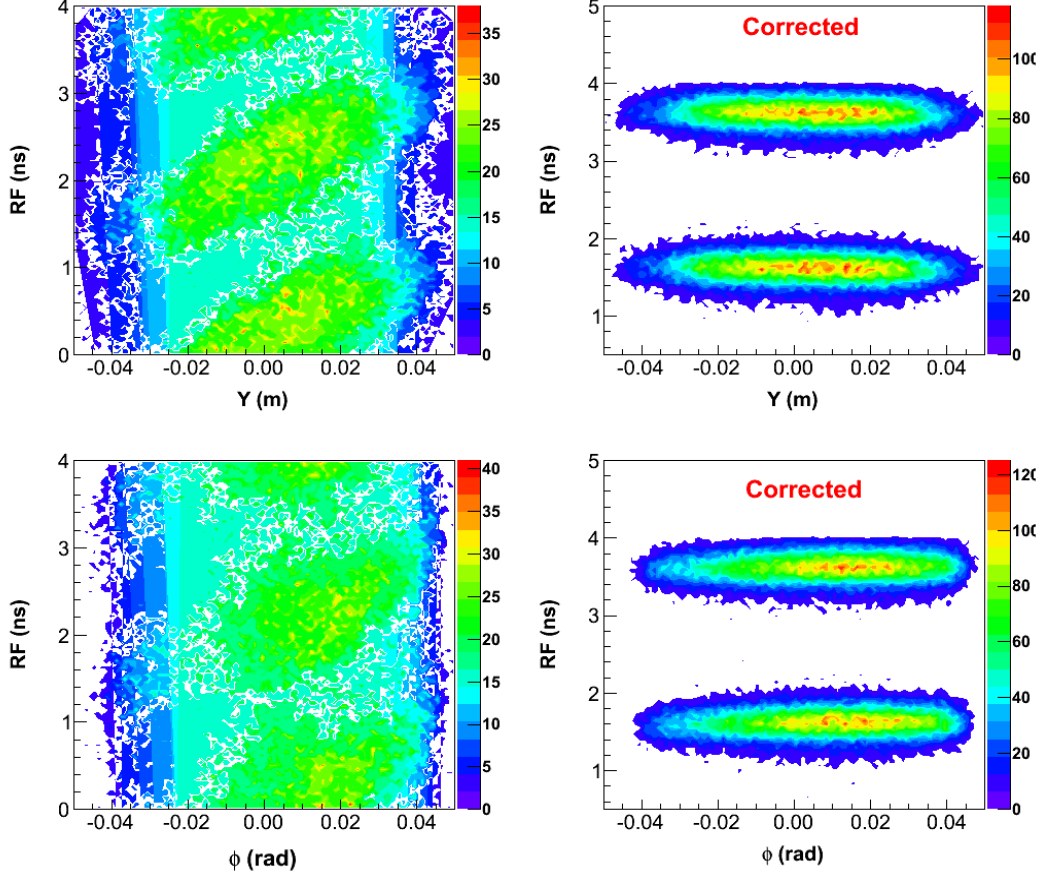


Figure 5.26: The y and ϕ dependences of RF without (left) and with (right) pathlength corrections.

follows :

$$t_{Ltw} = K \cdot \left(\frac{1}{\sqrt{ADC_L}} - \frac{1}{\sqrt{ADC_{mip}}} \right), \quad (5.30)$$

$$t_{Rtw} = K \cdot \left(\frac{1}{\sqrt{ADC_R}} - \frac{1}{\sqrt{ADC_{mip}}} \right), \quad (5.31)$$

where $ADC_{L(R)}$ is the ADC signal for left (right) PMT for a particular paddle and ADC_{mip} is an arbitrary timing offset declared for a MIP (minimum ionizing particle) for which the timewalk is zero. For our experiment, it was set to 50 ns.

Now if we write Eq.(5.26) in terms of all these corrections , we have,

$$RF_{LHRS} = t_{RF} - \frac{(t_{L.raw} - t_{Loff} - t_{Ltw} + t_{R.raw} - t_{Roff} - t_{Rtw})}{2} + \frac{Pathlength}{c} \quad (5.32)$$

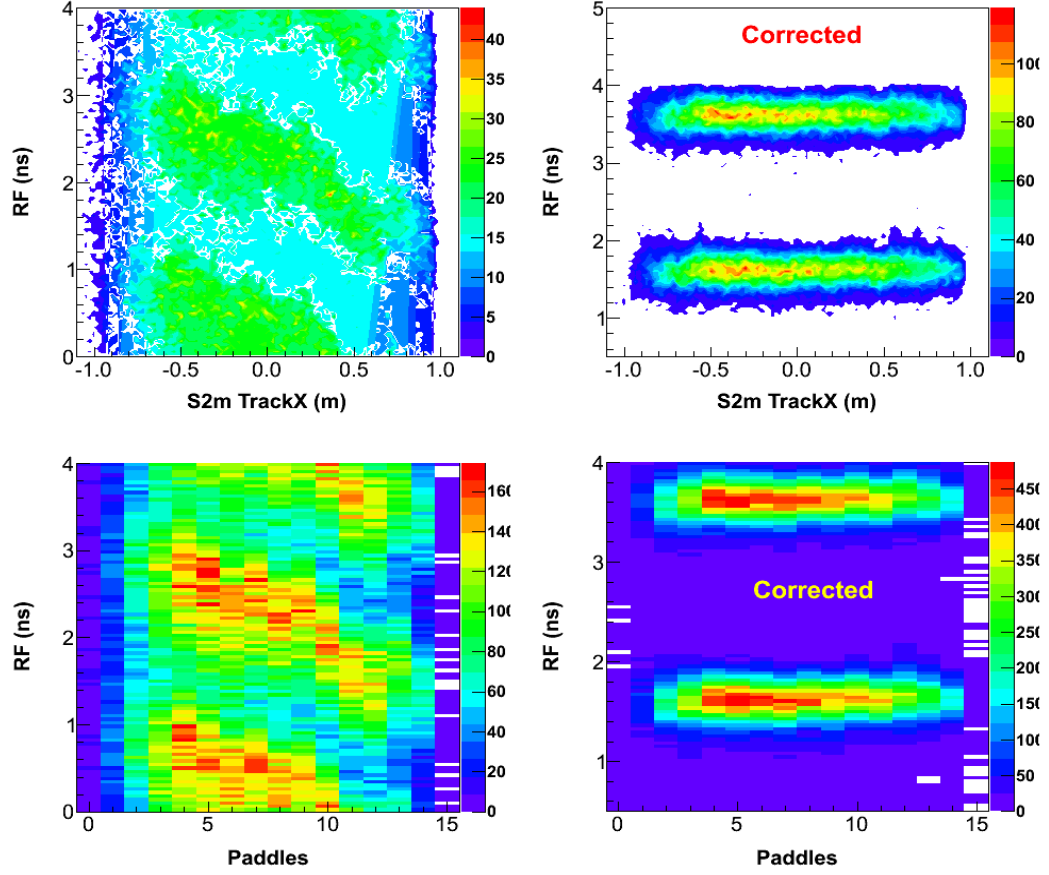


Figure 5.27: The x projection of the tracks in the S2m paddles and the time offsets before (left) and after (right) correction.

Rearranging the terms yields:

$$RF_{LHRS} = t_{RF} - \frac{(t_{L.raw} - t_{L.off} + t_{R.raw} - t_{R.off})}{2} + \frac{Pathlength}{c} + TW, \quad (5.33)$$

where TW is now defined as :

$$TW = K \cdot \left(\frac{1}{\sqrt{ADC_L}} + \frac{1}{\sqrt{ADC_R}} + constants \right). \quad (5.34)$$

Hence, in order to correct the timewalk effect, the RF_{LHRS} was plotted as a function of $\left(\frac{1}{\sqrt{ADC_L}} + \frac{1}{\sqrt{ADC_R}}\right)$ for each paddle and the slope K was determined. Once K was determined for each paddle, it was applied to the left and right TDCs with opposite signs to get rid of the overall effect. The timewalk effects and the respective corrections for both electrons and pions in the LHRS for a particular scintillator paddle are shown in the Fig. 5.28 and Fig. 5.29. Since the timewalk correction was only allowed for one particle in the analyzer

database, we chose to correct the pion timewalk effect as we got rid of the electrons in the LHRS anyway.

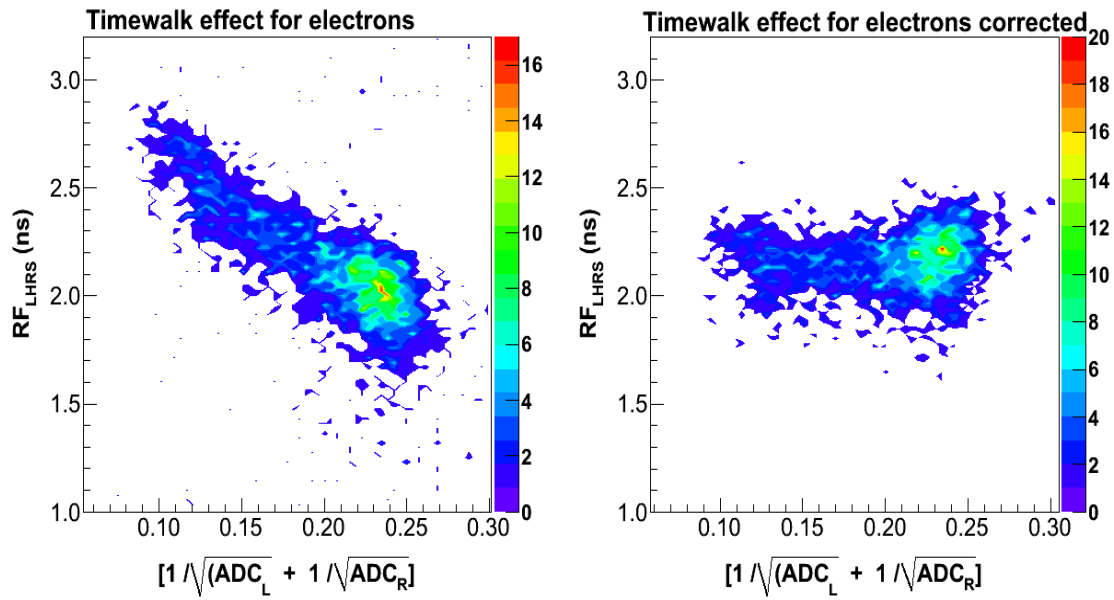


Figure 5.28: Timewalk effect for the electrons in S2m (paddle 8).

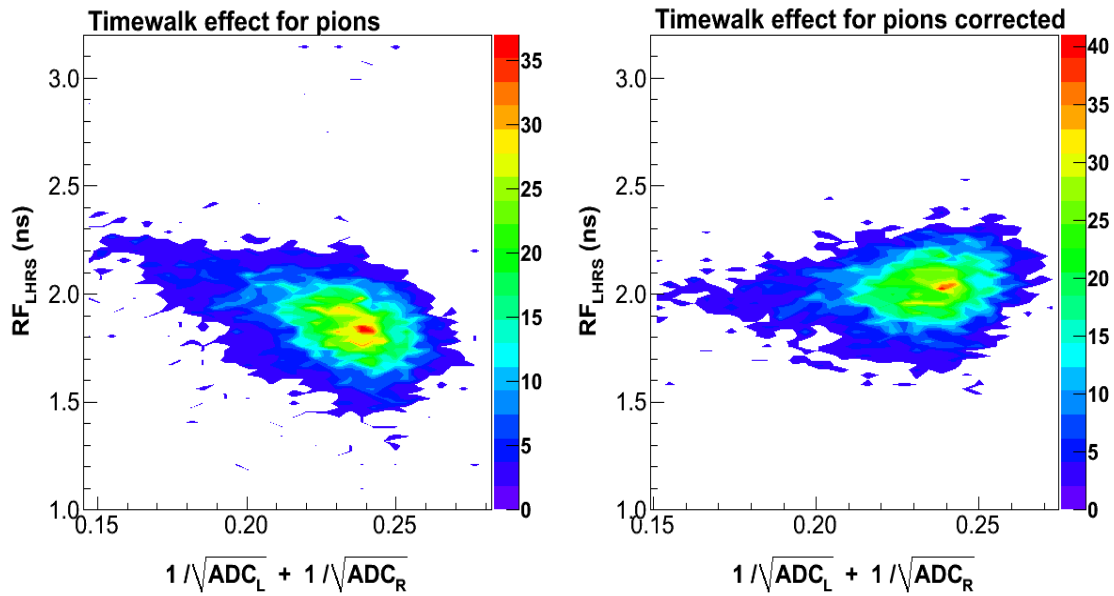


Figure 5.29: Timewalk effect for the pions in S2m (paddle 8).

After taking into account all these corrections, a resolution of ~ 140 ps was achieved for the RF structure in the LHRS. Fig. 5.30 shows the final RF structure after all the

corrections were applied.

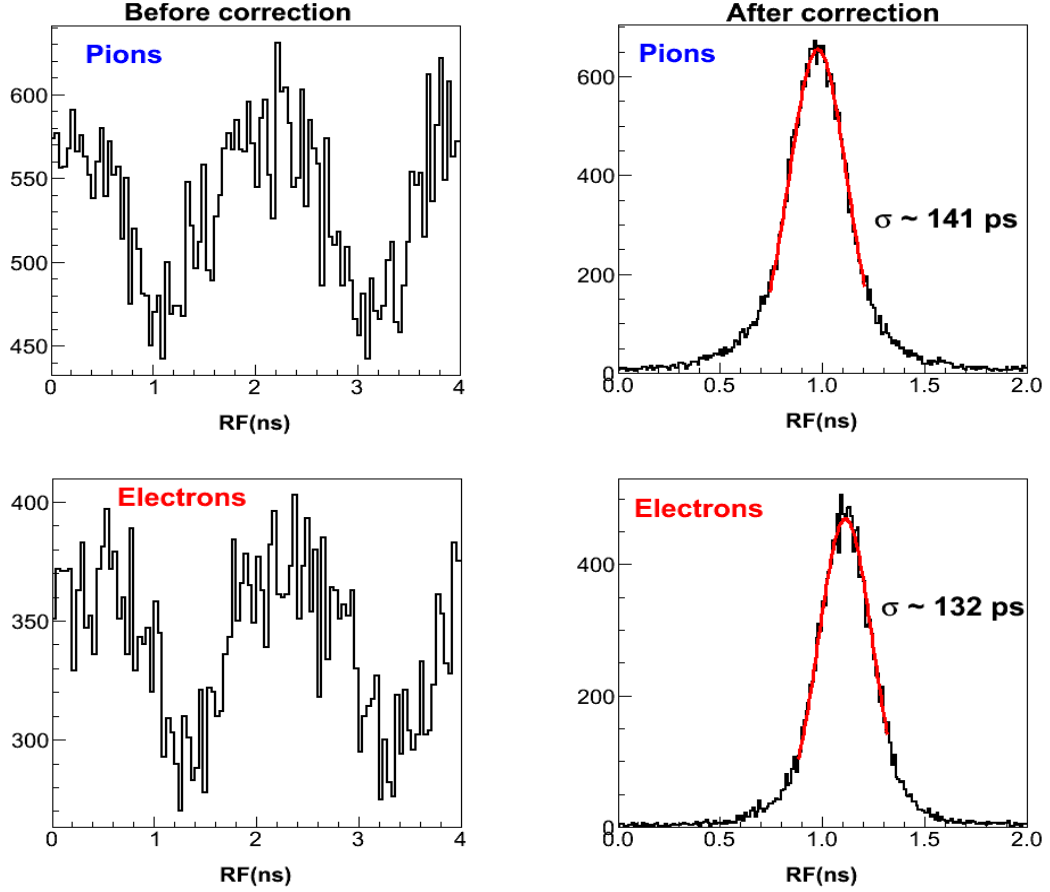


Figure 5.30: The RF structure in the LHRS for pions and electrons after all the corrections have been applied. The resolution of the pions is ~ 141 ps while that of the electrons is ~ 132 ps.

5.7.2 BigBite Timing Calibration

Similar to the LHRS timing calibration, the BigBite spectrometer timing calibration involved the same procedure of using the 2 ns RF structure of the beam bunch as a reference. The timing detector inside the BigBite spectrometer is a 13-bar scintillator plane inserted between the preshower and shower lead glass detectors. Here we have

$$RF_{BigBite} = t_{RF} - \frac{(t_L + t_R)}{2} + \frac{Pathlength}{c}, \quad (5.35)$$

where the definitions of the quantities in the equation are exactly the same as before in Eq.(5.26), but with respect to the BigBite scintillators. $RF_{BigBite}$ is comparatively sim-

pler as far as the contributions from different variables are concerned due to its shorter pathlength and similarity of the particles detected. The timing calibration for the BigBite spectrometer included the pathlength correction, time offset, and timewalk correction for the scintillators which will be discussed in the following subsections.

Pathlength correction

The BigBite spectrometer was at an angle of 30° with respect to the electron beam and at a distance of 1.5 m from the center of the target. Hence, due to its short distance from the vertex, the pathlength traversed by a generated or scattered particle in the reaction basically depended on the out of plane angle, θ_{vdc} , with respect to the plane perpendicular to the detector plane. A simple linear correlation was used to correct the pathlength differences:

$$\frac{L}{c} = 1.4 \cdot \theta_{vdc}, \quad (5.36)$$

where θ_{vdc} is the tangent of the vertical track angle measured by the Vertical Drift Chambers (VDC). θ_{vdc} is highly correlated with the vertical hit position on the chamber. Unlike the LHRS, any additional higher order terms on other tracking parameters were found not to make any noticeable improvement to this correction on θ_{vdc} .

Time offset calibration and timewalk correction

The time offset correction for all the paddles in the scintillator plane was done by selecting the events that fire only two neighboring paddles. In other words, for a particular paddle, either the paddle just above or just below was chosen and it was required that the selected events should fire both paddles together. Then the timing difference between these two paddles was minimized by applying an offset for each PMT.

The timewalk effects in the PMTs on the BigBite scintillators were comparatively larger than those in the LHRS. However, a very simple functional form could be defined to describe the behavior of the TDC signals as a function of the ADC signal amplitudes. Hence in this case the timewalk corrections could be expressed as :

$$TW_{BigBite} = -17.9(ADC - PED)^{-0.140}\text{ns}, \quad (5.37)$$

where ADC stands for the usual ADC signal channel peak and PED is the corresponding pedestal value for that PMT.

The final resolution of the RF time for the BigBite spectrometer was calibrated to ~ 270 ps (1σ) as shown in Fig. 5.31. The intrinsic resolution of the scintillator, the open geometry of the BigBite magnet, and the noisy environment limited any further improvement in the resolution.

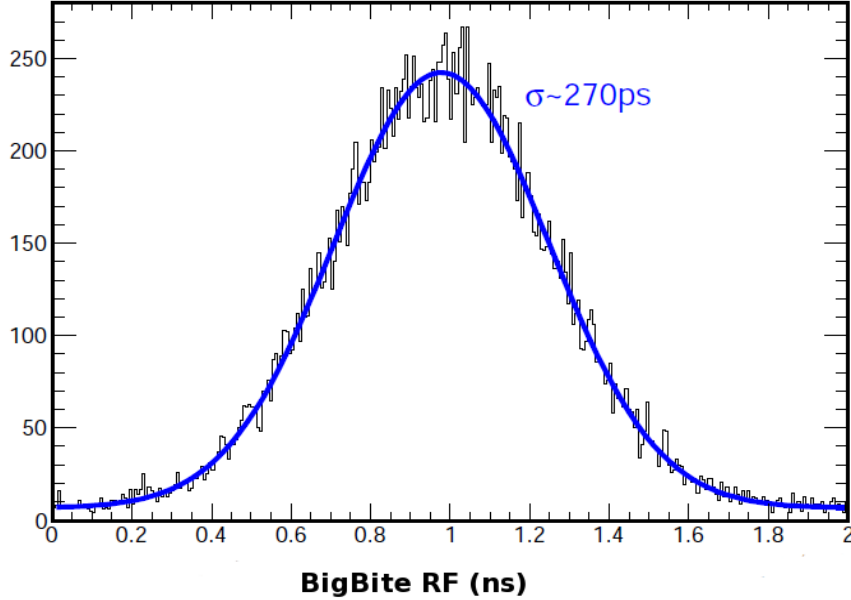


Figure 5.31: The RF structure in the BigBite scintillator for electrons after all the corrections were applied. The resolution in this case is ~ 270 ps [19].

5.7.3 Two Arm Coincidence Time Calibration

The two single arm RF calibrations (LHRS and BigBite as discussed above) were applied in Eq.(5.25) to achieve the final coincidence time-of-flight (CTOF) for the reaction $(e,e'\pi^\pm)$. The last term in Eq.(5.25) was measured by a TDC with a resolution of 60 ps. Another similar calibration was done for the reaction $(e,e'\gamma)$ as the BigBite spectrometer was considerably dominated by photon induced events. This latter calibration was useful to get rid of the photon backgrounds. For the reaction $(e,e'\pi^\pm)$, the resultant CTOF reached a resolution of ~ 340 ps (1σ) as shown in Fig. 5.32 whereas for the $(e,e'\gamma)$ reaction a resolution of ~ 400 ps was achieved.

Prior to taking production data in E06010, a preliminary check of the detectors and

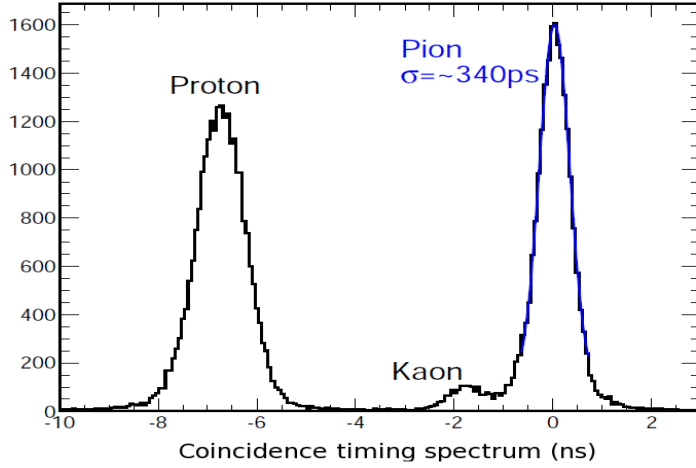


Figure 5.32: The final CTOF spectrum for the reaction $(e, e' \pi)$. Here, the CT spectrum is shown for the LHRS with positive polarity. When the LHRS was in negative polarity, the spectrum looks the same except that there would not be any proton peak on the left [19].

the target was performed by taking $\vec{e}^{-3}\vec{\text{He}}$ scattering data in the elastic region. As the ^3He elastic cross section and the asymmetry are known for a given electron beam energy and LHRS scattering angle, the elastic asymmetry measured from the data can be compared with the prediction and used to perform an initial check of the detectors as well as the target polarization. The analysis formalism and the results of the elastic data analysis are presented in the following section.

5.8 Calibration and Analysis of Elastic Events

At the beginning of the experiment, elastic $\vec{e}^{-3}\vec{\text{He}}$ data were taken on the cell “Maureen”. The incident beam energy was 1.230 GeV and the LHRS had a momentum setting of 1.21 GeV/c at an angle of 16° with respect to the electron beam. The elastic data have been used to determine the sign convention for beam helicity and target spin direction. The elastic physics asymmetry can be calculated precisely and a simulation was done before the experiment to predict the expected asymmetry at the respective settings of beam energy, spectrometer angle, and target spin direction. This calculated asymmetry was non-zero and the measured raw asymmetry was compared to the predicted value. Hence, this measurement was used to verify the sign of the product of beam and target polarizations. In E06010, we did not have the ability to polarize the ^3He gas longitudinally, i.e., along the

incoming beam direction. Hence, in order to collect the elastic data with the longitudinally polarized spins of the ^3He atoms, the atoms were polarized in the transverse direction first. Once a reasonable polarization ($\sim 45\%$) was achieved, the holding field was rotated from the transverse direction to the longitudinal direction and was left there during the data taking without any continuous pumping by the lasers. This implies that during data taking, the polarization of the ^3He gas was decreasing exponentially with time. The analysis details are presented in the later subsections. The data were taken by flipping the beam helicity at a rate of 30 Hz. In order to reduce any systematic effects, the beam half wave plate was inserted for part of the data so that the entire flipping sequence of the beam helicity got reversed.

In this section, the elastic $\vec{e}^-^3\vec{\text{He}}$ scattering formalism will be summarized and then the analysis results will be discussed and compared with the simulated results.

5.8.1 Physics Formalism of Elastic $\vec{e}^-^3\vec{\text{He}}$ Scattering

In elastic scattering, the energy of the scattered electron, E' , having an incident energy E_0 , is given by:

$$E' = \frac{E_0}{1 + \frac{2E}{M} \sin^2(\frac{\theta}{2})}, \quad (5.38)$$

where M is the mass of the target (^3He in this case) and θ is the scattering angle with respect to the direction of four momentum transfer Q^2 . It is:

$$Q^2 = 4E_0E' \sin^2(\frac{\theta}{2}). \quad (5.39)$$

Further the Rosenbluth formula for the unpolarized elastic cross section is [118]:

$$\frac{d^2\sigma}{d\Omega dE'} = \sigma_{MOTT} \left[2W_1(Q^2) \tan^2(\frac{\theta}{2}) + W_2(Q^2) \right], \quad (5.40)$$

where the Mott cross section, σ_{MOTT} , for the target nucleus with charge Z is given by :

$$\sigma_{MOTT} = \frac{Z^2\alpha^2 \cos^2(\frac{\theta}{2})}{4E^2 \sin^4(\frac{\theta}{2})}. \quad (5.41)$$

The form factors $W_1(Q^2)$ and $W_2(Q^2)$ that appear in the Rosenbluth formula are often expressed in terms of so called Sachs form factors as follows :

$$W_1(Q^2) = \tau G_M^2(Q^2), \quad (5.42)$$

$$W_2(Q^2) = \frac{G_E^2(Q^2) + \tau G_M^2(Q^2)}{1 + \tau}. \quad (5.43)$$

The Sachs form factors G_E^2 and G_M^2 are called the electric and magnetic form factors, respectively. The recoil factor τ is defined as :

$$\tau = \frac{Q^2}{4M^2}. \quad (5.44)$$

The electric and magnetic form factors are related to the Dirac form factor, $F_1(Q^2)$, and Pauli form factor, $F_2(Q^2)$, through the relations :

$$F_1(Q^2) = \frac{\tau G_M(Q^2) + G_E(Q^2)}{1 + \tau}, \quad (5.45)$$

$$F_2(Q^2) = \frac{G_M(Q^2) - G_E(Q^2)}{1 + \tau}. \quad (5.46)$$

One can express the unpolarized elastic cross section using different form factor notations as defined above. The charge and magnetic form factors of ^3He have been measured precisely and those can be related to the elastic unpolarized cross section as follows [119]:

$$\frac{d^2\sigma}{d\Omega dE'} = \frac{\sigma_{MOTT}}{\eta} \left[\frac{Q^2}{|\vec{q}|^2} F_c^2(Q) + \frac{\mu^2 Q^2}{2M^2} \left(\frac{1}{2} \frac{Q^2}{|\vec{q}|^2} - \tan^2\left(\frac{\theta}{2}\right) \right) F_m^2(Q) \right], \quad (5.47)$$

where $\eta = 1 - \frac{Q^2}{4M^2}$ and μ is the magnetic moment of ^3He . F_c and F_m are the electric and magnetic form factors of ^3He , respectively.

For the polarized elastic cross section, an additional electron helicity dependent term has to be added to the unpolarized cross section where it is assumed that the polarization of

the scattered electron is not measured. The formalism is extensively discussed in [120]. According to this formalism, the cross section difference for the polarized case is given by :

$$\left[\frac{d^2\sigma}{d\Omega dE'} \right]^{+1} - \left[\frac{d^2\sigma}{d\Omega dE'} \right]^{-1} = -\sigma_{MOTT} [V_{T'} R_{T'}(Q^2) \cos \theta^* + V_{TL'} R_{TL'}(Q^2) \sin \theta^* \cos \phi^*], \quad (5.48)$$

where θ^* and ϕ^* are the polar and azimuthal angle of the ${}^3\text{He}$ spins with respect to the three-momentum transfer \vec{q} . The superscripts +1 and -1 indicate the two helicity states of the incoming electrons. The response functions $R_{T'}$ and $R_{TL'}$ and the kinematic factors $V_{T'}$ and $V_{TL'}$ are defined as follows :

$$R_{T'}(Q^2) = \frac{2\tau E'}{E} (\mu_A F_m)^2, \quad (5.49)$$

$$R_{TL'}(Q^2) = -\frac{2\sqrt{2\tau(1+\tau)}E'}{E} (ZF_c)(\mu_A F_m), \quad (5.50)$$

$$V_{T'} = \tan \frac{\theta}{2} \sqrt{\frac{Q^2}{|\vec{q}|^2} + \tan^2 \frac{\theta}{2}}, \quad (5.51)$$

$$V_{TL'} = -\frac{Q^2}{\sqrt{2}|\vec{q}|^2} \tan \frac{\theta}{2}. \quad (5.52)$$

Now Eq.(5.47) gives the cross section averaged over the electron helicity states and Eq.(5.48) gives the cross section difference between the electron helicity states. Hence the elastic asymmetry can be formed by dividing Eq.(5.48) by Eq.(5.47) :

$$A_{elastic} = \frac{-\eta [V_{T'} R_{T'}(Q^2) \cos \theta^* + V_{TL'} R_{TL'}(Q^2) \sin \theta^* \cos \phi^*]}{\left[\frac{Q^2}{|\vec{q}|^2} F_c^2(Q) + \frac{\mu^2 Q^2}{2M^2} \left(\frac{1}{2} \frac{Q^2}{|\vec{q}|^2} - \tan^2 \left(\frac{\theta}{2} \right) \right) F_m^2(Q) \right]}. \quad (5.53)$$

5.8.2 Elastic Asymmetry Results and Target Spin Sign Convention

The elastic ${}^3\text{He}$ data were taken with an incoming beam energy of 1.23 GeV while the ${}^3\text{He}$ target was polarized along the beam direction, i.e. longitudinally with respect to the beam.

One important aspect of the elastic data taking was that we did not continuously pump and polarize ^3He while taking data as there was no provision to polarize ^3He longitudinally during this experiment. The ^3He gas was polarized using the transverse line of the lasers and then the holding field was rotated from the transverse to the longitudinal direction. It was left there during data taking. Once we took data for few hours and realized that the polarization reached a very low value, we stopped and restarted pumping in the transverse direction after rotating the holding field from the longitudinal to the transverse direction. The process was repeated until we had enough data to analyze the asymmetries. Figure 5.33 shows the average target polarization during each elastic run. As can be seen from the plot, the polarization decreased exponentially while we were taking data. Once we reached a minimum polarization value of $\sim 28\%$, we restarted the laser pumping to polarize the target which is shown by the arrow at point A in the plot.

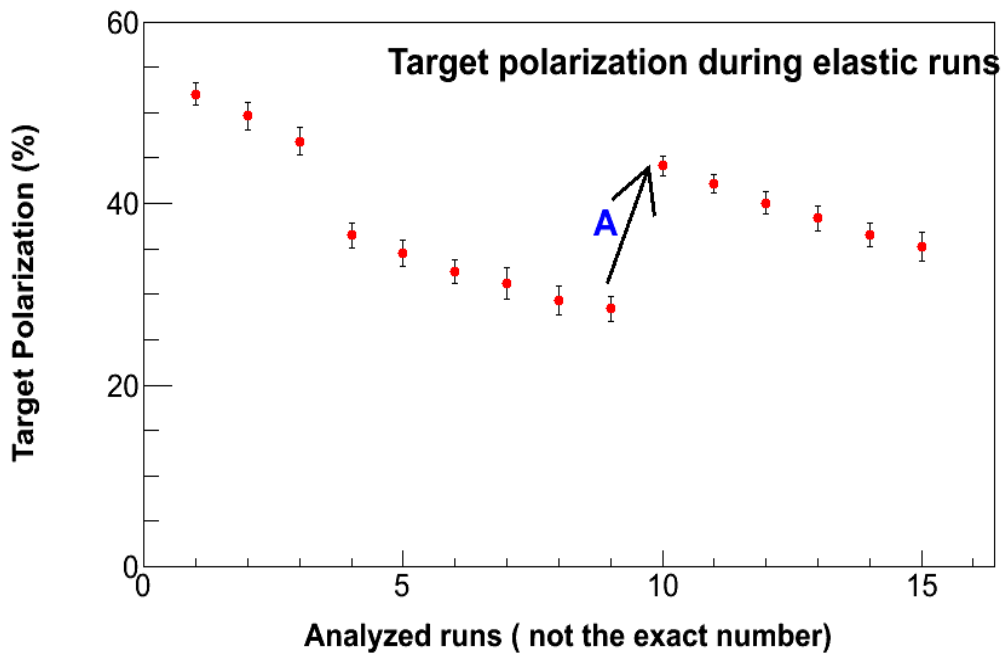


Figure 5.33: The polarization of the target during the elastic data taking. A few measurements of polarization were performed in between the runs. The points corresponding to each run were determined after an interpolation of the measured polarization value between the runs. The huge drop between the third and the fourth points was due to some technical issues in the Hall where we had to stop the beam and waited for some time without polarizing the target.

The raw asymmetries were calculated by choosing the elastic events within the elastic

peak in the ^3He invariant mass spectrum (W) for the two opposite helicity states of the electron beam (positive and negative). Then the ratio of the difference of the normalized yields between these two helicity states to the corresponding sum was formed. If N^+ and N^- denote the number of elastic events in the positive beam helicity state (+) and in the negative beam helicity state (-), respectively, then the raw elastic asymmetry can be expressed as :

$$A_{raw} = \frac{\frac{N^+}{Q^+L^+} - \frac{N^-}{Q^-L^-}}{\frac{N^+}{Q^+L^+} + \frac{N^-}{Q^-L^-}}, \quad (5.54)$$

where $Q^{+/-}$ and $L^{+/-}$ are the charge and livetime corrections, respectively, for the two beam helicity states (+/-). The raw asymmetries are shown in Fig. 5.34. Data were taken with both the beam half wave plate (BHWP) in and out as it can be seen from the plot that the asymmetry changes sign when the BHWP was inserted.

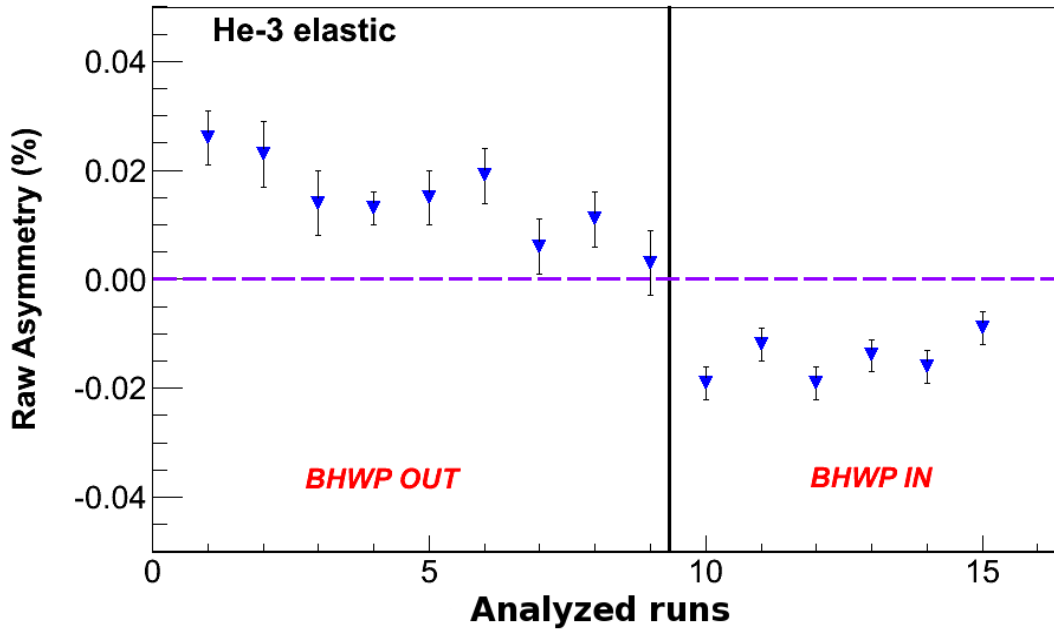


Figure 5.34: The ^3He raw elastic asymmetries.

In order to calculate the physics asymmetry, the raw ^3He asymmetry was corrected for the target polarization, the beam polarization, and the N_2 dilution. In addition, a correction factor of -1 had to be multiplied to the measured asymmetries when the BHWP was inserted. The corrected physics asymmetries are shown in Fig. 5.35 where A_{phy} is

defined as :

$$A_{phy} = \frac{1}{P_b \cdot P_t \cdot \eta_{N_2}} A_{raw}, \quad (5.55)$$

where the quantities in the above equation are :

- P_b : Polarization of the electron beam. The Møller measurement showed the beam polarization during the period of elastic data taking was $\sim 88\%$ with a statistical uncertainty of $\sim 0.2\%$.
- P_t : Polarization of the target. As shown in Fig. 5.33, a ^3He polarization number for each elastic run could be determined.
- η_{N_2} : N_2 dilution factor determined from a N_2 reference cell run compared to a polarized ^3He run in the elastic setting. This is discussed in an upcoming section. It was determined to be ~ 0.945 with a statistical uncertainty of ~ 0.005 .

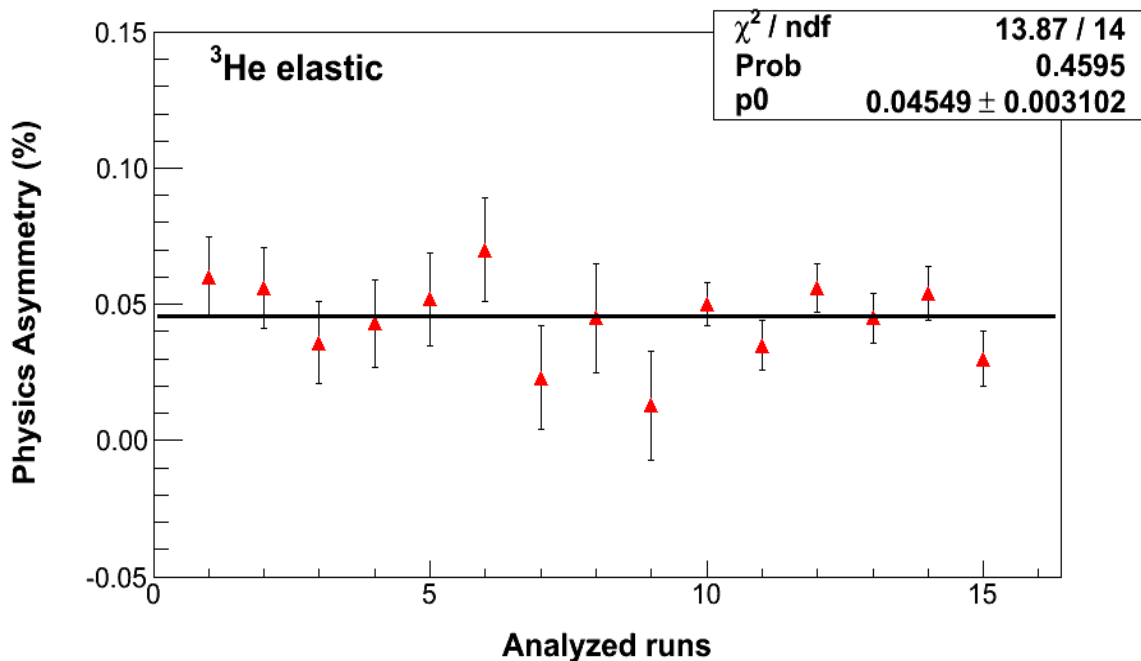


Figure 5.35: The ^3He physics elastic asymmetries.

The asymmetries for all the runs were fitted with a zeroth order polynomial and the final result with the LHRS at 16° and an incident beam energy of 1.230 GeV was obtained from the fit :

$$A_{phy} = 0.045 \pm 0.003. \quad (5.56)$$

The main objective of taking data in the elastic setting was to verify that our system was working reasonably well and hence, it was a good test of our detector and especially of the target system as the physics asymmetry for the data could be simulated well ahead with a reasonably good precision. The simulation was performed using the standard Hall A SAMC (Single Arm Monte Carlo) and the details can be found in [121]. The fundamental inputs to the simulation included the initial electron beam energy, the angle of the scattered electron and the target spin angle with respect to the beam (0° corresponds to the target spin parallel to the incoming beam and 180° to that of the target spin anti-parallel to the incoming beam). However, it was essential to implement all the same cuts that were used in the analysis and in addition, all the radiative corrections had to be applied. These included the energy loss of the incoming beam and the outgoing scattered electrons passing through different materials until they reached the detector. The complete table of the materials that the incoming electrons as well as the scattered electrons passed through and their radiation lengths can be found in Appendix C. Taking into account all the correction factors, the SAMC simulation yielded an elastic physics asymmetry for polarized ^3He target at our settings of

$$A^{MC}_{phy} = 0.048 \pm 0.02(\text{sys.}). \quad (5.57)$$

The dominant systematic uncertainties in the measured elastic asymmetry came from the beam and target polarizations along with the N_2 dilution. The systematic uncertainties in beam and target polarizations are 2.5% and 3%, respectively, whereas the uncertainty in the N_2 dilution is $\sim 0.5\%$. On the other hand, the systematic uncertainties in the SAMC simulation include the uncertainties in the magnetic form factor F_m (± 0.001), and the electric form factor F_c (± 0.002) [119]. Moreover, uncertainties in the beam energy (± 1 MeV), the central angle of LHRS ($\pm 0.06^\circ$, [122]), the central momentum of LHRS (± 0.00005 GeV/c, [117]), the target spin angle ($\pm 0.1^\circ$) and other radiative corrections due to the different materials present in path of the incoming and outgoing electrons lead to another systematic uncertainty of $\sim 1.1\%$ in the simulation. Thus, the total systematic uncertainty in the asymmetry from the simulation is $\sim 1.6\%$ and that from the measurement is $\sim 4\%$.

The measured elastic physics asymmetry was within 5% relative to the expected asymmetry from the simulation which indicated that our detector system as well as the target

systems were behaving properly and the target polarization measurement was reliable.

The absolute target spin sign could also be determined from this analysis. The SAMC results showed that the physics asymmetry for the target spin aligned parallel to the beam direction, i.e. at 0° , was positive. In the measurement, it was found that the raw asymmetry was positive when the target spins were aligned along the longitudinal holding field which was along the beam direction. It was defined as 0° which was consistent with the simulation. The target polarization P_t is positive in this case. On the other hand, if we would have rotated the target spins by 180° , the asymmetry would have become negative and in that case, we needed to put a negative sign in front of the polarization to make it consistent with the expected results. Thus, in conclusion, the measured elastic raw asymmetry was positive with the target spins parallel (+) to the beam direction and negative with the target spins anti-parallel (-) to the beam direction which was consistent with the results of the simulation.

5.9 Delta ($\Delta(1232)$) Asymmetry Results

A set of polarized ^3He data was also taken in the Δ resonance region. The purpose of taking this set of data was also to verify the system reliability to complement the results of the elastic analysis. The raw and physics asymmetries for the Δ kinematics were defined exactly the same way as in case of the elastic asymmetries. The data were taken with the ^3He atoms polarized in the transverse direction which means that the spins were aligned in the scattering plane perpendicular to the incoming electron beam. The only difference between this analysis and the elastic one was that the polarization during the entire period of data taking with the Δ resonance settings was not decreasing unlike the elastic case and hence, one ^3He polarization number for all the runs was applied to the fitted result of the raw asymmetries. The raw asymmetries in the Δ region for the polarized ^3He are shown in Fig. 5.36.

The Δ resonance asymmetries were measured with an incoming beam energy $E_0 = 1.230$ GeV and the LHRS at 16° with respect to the beam. The corresponding Q^2 was 0.08 GeV^2/c^2 . From Fig. 5.36 we find that the raw asymmetries are positive for the transverse “+” target polarization and negative for the transverse “-” target polarization. Our magnetic holding field configuration was defined in such a way that transverse “+” corresponded

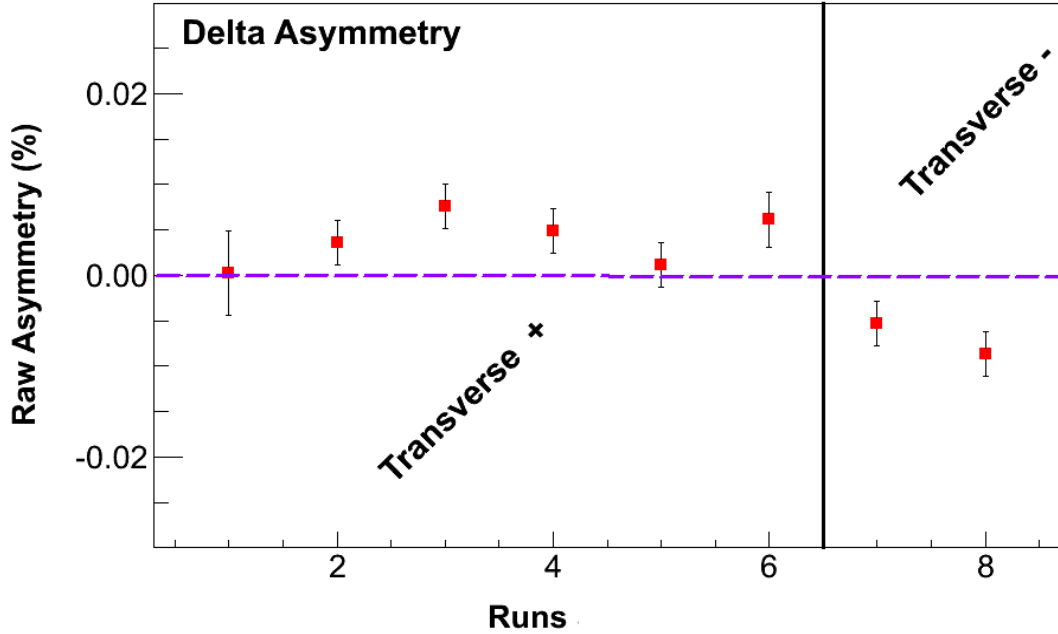


Figure 5.36: Raw Δ resonance asymmetries. The asymmetry changes sign as the polarization direction is reversed from transverse + to transverse -. All these measurements were done with the beam half wave plate inserted.

to the situation when the target spins were parallel to the holding field and the field itself pointed at 90° to the beam left (in plane). Similarly, the transverse “-” case was for the target spins aligned anti-parallel to the field which was at 270° to the beam right. Hence, the signs of the target polarization in both the cases are :

$$[P_t]_{transverse+} = +, \quad [P_t]_{transverse-} = -. \quad (5.58)$$

The raw asymmetries measured in these cases are :

$$[A_{raw}]_{transverse+} = -0.004 \pm 0.001, \quad [A_{raw}]_{transverse-} = +0.006 \pm 0.002. \quad (5.59)$$

These measurements were performed with the beam half wave plate inserted and hence a correction factor -1 was multiplied to the measured raw asymmetries. In order to estimate the physics asymmetries, an average target polarization of 45% and a N_2 dilution factor of 0.94 were employed with to beam polarization of 88% from the Møller measurement . Thus,

the physics asymmetries in both the cases were evaluated approximately as follows :

$$[A_{phy}]_{transverse+} = \frac{1}{P_t P_b \eta_{N_2}} (-0.004) = -1.1 \pm 0.002, \quad (5.60)$$

$$[A_{phy}]_{transverse-} = \frac{1}{-P_t P_b \eta_{N_2}} (0.006) = -1.6 \pm 0.002. \quad (5.61)$$

Thus taking the average, the final physics asymmetry is determined to be -1.3% at $Q^2 = 0.08 \text{ GeV}^2/c^2$.

5.10 N₂ Dilution in ³He

The polarized ³He target cell contains a very small amount of N₂ in order to quench any unpolarized light emitted in the optical pumping process. In other words, the optically pumped Rb or K atoms undergo a process of relaxation with the N₂ atoms where they do not get depolarized. The relaxation process of the alkali atoms with the N₂ is not accompanied by the emission of photons and hence it is named as *photon-less deexcitation* [104] as the energy is absorbed in the nitrogen's rotational and vibrational motions. Thus, filling the polarized ³He cell with N₂ improves the polarization of the alkali atoms in the pumping chamber and can be used as a buffer gas. However, during a scattering experiment, events are generated from reactions between the incoming electrons and the N₂ atoms as well. These cannot be distinguished from real scattering events off ³He atoms just by using various informations from the detectors. Since the N₂ is unpolarized and its cross section is large as compared to that of polarized ³He, the measured asymmetry of ³He is diluted by the events generated from the scattering off the N₂ atoms. Hence, in the analysis, a nitrogen dilution factor was determined by comparing the yield from nitrogen events generated in the reference cell and the yield from the polarized ³He cell normalized by charge, livetime, pressure, etc. The N₂ dilution factor can, thus, be defined as :

$$\eta_{N_2} = \frac{Y_{^3He}}{Y_{^3He} + Y_{N_2}} = \frac{\sigma_{^3He} \rho_{^3He}}{\sigma_{^3He} \rho_{^3He} + \sigma_{N_2} \rho_{N_2}}, \quad (5.62)$$

where $Y_{^3He}$ (Y_{N_2}) is the yield of ³He (N₂), $\sigma_{^3He}$ (σ_{N_2}) is the cross section of ³He (N₂) and $\rho_{^3He}$ (ρ_{N_2}) is the density of ³He (N₂) inside the polarized ³He cell. The filling densities for ³He and N₂ were used and are listed in Table. 5.3:

The dilution factor was calculated for each of the four x bins and is shown in Fig. 5.37. The x bins here represent the Bjorken x bins introduced in chapter 1 and chapter 2. Our

Table 5.3: The filling densities of ^3He and N_2 for all the three cells used in the experiment.

^3He cell	^3He density (amg)	N_2 density (amg)
Astral	8.08	0.110
Maureen	7.52	0.106
Brady	7.87	0.110

final data will be binned into these four x bins and hence, a N_2 dilution factor for each x bin had to be determined.

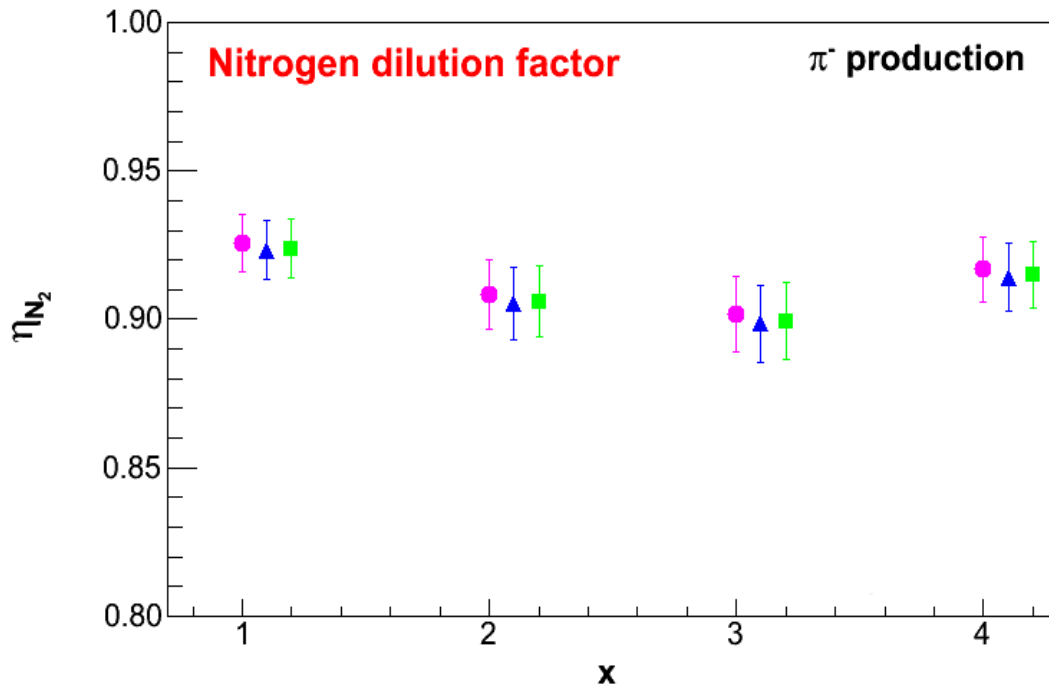


Figure 5.37: The N_2 dilution factors for all the four x bins. The three points for each bin correspond to the three cells used in the experiment. The points are for *Astral*, *Maureen*, and *Brady* respectively from the left for each x .

The uncertainties in the analysis include the relative uncertainty of the ^3He filling density ($\sim 2\%$), N_2 filling density ($\sim 5\%$), and the filling pressure in the N_2 reference cell (~ 1 psig). The radiative correction was assumed to be 10% of the cross section ratio $\frac{\sigma_{^3\text{He}}}{\sigma_{\text{N}_2}}$ [18]. The error bars in the Fig. 5.37 are determined by the following expression where the statistical uncertainties from the cross sections are combined with the systematic uncertainties mentioned above.

$$\Delta\eta_{N_2} = \eta_{N_2}^2 \frac{\sigma_{N_2} \rho_{N_2}}{\sigma_{^3\text{He}} \rho_{^3\text{He}}} \sqrt{\left(\frac{\Delta\sigma_{N_2}}{\sigma_{N_2}}\right)^2 + \left(\frac{\Delta\sigma_{^3\text{He}}}{\sigma_{^3\text{He}}}\right)^2 + (0.1)^2 + (0.05)^2 + (0.02)^2}, \quad (5.63)$$

where $\Delta\sigma_{^3\text{He}}(\Delta\sigma_{N_2})$ is the statistical uncertainty related to the ^3He (N_2) cross section. The final number of the N_2 dilution for each bin was determined by taking the average of all the three numbers for the three cells. The dilution factors are listed in Table 5.4:

Table 5.4: N_2 dilution factors for each x bin for π^- production.

x bin	$\eta_{N_2} \pm \Delta\eta_{N_2}$
1	0.9242 ± 0.006
2	0.9066 ± 0.007
3	0.8998 ± 0.008
4	0.9153 ± 0.007

5.11 BigBite Spectrometer Contamination Study

The BigBite spectrometer in E06010 was used to detect the electrons that were coincident with the hadrons in the LHRS within a momentum range of 0.6 GeV/c to 2.1 GeV/c. In addition, single electrons (T1/T6 trigger) that were not coincident with the hadrons in LHRS and single negatively charged pions (inclusive T1/T6 events) were also detected in order to extract inclusive asymmetries as witness channels. However, it turned out that the real coincidence electrons (T5 trigger) were mostly contaminated by photon induced electrons followed by negative hadrons. Since it was extremely difficult to separate the negative pions from kaons in the BigBite spectrometer, the term “negative hadrons” is used here. Nevertheless, the pions were the dominating particles. The BigBite spectrometer contamination study involved studying the contamination of photon induced electrons as well as different hadrons to the real DIS coincidence electron sample. This will be discussed in the next subsection. Prior to that, it is worthwhile to describe the various particle identification (PID) cuts used in the BigBite detector system in general as well as for different systematic studies. The coincidence cuts used in the final physics analysis will be discussed in chapter 6.

The PID in the BigBite spectrometer was achieved primarily by using the preshower and shower detector combined with the momentum reconstruction information from the MWDC.

The PID process was implemented to identify four different types of particles : *electron like*, *negative hadron like*, *positive hadron like*, and *photon like*. However, there were a few general cuts that had to be applied to all the charged particle identifications:

- **Charge type cut** : The simple dipole magnet in the BigBite spectrometer bends the negatively charged particles upwards while the positively charged particles are bent downwards. A clear separation of different charged particles can be achieved in the reconstructed vertical positions of the tracks in the MWDC planes. Consequently, both types of particles were flagged separately.
- **Optics validity cut** : The optics validity cut was implemented to exclude the very top and bottom sections of the BigBite magnet where the magnetic field was much weaker and hence, the optics reconstructions were not reasonable. Figure 5.38 shows the implementation of this cut.

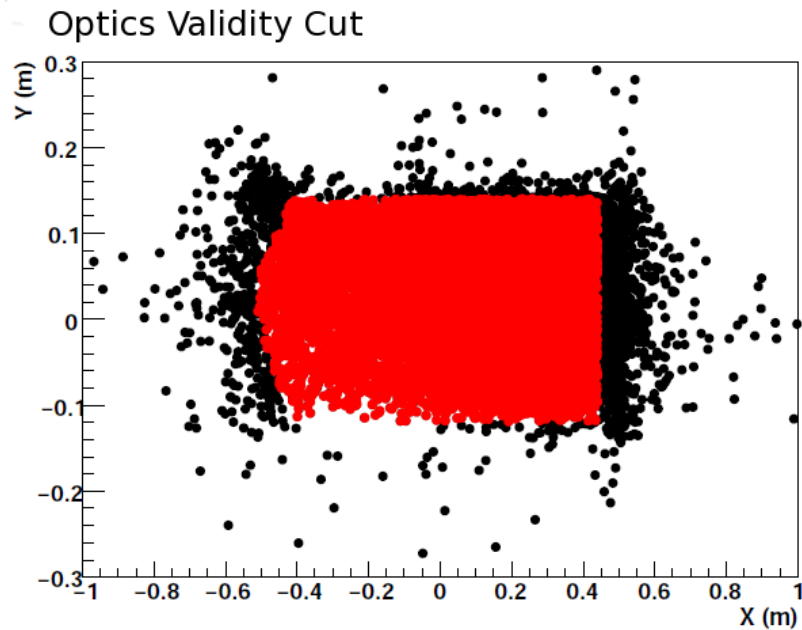


Figure 5.38: The optics validity cut in the BigBite spectrometer. The black points show all the reconstructed events in the spectrometer while the red points show the events that pass the optics validity cut. As can be seen, the events corresponding to the edges of the magnet have been removed.

- **Track quality cut** : The track quality cut is defined as follows :

$$t_\epsilon = \frac{\chi^2}{N_{df}} = \frac{1}{N_{df}} \sum_j \frac{[x_{recon} - x_{track}]^2}{r_j^2}, \quad (5.64)$$

where x_{recon} is the reconstructed hit position and x_{track} is the projected hit position. N_{df} is the degree of freedom which is related to the number of MWDC planes involved in the track reconstruction and r_j is the resolution assumed in the tracking software. A cut of $t_\epsilon < 2.4$ was used to get rid of the reconstructed tracks having higher t_ϵ . The details of the analysis can be found in [18].

- **Track matching cut** : The *track matching* implies the fact that the center of the reconstructed shower cluster position from the calorimeter should match the projected position of the reconstructed track on the shower [18]. Only events which pass this track matching cut are selected for the analysis.
- **Preshower/shower PID cut** : The PID in the preshower and shower detector was realized by using a 2-D cut on the energy deposited in the preshower vs. the ratio of the total energy to the reconstructed momentum ($\frac{E}{p}$) in the shower. Figure 5.39 shows a typical 2-D plot where the electrons and the negative pions are clearly separated.
- **Interaction vertex cut** : The interaction vertex cut is shown in Fig. 5.40.

In addition to the above mentioned general cuts, few specific cuts were applied to identify different particles in BigBite. Those are listed below:

Cuts for electron like events :

- Charge type cut = Negative.
- Energy in preshower $E_{ps} > 0.2$ GeV.
- Momentum cut: $0.6 \text{ GeV}/c < p < 2.5 \text{ GeV}/c$.
- Calorimeter $\frac{E}{p}$ cut (momentum dependent): For different momentum bins, the $\frac{E}{p}$ was fitted with a Gaussian function and a 2.5σ cut was applied to choose the electrons in each bin.

BigBite calorimeter PID

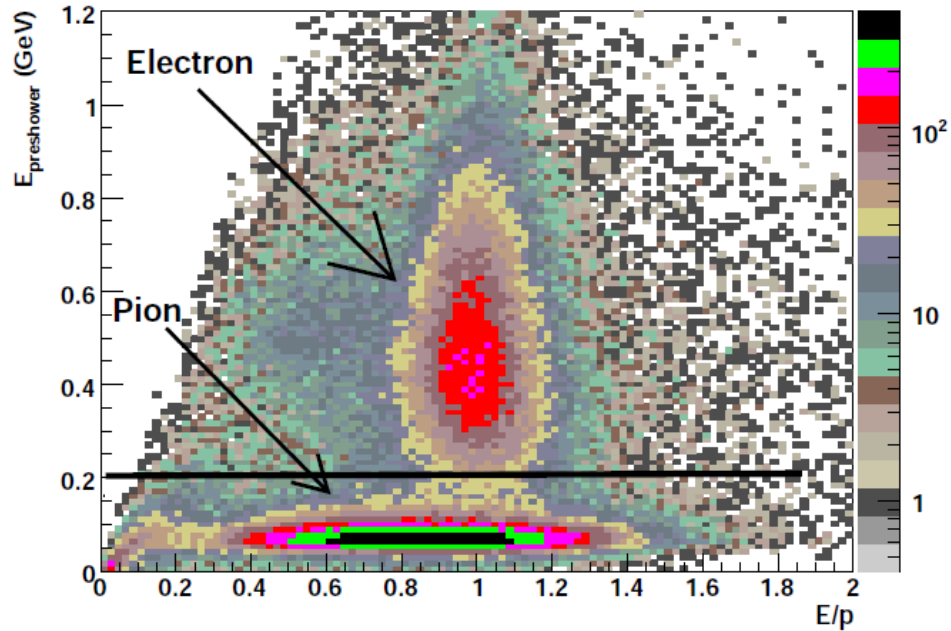


Figure 5.39: The energy deposition in the preshower vs. the $\frac{E}{p}$ of the total shower.

- Position match cut: As mentioned earlier in case of the general cuts, the shower cluster center was matched with the projected track position. For different momentum bins, the track match X and Y distributions were fitted with Gaussian functions and a 3σ cut was applied as a standard cut [18].

Cuts for positron like events:

- Charge type cut = Positive.
- Energy in preshower $E_{ps} > 0.2$ GeV.
- Momentum cut: $0.6 \text{ GeV}/c < p < 2.5 \text{ GeV}/c$.
- Calorimeter $\frac{E}{p}$ cut (momentum dependent): a 2.5σ cut was applied.
- Position match cut: a 2.5σ cut was applied.

Cuts for negative hadron like events:

- Charge type cut = Negative.

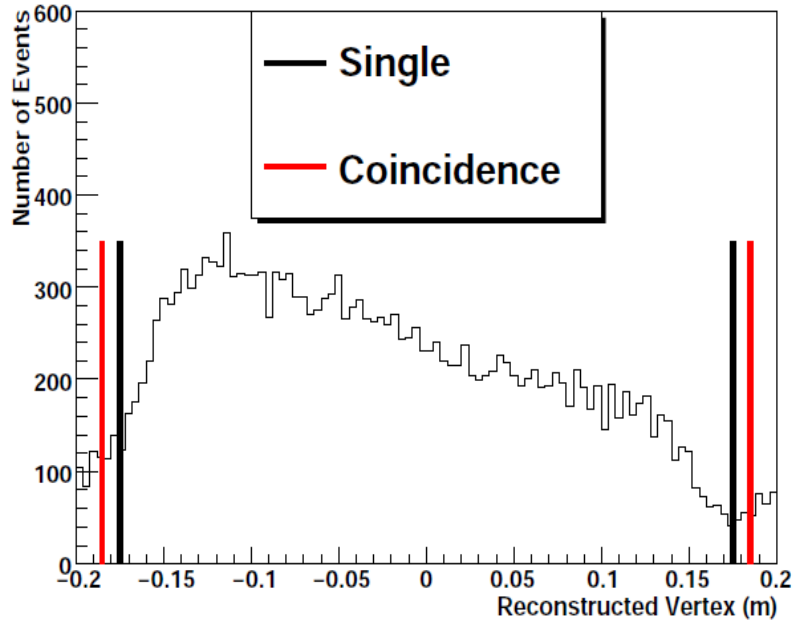


Figure 5.40: The reconstructed vertex. Electron like events were chosen to generate the plot. The cuts for the coincidence as well as singles events are shown which are slightly different.

- Energy in preshower $E_{ps} < 0.15\text{GeV}$.
- Momentum cut: $0.6 \text{ GeV}/c < p < 2.5 \text{ GeV}/c$.
- Position match cut: a 2σ cut was applied.

Cuts for positive hadron like events:

- Charge type cut = Positive.
- Energy in preshower $E_{ps} < 0.15\text{GeV}$.
- Momentum cut: $0.6 \text{ GeV}/c < p < 2.5 \text{ GeV}/c$.
- Position match cut: a 2σ cut was applied.

Cuts for photon like events:

- Energy in preshower $E_{ps} > 0.2\text{GeV}$.
- No total shower cluster found that matches the tracks. Photon like events do not have tracks.

- The shower cluster was matched with the preshower cluster.
- Total energy deposition is between 0.6 and 2.5 GeV.

5.11.1 π^- Contamination Study

In the BigBite spectrometer, one of the largest contamination to the electrons are the negative pions (π^-). However, having the calorimeters as the only PID detectors, there is no direct way to determine the π^- contamination to the electrons. Instead, the following method was employed to estimate the π^- contamination in the BigBite spectrometer. The comparison with the Monte-Carlo will be presented in the later sections. The contamination study was performed by X. Qian and K. Allada [18].

Integral method for T1 events (singles) :

In this method, the energy deposition of the preshower detector is plotted for different momentum bins without any cuts on the ADC channels. As shown in Fig. 5.41, the negative pion peak is centered around ADC channel 200 and fitted with a Gaussian function that is convoluted with Landau distribution function. On the other hand, the electron peak is fitted with a Gaussian from the ADC channel 400 onwards.

Then the π^- contamination of the electrons can be defined as :

$$\delta_{\pi^- \rightarrow e^-} = \frac{\int_{400}^{\infty} g(x) dx}{N_e(> 400)}. \quad (5.65)$$

Here, $g(x)$ is the Gaussian convoluted Landau distribution function integrated from channel 400 to the maximum. N_e is the number of electrons under the Gaussian peak above channel 400. Thus, the integral over $g(x)$ gives the number of negative pions leaking into the electrons when a cut on the ADC channel > 400 is applied. A similar procedure is applied with the T6 events as well. However, two methods were applied to calculate the pion contamination of the electrons in the case of the T5 coincidence events. The first method was the usual integral method explained above for the T1 events. The second method was the method that used the fact that the T5 trigger was formed from the T1 trigger and can be named as *suppression factor method*. It is described as follows:

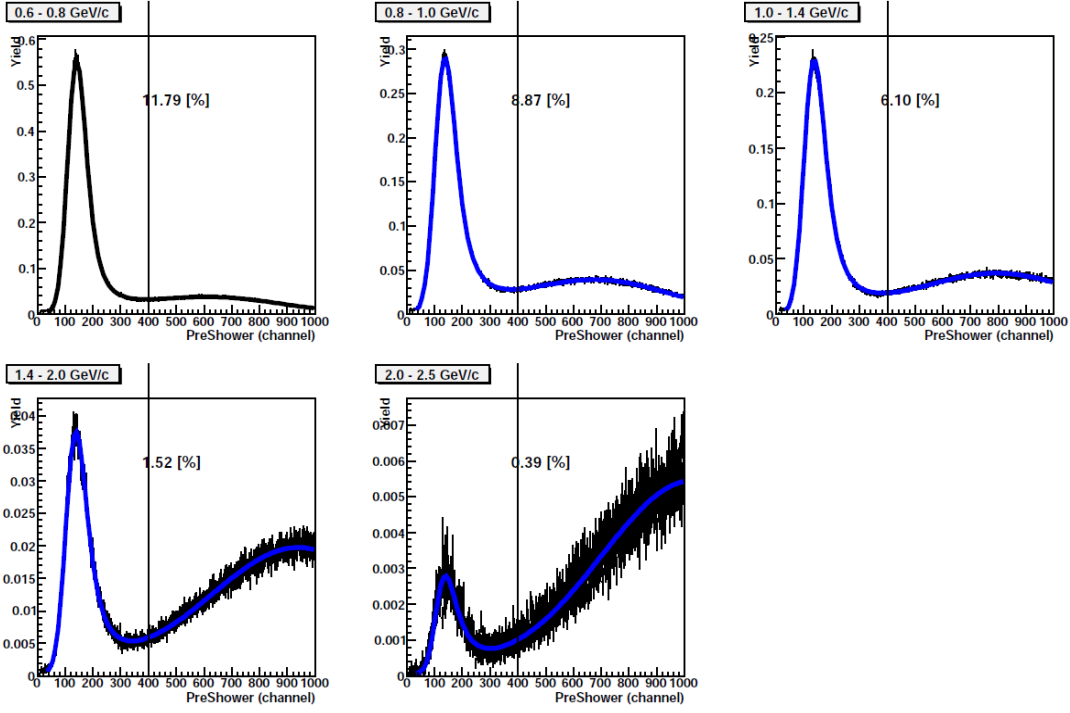


Figure 5.41: The pion contamination to electrons in BigBite for various momentum bins for T1 events.

Suppression factor method for T5 coincidence events:

In this method, we used the contamination number determined for the T1 events. A suppression factor can be defined as follows :

$$\gamma_{sup} = \frac{Y_{\pi^- \pi^\pm}^{T5} / Y_{\pi^-}^{T1}}{Y_{e\pi^\pm}^{T5} / Y_e^{T1}} = \frac{Y_{\pi^- \pi^\pm}^{T5}}{Y_{e\pi^\pm}^{T5}} \cdot \frac{1}{\delta_{\pi^- \rightarrow e^-}^{T1}}. \quad (5.66)$$

Here, $Y_{\pi^- \pi^\pm}^{T5}$ is the yield of the π^- mesons in the BigBite spectrometer which are coincident with the hadrons in the LHRS and $Y_{e\pi^\pm}^{T5}$ is the yield of the electrons coincident with the hadrons in the LHRS. Then the ratio $\frac{Y_{\pi^- \pi^\pm}^{T5}}{Y_{e\pi^\pm}^{T5}}$ gives the pion contamination of the electrons for the coincidence case which can be expressed as :

$$\delta_{\pi^- \rightarrow e^-}^{T5} = \gamma_{sup} \cdot \delta_{\pi^- \rightarrow e^-}^{T1}. \quad (5.67)$$

The results from both the methods are summarized in Table 5.5 where both the positive and negative polarities in the LHRS are considered. In all four momentum bins of the BigBite spectrometer, the negative pion contamination to the coincidence electrons in the

DIS region is below 3%.

Table 5.5: The T5 events pion to electron contamination study in BigBite.

LHRS polarity	Mom. range (GeV/c)	Integral method (%)	Suppression method (%)
negative	0.6 - 0.8	1.20	0.83
negative	0.8 - 1.0	0.60	0.45
negative	1.0 - 1.4	0.11	0.30
negative	1.4 - 2.0	0.12	0.07
positive	0.6 - 0.8	3.10	2.87
positive	0.8 - 1.0	1.44	2.13
positive	1.0 - 1.4	1.25	1.70
positive	1.4 - 2.0	0.27	0.47

5.11.2 Photon Induced Electron Contamination

The photon induced electrons contributed 70% to the contamination of the electrons in case of T1 trigger events. The origin of these photon induced electrons was neutral pions (π^0) generated during the scattering process. The π^0 meson has a very short mean lifetime of 8.4×10^{-17} s and the two main decay modes of the π^0 mesons are :

$$\pi^0 = \gamma + \gamma, \quad \pi^0 = \gamma + e^+ + e^-. \quad (5.68)$$

The main decay mode of the π^0 meson into two photons has a probability of 98% while the secondary decay mode into a photon and an electron-positron pair has a probability of 1%. Thus, a π^0 meson produced in the reaction quickly decays into photons inside the target cell. The photons generated from this decay then interact with the materials such as the cell walls, etc. and produce electron-positron pairs. Hence, irrespective of the decay modes that the neutral pions undergo, the final electrons could reach the spectrometer. These photon induced electrons were the largest contamination which could easily be misidentified as real DIS electrons. Since these photon induced electrons are always associated with the positrons produced in the same decay, the contamination of such electrons could be estimated with the help of the positrons. Assuming that the kinematics of the photon induced electrons and the positrons are the same, the BigBite polarity was switched to positive so that the positrons now were bent upwards analogous to the electrons in the negative mode. This allowed the positrons to have the same acceptance in the BigBite spectrometer as the electrons under

normal operation and thus, the yield of the positron in the positive polarity mode was compared to the yield of the electrons in the negative polarity mode. The comparison of the yields of the positrons and the electrons in both singles and coincidence cases is shown in Fig. 5.42.

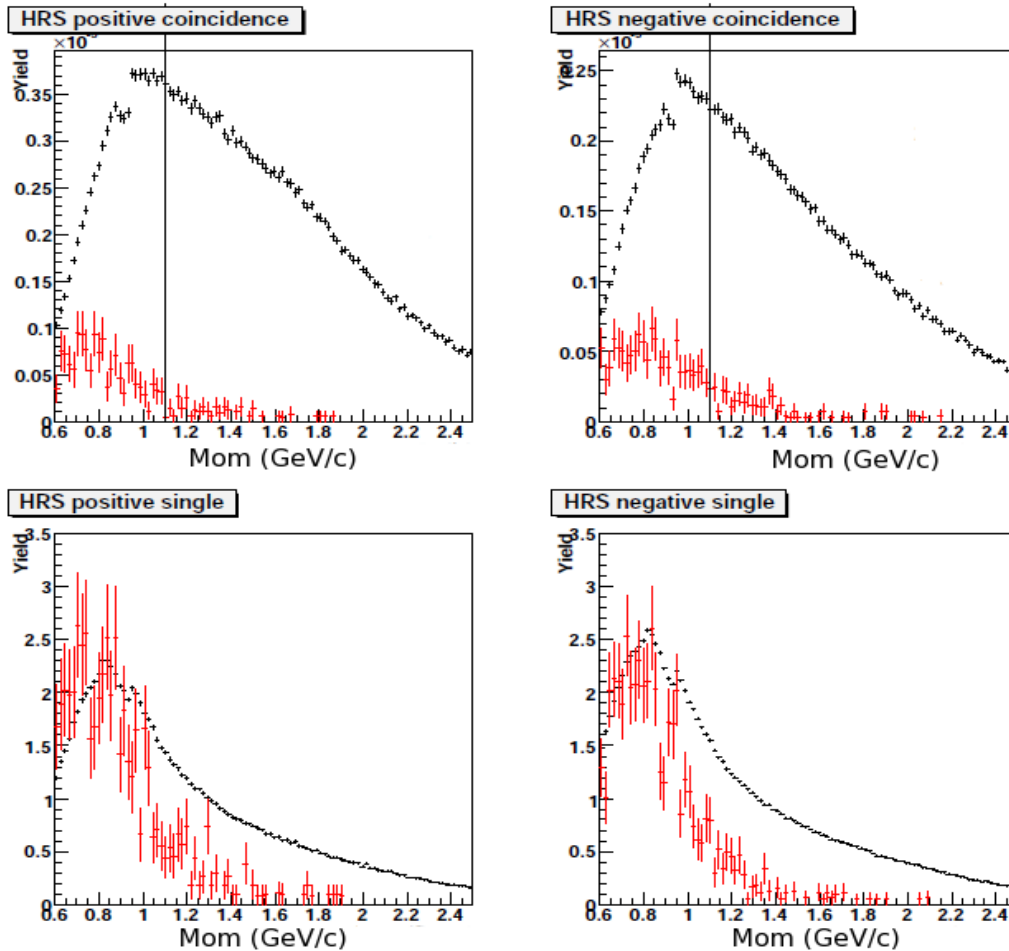


Figure 5.42: The yields of electron-like events in the negative polarity mode compared to the positron-like events in the positive polarity mode in the BigBite spectrometer. The red data points represent the positrons and the black data points represent the electrons. Both negative and positive polarities in the LHRS were considered. The large error bars indicate the low statistics of the positron-like events [18].

Both yields are comparable at low momentum because of the large π^+ contamination of the positrons. Once the π^- meson contamination of the electrons and π^+ meson contamination of the positrons were determined, the ratio of the positron to electron yields would give an estimation of the photon induced electron contamination of the DIS electrons. The

results are summarized in Table 5.6.

Table 5.6: The γ -induced electron contamination of the DIS electrons in the BigBite spectrometer for the coincidence events (T5 trigger).

LHRS polarity	Mom. range (GeV/c)	Contamination (T5)(%)
negative	0.6 - 0.8	22
negative	0.8 - 1.0	6.9
negative	1.0 - 1.4	1.7
negative	1.4 - 2.0	1.6
positive	0.6 - 0.8	19.6
positive	0.8 - 1.0	3.8
positive	1.0 - 1.4	1.2
positive	1.4 - 2.0	0.6

CHAPTER 6: ASYMMETRY ANALYSIS AND RESULTS

The primary physics goal of experiment E06010 was to extract the Collins and Sivers moments for different hadrons (π^+ , π^- , K^+ , and K^- -mesons) using a polarized ^3He target as an effective neutron target. This is the very first measurement of Collins and Sivers moments on a neutron target. Previous measurements by the HERMES and COMPASS collaborations were performed on proton and deuterium targets and are discussed at the beginning of this thesis. In this chapter, the preliminary results of the single target spin asymmetry in the semi-inclusive deep inelastic process $^3\text{He}\uparrow(e, e'\pi^-)X$ will be presented. The Collins and the Sivers moments on ^3He for π^- -mesons are extracted. The corresponding results for the neutron are presented as the final goal of this work after applying nuclear corrections. The inclusive asymmetries measured in the LHRS as well as in the BigBite spectrometer for all the detected particles (except for the electrons in case of the BigBite spectrometer) will be discussed in addition to the coincidence asymmetry results.

6.1 The Analysis Flow

The main objective of experiment E06010 was to measure the single target spin asymmetries of pions and kaons on a polarized ^3He target and extract the Collins and Sivers moments from the measured asymmetries. The schematic of the analysis flow from the raw data collected during the experiment to the final determination of the physics asymmetries is shown in the Fig. 6.1.

More than 10 Tb of raw data were stored on disk during the experiment. An extensive online monitoring of the data quality was performed during the process of data taking. The initial stage of the offline analysis involved calibrations of various detectors in order to make the particle identification process as well as the determination of the acceptance of the detectors efficient for the following physics analysis. Once all the detector calibrations were accomplished and the particle identification cuts were determined, the stability of the detectors was examined. This was done for each of the detectors and checked for each production run. Beam trips during a single run were removed in order to avoid any false asymmetries. All the problematic periods (any run which indicated problems) during the experiment were identified during the process of data stability check. The data stability check was an iterative process and was done several times. The data were replayed four

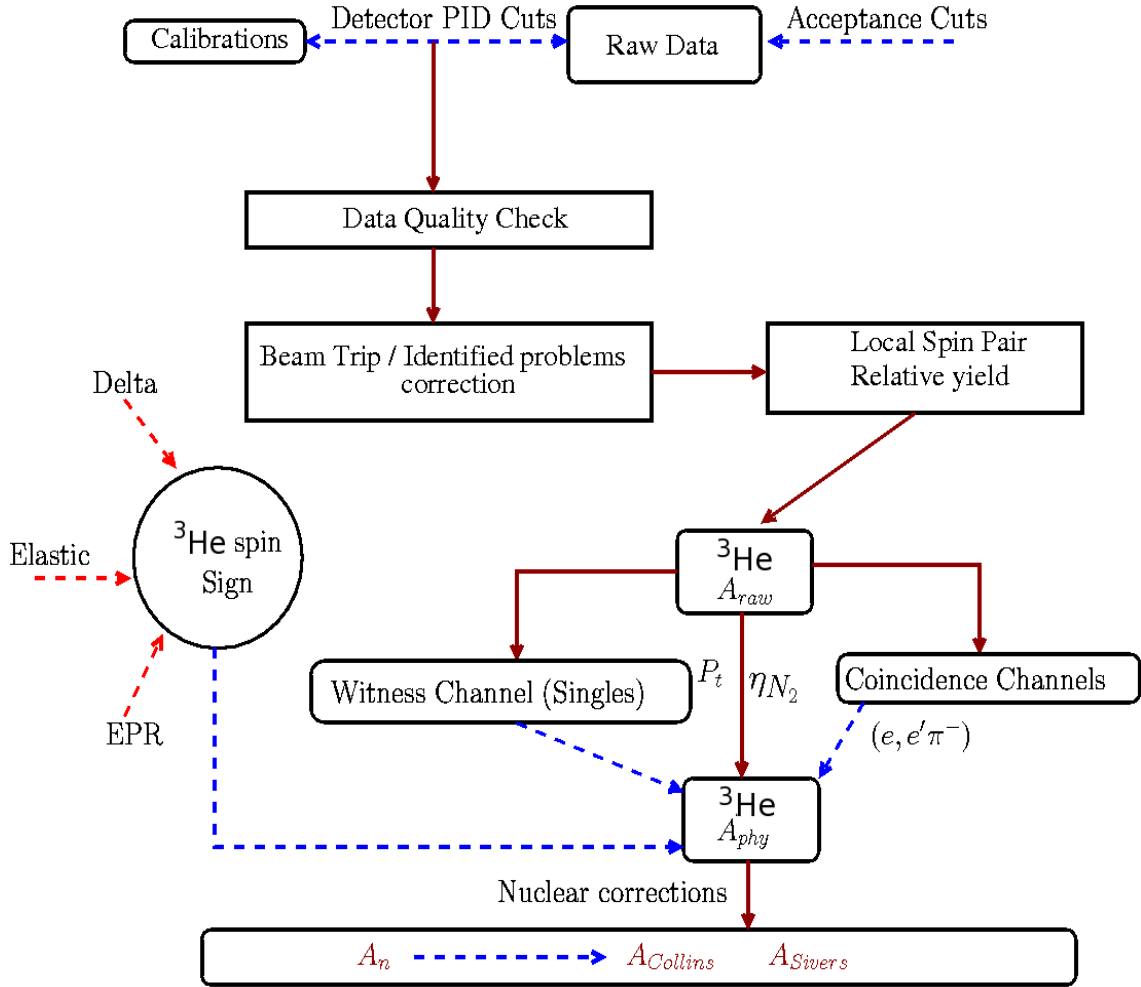


Figure 6.1: The analysis flow of the data in experiment E06010.

times during the stability check and correction process. The raw asymmetries were formed using two different methods¹ :

- Forming the ratio of the difference of the normalized yields² between the two target spin states over the corresponding sum for each run. At the end the average over all the runs was taken.
- Forming *local pairs/super local pairs* (discussed in the following section) after dividing the data into smaller periods and determining one asymmetry for each period to reduce

¹The asymmetries were formed by flipping the ^3He spins by 180° every 20 minutes during the data taking process. The flipping of the spins was done by sending an RF signal to the target (NMR discussed in chapter 4).

²The number of events detected after applying all the detector PID and kinematic cuts was corrected for the charge and livetime.

any systematic uncertainty and at the same time to incorporate reasonable statistics for the coincidence events. The asymmetries corresponding to different periods were then combined. In practice, in the *local pair method*, all the individual runs were combined and the data were divided into different periods depending on different experimental conditions experienced during the data taking. Then the data were further divided into two spin states in each period in order to form the asymmetry for that period. This method was implemented by X. Qian and is discussed in Ref. [18].

In addition to the primary semi-inclusive coincidence channel ($e, e'\pi^-$) presented in this thesis, there were several inclusive asymmetry measurements analyzed corresponding to the channels listed below:

- (e, π^-) using the LHRS (single: T3 trigger)
- (e, π^+) using the LHRS (single: T3 trigger)
- (e, e') using the LHRS (single: T3 trigger)
- (e, p) using the LHRS (single: T3 trigger)
- (e, π^-) using the BigBite spectrometer (single: T1 trigger)
- (e, e') using the BigBite spectrometer (single: T1 trigger)
- (e, γ) using the BigBite spectrometer (single: T1 trigger)

The (*local pair*) method was implemented in the final analysis for all the channels while the first method was used to cross check the results. Both methods are consistent with each other. The physics asymmetry was calculated by correcting the measured raw asymmetry for the target polarization (P_t) and the N_2 dilution factor (η_{N_2}). The beam polarization was irrelevant in the case of single target spin asymmetries and hence was not included in the corrections. The Collins and Sivers moments were extracted by fitting the ^3He asymmetry with the Collins and Sivers terms modulated by a sine function. The argument of the sine function contains the azimuthal angle of the target spin (ϕ_S) and the hadron plane angle (ϕ_h) with respect to the electron scattering plane. The detailed procedure of the extraction methods will be discussed in the following sections. The Collins and Sivers moments for the neutron are finally extracted from the ^3He results by applying nuclear corrections as discussed in section 6.11.

6.2 Asymmetry Formalism

The raw asymmetry is defined as :

$$A_{raw} = \frac{\frac{N^+}{Q^+L^+} - \frac{N^-}{Q^-L^-}}{\frac{N^+}{Q^+L^+} + \frac{N^-}{Q^-L^-}}, \quad (6.1)$$

where $N^{+/-}$ is the total number of events in spin state $+$ ($-$)³, $Q^{+/-}$ is the respective charge and $L^{+/-}$ represents the electronics livetime correction. If we assume that the livetime corrections are not statistically correlated with the number of events, then the uncertainty in the asymmetry can be expressed as

$$\delta A = \frac{2Y^+Y^-}{(Y^+ + Y^-)^2} \sqrt{\frac{1}{N^+} + \frac{1}{N^-}}, \quad (6.2)$$

where $Y^{(+/-)} = \frac{N^{(+/-)}}{Q^{(+/-)}L^{(+/-)}}$ is the yield in the respective spin state.

If the target polarization P_t and the dilution factor η_{N_2} are applied to correct the raw asymmetry, one can simply insert these terms to the above expressions for the asymmetry and the error in the asymmetry in order to calculate the respective physics quantities :

$$A_{phy} = \frac{1}{P_t \cdot \eta_{N_2}} \frac{\frac{N^+}{Q^+L^+} - \frac{N^-}{Q^-L^-}}{\frac{N^+}{Q^+L^+} + \frac{N^-}{Q^-L^-}}, \quad \delta A = \frac{1}{P_t \cdot \eta_{N_2}} \frac{2Y^+Y^-}{(Y^+ + Y^-)^2} \sqrt{\frac{1}{N^+} + \frac{1}{N^-}}. \quad (6.3)$$

6.3 Asymmetry : Local Pair Method/Super Local Pair Method

The motivation for forming the *local pairs* was to identify the existence of any temporal experimental problem which might be hidden and left unnoticed during the analysis process. In addition, the spectrometer yields in our experiment drifted with time due to the degradation of the shower blocks in the BigBite spectrometer. This might lead to the leakage of other false asymmetries into the real asymmetries over a long period of time. The formation of local pair minimizes this problem and it helps to reduce any possible systematic uncertainties. However, the local pair method has a couple of disadvantages :

- The determination of the uncertainty (Eq.(6.2)) would not be valid if the number of events in any of the two spin states ($+$ or $-$) is zero.

³In E06010, the spin state $+$ ($-$) corresponds to the ³He spin aligned vertically up (down) or to the left (right) with respect to the scattering plane containing the incoming beam.

- If the charge asymmetry between the + and the - state is large, the formation of local pair would make the statistical precision significantly worse.

The first disadvantage can be overcome by adopting the following formalism to combine the data [18]:

$$A = \frac{\sum_i (\frac{1}{P^i}) a^i \cdot (Y^{i+} - Y^{i-})}{\sum_i a^i \cdot (Y^{i+} + Y^{i-})}, \quad (6.4)$$

where the summation is over all the periods, P^i is the target polarization corrected for dilution effects and a^i is determined by the following condition:

$$\frac{\partial \delta A}{\partial a^i} = 0. \quad (6.5)$$

As it is extremely difficult to solve the above set of equations, the following approximation was implemented [18]:

$$A = \frac{\sum_i (\frac{1}{P^i}) a^i \cdot (Y^{i+} - Y^{i-})}{\sum_i a^i \cdot (Y^{i+} + Y^{i-})} = \frac{\sum_i A^i a^i \cdot (Y^{i+} + Y^{i-})}{\sum_i a^i \cdot (Y^{i+} + Y^{i-})} \approx \frac{\sum_i b^i A^i}{\sum_i b^i} \quad (6.6)$$

The best b^i and the best a^i can be expressed as :

$$b^i \sim \frac{1}{(\delta A^i)^2} \sim \frac{1}{\frac{1}{N^+} + \frac{1}{N^-}} \sim \frac{1}{\frac{1}{Y^+ L^+} + \frac{1}{Y^+ L^-}} \quad (6.7)$$

$$a^i = \frac{b^i}{Y^{i+} + Y^{i-}}. \quad (6.8)$$

The problem with large charge asymmetries in the local pairs can be reduced by the formation of *super local pairs* where each target spin state of the original local pair is further divided into two states. Figure 6.2 shows a comparison of the charge asymmetries for the two methods.

The *super local pair method* increases the number of local pairs originally formed almost by a factor of 2 and reduces the width of the charge asymmetry. Thus, it helps reducing the systematic uncertainties significantly. In the final analysis of extracting the asymmetries in E06010, *the super local pair method* has been utilized.

6.4 Detector PID Cuts, Acceptance and Kinematic (SIDIS) Cuts

The various detector cuts applied in the asymmetry analysis to detect the hadrons in the LHRS and electrons in the BigBite spectrometer are summarized below:

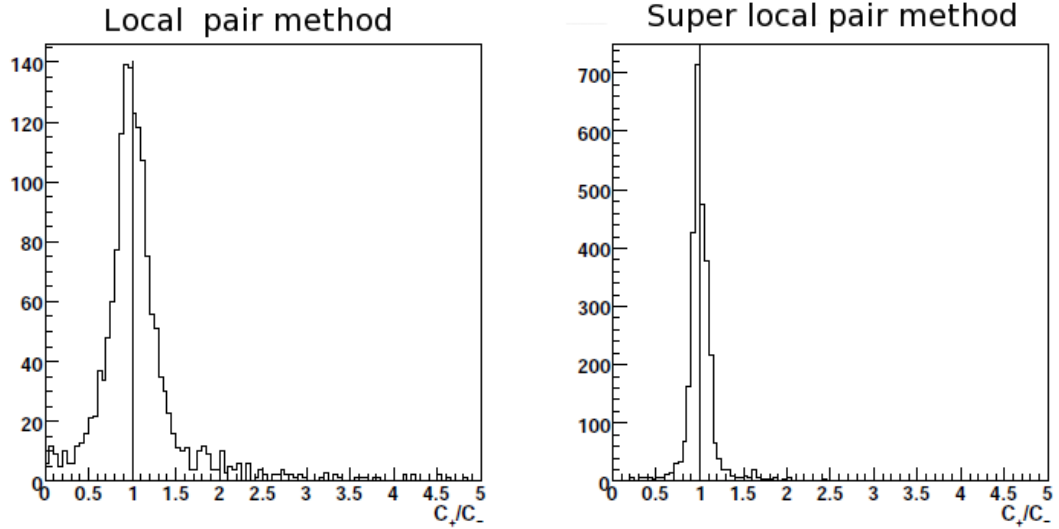


Figure 6.2: The charge asymmetry comparison between the *local pair method* (left) and the *super local pair method* (right) [18].

Detector PID cuts :

- LHRS : Gas Čerenkov ADC sum < 250 to identify π^- and K^- mesons.
- LHRS : Lead glass counter $\frac{E}{P} < 0.06$ to identify π^- mesons.
- LHRS : Aerogel Čerenkov ADC sum > 150 to identify π^- mesons.
- BigBite : Preshower energy ADC sum > 400 and preshower/shower $\frac{E}{P} > 0.80$ and < 1.2 to identify the electrons.
- Coincidence cuts : coincidence timing cut ± 3 ns on the $(e, e'\pi^-)$ spectrum using the T5 trigger only.

In addition to these PID cuts on the detectors, several other cuts such as one track event cut on the LHRS, track matching cut on the preshower and shower detectors in the BigBite spectrometer, the cut for negatively charged particle in the optics reconstruction, etc. were also implemented which are discussed in chapter 5. The LHRS acceptance cut (R-cut) was applied as well in the analysis and is discussed in Appendix D. Only events within the boundary defined by the R-cut in the LHRS (realized by the cut “*accep==1*” in the

analyzer) were chosen for the asymmetry analysis.

Semi-Inclusive DIS cuts/Kinematic settings⁴:

- $Q^2 > 1 \text{ GeV}^2$ (Fig. 6.3).

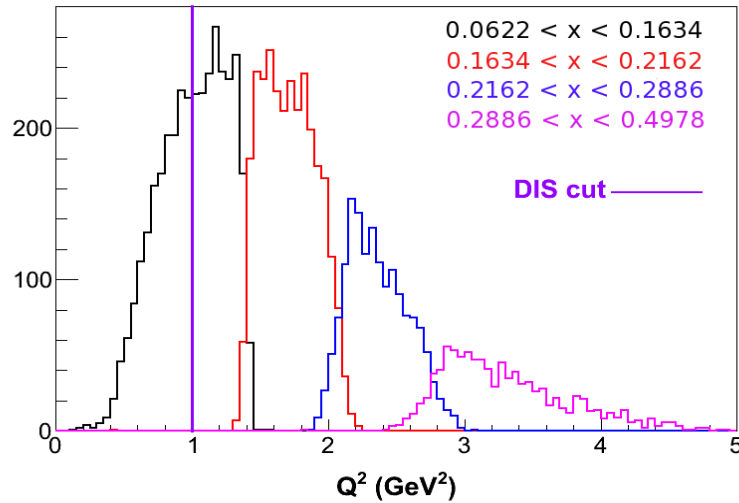


Figure 6.3: Q^2 distribution for each x-bin. The violet line shows the cut $Q^2 > 1 \text{ GeV}^2$.

- Invariant mass $W > 2 \text{ GeV}$ to avoid the nuclear resonance region (Fig. 6.4).

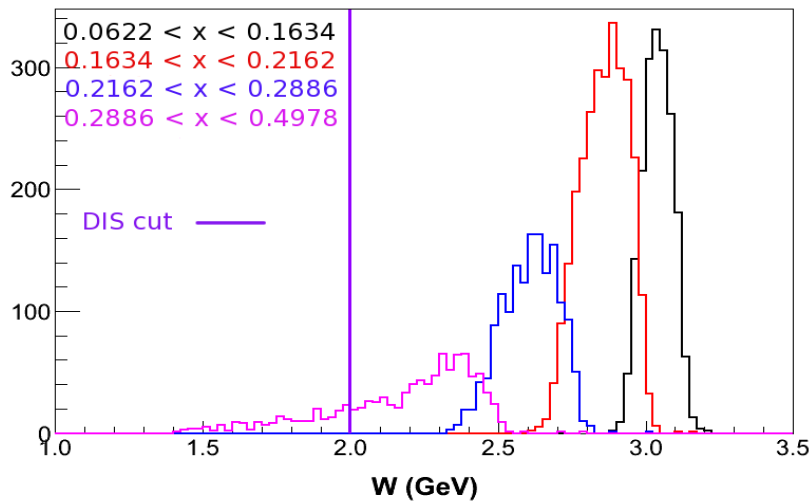


Figure 6.4: The invariant mass spectrum for each x-bin. The violet line shows the cut $W > 2 \text{ GeV}$.

- Invariant mass of the pion $W' > 1.5$ GeV to avoid the nuclear resonance region (Fig. 6.5).

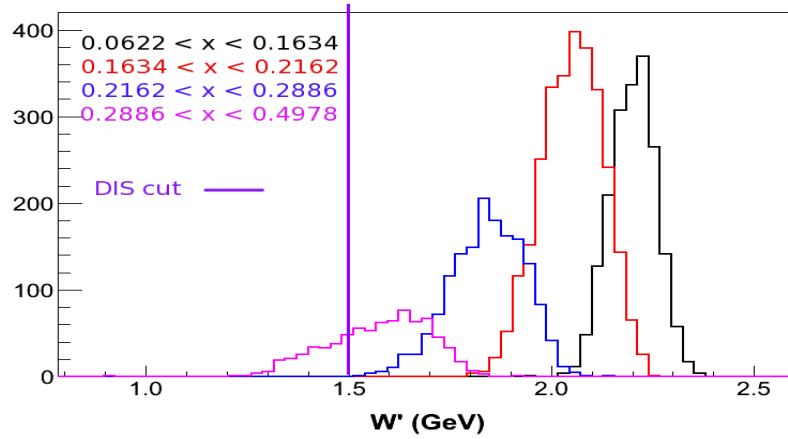


Figure 6.5: The invariant mass spectrum of the pions for each x -bin. The violet line shows the cut $W' > 1.5$ GeV.

- $0.3 < z < 0.7$ (Fig. 6.6).

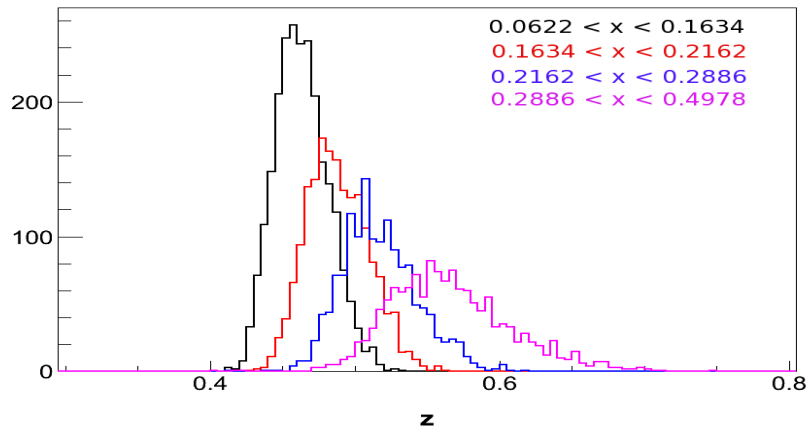


Figure 6.6: To ensure the current fragmentation region, a cut $0.3 < z < 0.7$ is chosen. z is shown for four different x -bins.

6.5 Phase Space and Angular Coverage

The phase space and the angular coverage for the SIDIS reaction $n^\dagger(e, e'\pi^-)X$ are shown in Fig. 6.7 and Fig. 6.8, respectively.

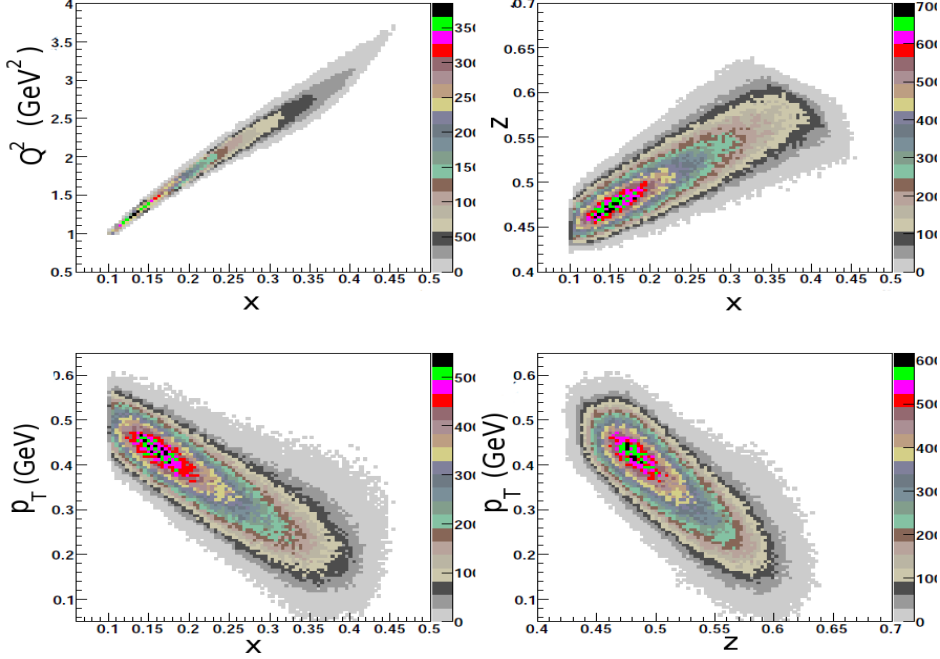


Figure 6.7: The phase space for the reaction $n^\uparrow(e, e'\pi^-)X$ in E06010. The plots are generated after applying all the relevant cuts used in the analysis [18].

6.6 Inclusive Asymmetries in the LHRS

The single spin target asymmetries for the inclusive DIS processes can be defined as:

$$A_{vert} = \frac{Y^\uparrow - Y^\downarrow}{Y^\uparrow + Y^\downarrow}, \quad A_{tran} = \frac{Y^\rightarrow - Y^\leftarrow}{Y^\rightarrow + Y^\leftarrow}. \quad (6.9)$$

Here, A_{vert} (A_{tran}) is the asymmetry in the vertical (transverse) target spin configuration. Y^\uparrow (Y^\downarrow) is the yield normalized by the charge and livetime when the target spins are vertically up (down). Similarly, Y^\rightarrow (Y^\leftarrow) is the yield normalized by the charge and livetime when the target spins are aligned to the right (left) in the horizontal plane with respect to the incoming beam.

The measured asymmetries in the LHRS involved the single asymmetries for (e, e') , (e, π^-) , (e, π^+) , and (e, p) on the polarized ^3He target. These were inclusive measurements with the T3 trigger only and data were taken in both the vertical and transverse ^3He polarization configurations. Fig. 6.9 and Fig. 6.10 show the ^3He asymmetries measured in vertical and transverse polarization directions, respectively. The asymmetries are corrected for the polarization but no N_2 dilution factor has been taken into account.

As can be seen from the plots, there is clearly a non-zero asymmetry for each of the

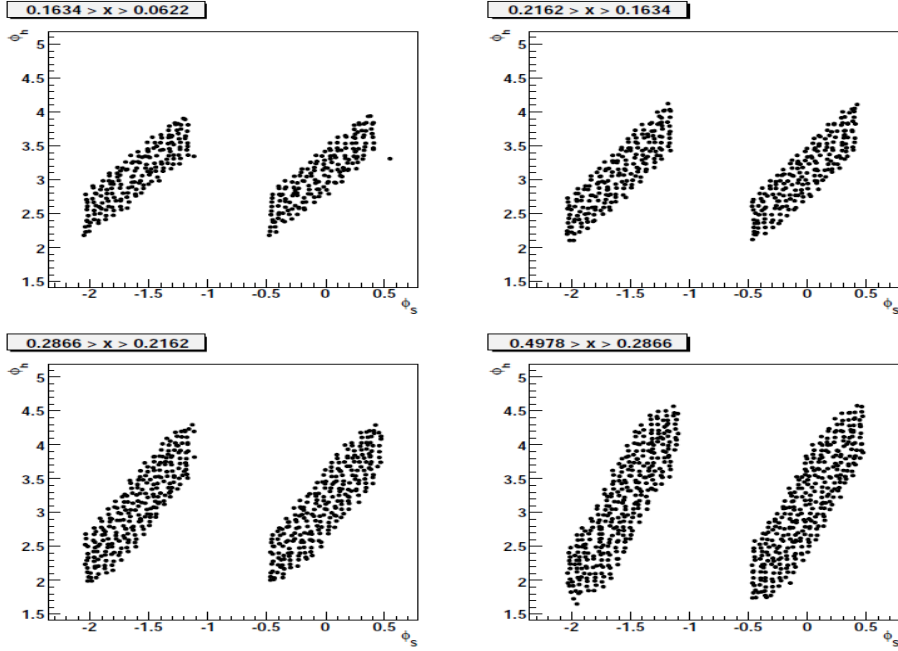


Figure 6.8: The angular coverage of the target spin angle (ϕ_S) and the outgoing hadron plane angle (ϕ_h) with respect to the scattering plane. The coverages for all the x-bins are shown [18].

identified particles in the vertical configuration while the asymmetries in the transverse target configuration are consistent with zero. This can be interpreted from Fig. 6.11 where both configurations are compared. In any inclusive reaction, there are three basic vectors: the momentum of the incoming particle (\vec{k}_1), the momentum of the outgoing particle that is observed (\vec{k}_2), and the target spin (\vec{S}_T). One can form only one independent scalar $(\vec{k}_1 \times \vec{k}_2) \cdot \vec{S}_T$ out of these three vectors. Now, in the case when the target spin is transversely polarized in plane (Fig. 6.11, left), the asymmetry is found to be small (may be even zero). On the other hand, when the target is vertically polarized (Fig. 6.11, right), the resultant scalar is different from zero and in fact, the asymmetry in this case is clearly non-zero.

The inclusive asymmetry in the case of vertical ^3He polarization for π^+ -mesons is positive while the asymmetry for π^- -mesons is negative. The sign of these hadron asymmetries can be compared to the results from experiment E704 at Fermilab [20]. E704 measured the analyzing power in inclusive π^+ and π^- production at high x_F (Feynman x) with a 200 GeV polarized proton beam. Figure 6.12 shows the dependence of the analyzing power A_N on x_F where A_N is defined as follows:

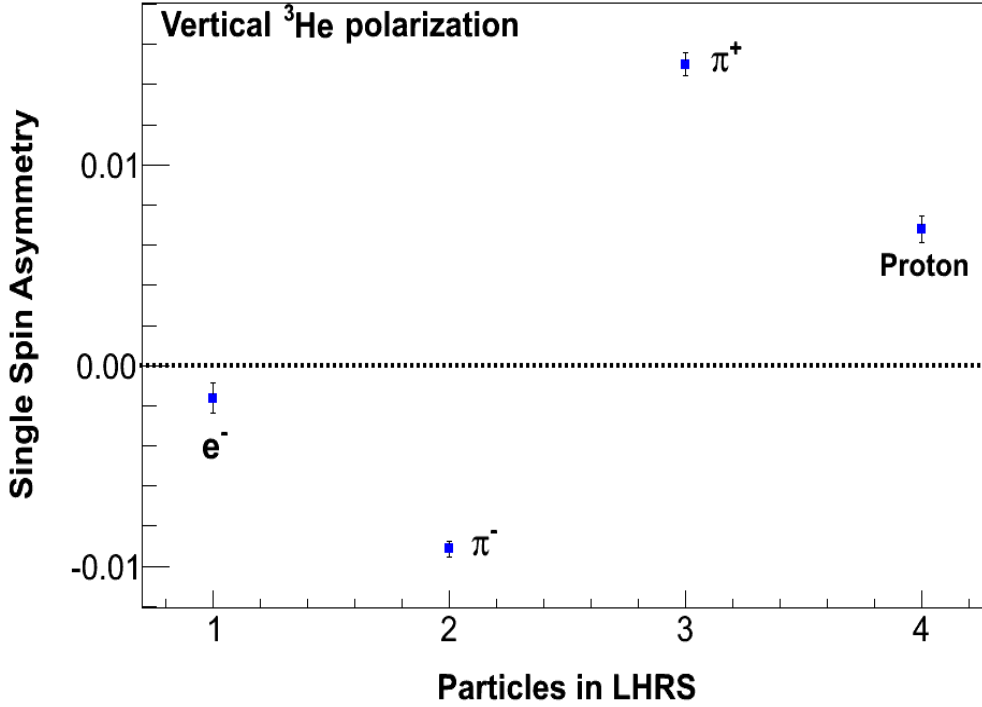


Figure 6.9: The single spin asymmetries measured in the LHRS for all the particles detected in the vertical ^3He polarization configuration. The particles include electrons, pions, and protons.

$$A_N = -\frac{1}{P_B \cos \phi} \frac{N_{\uparrow}(\phi) - N_{\downarrow}(\phi)}{N_{\uparrow}(\phi) + N_{\downarrow}(\phi)}, \quad (6.10)$$

ϕ is the azimuthal angle between the beam polarization direction and the normal to the π^{\pm} meson production plane. $N_{\uparrow(\downarrow)}$ is the number of pions produced for the beam polarization tagged as positive (negative) normalized to the beam flux. P_B represents the polarization of the beam. The negative sign in front of the equation is due to the fact that the hadrons were detected to the right side of the incoming beam. x_F is the Feynman x and is defined as:

$$x_F = \frac{P_L}{P_{L(max)}} = \frac{2P_L}{\sqrt{s}}, \quad (6.11)$$

where P_L is the longitudinal momentum of the particle and \sqrt{s} is the center of mass energy.

The plot shows that A_N increases from 0 to 0.42 with increasing x_F for the π^+ -mesons and decreases from 0 to -0.38 with increasing x_F for the π^- -meson data. The kinematic

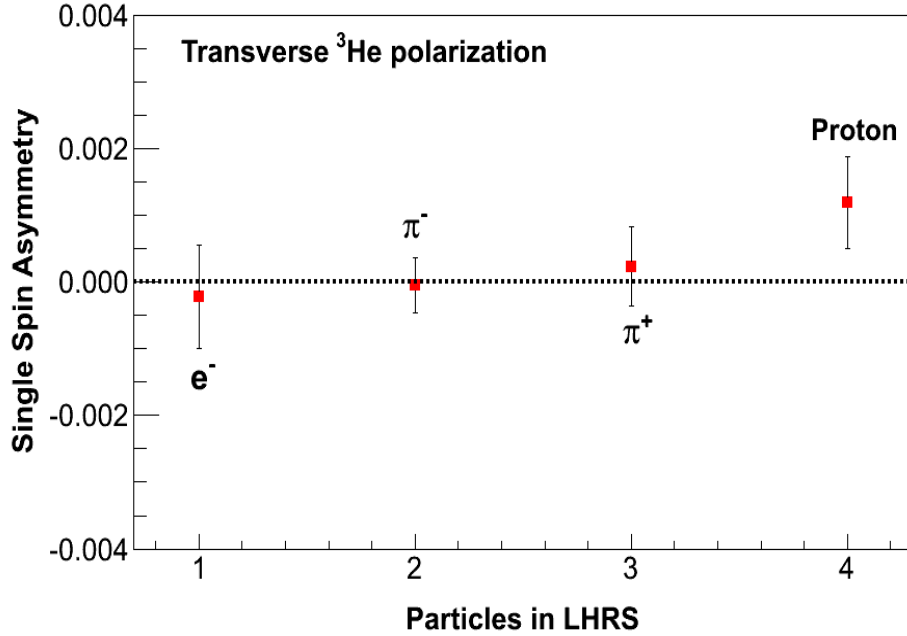


Figure 6.10: The single spin asymmetry measured in the LHRS for all the particles detected in the transverse ^3He polarization configuration. The particles include electrons, pions, and protons.



Figure 6.11: The formation of a scalar in case of inclusive reactions for both transverse (left) and vertical (right) target polarization configurations. \vec{k}_1 , \vec{k}_2 , and \vec{S}_T are defined in the text.

range covered was $0.2 \leq x_F \leq 0.9$ and $0.2 \leq p_T \leq 2.0$ GeV/c. In our case, $x_F = 0.39$ and our hadron (also electron in this case) detection was to the left side of the incoming beam. Moreover, unlike E704, in our case, the target was polarized and the asymmetry was defined with respect to the target spin direction and not to the incoming electron beam helicity. Hence, applying the appropriate corrections as compared to the E704 data, the sign of our asymmetries for the π^+ -mesons and the π^- -mesons are consistent. The inclusive asymmetries measured for all the hadrons and the electrons in the LHRS in the vertical

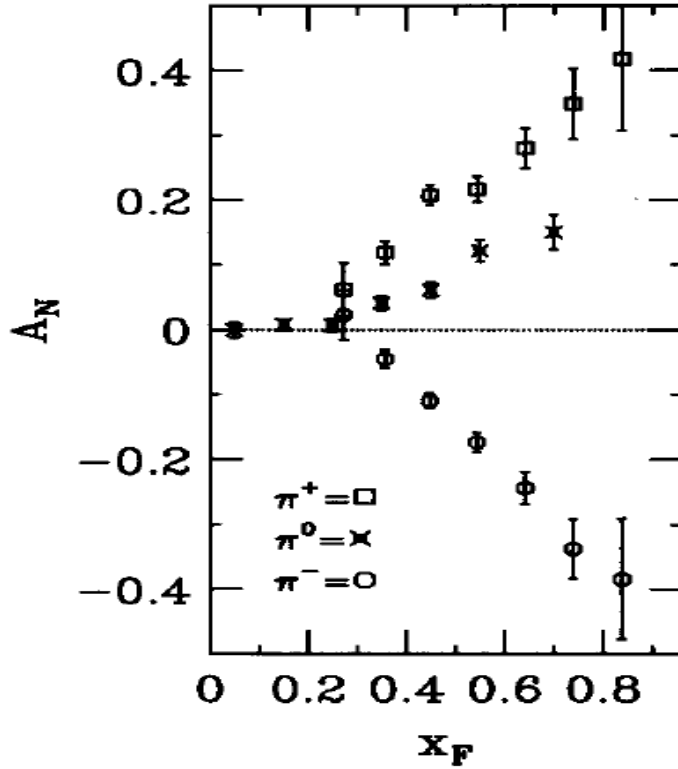


Figure 6.12: A_N for π^+ , π^- , and π^0 mesons as a function of x_F . The figure is reproduced from [20].

^3He target configuration are summarized in Table 6.1.

Table 6.1: Inclusive single spin asymmetries in the LHRS for the vertical target polarization. The asymmetries are corrected for polarization. No correction has been applied for the N_2 dilution.

Particle	$A_{phy} \pm stat.$
e^-	-0.0016 ± 0.0008
π^-	-0.0091 ± 0.0004
π^+	0.0150 ± 0.0006
p	0.0068 ± 0.0006

In the case of the transverse ^3He target polarization (in plane), the inclusive electron and pion asymmetries are consistent with zero while the proton asymmetries show a slightly positive non-zero single spin asymmetry at a 2σ level. The results are listed in Table 6.2.

Table 6.2: Inclusive single spin asymmetries in the LHRS for the transverse target polarization. The asymmetries are corrected for ^3He polarization. No correction has been applied for the N_2 dilution.

Particle	$A_{phy} \pm stat.$
e^-	-0.0002 ± 0.0007
π^-	-0.00005 ± 0.0004
π^+	0.0002 ± 0.0006
p	0.0010 ± 0.0007

6.7 Inclusive Asymmetries in the BigBite Spectrometer

The inclusive DIS asymmetries observed in the BigBite spectrometer for negative and positive hadrons are shown in Fig. 6.13 and Fig. 6.14. Inclusive electron asymmetries were also measured and are discussed in J. Katich's thesis [123]. In the BigBite spectrometer, pions and kaons were not identified and hence they are generally labeled as negative or positive hadrons.

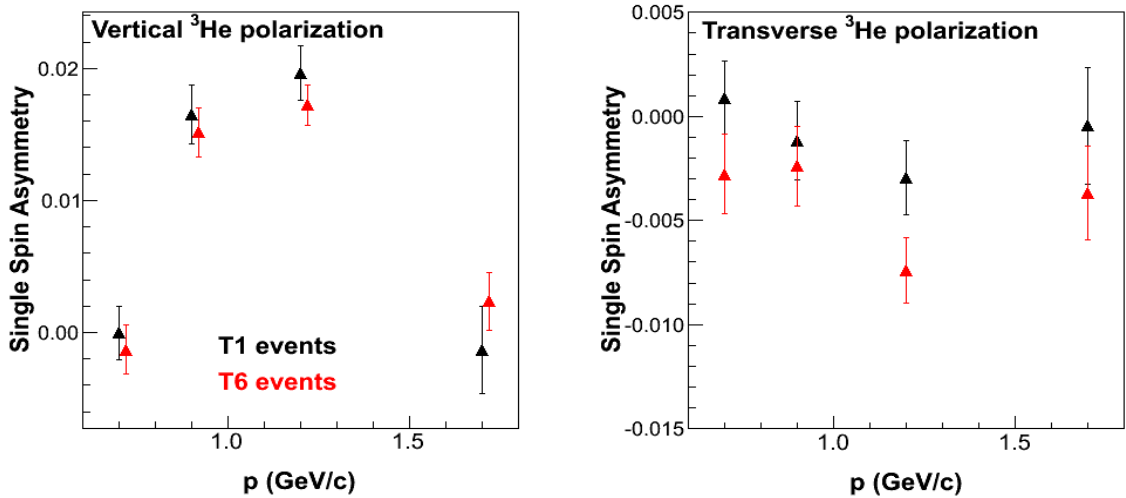


Figure 6.13: Single target spin asymmetries for the negatively charged hadrons in the BigBite spectrometer in the four momentum bins. The asymmetries are corrected for target polarization. However, no N_2 dilution factor has been taken into account. The red points correspond to the events with the T6 trigger and the black points correspond to the events with the T1 trigger.

The definition of the asymmetry in this case is the same as in case of the LHRS. However, the BigBite spectrometer was on the right side of the beam opposite to the LHRS.

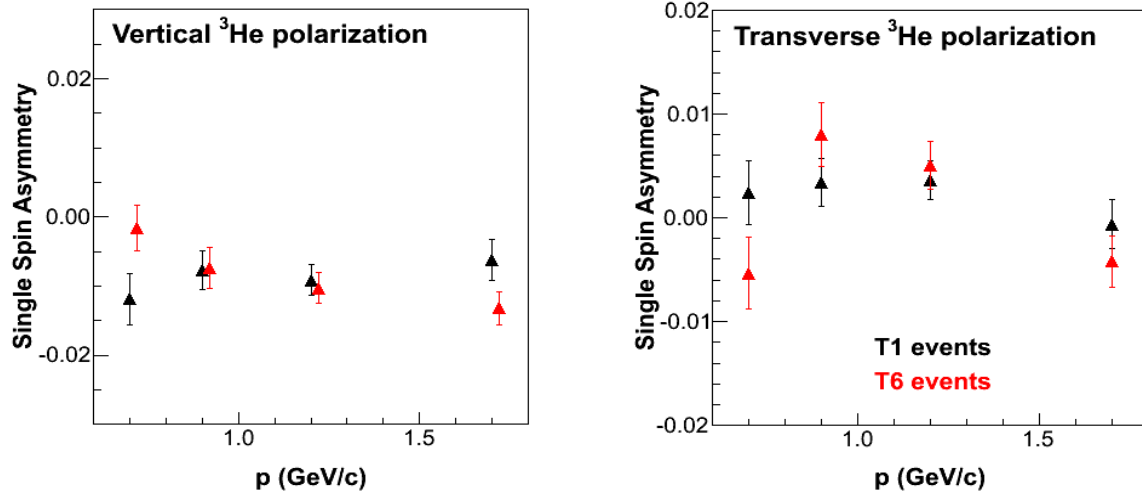


Figure 6.14: Single target spin asymmetries for the positively charged hadrons in the BigBite spectrometer in the four momentum bins. The asymmetries are corrected for target polarization. However, no N_2 dilution factor has been taken into account. The red points correspond to the events with the T6 trigger and the black points correspond to the events with the T1 trigger.

Hence, opposite signs of the asymmetries are expected for this spectrometer. Indeed, the asymmetry observed in the vertical configuration for negatively charged hadrons is positive in the BigBite spectrometer which is consistent with the observed negative asymmetry for π^- mesons in the LHRS. Similarly, the asymmetry for positive hadron is negative which is also as expected. However, unlike the LHRS, the asymmetries in the transverse target polarization configuration for both positive and negative hadrons are different from zero which can be attributed to the fact that the acceptance of the BigBite spectrometer is not symmetric. The difference between the T1 and T6 triggers is the threshold which was set at a higher value for the T6 trigger as compared to the T1 trigger.

6.8 Coincidence Single Spin Asymmetry

The single target spin asymmetries (SSA) in π^- electro-production via the semi inclusive deep inelastic reaction ${}^3\text{He}^\uparrow(e, e'\pi^-)X$ are given by:

$$A_{raw} = \frac{Y^+ - Y^-}{Y^+ + Y^-}. \quad (6.12)$$

Here Y^+ (Y^-) is the yield of the negative pions coincident with the electrons normalized by the charge and livetime when the ^3He spins are aligned vertically up (down) or to the left (right) of the incoming electron beam in the horizontal plane. The SSA on ^3He for different momentum bins in the BigBite spectrometer are shown in Fig. 6.15.

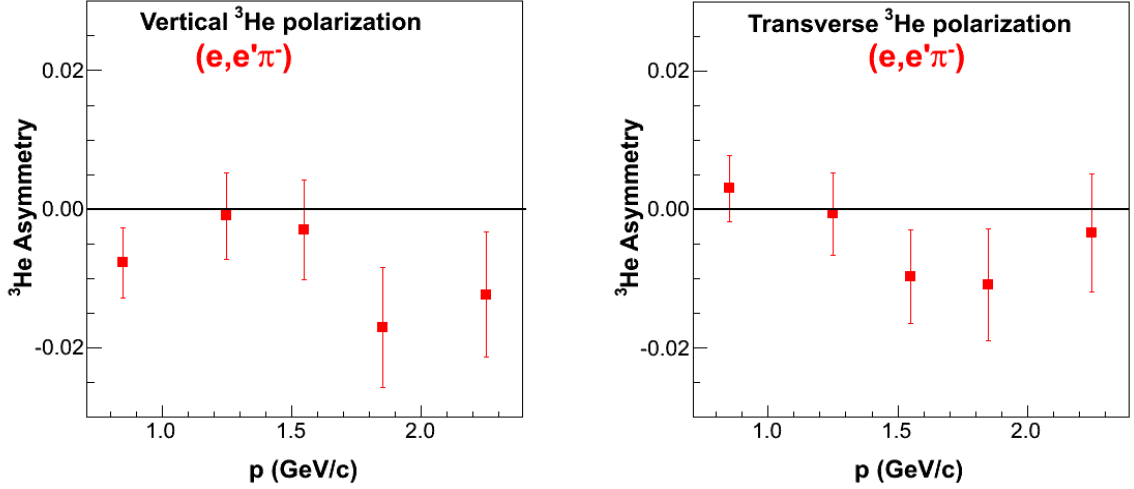


Figure 6.15: Single target spin asymmetries for π^- -mesons in the SIDIS $^3\text{He}\uparrow(e, e'\pi^-)X$ reaction for different momentum bins in the BigBite spectrometer. The asymmetries are corrected for ^3He polarization, but not for N_2 dilution.

The asymmetries for different momentum bins shown in Fig. 6.15 are corrected for ^3He polarization but no dilution factor for N_2 has been applied. As mentioned in chapter 5, the major contaminations to the BigBite coincidence electrons are photon induced electrons and negative pions. Hence, as a part of the background contamination study, the coincidence asymmetries for $^3\text{He}\uparrow(e, \pi^-\pi^-)X$ and $^3\text{He}\uparrow(e, \gamma\pi^-)X$ reactions are also extracted as shown in Fig. 6.16 and Fig. 6.17, respectively.

6.8.1 Extraction of Collins and Sivers Moments for π^- Mesons

Three different methods are employed in order to extract the Collins and Sivers moments from the measured ^3He asymmetries. The measured asymmetries are fitted with the following function :

$$A_{UT} = A_C \sin(\phi_h + \phi_S) + A_S \sin(\phi_h - \phi_S) + A_P \sin(3\phi_h - \phi_S), \quad (6.13)$$

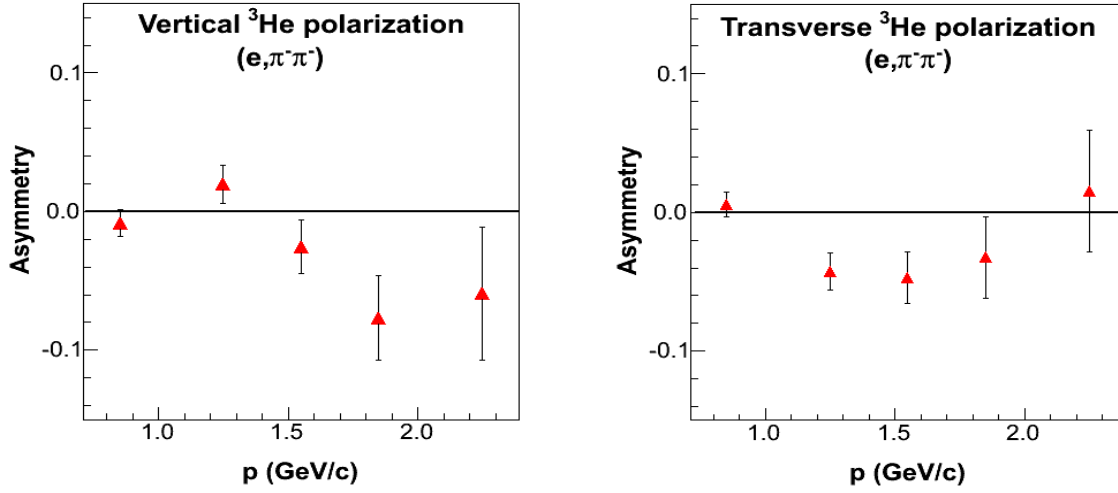


Figure 6.16: The single target spin asymmetries for the SIDIS ${}^3\text{He}\uparrow(e, \pi^-\pi^-)X$ reaction for different momentum bins in the BigBite spectrometer. The asymmetries are corrected for ${}^3\text{He}$ polarization, but not for N_2 dilution.

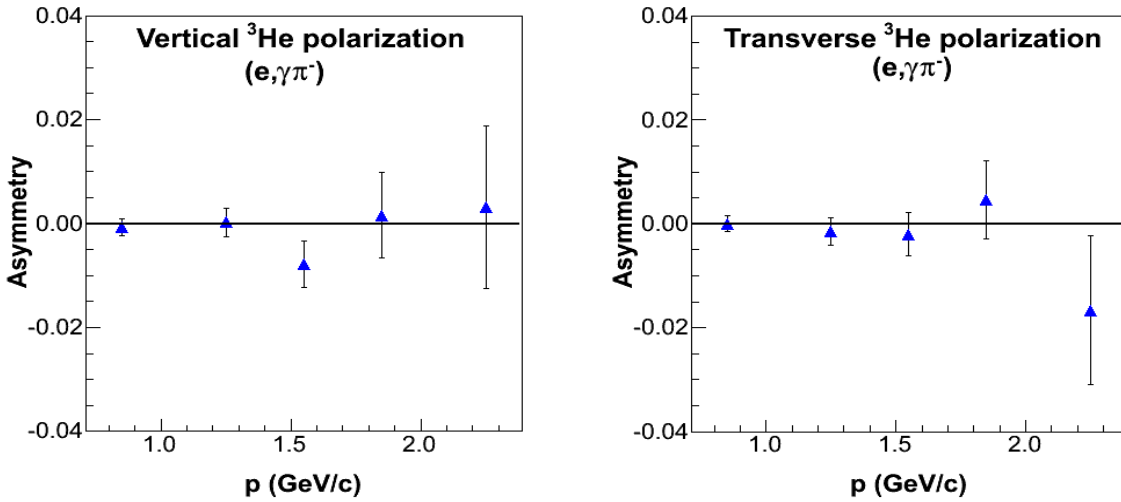


Figure 6.17: The single target spin asymmetries for the SIDIS ${}^3\text{He}\uparrow(e, \gamma\pi^-)X$ reaction for different momentum bins in the BigBite spectrometer. Only the correction for ${}^3\text{He}$ polarization has been applied. N_2 dilution factor has not been taken into account.

where A_{UT} is the measured ${}^3\text{He}$ asymmetry with an unpolarized (U) electron beam and a transversely (T) polarized target. A_C , A_S , and A_P are the fitted parameters which are identified as the Collins, Sivers, and Pretzelosity moments, respectively. ϕ_h is the angle between the plane containing the produced hadron (hadron plane) and the electron

scattering plane and ϕ_S is the angle of the target spins with respect to the electron scattering plane. The three methods are described as follows.

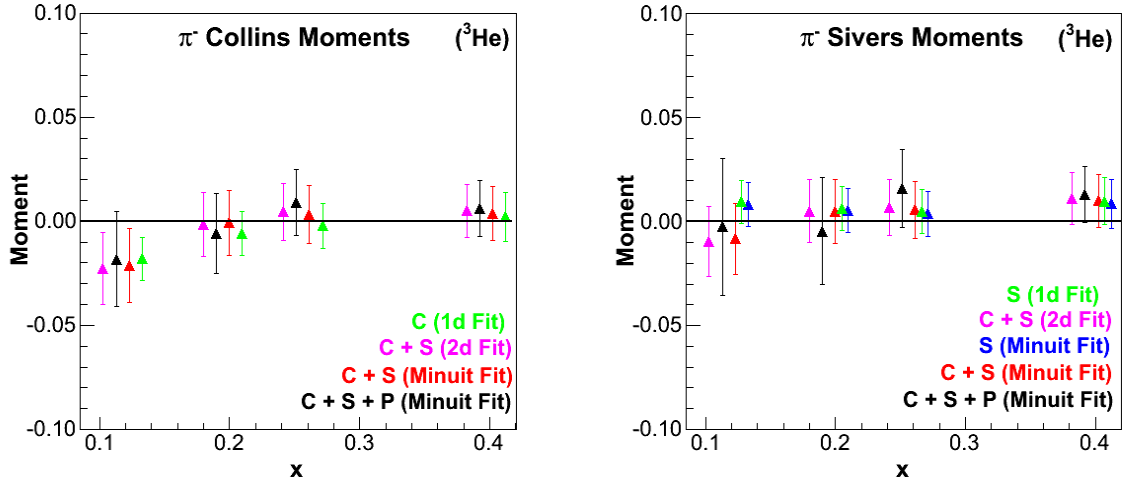


Figure 6.18: The Collins and Sivers moments extracted from different fitting methods of the angular dependences of ^3He raw asymmetries.

The methods are described as follows :

- One-dimensional fitting method :** In this method, the data were binned in $(\phi_h + \phi_S)$ (Collins angle) and $(\phi_h - \phi_S)$ (Sivers angle). The raw asymmetries were determined for each angular bin. The dependences were then fitted with a simple sine function. For the Collins asymmetry, the angular dependence was fitted with a function of the form $A_C \sin(\phi_h + \phi_S)$ while for the Sivers asymmetry, the functional form $A_S \sin(\phi_h - \phi_S)$ was used. The coefficients (results of the fit) A_C and A_S give the Collins and Sivers moments, respectively. In Fig. 6.18, the symbols corresponding to “*1d Fit*” are the results obtained by this method.
- Two-dimensional fitting method :** This method is similar to the one-dimensional fit method in the sense that a simple fitting function was implemented in this case as well. The data were binned in ϕ_h and ϕ_S and then the angular dependences were fitted with only two terms in the above fitting function. Hence, in this two dimensional fitting method, the data were fitted with the function $A_C \sin(\phi_h + \phi_S) + A_S \sin(\phi_h - \phi_S)$. Both the Collins and Sivers moments were extracted simultaneously in this case. The results corresponding to “*C+S 2d Fit*” are attributed to this method (see Fig. 6.18).

- **MINUIT⁵ minimization:** This analysis code was developed by X. Qian based on “Minuit 2” (details can be found in [18]) and it uses a χ^2 minimization procedure. In Fig. 6.18, all the results from the “*Minuit Fit*” correspond to this procedure of fitting. Functional forms such as $A_s \sin(\phi_h - \phi_S)$ (S), $A_c \sin(\phi_h + \phi_S) + A_S \sin(\phi_h - \phi_S)$ (C+S), and $A_c \sin(\phi_h + \phi_S) + A_S \sin(\phi_h - \phi_S) + A_P \sin(3\phi_h - \phi_S)$ (C+S+P) were used to compare the resultant moments in each case.

The methods summarized above are consistent within the statistical uncertainties as can be seen from Fig. 6.18. Especially, the agreement between the Minuit minimization results and the simple fitting results (blue and green points, red and magenta points) indicates the reliability of the analysis process. However, it turns out that the statistical uncertainties of the moments increase with the inclusion of more terms in the fitting function. It is evident from the results that when all the three terms (Collins, Sivers, and Pretzelosity) are taken into account, the statistical error bars increase as compared to the results when fewer terms are included. This is attributed to the fact that the angular coverages of ϕ_h and ϕ_S are not complete due to the experimental limitations. Hence, the statistical uncertainties depend on the number of the terms included in the fits of the angular distributions. In the ideal case, when the ϕ_h and ϕ_S have full coverages, the statistical uncertainties are independent of the number of terms modulated by the angles themselves.

Results for π^- mesons on ^3He

The results of the Collins and Sivers moments as a function of x for ^3He are presented in Fig. 6.19. The error bar associated with each point in each x bin represents the statistical uncertainty. The systematic uncertainties are presented as a blue band at the bottom of the plot. The systematic uncertainties in the measurement will be discussed in the next section. The theoretical prediction done by Anselmino *et al.* is plotted as a purple line for each of the extracted moments [21].

Observation :

It is evident from the Fig. 6.19 that both the Collins and Sivers moments for π^- -mesons in all the x bins are consistent with zero within the experimental uncertainties. The Collins moments agree with the theoretical predictions within experimental uncertainties as shown.

⁵MINUIT is a software used for fitting purposes and it is available in the ROOT analysis software package.

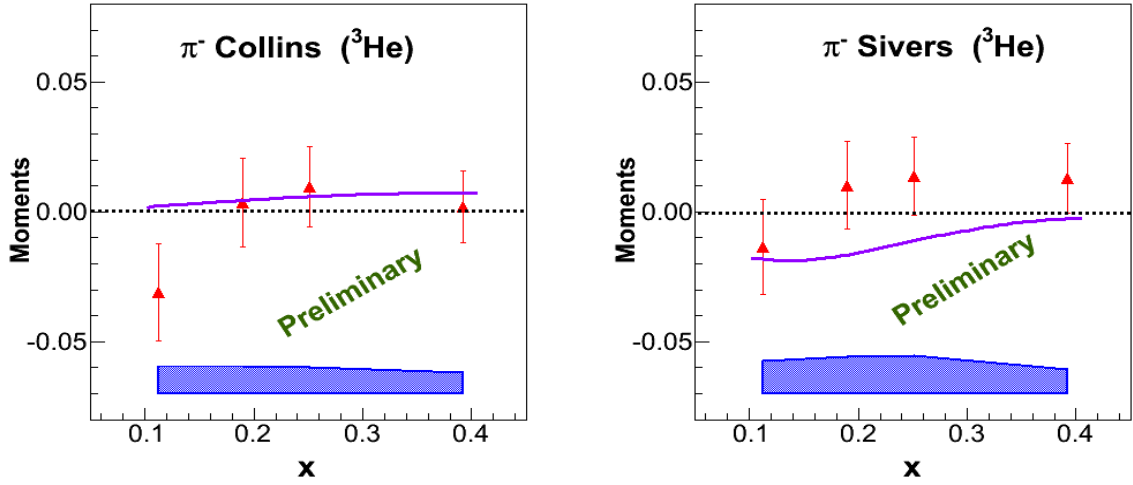


Figure 6.19: The Collins and Sivers moments for π^- mesons extracted from the ^3He asymmetries for different x bins. The error bars show the statistical uncertainties. The blue band represents the systematic uncertainties. The theoretical prediction from Anselmino *et al.* is shown by the purple line [21]. The dashed line is drawn to show zero. The results are prior to any radiative corrections (Preliminary).

However, the Sivers moments show a slight tendency to be positive while the theoretical prediction favors negative values.

6.9 Systematic Uncertainties

The various systematic uncertainties involved in the extraction of the Collins and Sivers moments of ^3He for π^- mesons from the E06010 data are summarized in this section. The details are presented in [18].

- **Contamination effect :** The largest contamination to the coincidence electrons in the BigBite spectrometer were photon-induced electrons and negative pions. On the other hand, the contamination in detecting coincidence π^- mesons in the LHRS was mainly due to K^- mesons. The electrons in the LHRS were rejected very efficiently by the Gas Čerenkov and the lead glass counters and hence the contamination was negligible (discussed in chapter 5).

In the BitBite spectrometer, the reaction channels $^3\text{He}e^\uparrow(e, \pi^-\pi^-)X$ and $^3\text{He}e^\uparrow(e, \gamma\pi^-)X$ could lead to false asymmetries which might contribute to the measured $^3\text{He}e^\uparrow(e, e'\pi^-)X$

asymmetry. The systematic effect of these false asymmetries can be analyzed by treating the π^- mesons and the positrons (they follow the same kinematics as the γ -induced electrons as discussed in chapter 5) in the BigBite spectrometer like normal coincidence electrons and determining the Collins and Sivers moments for those. Then the central values of these moments of ${}^3\text{He}^\uparrow(e, \pi^-\pi^-)X$ and ${}^3\text{He}^\uparrow(e, \gamma\pi^-)X$ processes were compared to the central values of the real ${}^3\text{He}^\uparrow(e, e'\pi^-)X$ process. The difference between the central values of the moments between the *false* processes and the real process is treated as a systematic uncertainty after proper weights had been applied due to the respective contaminations. The effect of the false asymmetry due the π^- meson contamination to the coincidence electrons in the BigBite spectrometer is ~ 0.1 - 2.5% of the statistical uncertainties while the effects of the γ -induced electrons are about 32%, 19%, 6%, and 6% for the four x bins. In case of the LHRS, the K^- meson contamination to π^- mesons is $\sim 0.3\%$ with a $\pi^-:K^-$ rejection ratio better than 10:1 by using the Aerogel detectors. The analysis of the Collins and Sivers moments for K^- meson can be found in [18]. The effect of the K^- contamination is less than 4% of the statistical uncertainties for each x bin.

- **BigBite calorimeter gain drop (Yield drift):** During the period of data taking, the preshower blocks in the BigBite spectrometer experienced continuous radiation damage. As a consequence, the yield measured in the spectrometer drifted with time during the experiment. However, there could also be other experimental factors such as target density, LHRS polarity change, etc., that might lead to a drift in the yield. The preshower gain drop was corrected in the offline analysis and checked several times for its stability. The *super local pair method*, as discussed earlier corrected the yield drift while forming the asymmetries. The data were divided into different sections and the yield in each section could be fitted with a first order polynomial. In practice, the yield in each spin state in the *super local pair method* was fitted. Thus, a correction could be implemented for different periods if needed. The details are presented in [18]. A drift in the yield can cause a change in the central values of the Collins and Sivers moments. However, this change was determined to be $\sim 11\%$, 2%, 2%, and 2% of the statistical uncertainties for the four x -bins, respectively.

- **Target polarization :** 5% relative to the central value of the measured asymmetries.

- **Target density** : The target density fluctuations due to the fluctuation in the target temperatures were corrected. This effect is $\sim 2.1\%$ of the statistical uncertainties.
- **N₂ dilution** : The systematic uncertainty is $\sim 0.3\text{-}0.6\%$ with respect to the central value of the asymmetries. The N₂ dilution analysis is discussed in chapter 5.
- **Livetime Correction** : The livetime correction to the data yielded 1.5% of the statistical uncertainties.
- **Tracking**: LHRS single track cut leads to 1.5% of the statistical uncertainties while the BigBite spectrometer tracking quality cut also leads to 1.5% of the statistical uncertainties.

Radiative corrections are not included in the analysis and hence the results presented in this thesis are not corrected for radiation effects. However, in our kinematics which is comparable to HERMES, the radiative corrections are expected to be small (less than 10% [124]). In addition, the diffractive vector meson production has also not been taken into account as a correction. The simulation for the experiment is being developed and the rest of the corrections will soon be estimated before the first publication. Table 6.3 summarizes all the systematic uncertainties that have been taken into account in the analysis.

Table 6.3: The systematic uncertainties in E06010 for the SIDIS process ${}^3\text{He}e^\uparrow(e, e'\pi^-)X$. Type A represents the systematic uncertainty with respect to the central value of the asymmetry. The type B represents the systematic uncertainty as percentage of the statistical uncertainty in the asymmetry.

Sources of error	Systematic Uncertainty	Uncertainty type
${}^3\text{He}$ target polarization	5%	A
${}^3\text{He}$ target density	2.1%	B
N ₂ dilution	0.3% \rightarrow 0.6%	A
K^- contamination in LHRS	4%	B
γ -induced e^- cont. in BigBite	32%, 19%, 6%, 6%	B
π^- contamination in BigBite	0.1% \rightarrow 2.5%	B
LHRS single track cut	1.5%	B
BigBite tracking quality cut	1.5%	B
Livetime correction	1.5%	B
Yield drift	11%, 2%, 2%, 2%	B

Two additional systematic uncertainties which were identified due to the applied vertex cut and the bin centering corrections are not discussed here and can be found in [18]. Both

of them are less than 20% of the statistical uncertainties. In addition to these experimental systematic uncertainties discussed above, the contributions from the terms besides the Collins and Sivers to the measured asymmetries can be treated as systematic uncertainties in the fitting procedure (see Appendix G). The final results include all of these systematic uncertainties.

6.10 Nuclear Correction

The experimentally determined ${}^3\text{He}$ asymmetry ($A_{3\text{He}}$) can be approximated by the following expression derived in Ref. [26].

$$A_{3\vec{\text{He}}} \approx f_n P_n A_{\vec{n}} + 2f_p P_p A_{\vec{p}}, \quad (6.14)$$

where $f_{n(p)}$ is the neutron (proton) *dilution factor*. In this formalism of defining a ${}^3\text{He}$ asymmetry, different nuclear effects such as Fermi motion and binding effects are taken care of by introducing the *effective polarization* of neutrons (P_n) and protons (P_p) in ${}^3\text{He}$. The expression holds for both the Collins and the Sivers asymmetries. The vector sign indicates the polarization associated with the asymmetries, i.e., the asymmetries are determined with polarized ${}^3\text{He}$ and hence, polarized nucleons. The neutron asymmetry can be extracted from the measured ${}^3\text{He}$ asymmetry by inserting the dilution factors and the effective polarizations of the neutrons and the protons into the asymmetry expression :

$$A_{\vec{n}} \approx [A_{3\vec{\text{He}}} - 2f_p P_p A_{\vec{p}}] \frac{1}{f_n P_n}. \quad (6.15)$$

Here we used a model prediction for $A_{\vec{p}}$ which will be discussed in the next subsection.

6.10.1 Effective Nucleon Polarization in ${}^3\text{He}$

The effective neutron (proton) polarization P_n (P_p) is defined by the model calculation described in Ref. [125] as follows :

$$P_n = P_n^+ - P_n^- = 1 - 2\Delta, \quad (6.16)$$

$$P_p = P_p^+ - P_p^- = -2\Delta'. \quad (6.17)$$

Here, $P_n^{+(-)}$ is the probability of finding a neutron with spin parallel (anti-parallel) to the spin of the ${}^3\text{He}$ nucleus. Similar definitions hold for the proton. The ${}^3\text{He}$ -neutron and

^3He -proton density matrices Δ and Δ' are defined as :

$$\Delta = \frac{1}{3}[P(S') + 2P(D)], \quad (6.18)$$

$$\Delta' = \frac{1}{6}[P(D) - P(S')], \quad (6.19)$$

where $P(S')$ and $P(D)$ are the probabilities of the S' and D states of ^3He , respectively. These are evaluated by fitting the results of various model calculations as a function of the ^3He binding energy as discussed in Ref. [125]. The fitting results yielded the following values for a ^3He binding energy of 7.72 MeV :

$$\Delta \approx 0.071 \pm 0.01, \quad \Delta' \approx 0.0142 \pm 0.002. \quad (6.20)$$

Therefore, the effective nucleon polarizations are :

$$P_n = 0.86_{-0.02}^{+0.036}, \quad P_p = -0.028_{-0.004}^{+0.009}. \quad (6.21)$$

If the polarized ^3He nucleus were a perfect effective neutron, then $P_n=1$ and $P_p=0$ with all the nucleons are in S state.

The dilution factors can be expressed as [26]:

$$f_{n(p)}(x, z) = \frac{\sum_q e_q^2 f_1^{q,n(p)}(x) D_1^{q,h}(z)}{\sum_{n,p} \sum_q e_q^2 f_1^{q,(n,p)}(x) D_1^{q,h}(z)}, \quad (6.22)$$

where the numerator contains the unpolarized parton distribution, f_1 , for the nucleon associated with the unpolarized fragmentation function, D_1 , summed over all the quark and antiquark flavors. The denominator contains the same quantities as the numerator but additionally summed over the nucleons. e_q represents the charge of the quark with flavor q and h is the outgoing hadron. The parametrizations used in the different terms (parton distribution and fragmentation function) in this $x - z$ separation are explained in [26]. The neutron dilution factors f_n for π^- -mesons were extracted for each x -bin and are shown in Fig. 6.20. The proton dilution factors f_p can be directly calculated by using $f_p = 1 - f_n$.

The numerical values of the neutron dilution factors f_n are also listed in Table 6.4:

In order to extract the neutron asymmetry $A_{\bar{n}}$ from Eq.(6.15), a correction for the proton asymmetry, $A_{\bar{p}}$, has to be applied. We used the results of Anselmino *et al.* [21] to correct for $A_{\bar{p}}$. Fig. 6.21 shows the predictions of Collins and Sivers moments for the proton and the neutron from Anselmino *et al.* for the production of π^- mesons.

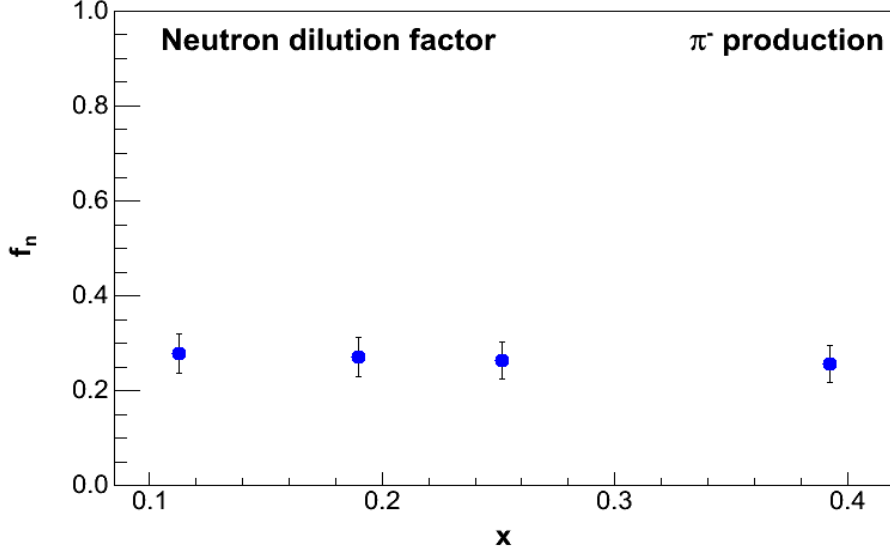


Figure 6.20: The neutron dilution factors from model calculations for all the four x bins in π^- meson production.

Table 6.4: The values of the neutron dilution factors used in the extraction of the neutron asymmetries from the measured ^3He asymmetries.

x -bin	Neutron dilution factor (f_n)	Uncertainty
0.1128	0.2775	0.042
0.1898	0.2712	0.040
0.2514	0.2632	0.039
0.3922	0.2561	0.038

6.11 The Collins and Sivers Moments for π^- Mesons On the Neutron

The Collins and Sivers moments on the neutron were extracted from the results on ^3He by applying nuclear corrections. The results of the Collins and Sivers moments on the neutron for π^- production are shown in Fig. 6.22. The theoretical predictions from different groups are listed below :

- The purple curves in both plots are predictions by Anselmino *et al.*. The prediction for the Collins moments is based on a global analysis of the HERMES, COMPASS and Belle data [6], [7], [126]. In this calculation, the behavior of the unpolarized distribution function and the unpolarized fragmentation function are assumed to be

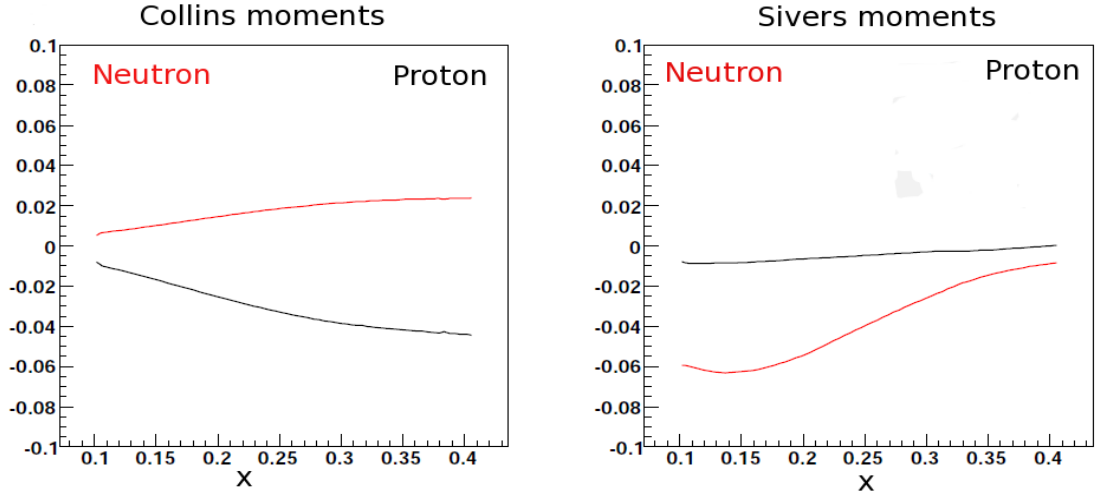


Figure 6.21: The Collins and Sivers moments for π^- -mesons produced off neutrons and protons as predicted by Anselmino *et al.* [21].

of Gaussian form in the transverse momenta of the initial quark and the final hadron, respectively. The prediction for the Sivers moment is based on the HERMES data. The details of the parametrization can be found in Ref. [21] and [46].

- The black curve for the Collins moment is a prediction by Ma *et al.* based on the sum rules of nucleon tensor charges [23] and [24].
- The green curve for the Collins moment is a calculation done by Pasquini. Here, the calculations are based on the light-cone constituent quark model (CQM) [127]. The transverse momenta of the quarks were assumed to be of Gaussian form in both distribution and fragmentation functions [22], [128].

The error bars associated with each point in Fig. 6.22 are statistical only. The systematic uncertainties are represented by the blue band at the bottom of each plot.

Observations :

All the extracted moments are consistent with zero within the experimental uncertainties. The extracted Collins moments agree well with all the theoretical predictions. The Sivers moments show a slight tendency to favor positive values (zero within error bars) while the theoretical prediction clearly shows a negative trend. The final results are summarized in Table 6.5 with the statistical and all the systematic uncertainties.

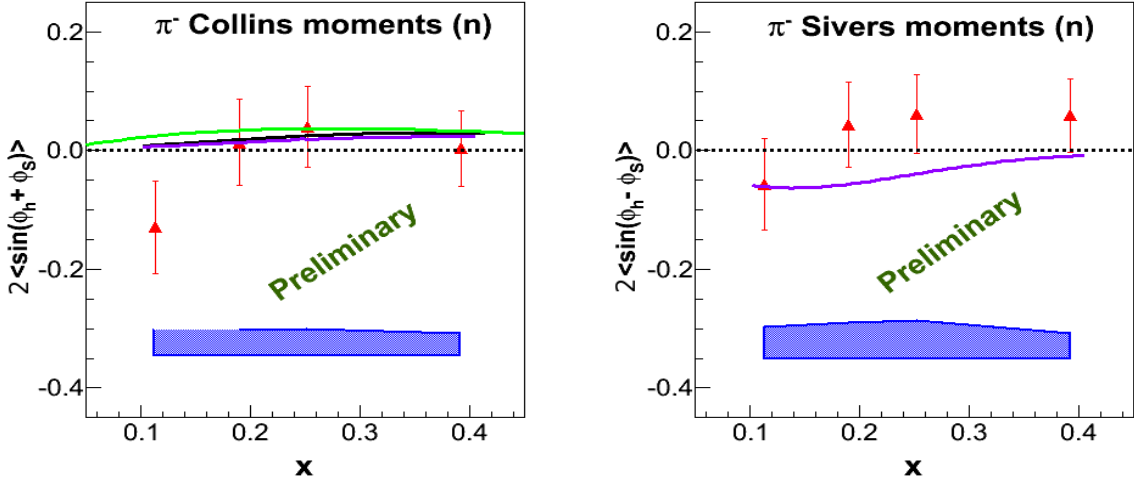


Figure 6.22: The neutron Collins and Sivers moments for π^- meson production as a function of x . The statistical uncertainties are shown as the error bars associated with the points. The blue band represents the experimental systematic uncertainties. Different theoretical predictions are shown for comparison. The purple curve shows the prediction by Anselmino *et al.* [21], the green curve shows the prediction by Pasquini, [22], and the black curve is from Ma *et al.* [23], [24]. The dashed line shows indicates zero. The results are prior to any radiative corrections (Preliminary).

Table 6.5: The results of the Collins (A_C) and Sivers moments (A_S) on the neutron for four x bins. The statistical and the total systematic uncertainties are represented by σ_{stat} and σ_{sys} , respectively.

x -bin	$A_C \pm \sigma_{stat} \pm \sigma_{sys}$	$A_S \pm \sigma_{stat} \pm \sigma_{sys}$
0.1128	$-0.129 \pm 0.078 \pm 0.044$	$-0.057 \pm 0.077 \pm 0.053$
0.1898	$0.014 \pm 0.073 \pm 0.044$	$0.044 \pm 0.072 \pm 0.061$
0.2514	$0.039 \pm 0.068 \pm 0.045$	$0.061 \pm 0.066 \pm 0.065$
0.3922	$0.004 \pm 0.063 \pm 0.039$	$0.059 \pm 0.062 \pm 0.042$

CHAPTER 7: SUMMARY AND OUTLOOK

E06010 acquired data in Hall A at Jefferson Lab for almost three months starting from the second week of November 2008 to the first week of February 2009 with a polarized ^3He target and a continuous electron beam with an energy of 5.9 GeV. This was the first experiment that measured single target spin asymmetries in the electro-production of pions and kaons in the deep inelastic region using a transversely polarized ^3He target as an effective neutron target. Two previous measurements at HERMES with a transversely polarized hydrogen target and at COMPASS with transversely polarized deuterium and NH_3 (proton) targets already published results on single spin asymmetries and extracted the Collins and Sivers moments for the proton and the deuteron as discussed in chapter 2. Here, the Collins and Sivers moments have been extracted from the measured ^3He asymmetries and preliminary results on the neutron are presented for the first time after implementing the nuclear corrections to the ^3He results. The extracted moments are extremely important in order to access information about the transverse momentum dependent distribution and fragmentation functions as these are convoluted with each other and cannot be measured explicitly in experiments. Hence, the extraction of these moments experimentally is very important as an initial step towards the determination of the distribution functions as well as the fragmentation functions.

In the analysis, extensive care has been taken in the process of particle identification to separate the π^- mesons from the electrons and also from the K^- mesons. The asymmetries were calculated using a *super local pair method* in order to minimize any possible systematic effects. The final Collins and Sivers moments have been extracted by fitting the measured asymmetries with a functional form that contains the sine modulations of the Collins and Sivers angles only as discussed in chapter 6. However, the systematic effects of the other higher order terms in the fitting procedure have been studied and quoted as systematic uncertainties. A comparison of the results on the neutron from this work with existing results on the proton from the HERMES experiment reveals that while the Collins moments for π^- mesons are negative for the proton, they are consistent with zero for the neutron target within experimental uncertainties. In the case of the Sivers moments, the HERMES data on the proton show values comparable to zero for π^- mesons. Our Sivers moments on the neutron are consistent with zero as well. However, the results from the COMPASS collabo-

ration on the deuteron target show that the Collins moments are consistent with zero while the results on the proton target reveal a non-zero behavior for the charged unidentified hadrons. The Sivers moments are also consistent with zero for both the deuteron and the proton targets. However, the results from the COMPASS experiment correspond to a larger range of x (including down to lower x) as compared to the range covered in E06010.

The results presented in this thesis are very important as this is the first independent measurement on the neutron so far. The extracted Collins and the Sivers moments are consistent with zero which is not only interesting but also very exciting when compared to the existing results mentioned above. The results for the Collins moments are in good agreement with the theoretical predictions while the Sivers moments show a slight deviation from the prediction. A comparison of the observed Sivers moments in this experiment with the existing HERMES results might lead to a naïve qualitative explanation which supports the small gluon orbital momentum. The Sivers moments for the π^+ mesons on a proton target [6] have opposite sign as compared to the Sivers moments on a neutron target [18]. This can be interpreted with the similar behavior of the anomalous magnetic moments of the proton and the neutron, and the Sivers single spin asymmetries discussed in Ref. [129]. Using the isospin symmetry, the Sivers single spin asymmetries for the π^+ mesons on a proton target should have an opposite sign as compared to the asymmetries on a neutron target. This already explains the opposite signs for the HERMES data [6] and the E06010 data [18]. Similar explanation is valid for the case of the π^- mesons. The formalism presented in Ref. [129] predicts a negative sign for the Sivers single spin asymmetries for π^- mesons on a proton target which implies that for a neutron target, the Sivers single spin asymmetries should show a positive trend. However, as the magnitude of the asymmetries are governed by the square of the quark charges, the effect in the case of the π^- mesons are suppressed as compared to the case of π^+ mesons. This is because the fragmentation of π^- meson is favored by the d -quark which has a charge of $-1/3$ as compared to the charge ($2/3$) of the u -quark. Now if the π^- meson in the reaction is produced by a mechanism pertaining to the gluon orbital angular momentum, the u -quark and d -quark single spin asymmetries add constructively, for a gluon in a nucleon Fock state will produce $u\bar{u}$ or $d\bar{d}$ pairs with equal weight. However, this mechanism can be realized mostly in the region where $z \rightarrow 1$. This can also contribute in our x region which is between 0.13 and 0.41. Thus, our Sivers single spin asymmetries for π^- mesons which do not show any large deviation from zero

but show a very tiny positive trend, might put a limit on the small contribution from the gluons to the orbital angular momentum of the nucleon [130]. Our results of the Collins and Sivers moments on neutron are of great importance as these can be used together with the world data to extract the transversity distribution and Sivers distribution functions for various quark flavors. This would not only extend the prevailing knowledge of the transverse distribution of quarks in a nucleon but also provide useful information regarding the contribution of angular momentum of quarks to the nucleon spin in the future.

Future

In addition to the existing experiments at HERMES, COMPASS, Belle, Jefferson Lab, and RHIC (Relativistic Heavy Ion Collider at Brookhaven National Laboratory in Upton, USA), the Hall A collaboration at Jefferson Lab proposed to carry out further precision measurements of single spin asymmetries. Semi-inclusive electro-production of charged pions from a transversely polarized ^3He target in deep inelastic kinematics are planned using electron beams with energies of 8.8 GeV and 11 GeV. These measurements with a newly proposed solenoid spectrometer (soLID) will provide precise measurements of the Collins, Sivers, and Pretzelosity asymmetries for the neutron with more control on the systematics as compared to E06010 and a full 2π coverage of ϕ_S , and a large azimuthal angular coverage on ϕ_h . The proposal has been accepted and the experiment is expected to take data in 2013. Another measurement is the PAX experiment which will use the proposed high energy anti-proton storage ring at GSI in Germany to access to the transversity distribution in the Drell-Yan process. The Sivers distribution function can also be extracted from this proton-antiproton scattering experiment. The knowledge of the transverse momentum dependent distribution functions as well as the fragmentation functions is in a very early stage. However, on the theoretical front, extensive efforts have been made in order to understand the existing data and provide predictions for future experiments. With the proposed measurements and further analysis of the existing data, we expect to access more information about these different distribution functions and hope to enrich the knowledge of the transverse degrees of freedom of the quarks inside the nucleon.

Appendix A: LIGHT-CONE COORDINATES

The light cone vector is defined as:

$$a^\mu = [a^-, a^+, \vec{a}_\perp] = \left[\frac{a^0 - a^3}{\sqrt{2}}, \frac{a^0 + a^3}{\sqrt{2}}, a^1, a^2 \right]. \quad (\text{A.1})$$

The first two components correspond to the x^- and x^+ axes, respectively, as shown in Fig. A.1.

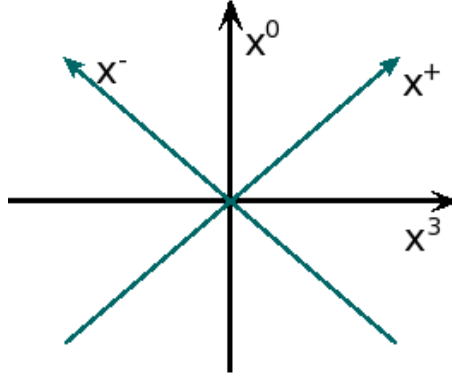


Figure A.1: The light-cone coordinates.

The scalar product of two light-cone vectors can be expressed as:

$$a \cdot b = a^+ b^- + a^- b^+ - \vec{a}_\perp \cdot \vec{b}_\perp \quad (\text{A.2})$$

In the light-cone coordinates, the four momentum of the nucleon and the virtual photon in the limit ($Q^2 \rightarrow \infty$, x constant) can be written as:

$$P^\mu = \left[\frac{M^2}{2P^+}, P^+, \vec{0} \right] \quad (\text{A.3})$$

$$q^\mu = \left[\frac{Q^2}{2xP^+}, -xP^+, \vec{0} \right] \quad (\text{A.4})$$

The metric tensor:

The metric tensor used here is

$$g^{\mu\nu} = \begin{pmatrix} 1 & 0 & 0 & 0 \\ 0 & -1 & 0 & 0 \\ 0 & 0 & -1 & 0 \\ 0 & 0 & 0 & -1 \end{pmatrix} \quad (\text{A.5})$$

where the indices run over 0,1,2,3. Repeated indices are summed.

Dirac matrices:

The Dirac matrices are expressed in terms of Pauli matrices in the chiral representation:

$$\gamma^0 = \begin{pmatrix} 0 & \mathbb{1} \\ \mathbb{1} & 0 \end{pmatrix} \tag{A.6}$$

$$\gamma^i = \begin{pmatrix} 0 & -\sigma^i \\ \sigma^i & 0 \end{pmatrix} \tag{A.7}$$

$$\gamma^5 = \begin{pmatrix} \mathbb{1} & 0 \\ 0 & -\mathbb{1} \end{pmatrix} \tag{A.8}$$

with the Dirac structure :

$$\sigma^{\mu\nu} \equiv \frac{i}{2}[\gamma^\mu, \gamma^\nu]. \tag{A.9}$$

Levi-Civita Tensor :

In 3-D, the *Levi-Civita* tensor is defined as follows :

$$\epsilon_{ijk} = \begin{cases} +1 & \text{if } (i, j, k) \equiv (1, 2, 3), (2, 3, 1), (3, 2, 1), \\ -1 & \text{if } (i, j, k) \equiv (1, 2, 3), (2, 3, 1), (3, 2, 1), \\ 0 & \text{if } (i = j), (j = k), (k = i). \end{cases} \tag{A.10}$$

In other words, the tensor ϵ_{ijk} is 1 if (i, j, k) are cyclic, -1 if (i, j, k) are anti-cyclic, and 0 if any of the indices gets repeated.

Appendix B: OPTICAL THEOREM

The Optical theorem is a general law of wave scattering theory. It is a powerful theorem which relates the forward scattering amplitude to the total cross section of the reaction. This can be written as:

$$\sigma_t = \frac{4\pi}{q} \text{Im}f(0) \quad (\text{B.1})$$

where σ_t is the total cross section and $\text{Im}f(0)$ is the imaginary part of the forward scattering amplitude, i.e., $\theta_{CM} = 0$. q represents the center-of-mass four-momentum. Here, the total cross section term σ_t includes both the elastic and inelastic contributions. The derivation of the optical theorem is based on the conservation of energy and on the conservation of probability in quantum mechanics. It is widely used in scattering theory.

In the case of DIS, the optical theorem relates the cross section to the imaginary part of the forward amplitude of the doubly virtual Compton process as shown in Fig. B.1.

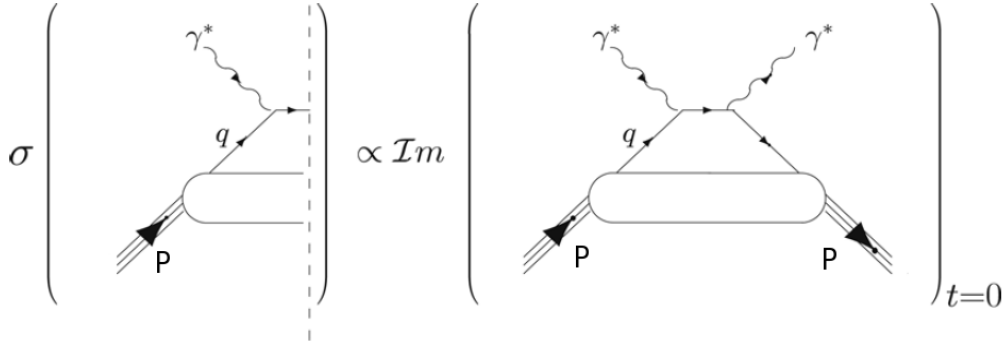


Figure B.1: The optical theorem relates the cross section in DIS to the imaginary part of the forward virtual Compton scattering [25].

If the forward Compton scattering amplitude is represented by \mathcal{A} and the hadronic tensor in the DIS process by $W_{\mu\nu}$, then

$$W_{\mu\nu} \sim \text{Im}[\mathcal{A}^{\mu\nu}] \quad (\text{B.2})$$

where

$$\mathcal{A}^{\mu\nu} = i \int d\xi^4 e^{iq \cdot \xi} \langle P, S | A(J^\mu(\xi) J_\nu(0)) | P, S \rangle. \quad (\text{B.3})$$

$A(J^\mu(\xi)J_\nu(0))$ is the time-ordered product. Since the structure functions correspond to the matrix elements in QCD and the matrix elements in QCD can be related to the forward Compton process, the optical theorem helps to express the leading twist quark distribution functions $q(x)$, $\Delta q(x)$, and $\delta q(x)$ in terms of quark-nucleon forward amplitudes.

Appendix C: RADIATION LENGTH

In this appendix, the radiation lengths and the thicknesses of different materials that the incoming electrons and the scattered particles passed through during the experiment are summarized. This information has been used in the Single Arm Monte Carlo (SAMC) simulation to estimate the elastic ^3He asymmetries in our kinematic settings. In addition, these radiation lengths and thicknesses were used for the optics optimization of the LHRS and the BigBite spectrometer.

Materials before scattering

- Exit Be window of the beam pipe : 0.0254 cm
- ^4He inside the target enclosure : 22.86 cm
- ^3He cell window (glass) : 0.01 cm
- ^3He (Half of the cell length inside the cell : 19.9 cm

Materials after scattering:

- ^3He inside the cell : 3.44 cm

If we assume that the reaction vertex is at the center of the cell, the effective thickness of the ^3He gas inside the cell that the outgoing particle has to travel through can be expressed as:

$$h = \frac{r}{\sin \theta} \tag{C.1}$$

where r is the radius of the cell. In our case, $\theta = 16^\circ$ and $r \approx 0.95$ cm. This is shown in Fig. C.1.

- Glass (cell wall) : 0.399 cm

This is determined by using Eq.(C.1) where we used a value of 0.11cm for the glass thickness (r).

- ^4He inside the target enclosure : 79.05 cm

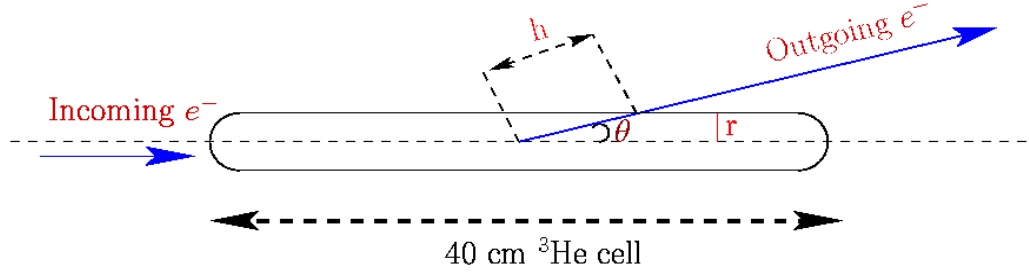


Figure C.1: The incoming and outgoing electron after scattering. The scattering angle $\theta = 16^\circ$.

- Yellow target enclosure G10 Glass Reinforced Epoxy : 0.0254 cm
- Air gap between the target enclosure and the LHRS entrance window : 51.23 cm
- LHRS Kapton entrance window : 0.0254 cm

The densities (ρ) and the radiation lengths (X_0) of the materials are listed in Table C.1:

Table C.1: The radiation lengths of different materials. These were used in the MC studies and other optics calibrations for the detectors.

Material before scattering	X_0 (cm)	ρ ($\frac{gm}{cm^3}$)	Thickness (cm)	# of X_0
Be	35.28	1.848	0.0254	0.000719
^4He	528107.5	0.00166	22.86	0.0000433
Glass	7.038	2.76	0.01	0.00142
^3He	43423	0.00125	19.9	0.000456
				$\Sigma = 0.00263$
Material after scattering				
^3He	43423	0.00125	3.44	0.0000792
Glass	7.038	2.76	0.399	0.0566922
^4He	528107.5	0.00166	79.05	0.0001496
Air	30423	0.00121	51.23	0.0016839
Kapton	28.6	1.42	0.0254	0.0008881
				$\Sigma = 0.05949$

Appendix D: ACCEPTANCE CUTS (R-CUT)

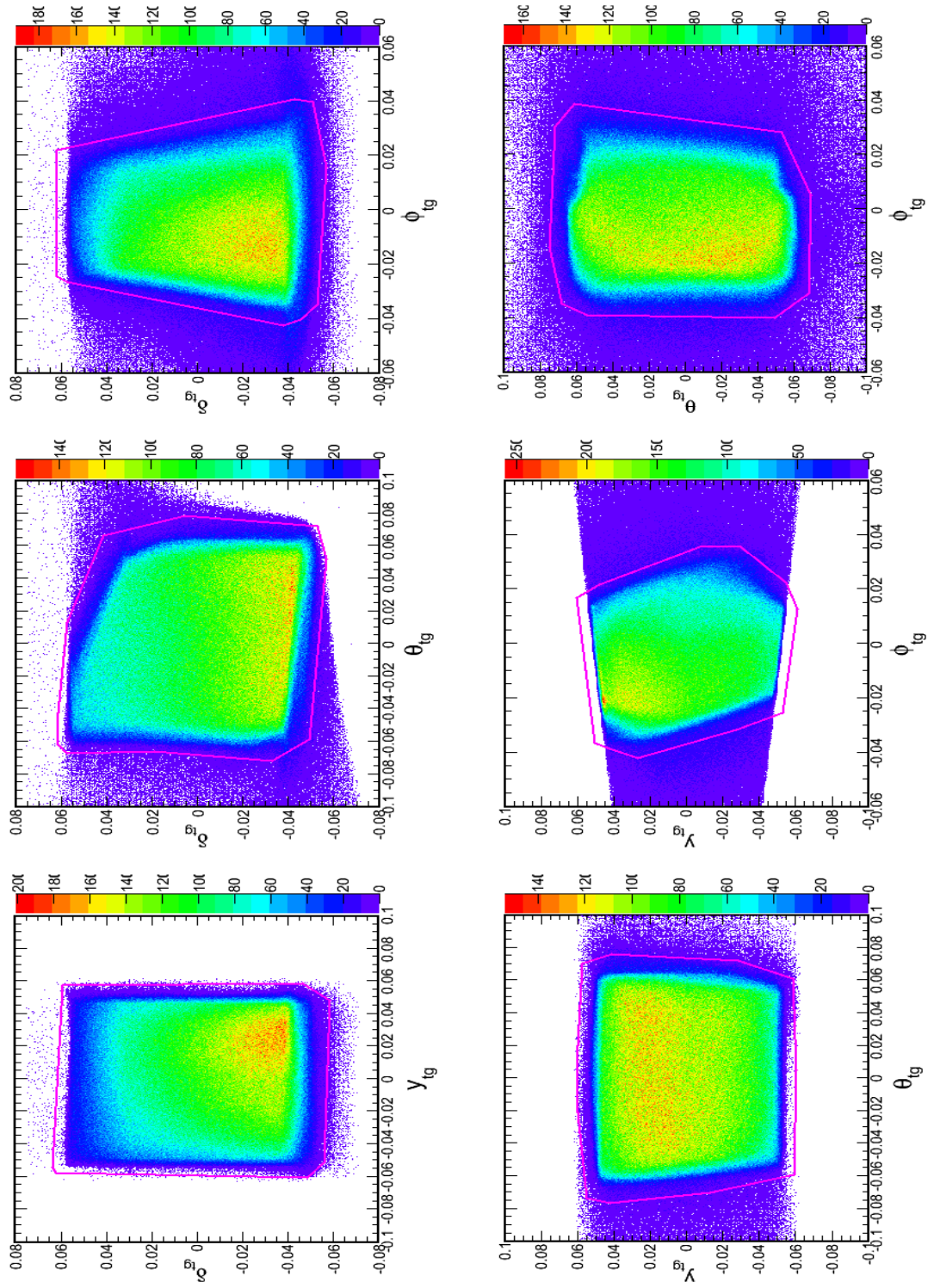
The LHRS acceptance cuts to select a good data sample of all the particles entering into the spectrometer were determined by a method based on utilizing the R-function formalism. This formalism allows to use equations of boundaries of a geometrical object to construct functions that are equal to 0 on the boundary of the object and have different signs inside and outside the object [88].

An R-function is a real valued function whose sign is completely determined by the signs of its arguments. A simple example of an R-function is $f(x, y) = 1 - (x^2 + y^2)$ which can be used to define a circle of radius 1. As mentioned above, the function $f = 0$ on the boundary (i.e. radius = 1) and $f > 0$ inside and $f < 0$ outside the boundary. Thus, the R-function behaves like a Boolean function and one can define different R-functions to incorporate various complicated geometrical cuts at the same time. In case of LHRS in Hall A, the acceptance of the spectrometer for a fixed beam position (x, y) depends on the following target variables:

- in plane angle ϕ_{tg}
- out-of-plane angle θ_{tg}
- position of the reaction point y_{tg}
- momentum fraction δ_{tg}

The LHRS acceptance is shown in Fig. D.1 on the next page where the 4-dimensional acceptance can be realized through the distribution of the variables δ_{tg} , θ_{tg} , ϕ_{tg} , and y_{tg} for a given x_{tg} . The solid line represents the cut in each plot. All events inside the cut were considered as *good events* and were chosen in the analysis [19]. The boundary is defined in such a way that $R=0$ at the boundary. In order to realize a good acceptance in the analysis, a cut $R=1$ was implemented. The reaction vertex cut applied in the analysis was ± 18.5 cm from the center of the target. Thus, the target windows were excluded.

Figure D.1: The acceptance cuts for the LHRS used in the analysis. The solid boundary represents the cuts. All the events inside the boundary were chosen for the asymmetry analysis [19].



Appendix E: TARGET WINDOW ASYMMETRY IN THE LHRS

The polarized ^3He cell used in the experiment was 40 cm long and made of glass (GE180). It had a diameter of ~ 2 cm. The ends were sealed with spherically shaped endcaps of the same glass material and are referred to as *target windows*. In the asymmetry analysis, these two target windows were excluded in order to avoid any kinds of false asymmetries that could be generated from them. The reaction vertex along the ^3He target with the target windows included is shown in Fig. E.1.

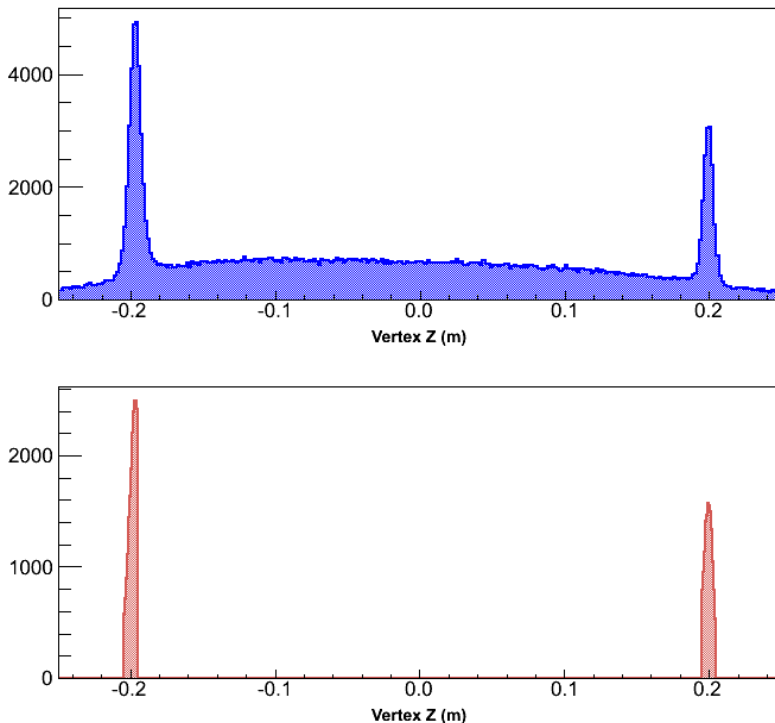


Figure E.1: The reaction vertex along the ^3He target with the target windows included (top) and the target windows only (bottom).

As a part of the false asymmetry analysis, the inclusive asymmetries for different particles in the LHRS emerging from the target windows were studied. A cut of ± 5 mm was used for both windows 0.20 m being the center for the windows for this particular asymmetry analysis, i.e., only the target windows were chosen excluding the rest of the length. In principle, since the target windows (i.e. glass) are unpolarized, all asymmetries determined by flipping the ^3He spins in the cell should be zero. However, we still see non-zero asymmetries

in the case of vertical target polarization. These asymmetries are small as compared to the inclusive ^3He asymmetries measured in the LHRS ($\sim 10\%$ of the ^3He asymmetries) for the detected particles. Fig. E.2 and Fig. E.3 show the target window asymmetries for different particles in the LHRS for both vertical and transverse ^3He polarizations¹. One possible explanation for the existence of these non-zero asymmetries in the vertical case can be the amount of ^3He still present inside the cuts applied to form the asymmetries. On the other hand, in the case of transverse magnetic field direction, the observed inclusive asymmetries are already consistent with zero and hence, even if there is some remaining ^3He gas inside the cuts, it would not have any contribution unlike in the vertical case.

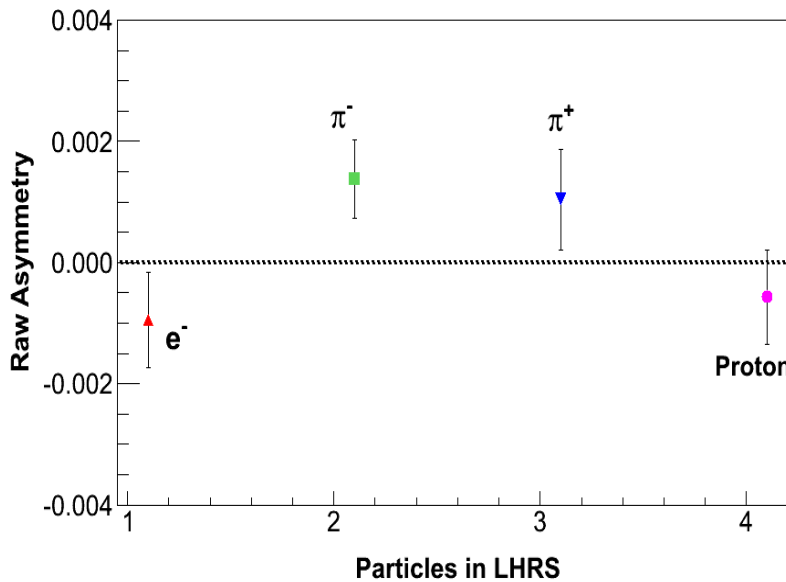


Figure E.2: The measured asymmetries from the target windows for the identified particles in the case of the vertical magnetic field configuration.

¹Here, the vertical and transverse ^3He polarization directions refer to the holding magnetic field directions. In principle, when only the target windows are chosen, there should not be any ^3He atoms and hence, for this particular analysis, ^3He polarization direction is irrelevant. The directions just represent the usual convention used in the analysis for the production data.

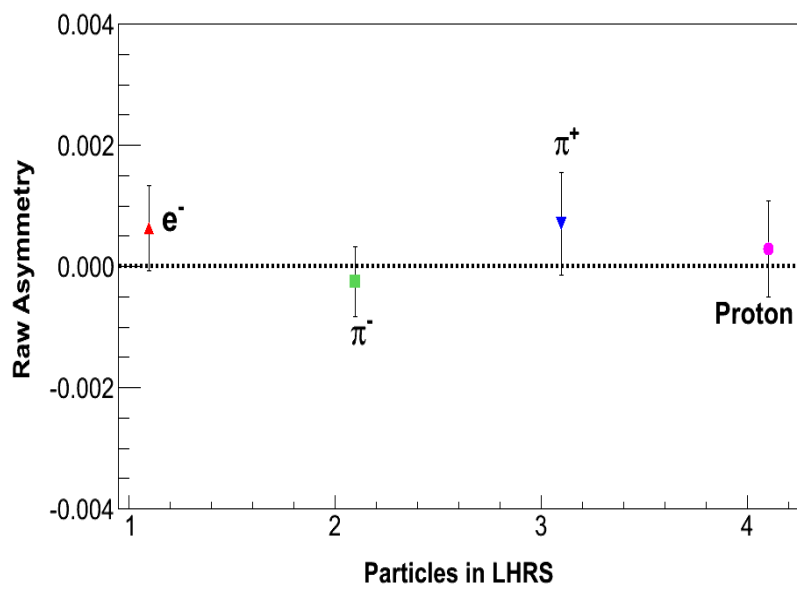


Figure E.3: The measured asymmetries from the target windows for the identified particles in the case of the transverse magnetic field configuration.

Appendix F: EXTRACTION OF THE NEUTRON SINGLE SPIN ASYMMETRY FOR SIDIS OFF TRANSVERSELY POLARIZED ${}^3\text{He}$

In the calculations presented by Scopetta *et al.* [26], a three body AV18 interaction model is used in the Impulse Approximation (IA) in order to realize a description of the nuclear dynamics. The formal expressions of the Collins and Sivers contributions to the azimuthal single spin asymmetries for π^- mesons have been derived, including the initial transverse momentum of the struck quark. In Ref. [26], extensive discussions are presented about a formalism to take into account the momentum and energy distributions of the bound nucleons inside the ${}^3\text{He}$ nucleus for the kinematics of E06010.

The Impulse Approximation (IA) approach in this case assumes that in semi-inclusive DIS, the interacting single neutron has no further interaction with the recoiling nuclear system or the produced hadron. In addition, it also assumes that the internal structure of the bound neutron is not any different from that of a free neutron. However, the nuclear dynamics in ${}^3\text{He}$ definitely affects the momentum and binding energy distributions of the bound neutron. This approximation has been used in the calculation of Collins and Sivers asymmetries of ${}^3\text{He}$. The extraction of the neutron Collins and Sivers asymmetries are presented after considering the effective polarizations of the neutrons and protons in ${}^3\text{He}$. The formalism to calculate the neutron and proton dilution factors by using the $x - z$ separation of the parton distribution and fragmentation functions is also discussed in Ref. [26]. Fig. F.1 shows the model calculations for the Collins and Sivers asymmetries for π^- mesons on the neutron.

The solid curve represents the full calculation of the asymmetries. The dotted curve assumes that the proton polarization in ${}^3\text{He}$ is zero, i.e. there is no nuclear effect and all the nucleons are in a pure S state in ${}^3\text{He}$. On the other hand, the dashed curve corresponds to the asymmetries extracted from the full calculation by taking into account the effective polarizations of both the neutron and the proton in ${}^3\text{He}$. In Fig. F.1, the asymmetries have been calculated as a function of x for different values of z at a Q^2 value of $2.2 \text{ GeV}^2/c^2$. The nuclear effects can be realized clearly in the plot showing the difference between the full curve and the dotted one. In the range of the x and z values relevant to E06010 (i.e. $0.13 < x < 0.41$ and $0.46 < z < 0.59$), this effect is $\sim 10\text{--}15\%$. However, the difference

between the full curve and the dashed curve is only a few percent. This indicates that the extraction of the neutron asymmetries from the ${}^3\text{He}$ asymmetries by using effective polarizations of the nucleons and dilution factors as expressed by Eq.(6.14) in chapter 6 can be reasonably well applied to the E06010 data. In addition, the processes that can be important beyond the Impulse Approximation (IA) include mainly nuclear shadowing¹ and final state interactions (FSI). However, in the kinematic range of E06010, the shadowing effects are negligible. On the other hand, as the π^- mesons produced in the reaction had a very high energy of 2.35 GeV and were within $0.46 < z < 0.59$, the effect of final state interactions is assumed to be small. The effect of final state interactions is being studied and more realistic models will be formulated in the future.

¹In DIS, it was found that the structure function of the bound nucleon is smaller than that of a free nucleon in the region $x < 0.1$. This phenomenon is called *nuclear shadowing*.

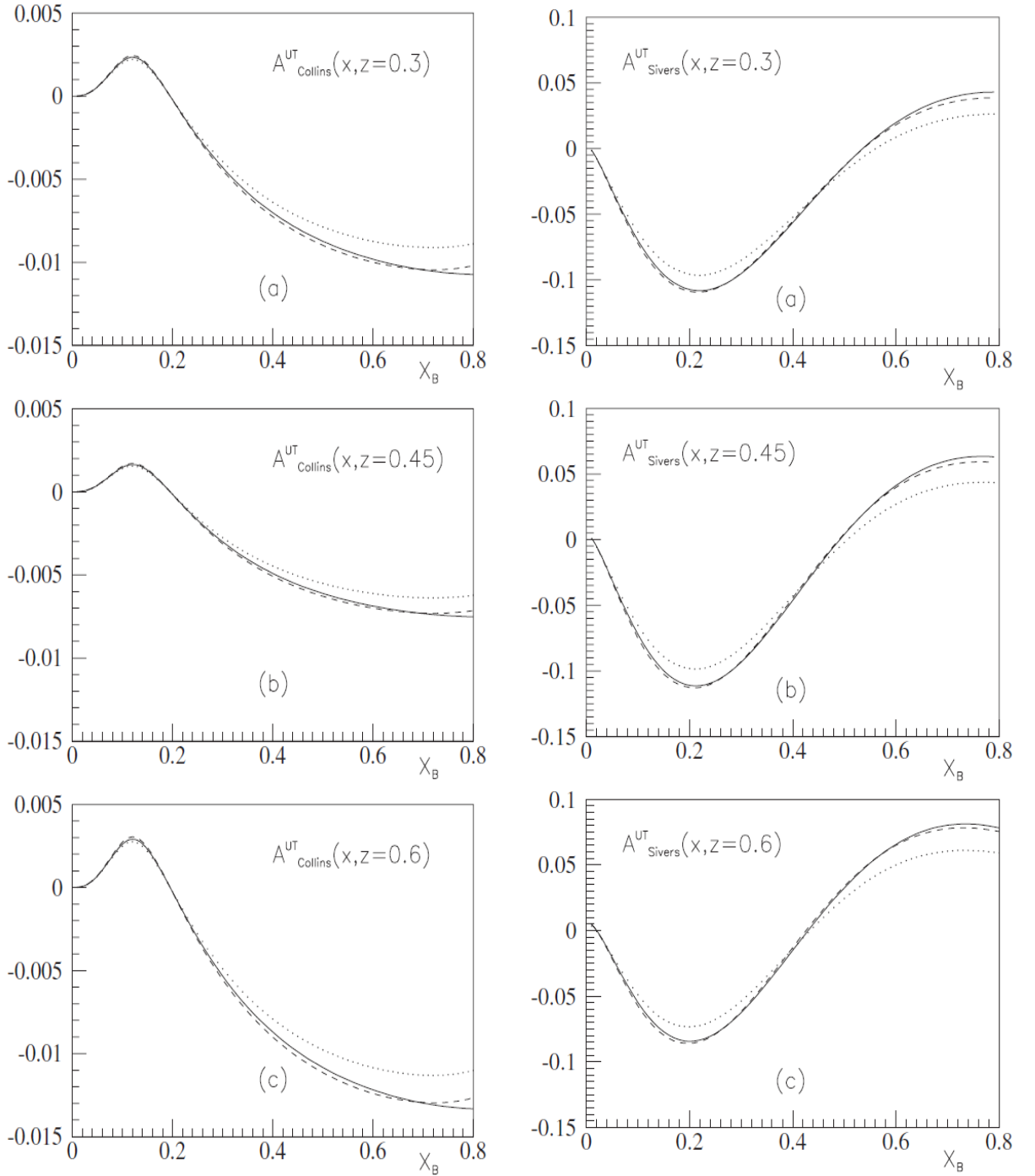


Figure F.1: The Collins asymmetry (left) and the Sivers asymmetry (right) of the neutron for the electroproduction of π^- mesons. The full curve shows the complete calculation of the asymmetries while the dotted curve represents the corresponding asymmetries with only neutron polarization. The dashed curve is the relevant one for our purpose where the effective polarizations of both neutrons and protons along with their dilution factors are taken into account. The plots are corresponding to $z = 0.3, 0.45,$ and 0.6 from the top to bottom panels. For all of them, a Q^2 value of $2.2 \text{ GeV}^2/c^2$ is considered. The figure is taken from Ref. [26].

Appendix G: SYSTEMATIC UNCERTAINTY BUDGET

The results of the Collins and Sivers moments for π^- mesons produced on ^3He nuclei as well as neutrons are attributed to the fitting of only the Collins and Sivers terms where the angular dependences are associated with $\sin(\phi_h + \phi_S)$ and $\sin(\phi_h - \phi_S)$, respectively. However, there are other terms such as *the Pretzelosity* corresponding to a $\sin(3\phi_h - \phi_S)$ dependence as well as $\sin(\phi_h)$ and $\sin(2\phi_h)$ terms due to small longitudinal polarization leaking into the transverse polarization. The higher order terms associated with $\sin(2\phi_h - \phi_S)$, $\sin(\phi_S)$, $\cos(\phi_h)$ (*Cahn effect*), $\cos(2\phi_h)$ (*Boer-Mulder effect*), etc. also contribute to the asymmetries. These are neglected in the fitting procedure. Nevertheless it is important to study the effect of neglecting these terms for the systematic uncertainty estimates. The absolute values of these contributions for neutrons are assumed to be equal or similar to those of protons as explained in Ref [18]. An extensive study was performed by X. Qian [18]. Table G.1 summarizes all the uncertainties associated with the different terms for π^- meson production in case of ^3He as well as the neutron. The systematic uncertainties are presented in the unit of statistical uncertainties of the fitting results. The uncertainties in the Collins and Sivers asymmetry moments are also extracted for all the four x bins used in E06010. They are reflected by the respective ranges presented in the table.

Table G.1: Systematic uncertainties contributing to the extracted asymmetries which are not included in the fitting procedure. The uncertainties presented in the table are in percent of the statistical error bars in the asymmetries. The contributions to the Collins and Sivers moments represent the uncertainty values in the four x bins used in E06010. In the calculation of the uncertainties for ^3He , the small dilution due to proton (-2.8%) was not taken into account.

Neglected terms	neutron (π^-)	^3He (π^-)	Collins (π^-)	Sivers (π^-)
$\sin(3\phi_h - \phi_S)$	-	-	17-42%	24-75%
$\sin(\phi_h), \sin(2\phi_h)$	3%	0.6%	< 0.1%	< 0.1%
$\sin(\phi_S)$	5%	1%	30-47%	32-49%
$\sin(2\phi_h - \phi_S)$	2%	0.4%	10-11%	28-32%
$\cos(\phi_h)$	5%	5%	1-7%	1-4%
$\cos(2\phi_h)$	5%	5%	1-3%	1-3%

BIBLIOGRAPHY

- [1] W. C. Chen, T. R. Gentile, T. G. Walker, and E. Babcock, *Phys. Rev. A* **75**, 013416 (2007).
- [2] J.I. Friedman, *Ann. Phys* **10**, (2001).
- [3] S. Bethke, arXiv:hep-ph/0908.1135v2 (2009).
- [4] W.M. Yao *et al.*, (PDG), *Phys. G* 33,1, 2006.
- [5] A. Drago V. Barone and P.G. Ratcliffe, *Phys. Rept.* **359**, 1 (2002).
- [6] M. Diefenthaler, arXiv:hep-ex/0706.2242v2 (2007).
- [7] M. Alekseev, *Phys. Lett. B* **673**, 127 (2009).
- [8] S. Levorato, arXiv:hep-ex/0808.0086v2 (2008).
- [9] Yi Qiang, Private Communication.
- [10] A. Kolarkar, Ph.D. thesis, University of Kentucky, 2008.
- [11] K. Slifer, Ph.D. thesis, Temple University, 2004.
- [12] J. Alcorn *et al.*, *Nuclear Instruments and Methods in Physics Research Section A: Accelerators, Spectrometers, Detectors and Associated Equipment* **522**, 294 (2004).
- [13] Y. Qiang, Ph.D. thesis, Massachusetts Institute of Technology, 2007.
- [14] A. Gavalya, Private Communication.
- [15] Kalyan Allada, Ph.D. thesis, University of Kentucky, 2010.
- [16] R. Michael, <http://hallaweb.jlab.org/equipment/daq/trigger.html>, 2003.
- [17] G. Phelps, Private communication.
- [18] Xin Qian, Ph.D. thesis, Duke University, 2010.
- [19] Jin Huang, Private Communication.
- [20] D. L. Adams *et.al*, *Phys. Lett. B* **264**, 462 (1991).

- [21] M. Anselmino *et al.*, Phys. Rev. D **71**, 074006 (2005).
- [22] B. Pasquini, Private communication.
- [23] B.Q. Ma and I. Schmidt, J.Phys G **24**, 71 (1998).
- [24] J. She, Private communication.
- [25] Progress in Particle and Nuclear Physics **61**, 2008.
- [26] S. Scopetta, Phys. Rev. D **75**, 054005 (2007).
- [27] M. Gell-Mann, Phys. Lett **8**, 214 (1964).
- [28] G. Zweig, CERN pre-print 8182/TH 401, 1964.
- [29] M. Gell-Mann, California Institute of Technology Synchrotron Laboratory Report, CTSL-20 (1961).
- [30] Y. Ne'eman, Nucl. Phys. **26**, 222 (1961).
- [31] J.D. Bjorken, arXiv:hep-ph/0008048v1 **1**, (2000).
- [32] S. Capstick, arXiv:hep-ph/0012238v1 **1**, (2000).
- [33] E. D. Bloom, D. H. Coward, H. DeStaebler, J. Drees, G. Miller, L. W. Mo, R. E. Taylor, M. Breidenbach, J. I. Friedman, G. C. Hartmann, and H. W. Kendall, Phys. Rev. Lett. **23**, 930 (1969).
- [34] M. Breidenbach, J. I. Friedman, H. W. Kendall, E. D. Bloom, D. H. Coward, H. DeStaebler, J. Drees, L. W. Mo, and R. E. Taylor, Phys. Rev. Lett. **23**, 935 (1969).
- [35] J. D. Bjorken, Phys. Rev. **179**, 1547 (1969).
- [36] A. Pich, arXiv:hep-ph/950523v1 **1**, (1995).
- [37] Y. Nambu and A. Shalit, *Precludes in Theoretical Physics*, North Holland, Amsterdam 133 (1966).
- [38] Y. Nambu and M. Y. Han, Phys. Rev. D **10**, 674 (1974).
- [39] G.S. Bali, Phys. Rept. **343**, 1 (2001).

- [40] G. Baum *et al.*, Phys. Rev. Lett. **51**, 1135 (1983).
- [41] M.J Alguard *et al.*, Phys. Rev. Lett. **37**, 1258 (1976).
- [42] John Ellis and Robert Jaffe, Phys. Rev. D **9**, 1444 (1974).
- [43] J. Ashman *et al.*, Phys. Lett. B **206**, 364 (1988).
- [44] J. Ashman *et al.*, Nucl. Phys.B **328**, 1 (1989).
- [45] F. Bradamante, Progress in Particle and Nuclear Physics **61**, 229 (2008).
- [46] M. Anselmino *et al.*, arXiv:hep-ph/0701006 (2007).
- [47] M. Burkardt, Phys. Rev. D **66**, 114005 (2002).
- [48] D. Sivers, Phys. Rev. D **41**, 83 (1990).
- [49] J.C. Collins, Nucl. Phys.B **396**, 161 (1993).
- [50] J.D. Bjorken and S.C. Drell, *Relativistic quantum fields* (Mc.Graw-Hill, New York, USA, 1965).
- [51] A. Efremov M. Anselmino and E. Leader, Phys. Rept. **261**, 1 (1995).
- [52] J. P. Chen, The European Physics Journal **162**, 103 (2008).
- [53] B. Adeva *et al.*, Phys. Rev. D **60**, 072004 (1999).
- [54] B. Adeva *et al.*, Phys. Rev. D **58**, 112001 (1998).
- [55] D. Reggiani, *Precise result of g_1^p and g_1^d and First Measurement of the Tensor Structure Function b_1^d with the HERMES Experiment* 13th International Workshop on DIS (2005), Madison, Wisconsin, 2005.
- [56] P.L. Anthony *et al.*, Phys. Lett. B **463**, 339 (1999).
- [57] P.L. Anthony *et al.*, Phys. Lett. B **493**, 19 (2000).
- [58] K. Abe *et al.*, Phys. Rev. D **58**, 112003 (1998).
- [59] P.L. Anthony *et al.*, Phys. Lett. B **553**, 18 (2003).
- [60] R.P. Feynman, Phys. Rev. Lett. **23**, 1415 (1969).

- [61] C.G. Callan and D.J. Gross, Phys. Rev. Lett. **33**, 156 (1969).
- [62] S.E. Kuhn J.P. Chen and E. Leader, arXiv:hep-ph/0812.3553v1 (2009).
- [63] G.T. Bodwin and J. Qiu, Phys. Rev. D **41**, 2775 (1990).
- [64] V.N. Gribov and L.N.Lipatov, Sov.J.Nucl.Phys **15**, (1972).
- [65] Y.L. Dokshitzar, Sov.Phys JETP **46**, (1977).
- [66] G. Altarelli and G. Parisi, Nucl. Phys.B **126**, 298 (1977).
- [67] R.L. jaffe, arXiv:hep-ph/9602236v1 (1996).
- [68] J. Soffer, Phys. Rev. Lett. **74**, 1292 (1995).
- [69] D.W. Sivers, Phys. Rev. D **41**, 83 (1990).
- [70] A. Metz A. Bacchetta, R. Kundu and P.J. Mulders, Phys. Lett. B **506**, 155 (2001).
- [71] G. Ingelman B. Anderson, G. Gustafson and T. Sjostrand, Phys. Rept. **97**, 31 (1983).
- [72] B. Anderson, Camb. Monogr. Part. Phys. Nucl. Phys. Cosmol **7**, 1 (1997).
- [73] R. Sassot D.de Florian and M. Stratmann, arXiv:hep-ph/007.1506v1 (2007).
- [74] A. Bacchetta *et al.*, arXiv:hep-ph/0611265 (2007).
- [75] A. Bacchetta *et al.*, Phys. Rev. D **70**, 117504 (2004).
- [76] Luciano Libero Pappalardo, Ph.D. thesis, 2008.
- [77] A. Airapetian *et al.*, Phys. Rev. Lett. **94**, 012002 (2005).
- [78] M. Diefenthaler, arXiv:hep-ph/0507013 (2005).
- [79] V.Y. Alexakhin *et al.*, Phys. Rev. Lett. **94**, 202002 (2005).
- [80] Alessandro Bacchetta, Ph.D. thesis, 2002.
- [81] M. Anselmino *et al.*, Phys. Rev. D **65**, 114014 (2002).
- [82] M. Anselmino *et al.*, Phys. Rev. D **60**, 054027 (1999).
- [83] J.P. Ma X. Ji and F. Yuan, Phys. Lett. B **597**, 299 (2004).

- [84] J.P. Ma X. Ji and F. Yuan, Phys. Rev. D **71**, 034005 (2005).
- [85] A. Airapetian *et al.*, arXiv:hep-ex/0906.3918v2 (2009).
- [86] Christoph W. Leemann *et al.*, Annual Review of Nuclear and Particle Science **51**, 413 (2001).
- [87] C.K. Sinclair *et al.*, Phys. Rev. ST Accel. Beams **10**, 023501 (2007).
- [88] X. Zheng, Ph.D. thesis, Massachusetts Institute of Technology, 2002.
- [89] <http://hallaweb.jlab.org/equipment/beam.html>.
- [90] Brad Sawatzky, Private communication.
- [91] <http://www.jlab.org/geraud/unser.html>.
- [92] K. Unser, IEEE Trans. Nucl. Sci. **28**, 2344 (1981).
- [93] Hall A Operational Manual, Jefferson Laboratory.
- [94] L. Todor C. Hyde-Wright and G. Laueissiere, Jefferson Lab Hall A technote, JLAB-TN-01-001 (1999).
- [95] <http://www.jlab.org/moller/e06-010.html>.
- [96] <http://www.jlab.org/fissum/vdcs/documentation/docs.html>.
- [97] P.A. Čerenkov, Phys. Rev. **52**, 378 (1937).
- [98] E. Cisbani *et al.*, Nuclear Instruments and Methods in Physics Research Section A: Accelerators, Spectrometers, Detectors and Associated Equipment **595**, 44 (2008).
- [99] A.P. Serebrov *et al.*, Phys. Rev. C **78**, 035505 (2008).
- [100] M. Ebert *et al.*, Lancet **347**, 1996.
- [101] P.J. Nacher and M. Leduc, J.Phys(Paris) **46**, 2057 (1985).
- [102] T.E. Chupp *et al.*, Phys. Rev. C **36**, 2244 (1987).
- [103] S. Appelt *et al.*, Phys. Rev. A **58**, 1412 (1998).
- [104] W. Happer *et al.*, Rev. Mod. Phys. **44**, 169 (1972).

- [105] Earl Babcock *et al.*, Phys. Rev. Lett. **91**, 123003 (2003).
- [106] F.M. Pipkin L.W. Anderson and J.C. Baird, Phys. Rev. **116**, 87 (1959).
- [107] K. Kramer, Ph.D. thesis, The College of William and Mary, 2003.
- [108] M.V. Romalis, Ph.D. thesis, Princeton University, 2003.
- [109] M.V. Romalis and G. Cates, Phys. Rev. A **58**, 3004 (1998).
- [110] A. S. Barton, N. R. Newbury, G. D. Cates, B. Driehuys, H. Middleton, and B. Saam, Phys. Rev. A **49**, 2766 (1994).
- [111] N. R. Newbury, A. S. Barton, P. Bogorad, G. D. Cates, M. Gatzke, H. Mabuchi, and B. Saam, Phys. Rev. A **48**, 558 (1993).
- [112] M.V. Romalis and G.D. Cates, Phys. Rev. A **58**, 3004 (1998).
- [113] J. Singh, Private communication.
- [114] Jaideep Singh, Ph.D. thesis, University of Virginia, 2010.
- [115] <http://halloweb.jlab.org/experiment/transversity/>.
- [116] ROOT webpage, <http://root.cern.ch/drupal/>.
- [117] Nilanga Liyanage, Jefferson Lab Hall A technote, JLAB-TN-02-012 (2002).
- [118] R.G. Roberts, *The Structure of the Proton* (Cambridge University Press, New York, USA, 1990).
- [119] A. Amroun, Nucl. Phys A **579**, 596 (1994).
- [120] T.W. Donnelly and A.S. Raskin, Annals of Phys. **169**, 247 (1986).
- [121] A. Deur, Jefferson Lab Hall A technote, JLAB-TN-01-004 (2000).
- [122] Hassan Ibrahim *et al.*, Jefferson Lab Hall A technote, JLAB-TN-02-032 (2002).
- [123] J. Katich, Ph.D. thesis, College of William and Mary, 2010.
- [124] J. P. Chen, Private Communication.
- [125] J.L. Friar *et al.*, Phys. Rev. C **42**, 2310 (1990).

- [126] R.C. Seidl, arXiv:hep-ex/0607014 (2006).
- [127] S. Cazzaniga B. Pasquini and S. Boffi, Phys. Rev. D **78**, 034925 (2008).
- [128] B. Pasquini S. Boffi, A.V. Efremov and P. Schweitzer, Phys. Rev. D **79**, 094012 (2009).
- [129] Stanley J. Brodsky and Susan Gardner, Phys. Lett. B **643**, 22 (2006).
- [130] S. Gardner, Private Communication.

VITA

Chiranjib Dutta

- **Date and place of birth:**

- January 29, 1980; Tinsukia, India.

- **Educational institutions attended and degrees awarded:**

- University of Kentucky, Ph.D. 2010 (expected)

- **Professional positions held:**

- Research Assistant, University of Kentucky, 2005-2010

- Teaching Assistant, University of Kentucky, 2003-2005

- **Scholastic and professional honors:**

- Recipient of JSA Travel Fellowship, 2009

- Recipient of DNP Travel and Registration Grant, 2009

- Nominated by the Department of Physics and Astronomy, University of Kentucky for the graduate fellowship, 2008

- Recipient of University of Kentucky Huffaker Travel Grant, 2007

- Recipient of the Southeastern Universities Research Association (SURA) fellowship, 2007

- State scholarship for holding a position in top 50 students in Higher Secondary Certificate Examination in the entire state among 50000+ students, 1997

- Ranked 1st in the High School Leaving Certificate Examination in the entire state among 90000+ students (STATE GOLD MEDAL, 1995)

- **Professional Publications:**

1. **Hard Photodisintegration of a Proton Pair**, I. Pomerantz *et al.*, *Phys. Lett. B* **684**:106-109, (2010); e-print : nucl-ex/0908.2968

2. **The Proton Elastic Form Factor Ratio $\mu_p G_E^p/G_M^p$ at Low Momentum Transfer**, G. Ron *et al.*, *Phys. Rev. Lett.* **99** 202002(2007); e-print : nucl-ex/0796.0128